Modelling the Rocking Dynamics of Objects with Irregular Geometry



M. David Burton

Brasenose College

University of Oxford

A thesis submitted for the degree of

Doctor of Philosophy

Trinity 2022

This thesis is dedicated to Grace, my consistent supporter, lockdown sanity provider, and fellow adventurer. Moving overseas, navigating the pandemic, and completing our work in Oxford would not have been possible without you. I'm excited for the places we'll go from here...

Soli Deo gloria

Acknowledgements

I express my sincere thanks to the Clarendon Fund for providing funding to pursue this research. I also thank my supervisor Manolis Chatzis for accepting me as his student and offering countless hours of support in order to produce this thesis. I certainly would not have completed this work without him. I am also grateful for Peter Walters, the Department's 3-D Printing Engineer, for his knowledge and expertise in 3-D modeling and printing related to this work.

In addition to the professional and academic support I received, I also acknowledge the contributions of many people to my time in Oxford. I greatly enjoyed the pre-pandemic lunches with other civil students, playing and coaching for the Oxford University Association Football Club, and getting to know many remarkable people at Brasenose, St Ebbes, and elsewhere.

Finally, I need to thank my family and in-laws for all the support they have provided us, and particularly for blessing our decision to move overseas. I am extremely grateful for my parents and their incomparable contribution to my educational and personal development that enabled me to complete this thesis.

Abstract

Free-standing objects are all around us. Computer monitors and towers, bottles, kitchen containers, museum artifacts, tables, chairs, and medical equipment are just a few of the objects which may be prone to rocking and toppling due to external forcing or support excitation. Many objects with irregular geometry are able to rock about their edges and vertices, twist, topple, and impact their support, and could thus pose hazards to the integrity of the object and also to surrounding structures, objects, and even human life. However, previous rocking models are not adequate to handle objects with irregular geometry due to their assumptions. Thus, this thesis aims to fill the knowledge gap of the dynamics of irregular objects by introducing new rocking models for planar and 3-D rocking which take into account the full irregular geometry of such objects. The planar rocking model assumes a rigid body and rigid support and fully considers sliding, free flight, and a variable location for the impulses at impact. The 3-D model similarly uses a rigid body and rigid support with a variable location for the impulses, but assumes no sliding or free flight, as it focuses on the pure rocking response of such systems and how this can lead to substantially more complicated responses of the body when taking into account the geometry. Examples of objects in both planar and 3-D rocking are provided and conclusions are drawn on the importance of irregular geometry, sliding, free flight, and a variable location for the impulse. Finally, the 3-D model is used to describe the rolling dynamics of various objects with curved geometry, offering a new dynamic model to describe these motions that is efficient and

qualitatively similar to the experimental dynamic responses.

Contents

1 Introduction **1**

1.1 Literature Review 2

1.2 Thesis Objectives & Outline 6

2 The Planar Rocking Dynamics of Objects with Irregular Geometry **9**

2.1 Introduction 9

2.2 Generalized Coordinates 12

2.3 Computational Geometry for an Irregular Body 15

2.4 Equations of Motion 19

2.4.1 Rocking Patterns 19

2.4.2 Patterns with Multiple Vertices Contacting Support Medium 20

2.4.3 Pattern without Contact Points 21

2.4.4 The Patterns of Motion and Their Constraints 21

2.4.5 The Degrees of Freedom and the Equations of Motion 24

2.5 Transitions Between Patterns 27

2.5.1 Transitions Without Impact 27

2.5.2 Transitions with Impact 29

2.5.3 Validity Conditions for Post-Impact Patterns 33

2.5.4 Energy-Based Transitions 37

2.5.5 Summary of Transitions 38

2.6 Numerical Integration of the Equations of Motion 39
2.7 Examples of the Planar Rocking Behavior of Bodies with Irregular Geometry 39
2.7.1 Example 1: Shelving Unit Subjected to Sinusoidal Pulses 39
2.7.2 Example 2: Shelving Unit Subjected to Earthquake 44
2.7.3 Example 3: Precariously Balanced Rock Subjected to Sinusoidal Pulses 47
2.7.4 Example 4: The *David* Sculpture Subjected to an Earthquake . . . 52
2.7.5 Example 5: The *David* Sculpture Subjected to Sinusoidal Pulses . . 55
2.7.6 Example 6: 3-D Terracotta Warrior Sculpture Constrained to Rotate in Plane and Subjected to Sinusoidal Pulses 58
2.8 Conclusions 62

3 The 3-D Pure Rocking Dynamics of Objects with Irregular Geometry 65
3.1 Introduction 65
3.2 Generalized Coordinates 67
3.3 3-D Computational Geometry 68
3.4 The Equations of Motion 71
3.4.1 Degrees of Freedom 71
3.4.2 Angular Velocity of the Body 73
3.4.3 Single Degree of Freedom Rocking Formulation 73
3.4.4 Lagrange's Equations of Motion 78
3.4.4.1 Kinetic Energy of the Body 79
3.4.4.2 Generalized Forces 79
3.5 3-D Patterns of Motion 80
3.6 Forces Acting on Body 82
3.7 Kinematic Constraints for Each Pattern 84
3.8 Solving the Equations of Motion 85
3.9 Transitions Between Patterns 87

3.9.1 Transitions Without Impact 88
3.9.2 Transitions Involving Impact 91
3.10 Impacts 91
3.10.1 Momentum Equations 91
3.10.2 Line Impacts 93
3.10.3 Surface Impacts 94
3.10.3.1 Location of Impulses 96
3.10.4 Post-Impact Kinematic Constraints 97
3.10.4.1 Post-Impact PR1 98
3.10.4.2 Post-Impact PR2 98
3.10.5 Verification of Impact Validity 99
3.10.6 Algorithmic Procedure for Surface Impacts 101
3.10.7 Energy-Based Transitions 101
3.11 Numerical Time Integration 103
3.12 Examples of 3-D Pure Rocking Dynamics 104
3.12.1 Example 1: The *Doryphoros* Sculpture Subjected to an Earthquake 105
3.12.2 Example 2: The *Doryphoros* Subjected to Sinusoidal Acceleration Pulses 109
3.12.3 Example 3: Investigating the Stability of the *Discobolus* Sculpture . 114
3.13 Conclusions 116

4 The Dynamics of Objects with Curved Surfaces 119

4.1 Introduction 119
4.2 Modeling Rolling Dynamics with Lagrange Multipliers 123
4.3 Examples of the Dynamics of Objects with Curved Geometry 130
4.3.1 Example 1: Right Prisms with Regular Polygonal Bases Subjected to Sinusoidal Pulses 130
4.3.1.1 Unidirectional Sinusoidal Pulses 131

4.3.1.2 Sinusoidal Pulses with Variable Direction 134
4.3.2 Example 2: Further Investigation of a Cylinder Under Free Vibration 138
4.3.3 Example 3: Euler's Disk 142
4.3.3.1 The Disk Set into Spinning Motion 142
4.3.3.2 The Disk Released from Rest 151
4.3.4 Example 4: The Rattleback 156
4.3.5 Example 5: The Gömböc 160
4.3.6 Example 6: The Tippe Top 164
4.3.6.1 Release from Rest 165
4.3.6.2 Release with Non-zero Initial Velocity 169
4.4 Conclusions 173

5 Conclusions **175**

5.1 Directions for Future Work 179

Bibliography **181**

List of Figures

2.1 Objects with irregular geometry which would exhibit planar rocking. 10
2.2 A rectangular rocking block. 12
2.3 A rigid body with an irregular geometry. 13
2.4 A 3-D triangulation of a rigid body extruded in the Z-direction. 15
2.5 A flowchart showing the steps required to manage the computational geometry of an irregular, concave body. 16
2.6 An irregular body with its convex hull shown and its angles with the horizontal defined. 18
2.7 The forces acting on a rocking rigid body. 20
2.8 The vectors and forces relevant to a rigid body in the static pattern or pure sliding with an edge of the convex hull contacting the support surface. . . . 20
2.9 An irregular body without contact with the support medium and reactions set to zero. 22
2.10 The five patterns of motion with their independent DOFs and constraints specified. (a) the static pattern with pin and roller contacts; (b) pure sliding with two rollers; (c) pure rocking with one pin; (d) slide rocking with one roller; (e) free flight with no contact with the support. 22

2.11 Upper diagram: From left to right shows an irregular body rocking on p, impacting the support surface, and continuing to rock on i. The open circles indicate the rocking vertices. Lower diagram: From left to right shows an irregular body in free flight, impacting the support surface at i, and returning to free flight. Positive velocity conventions are shown. 31
2.12 A flowchart displaying how impacts are handled where PR = Pure Rocking, SR = Slide Rocking, and FF = Free Flight. 36
2.13 Diagram showing the non-impact and energy-based transitions between the five patterns of motion. 38
2.14 Flowchart showing the overall structure of the code. 40
2.15 A shelving unit with several base configurations. a) Flat base. b) Quarter circle feet. c) Extensions on either side. d) Uneven feet. 41
2.16 Stability diagrams with boundaries between survival and failure marked. a) Initial positive (left) support acceleration. b) Initial negative (right) support acceleration. 43
2.17 Earthquake acceleration time history for the Chiapas, Mexico earthquake from 2017. The accelerations shown are scaled to 35% of those recorded. . 44
2.18 Each of the six states of the shelving unit with uneven feet when exposed to the Chiapas earthquake resulting in toppling failure. 45
2.19 Each of the six states of the shelving unit with raised extensions when exposed to the Chiapas earthquake resulting in survival. 45
2.20 The time history of θ and impact times for the shelving units with uneven feet and raised extensions when exposed to the Chiapas earthquake. 46
2.21 A diagram showing the shape, dimensions, and coordinate system for the PBR studied. 47
2.22 Stability diagrams for the PBR. (a) the results for an initial negative support acceleration; (b) the results for an initial positive support acceleration. . . . 48

2.23 Stability diagrams for the PBR with initial positive (left) support acceleration for different coefficients of friction μ. (a) $\mu = 0.75$; (b) $\mu = 0.5$. 49

2.24 Time histories of $\dot{X}_{op}$, Y_{op}, and θ for the PBR with the same pulse applied (point M from Figure 2.22a) but different μ. (a) The horizontal velocity $\dot{X}_{op}$ of the active rocking vertex. (b) The vertical position Y_{op} of the active rocking vertex (or the last rocking vertex in the case of free flight). (c) The angle θ of the body. 50

2.25 Representations of Michelangelo's *David*. (a) The sculpture without a pedestal; (b) the sculpture with a solid pedestal; (c) a detail of the solid pedestal; (d) a detail of the hollow pedestal; (e) a detail of the chamfered pedestal; (f) a detail of the solid pedestal with small triangular feet at b and c. 53

2.26 Support accelerations from the Rocchetta, Italy earthquake in October 2016. 53

2.27 The time histories of each state of $\boldsymbol{Q}$ for the *David* without a pedestal and $\mu = 0.5$, $\epsilon = 0.1$, and $\lambda = 0$. (a) θ; (b) $\dot{\theta}$; (c) X_{oc}; (d) Y_{oc}; (e) $\dot{X}_{oc}$; (f) $\dot{Y}_{oc}$. The labels PR and SR on the time histories correspond to the beginning of pure rocking and slide rocking, respectively. 54

2.28 The time histories of θ for the $David$ with no pedestal, the solid pedestal with $\lambda = 0$, and the hollow pedestal. 55

2.29 A diagram showing the survival and failure boundaries for the various base conditions of the *David* sculpture. 56

2.30 An STL representation of a terracotta warrior from Shaanxi, China. (a) a front view of the sculpture with the body's centroid vertically aligned with the centroid and geometric center of the pedestal; (b) a rear view of the sculpture; (c) a depiction of the eccentricity of 0.008 m applied to the pedestal. The dashed and solid lines correspond to the outline of the centered and 0.008 m offset pedestal respectively. 59

2.31 Stability diagrams for the terracotta warrior sculpture with $\lambda = 0$. (a) no eccentricity; (b) 1% eccentricity and an initial positive support acceleration; (c) 1% eccentricity and an initial negative support acceleration. 61
2.32 The time history for the active rocking vertex horizontal position and velocity, X_{op} and $\dot{X}_{op}$, for point K from Figure 2.31 showing slide rocking leading to failure. 62

3.1 An example of a rigid body with irregular geometry. 67
3.2 Detail A of the *Doryphoros* as referenced in Figure 3.1, showing a cutout of the triangulation of the STL file and the vertices and edges for two faces highlighted. 69
3.3 The *Doryphoros* with its convex hull triangulation superimposed. 70
3.4 The three sequential Euler angles forming a 2-3-1 combination. (a) ψ about $\boldsymbol{e}_y$. (b) θ about $\boldsymbol{e}_z^1$. (c) ϕ about $\boldsymbol{e}_x^2$. 71
3.5 *The Doryphoros* rotating about $\hat{\mathbf{n}}$ parallel to $E_{p_1p_2}$. Base R had the orientation shown by the $\mathbf{e}_x^{R_0}$, $\mathbf{e}_y^{R_0}$, $\mathbf{e}_z^{R_0}$ unit vectors when it began rocking about $E_{p_1p_2}$ at time t^* and subsequently rotated by γ about $\hat{\mathbf{n}}$ to give the base R unit vectors shown. 74
3.6 A rigid body with generalized force $\mathbf{F}_i$ acting at p_i. 80
3.7 Diagrams of the three patterns of motion. a) SP, b) PR1, and c) PR2 with their kinematic constraints and DOFs shown. 80
3.8 Diagrams depicting the forces acting on the *Doryphoros* in each pattern. (a) SP. (b) PR1. (c) PR2. 83
3.9 The base of an irregular body during SP showing its convex hull (blue line) and the location of r_x, r_z, and r_y, which is defined by X_{cr_y} and Z_{cr_y}. 83
3.10 A diagram showing the possible transitions between patterns in this pure rocking model. 88

3.11 The base of an irregular body in SP with its convex hull and three arbitrary paths showing possible paths of the location of F_y. Path 1 results in PR1 about point p_1, Path 2 results in PR2 about p_2 and p_3, Path 3 has no transition from SP. 89
3.12 A diagram showing (a) an object initially in PR2 with F_y between points p_1 and p_2 which define the edge. (b) at some time, F_y reaches point p_2 and the body begins PR1 about p_2. 90
3.13 A diagram of an irregular object experiencing a line impact: a) before impact the object rocks in PR1 about p^-, b) the object impacts the support at point p^+, and c) after impact the object rocks in PR1 about p^+. 93
3.14 The pre- and post-impact rocking vertices during a line impact with the impulses and bases S and P defined. 93
3.15 The *Doryphoros* sculpture experiencing a surface impact. a) the body rocks about p^-, b) the body experiences a surface impact, and c) the body continues rocking about i^* after impact. The vertices impacting the support are shown by the blue line along the base of the sculpture. 95
3.16 Two examples of a surface impact. a) shows an object initially in PR2 transition to PR1 after impact and b) shows an object initially in PR1 transition to PR2 after impact. The locations of the impulses j_x, j_y, and j_z are shown along with the pre- and post-impact rocking vertices. 96
3.17 An example of a surface impact with an object entering post-impact PR1 with the allowable range for ω^+ shown. 100
3.18 A flowchart showing the iterations and program flow for line and surface impacts in the irregular geometry model. 102
3.19 A flowchart showing the program flow for the full 3-D irregular geometry model. 104

3.20 The orientation of the *Doryphoros* sculpture at the beginning of the Kobe, Japan earthquake. 106
3.21 The support acceleration time history for the Kobe, Japan earthquake of 1995. 106
3.22 Plots of (a) the Euler angles and (b) the displacement of the centroid over time for the *Doryphoros* sculpture during the Kobe, Japan earthquake of 1995. 107
3.23 A plot of the *Doryphoros* support contacts and location of F_y for the first seven seconds of the Kobe, Japan earthquake. The small black points are the support contacts of the sculpture, the large black point is the projection of c on the base, the red line is the convex hull of the support contacts, and the blue line and points are the location of F_y over time. 108
3.24 Blue line: the minimum failure amplitude in g of the *Doryphoros* for sinusoidal pulses applied at various angles with frequency 0.5 Hz. Red line: the convex hull of the contact vertices showing the orientation of the base relative to the pulses. Black points: the actual contact vertices for the *Doryphoros*. Green dashed lines: two angles of β for which stability diagrams are made. The angle β is positive in the direction shown in the figure while the base is oriented with the centroid over o as shown by the unit vectors $\mathbf{e}_x$ and $\mathbf{e}_z$. 110
3.25 Stability diagrams for the *Doryphoros* under sinusoidal pulse support accelerations where red indicates failure by overturning and green indicates survival of the pulse. (a) $\beta = 60°$. (b) $\beta = 300°$. 111
3.26 Stability diagrams for the *Doryphoros* under single-cycle sinusoidal pulse support accelerations with $\beta = 60°$. (a) $\lambda = 0.15$. (b) $\lambda = 0.30$. 113
3.27 The initial position of the *Discobolus* sculpture before being subjected to the Kobe, Japan earthquake. 115

3.28 Plots of (a) the Euler angles and (b) the location of the centroid c of the *Discobolus* for the support accelerations produced by the Kobe, Japan earthquake of 1995. 116

4.1 Objects with curved surfaces that display rolling. 120

4.2 A diagram showing a portion of a rigid body with a curved surface and the contact point p_i over time for pure rocking and rolling models from time t_{start} to t_{end}. Black lines: A smooth curved surface. Orange lines and points: a polyhedral approximation of the curved surface. Blue line and points: the movement of the pure rocking vertex over time from vertex p_1, p_2, ..., p_7. Red line and points: the movement of the rolling contact p_i. . . . 124

4.3 A rigid body with three portions defined by three equations. Green surface: g_1, blue surface: g_2, and red surface: g_3. 125

4.4 A rigid body which depicts two curved surfaces defined by g_1 and g_2 in black, which connect at points P_1 and P_2. The convex hull of the body is shown with red dashed lines. 128

4.5 Polygonal base configurations with α^* defined for bodies tested with ground accelerations. 131

4.6 Stability diagrams for various base configurations and angles of application α. a) $\alpha = 0$ with selected $\alpha = \alpha^*$. b) $\alpha = 0.99\alpha^*$. 133

4.7 Time history of 1024-gon with variable-direction sine pulse applied. 135

4.8 Time history of 24-gon with variable-direction sine pulse applied. 136

4.9 The initial position of a solid cylinder with radius 0.051 m and height of centroid 0.069 m. Initial conditions: $\phi = \pi/6$ rad, $\psi = 0$, $\theta = 0.0812$ rad, $\dot{\phi} = -5$ rad/s, $\dot{\psi} = \dot{\theta} = 0$. (a) Euler angles in rad. (b) Displacement of centroid in m. (c) Euler angle time derivatives in rad/s. (d) Translational velocity of centroid in m/s. 138

4.10 The time history for a solid cylinder with radius 0.051 m and height of centroid 0.069 m. Initial conditions: $\phi = \pi/6$ rad, $\psi = 0$, $\theta = 0.0812$ rad, $\dot{\phi} = -5$ rad/s, $\dot{\psi} = \dot{\theta} = 0$. a) Euler angles in rad. b) Displacement of c in m. c) Time derivatives of Euler angles in rad/s. d) Velocity of c in m/s. 139

4.11 The location of the rocking vertex throughout the motion of the solid cylinder with radius 0.051 m and height of centroid 0.069 m. Line segments connect successive rocking vertices. The initial rocking vertex is set to $X_{op} = Y_{op} = 0$. Initial conditions: $\phi = \pi/6$ rad, $\psi = 0$, $\theta = 0.0812$ rad, $\dot{\phi} = -5$ rad/s, $\dot{\psi} = \dot{\theta} = 0$. 141

4.12 The initial position of Euler's disk (made from a 42-gon) before being released. Initial conditions: $\phi = 0.26$, $\psi = 0$, $\theta = 0$, $\dot{\phi} = \dot{\theta} = 0$, $\dot{\psi} = 20$. . . . 143

4.13 The time history of the spinning motion of Euler's disk. Initial conditions: $\phi = 0.26$, $\psi = 0$, $\theta = 0$, $\dot{\phi} = \dot{\theta} = 0$, $\dot{\psi} = 20$. a) Euler angles in rad. b) Displacement of c in m. c) Time derivatives of Euler angles in rad/s. d) Velocity of c in m/s. 144

4.14 A diagram showing the density of impacts for Euler's disk over time when released from rest. Each impact is drawn as a vertical line on the plot. Initial conditions: $\phi = 0.26$, $\psi = 0$, $\theta = 0$, $\dot{\phi} = \dot{\theta} = 0$, $\dot{\psi} = 20$. 144

4.15 Plots of the vertical reaction force F_y and the vertical impulse J_y for the spinning Euler's disk. 145

4.16 A plot of the time history for the 32-sided STL of Euler's disk. Initial conditions: $\phi = 0.26$, $\psi = \theta = 0$, $\dot{\phi} = \dot{\theta} = 0$, $\dot{\psi} = 20$. a) Euler angles in rad. b) Displacement of c in m. c) Time derivatives of Euler angles in rad/s. d) Velocity of c in m/s. 149

4.17 A plot of the time history for the 256-sided STL of Euler's disk. Initial conditions: $\phi = 0.26$ rad, $\psi = \theta = 0$, $\dot{\phi} = \dot{\theta} = 0$, $\dot{\psi} = 20$ rad/s. a) Euler angles in rad. b) Displacement of c in m. c) Time derivatives of Euler angles in rad/s. d) Velocity of c in m/s. 150

4.18 The initial position of Euler's Disk before being released. Initial conditions: $\phi = \pi/9$ rad, $\psi = 0$, $\theta = 0.01$ rad, $\dot{\phi} = \dot{\psi} = \dot{\theta} = 0$. 151

4.19 The time history of Euler's Disk as it vibrates freely. Initial conditions: $\phi = \pi/9$ rad, $\psi = 0$, $\theta = 0.01$ rad, $\dot{\phi} = \dot{\psi} = \dot{\theta} = 0$. a) Euler angles in rad. b) Displacement of c in m. c) Time derivatives of Euler angles in rad/s. d) Velocity of c in m/s. 152

4.20 The location of the rocking vertex for the initial near surface impact of Euler's disk around 0.2 seconds. Line segments connect successive rocking vertices and the first rocking vertex is set to $X_{op} = Z_{op} = 0$. The lines and points marking the rocking vertex locations are displayed as darker as time goes on. Initial conditions: $\phi = \pi/9$ rad, $\psi = 0$, $\theta = 0.01$ rad, $\dot{\phi} = \dot{\psi} = \dot{\theta} = 0$. 153

4.21 The location of the rocking vertex for the motion of the Euler's Disk until its energy is spent. Line segments connect successive rocking vertices and the first rocking vertex is set to $X_{op} = Z_{op} = 0$. The lines and points marking the rocking vertex locations are displayed as darker as time goes on. Initial conditions: $\phi = \pi/9$, $\psi = 0$, $\theta = 0.01$, $\dot{\phi} = \dot{\psi} = \dot{\theta} = 0$. 154

4.22 The location of the rocking vertex of Euler's Disk from 0.79 seconds to 0.84 seconds. Line segments connect successive rocking vertices and the location of the rocking vertex at $t = 0.79$ seconds is set to $X_{op} = Z_{op} = 0$ and the lines and points marking the rocking vertex locations are displayed as darker as time goes on. Initial conditions: $\phi = \pi/9$, $\psi = 0$, $\theta = 0.01$, $\dot{\phi} = \dot{\psi} = \dot{\theta} = 0$. 155

4.23 A diagram showing the density of impacts for Euler's Disk over time when released from rest. Each impact is drawn as a vertical line on the plot. Initial conditions: $\phi = \pi/9$ rad, $\psi = 0$, $\theta = 0.01$ rad, $\dot{\phi} = \dot{\psi} = \dot{\theta} = 0$. 155
4.24 The initial position of the rattleback when set in motion. 157
4.25 The time history of the rattleback's motion with initial conditions $\dot{\psi} = 6$ and $\dot{\phi} = \dot{\theta} = 0$. a) Euler angles in rad. b) Displacement of c in m. c) Time derivatives of Euler angles in rad/s. d) Velocity of c in m/s. 157
4.26 The outline of the rattleback and its rocking vertices depicted by points and connected by line segments. The line and point color turns darker as time goes on. The initial rocking vertex is set to $X = Z = 0$. 158
4.27 Diagrams showing the geometry and orientation of the gömböc in (a) its stable equilibrium and (b) in its rotated state from which it is released for dynamic analysis. 160
4.28 Time histories for all states of the gömböc during free vibration when released from rest with initial conditions: $\phi = 5\pi/12$ rad, $\psi = 0$, $\theta = 3.32$ rad, $\dot{\phi} = \dot{\psi} = \dot{\theta} = 0$. a) Euler angles in rad. b) Displacement of c in m. c) Time derivatives of Euler angles in rad/s. d) Velocity of c in m/s. 161
4.29 Phase space diagrams for X_{oc} and Z_{oc}. Positions are plotted in m and velocities in m/s. The dashed line shows the value of the DOF for which equilibrium will occur. 163
4.30 Images of the tippe top with its initial and overturned orientations depicted. 164
4.31 Diagrams of the initial position of the tippe top when released from rest with the initial rotations specified. 166
4.32 A time history for the tippe top released with $\theta = 0.52$ rad and with all other angles and velocities initially zero. a) Euler angles in rad. b) Displacement of c in m. c) Time derivatives of Euler angles in rad/s. d) Velocity of c in m/s. 166
4.33 μ_{min} over time for the top when released with initial condition: $\theta = \pi/6$ rad. 167

4.34 A time history for the tippe top released with initial conditions: $\phi = 2.27$ rad and with all other angles and velocities initially zero. a) Euler angles in rad. b) Displacement of c in m. c) Time derivatives of Euler angles in rad/s. d) Velocity of c in m/s. 168
4.35 A time history for the tippe top released with initial conditions: $\theta = 0.035$ rad and $\dot{\psi} = 100$ rad/s with all other angles and velocities initially zero. a) Euler angles in rad. b) Displacement of c in m. c) Time derivatives of Euler angles in rad/s. d) Velocity of c in m/s. 170
4.36 Plots of the location of the tippe top's centroid and rocking vertex over time. 170
4.37 Plot of μ_{min} over time during rocking and at impacts while the tippe top is spinning. 171

Chapter 1

Introduction

The dynamics of rocking objects, i.e. those that are not attached or fastened to their support medium, has been a topic of interest to researchers in engineering and physics for many decades. These primarily non-structural components may contribute to the majority of economic costs from earthquake damage and can be a life safety risk as well (2). Many objects of this type are subjected to vibration induced by earthquakes or other excitations, while others are more deliberately placed into motion by humans either by design or accident. These objects include art objects such as sculptures, pottery, and glasswork; expensive medical equipment in hospitals; ancient structures such as Greek and Roman columns; computer towers and monitors; bookcases; storage tanks; and even fine wines in bottles at a supermarket or warehouse. Other objects that are intentionally set in motion by humans include spinning coins or disks, toy tops, and a number of other objects, which are commonly set in motion for entertainment or education. Many individuals and organizations have an interest in understanding the dynamics of these objects, whether to protect them from damage due to their high value or for pure academic or entertainment purposes. Notably, most of the objects mentioned above do not have simple geometries, i.e., they are not rectangular prisms. Particularly, the most delicate and culturally important of these objects, such as sculptures, have irregular geometries, i.e., geometries that cannot

be approximated sufficiently by a simple geometric shape, with uneven mass distributions. Various objects with irregular geometry display rocking motions on a horizontal support surface and these motions are thus worth studying.

In recent decades, researchers have made considerable progress in understanding the non-linear dynamics of rocking rigid bodies (54; 57; 95; 89; 30). However, most previous research is typically focused on bodies with simple geometries such as rectangular blocks (88; 98; 33; 120) or cylinders (100; 63; 110), with more complicated geometries often being approximated by rectangular prisms (26; 96; 112). This thesis demonstrates that the irregular geometry of such objects and other factors mentioned above affect their response in both planar and 3-D motion, and therefore must be studied to accurately model their dynamics.

1.1 Literature Review

To study the behavior of rocking objects, appropriate mathematical and physical models are required. Housner postulated one of the first dynamic models for rocking in 1963, dubbed the inverted pendulum model (IPM), which examined the planar behavior of a rectangular rocking block (54). Housner introduced several assumptions in his model including the rocking response being planar, the body and foundation being rigid, the angular momentum of the body being conserved about the post-impact rocking vertex, and sliding and free flight being neglected. This model allows for a qualitative understanding of the rocking response of a body and is hence still the most popular model in the literature. Several studies on the rocking response of bodies have been conducted using the IPM (98; 106; 118).

Researchers have shown that removing some of Housner's initial assumptions affect the response of a rocking body in a potentially nonconservative manner. Ishiyama introduced a planar model that examined both sliding and free flight giving six possible types of motion: rest, slide, rotation, slide rotation, translation jump, and rotation jump, finding that sliding

and free flight should both be considered (57). Shenton and Jones provided a detailed formulation of a planar rocking model for rigid bodies accounting for sliding and free flight on which the planar irregular geometry model introduced in this thesis builds (95; 56). Lipscombe and Pellegrino showed experimentally and numerically that the transition to free flight of rocking rigid bodies becomes more critical as the blocks become more stocky, i.e. as the distance between the support contacts increases relative to the height of the centroid from the support surface, moreover proving that bouncing and free flight should not be neglected in the solution to the rocking problem (89). Additionally, 3-D motion, a variable location for the impulse at impact, and support deformability have been shown to produce nonconservative rocking results compared to Housner's model. These topics are discussed in more detail in the following.

More broadly, rocking researchers have conducted studies with foci on a number of different aspects of rocking. These include studies on deformable bodies (111; 12; 13), structural components such as columns and frames (116; 36; 46; 4; 5; 38), deformable supports (30; 33; 116; 64), modifications for rocking (7; 51; 14; 67), the risk or probability of failure for rocking objects (117; 38; 50; 49; 68), and systems or assemblies of rocking bodies (8; 71; 41; 32). Each of these areas of study has been proven important for rocking. Detailed discussion of the risk of rocking objects can be found in (49).

The primary topic of research for this thesis is the rocking dynamics of objects with irregular or arbitrary geometry. Several researchers have made an initial step toward irregular geometries by studying simple block geometries and including parameters to account for eccentricity in the center of mass compared with the geometric center of the block in both 2-D and 3-D (86; 120; 23; 10; 3). However, these models have omitted sliding and free flight. Such a treatment does not account for other important consequences of an irregular geometry, such as the existence of multiple potential rocking vertices. A further consequence of multiple rocking vertices in irregular objects is that it becomes difficult to characterize such objects as slender or stocky due to the many equivalent heights and

widths for every possible orientation of the body. These studies have shown that bodies with centroidal eccentricity may overturn more easily than their symmetric counterparts but they do not take into account irregular base geometries, i.e., any base other than a flat one with two potential rocking vertices.

Another assumption of Housner's IPM is that the resultant of the vertical impulse at impact occurs at the post-impact rocking vertex. Consequently, the reduction of energy due to an impact is uniquely determined by the geometry of the block (54). The same assumption is used in other studies (119; 117; 37; 113). However, experimental results have been shown to differ from the theoretical values for this reduction of energy factor (87; 11). Chatzis et al. showed that the location of the vertical impulse for a block does not have to be at the post-impact rocking vertex but is permitted to be between the post-impact rocking vertex and the midpoint of the impacting base (31). Varkonyi et al. have extended the 2-D model presented in (31) to 3-D to consider a variable location of the impulse for a 3-D rectangular prism (108). The effect of the location of the impulse is also important for irregular geometries and thus is an integral part of the models presented in this thesis.

Researchers have more recently begun studying rocking in 3-D. Chatzis and Smyth first examined 3-D rocking with two models for a block rocking on a deformable support that fully account for both sliding and free flight, finding that analyzing blocks in 3-D is essential in order to reach more accurate conclusions regarding their response (33). This work proved that critical sections do not exist for 3-D rocking due to twisting that can cause failure when it would not occur in a planar model. Other researchers have also examined the 3-D response of rigid blocks on rigid supports. Zulli et al. considered a 3-D rigid body and support model that examined homogeneous rectangular blocks as well as those with eccentric centroids (120). These studies have confirmed that studying blocks in 3-D is important to more accurately and conservatively model their response. Rocking cylinders have also been studied in 3-D arising from free vibration (100) and earthquakes (115; 110). Other studies have been done on rocking blocks and suitcases with wheels

(29; 85). Previous researchers have not numerically studied the rocking of irregular shapes without major geometric simplification or while taking into account the potential for more than four rocking vertices, an eccentric configuration of the body's centroid, and a variable location for the impulse at impact. Chapter 3 of this thesis will thus address all of these knowledge gaps.

A number of researchers have specifically studied museum artifacts and ancient structures as they consist of some of the most valuable objects prone to rocking. Studies on artifacts and their response to vibrational excitations have been conducted both numerically and experimentally. Manos and Demosthenous experimentally studied the effect of earthquakes on ancient Greek and Roman columns modeled as rigid bodies resting on their foundation (72) and several researchers have studied rocking for museum artifacts using rigid block or rectangular planar rocking approximations opposed to studying the full irregular geometry (6; 69; 19; 73). The rigid block approximation methods may work for some museum artifacts but many museum artifacts have geometries much different from a rectangular block and thus more attention should be paid to their irregular geometry. Berto et al. studied Michelangelo's Galleria dei Prigioni sculptures, assessing their seismic risk to planar rocking and overturning by studying approximate rectangular blocks with their centroid projected on a rectangular plane (19). The original geometry of the block was not used, and only the planar rocking response of the bodies were tested. These previous models for museum sculptures do not allow for more than two rocking vertices or consideration of the 3-D irregular geometry or 3-D motion of museum sculptures. This knowledge gap will also be filled by Chapter 3, where a 3-D irregular geometry rocking model will be introduced and applied to museum sculptures.

The rocking of curved objects, i.e., those that have curved surfaces opposed to only flat faces, has been limited to the study of cylinders by previous rocking researchers leaving more irregular curved objects such as toy tops, disks, and other objects and their characteristic spinning and rolling motions to be studied by other means, if at all. These curved objects are

studied by various researchers in engineering and physics using rolling models that employ a continuous rolling or sliding contact. An overview of these models will be provided in Chapter 4 and the irregular geometry rocking model introduced in Chapter 3 will be shown to be valuable when considering the motions of various curved objects: the counterintuitive 3-D motion of cylinders, the spinning motion of Euler's disk, the peculiar reversal of spin direction of the rattleback, the fascinating geometric and equilibrium parameters of the gömböc, and the overturning or inversion of a tippe top when spun. Chapter 4 will examine the dynamics of these curved geometries and the insights that the model introduced in this thesis produces for them. The background literature on each of the curved objects mentioned above will be presented in the introduction of Chapter 4.

The objectives of this thesis include expanding the study of rocking to include objects with any irregular geometry and to determine how different parameters such as the base configuration, geometry, pulse type, sliding, free flight, assumptions about the impulse at impact, and 3-D motion affect the dynamic response and stability of various objects. This thesis looks at rigid bodies on rigid supports as a first foray into irregular geometries to obtain results that focus on the geometry of rocking objects with minimal computational cost. While deformable bodies and supports are certainly valuable pursuits, the models presented here may provide building blocks upon which the study of these wider topics can be built for objects with irregular geometry.

1.2 Thesis Objectives & Outline

This thesis addresses the knowledge gap in the study of the rocking dynamics of irregular bodies by introducing two new models (2-D and 3-D) that can examine the motion of a body with an irregular polygonal geometry when subjected to a vibrational excitation or dynamic initial conditions. The content of this thesis is organized in three main chapters. The first covers the 2-D model and important findings derived from its application to a

number of planar rocking problems. The second chapter introduces the 3-D rocking model and presents the dynamic results of museum sculptures subjected to earthquakes and other forms of support acceleration. The final chapter examines the motion of objects with curved surfaces and the connection between pure rocking and their 3-D rolling motion. A number of irregular curved objects are studied and new insights are gleaned from each example.

Chapter 2 introduces the planar rocking model which utilizes the geometry of the body as an input, e.g., in the form of a stereolithography (STL) file (52) along with the object's density and any applied support accelerations. The planar model is designed for objects that can be assumed to experience planar rocking and takes into account sliding and free flight as well as a variable location for the vertical impulse at impact. The dynamic problem is formulated and solved using Newtonian equations of motion and impacts are treated as hard and instantaneous. A robust framework for integrating the occurring discontinuous equations of motion using ode45 (94; 40) and automatically detecting transitions between patterns of motion and impacts, using Matlab, is also included. Suitably chosen examples demonstrate the importance of accounting for the detailed irregular geometry and associated parameters such as the mass moment of inertia of the rocking body studied. It also proves the importance of considering the effect different base configurations have on an object's rocking response, a variable location for the vertical impulse at impact, and sliding and free flight motions which can produce greater instability than models that neglect such patterns. Overall, the 2-D model and the examples to which it is applied provide evidence that the dynamic response of irregular objects is substantially richer and more complex than objects with simplified geometry.

Chapter 3 introduces the 3-D pure rocking model which expands the considerations of the planar model to the more broadly applicable 3-D geometry and rocking response of various objects. Three-dimensional objects from sculptures to toy tops can have intricate irregular geometry including holes, irregular locations of their centroids, and concave geometries and most are not kinematically or mechanically constrained to rotate in a plane. The 3-D model

employs similar functions and assumptions as the 2-D model with the added restriction that the object may not slide or enter free flight and is thus a "pure" rocking model. Instead of Newtonian equations of motion, the 3-D model uses a Lagrangian formulation and also solves several problems in computational geometry and those arising from more complex impact conditions to allow for the study of 3-D rocking dynamics. The first examples of irregular objects rocking due to earthquake and other support accelerations are provided and the importance of considering the 3-D geometry is shown.

Finally, Chapter 4 examines the 3-D model applied to objects that resemble curved surfaces but in reality have polyhedral geometry due to their manufacturing process, e.g., 3-D printing, or damage they have sustained. To the best of the author's knowledge, objects of this type are studied for the first time with a rocking model to offer new perspectives on the dynamics of such objects. The pure rocking model surprisingly provides a result of these dynamics that resembles rolling and thus allows for study of a variety of problems related to the dynamics of objects with curved surfaces. Examples are provided for cylinders and disks as well as for lesser known objects including rattlebacks, gömböcs, and tippe tops. Explanations for various interesting phenomena that these objects exhibit are provided including new insights into Euler's disk and simulations of the dynamics of the other objects.

Chapter 2

The Planar Rocking Dynamics of Objects with Irregular Geometry

2.1 Introduction

Planar rocking, where the body rocks in 2-D without out-of-plane motion, makes up the majority of previous rocking studies, and is an acceptable assumption for many cases. If an object has a base with a large length to width ratio, i.e., two or greater, or has a specific geometry such as the rocking horse pictured in Figure 2.1, it is likely that the object would undergo planar rocking if subjected to external forces or support accelerations. Examples of irregular objects which would display planar rocking are provided in Figure 2.1.

Each of these objects has a unique geometry overall, but of particular note are the differences their base configurations. The Egyptian sculpture has a stone base with a rough, uneven geometry underneath. The computer has an extruded, or uniform geometry in the approximate into-the-page direction, but has irregular rounded "feet", or protrusions in the geometry of the body that are usually designed to make contact with the support surface. Additionally, the geometry of the computer is such that other vertices of the body such as the labeled vertex s may be engaged as rocking vertices but may not necessarily result in



Fig. 2.1. Objects with irregular geometry which would exhibit planar rocking.

failure. The rocking horse is different from the other objects as it would be expected to rock with an angular velocity vector perpendicular to the base contacts shown in Figure 2.1 due to its geometry. However, the rocking horse's base configuration means it will exhibit rolling motion about its curved base and if tilted far enough in either direction would engage other rocking vertices such as the smaller curved feet on either end of the slats that make the horse's base. Finally, the table exhibits a roughly extruded geometry yet has a more detailed base configuration than might be seen at first glance. The small, circular feet of the table are common for many tables and actually allow for more than a single point of contact with the support in a similar way as the computer and rocking horse.

Each of these objects and many more display irregular geometry as well as the potential for planar rocking. However, the rocking of objects with such geometries, particularly those with irregular base configurations, has not been studied. The geometric properties of these bodies are much different than the simple rectangular block geometries commonly studied in the literature, and thus, this work introduces a model that takes into account the irregular polygonal geometry of any rigid body and allows for study of its planar rocking.

The multiple potential rocking vertices and interfaces resulting from such a geometry are taken into account along with sliding and free flight. The geometry of an object can be input to the model in the form of a stereolithography (STL) file commonly used in 3-D scanning and printing (52) and correspond to the projected geometry of the body in the expected plane of rocking. The equations of motion arising from the rocking formulation are used to study the dynamic response of objects under support excitations. This allows for the user to obtain dynamic rocking results for any 3-D rigid body that would be assumed to display planar rocking after specifying the geometry (STL), the density of the body, and the applied excitation. For easier comparison to Shenton and Jones' model (95), to maintain a low computational cost, and for simplicity, the assumptions of a rigid body and support are kept.

The model includes all possible patterns of motion related to sliding, rocking and free flight. The equations of motion are obtained in a unified manner using a Newtonian formulation and the implementation of kinematic constraint equations for each pattern. The resulting equations for the independent degrees of freedom (DOFs) are obtained symbolically in Matlab and are integrated numerically using a Runge-Kutta (4-5) formula, the Dormand-Prince pair (94; 40), which allows for automated event detection which find the time of transitions between patterns and impacts. Similarly, a unified framework is presented for dealing with impacts, which is capable of handling different post-impact patterns and different assumptions on the location of the vertical impulses during impact.

Finally, appropriate examples of the model for different irregular objects are presented. These examples include a shelving unit such as those found in warehouses, a precariously balanced rock (PBR), and studies on museum artifacts. Useful conclusions are produced on the rocking dynamics and interplay of irregular geometry, sliding, centroidal eccentricity, various base configurations, and a variable location of the impulse at impact.

2.2 Generalized Coordinates

Generally, previous research examined the dynamics of a rectangular block such as the one shown in Figure 2.2. This rectangular block has half-height h and half-width b. R is the length of the diagonal defined from the rocking vertex p to its centroid c and α is the angle between the long edge and R as shown in Figure 2.2. The coordinate axes X and Y are defined at the origin o on the support surface. The external forces f_x and f_y are applied at the centroid in the horizontal and vertical directions, respectively.

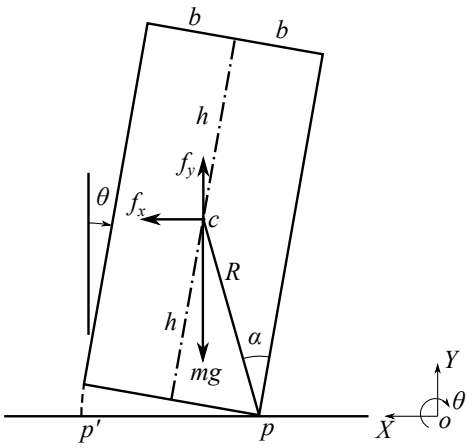


Fig. 2.2. A rectangular rocking block.

Without any loss of generality, Figure 2.2 demonstrates the body when it is rocking with respect to the right vertex p. The block has been rotated by an angle θ considered to be positive when clockwise. It is very likely that the weight and external forces applied on the block will cause a subsequent impact between the body and its support medium, after which the block will rotate about its left rocking vertex p'.

Most models, however, are limited to a rectangular block and do not allow for the analysis of a rigid body with an irregular geometry such as those shown in Figure 2.1. These bodies have irregular geometry but would also be expected to exhibit planar rocking due to the large length to width ratio of their bases. Another example of a rigid body is provided in Figure 2.3. The position vectors from the centroid c of each of the bodies in Figures 2.1

and 2.3 to each rocking vertex, and its angle with a reference axis, are not constant, making this a significantly more complicated problem than the rectangular block.

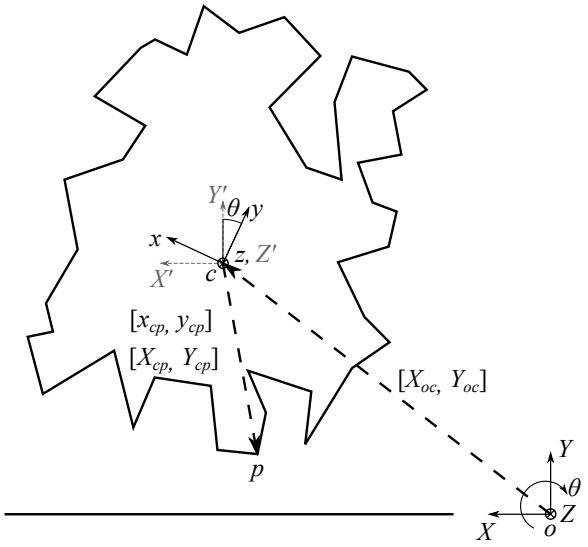


Fig. 2.3. A rigid body with an irregular geometry.

A system of Cartesian axes, base S denoted by $oXYZ$, is fixed on an origin o on the support surface as shown in Figure 2.3. An additional base S', parallel to base S, is fixed at the centroid of the body c with axes $cX'Y'Z'$ and the body has mass m. The Cartesian coefficients of the vector defined from point i to j, $\mathbf{r}_{ij}$, are denoted as the uppercase row vector $[X_{ij},\ Y_{ij},\ Z_{ij}]$. After the calculation of the object's physical parameters as will be discussed in the following section, the third dimension coordinates, Z_{ij}, can be ignored as rocking is constrained to the XY plane. Z_{ij} will normally be omitted from the presented coordinates throughout this chapter for conciseness as the rocking vertices of the objects studied are assumed to be homogeneous in the Z direction. The Cartesian coordinates of point i are defined as $[X_{oi},\ Y_{oi}]$. The additional coordinate system, base R denoted by $cxyz$, is fixed on the body. The coefficients of $\mathbf{r}_{ij}$ with respect to the rotating system are defined as the lowercase row vector $[x_{ij},\ y_{ij}]$. Note that for two points p_i and p_j both belonging to the rigid body, the coefficients $[x_{p_ip_j},\ y_{p_ip_j}]$ do not change as the body moves in space. It is convenient to create a registry of the vectors from the centroid to the vertices p_i, $i = 1, ..., N$ for the N vertices of the body.

A rotation matrix, $\mathbf{R}_\theta$, defined in the following equation (2.1) is used to transform from base R to the Cartesian base S':

$$\mathbf{R}_\theta = \begin{bmatrix} \cos\theta & \sin\theta \\ -\sin\theta & \cos\theta \end{bmatrix} \qquad [X_{ij},\ Y_{ij}] = [x_{ij},\ y_{ij}]\mathbf{R}_\theta \tag{2.1}$$

The Cartesian coefficients of $\mathbf{r}_{oc}$ are denoted X_{oc} and Y_{oc}. Using the transformations in (2.1), the Cartesian coordinates of a point, X_{op_i} and Y_{op_i}, can be found as:

$$\begin{aligned} X_{op_i} &= X_{oc} + X_{cp_i} = X_{oc} + x_{cp_i}\cos\theta - y_{cp_i}\sin\theta \\ Y_{op_i} &= Y_{oc} + Y_{cp_i} = Y_{oc} + x_{cp_i}\sin\theta + y_{cp_i}\cos\theta \end{aligned} \tag{2.2}$$

The Cartesian coefficients of the horizontal and vertical velocities and accelerations of any point, p_i, are then defined as:

$$\begin{aligned} \dot{X}_{op_i} &= \dot{X}_{oc} + \dot{X}_{cp_i} = \dot{X}_{oc} - (x_{cp_i}\sin\theta + y_{cp_i}\cos\theta)\dot{\theta} \\ \dot{Y}_{op_i} &= \dot{Y}_{oc} + \dot{Y}_{cp_i} = \dot{Y}_{oc} + (x_{cp_i}\cos\theta - y_{cp_i}\sin\theta)\dot{\theta} \end{aligned} \tag{2.3}$$

$$\begin{aligned} \ddot{X}_{op_i} &= \ddot{X}_{oc} + \ddot{X}_{cp_i} = \ddot{X}_{oc} - (x_{cp_i}\sin\theta + y_{cp_i}\cos\theta)\ddot{\theta} - (x_{cp_i}\cos\theta - y_{cp_i}\sin\theta)\dot{\theta}^2 \\ \ddot{Y}_{op_i} &= \ddot{Y}_{oc} + \ddot{Y}_{cp_i} = \ddot{Y}_{oc} + (x_{cp_i}\cos\theta - y_{cp_i}\sin\theta)\ddot{\theta} - (x_{cp_i}\sin\theta + y_{cp_i}\cos\theta)\dot{\theta}^2 \end{aligned} \tag{2.4}$$

where $\dot{(\cdot)}$ and $\ddot{(\cdot)}$ represents the first and second derivative with respect to time, respectively.

The generalized coordinates that describe the motion of an unconstrained rigid body are thus X_{oc}, Y_{oc}, and θ.

2.3 Computational Geometry for an Irregular Body

When working with a uniform-density rectangular block, it is straightforward to find the location of c and the inertia tensor $[\boldsymbol{I}]$ about c in base R. However, when the geometry becomes more complicated, a different method is required to find the location of c and $[\boldsymbol{I}]$ of the object. In this work, the starting point is an STL file of an object that would exhibit planar rocking. An example of such an object is shown in Figure 2.4. The STL file provides the geometry for the studied body. The location of c and the value of $[\boldsymbol{I}]$ must then be derived from the STL. An STL file consists of the 3-D coordinates and a triangulation of the external surface of the 3-D object. It provides a matrix of the x-, y-, and z-coordinates of each vertex on the surface of the object and a connectivity matrix identifying the indices of the three vertices that create each triangle around the exterior of the object (79).

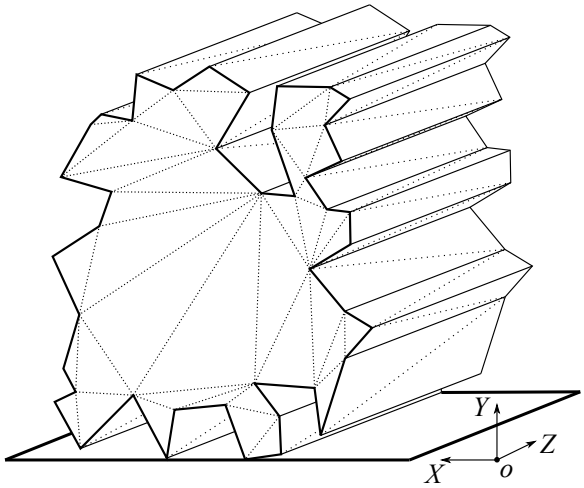


Fig. 2.4. A 3-D triangulation of a rigid body extruded in the Z-direction.

The flowchart presented in Figure 2.5 demonstrates the steps required to manage the computational geometry of an irregular body for rocking studies. STL files are easily created in computer aided drafting (CAD) programs or from 3-D scans of existing objects and are initially an ASCII or binary file. The STL file is imported into Matlab using the stlread function (60) by creating an nx3 matrix $\mathbf{M}_v$ of the n vertex coordinates and an mx3 triangulation matrix $\mathbf{M}_f$ defining the m faces of the object. As the stlread function

duplicates many of the object's vertices upon import, the Matlab patchslim function is used to slim the matrices so that each vertex is only listed once in $\mathbf{M}_v$ and the minimum number of faces to completely define the geometry of the body are recorded in $\mathbf{M}_f$ (45). The patchslim function reduces the triangulation to the minimum set of non-overlapping triangles so that every edge of every triangle is only shared by two triangles.

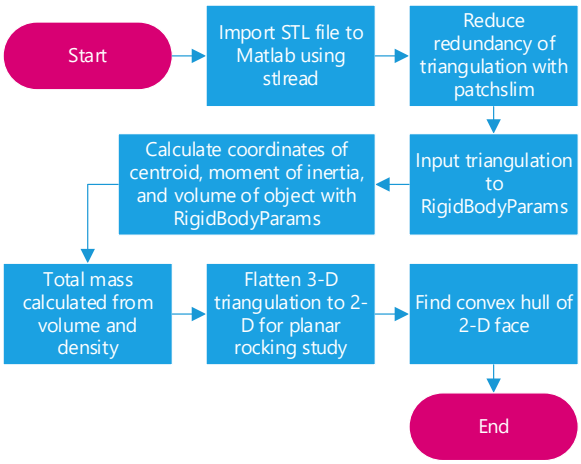


Fig. 2.5. A flowchart showing the steps required to manage the computational geometry of an irregular, concave body.

To find the location of c, $[\boldsymbol{I}]$, and the volume V of the body, the triangulation from the STL file is supplied to the RigidBodyParams function (93) which uses the divergence theorem (43) to calculate the quantities. A similar procedure is described in Chatzis and Smyth (33) for calculating penetration volumes and their centroids where the use of the divergence theorem and the related formulas is further explained. As the body is assumed to rotate with respect to the z-axis only, the scalar principal moment of inertia about the z-axis is used as the relevant moment of inertia I_c. If previously unknown, m is found by multiplying V by the density of the body assuming uniform density. The model can also handle objects of nonuniform density by breaking the object into portions of the same density, finding m, V, and the location of c for each portion, and aggregating the results from each portion by weighting each section based on its total mass to find the location of c and $[\boldsymbol{I}]$ for the whole body.

As only the planar rocking of the body is examined in this chapter, the 3-D body should have a base configuration for which only rotation about the Z-axis is permitted. This type of configuration can be achieved in many ways such as the table legs or rocking horse slats shown in Figure 2.1. The examples of this chapter consider both extruded geometries and those that vary in the Z direction. For bodies with uniform Z geometry, the 2-D projection of the body is used as shown in Figure 2.4.

Finally, the convex hull of the body is determined. The convex hull of a set of points P is the intersection of all convex sets containing P (114). The contact of the rigid body with a flat horizontal surface can only occur at points which belong to the convex hull of the body. The convex hull of the body in Figure 2.3 is shown in Figure 2.6. The most likely point to be in contact with the support surface after rocking begins is the point q_i with the minimum Y-coordinate. When $Y_{oq_i} = 0$ the point q_i is in contact with the support and is thus either a rocking vertex or support contact during the static pattern. Any point on the interior of the blue convex hull polygon cannot touch the support surface regardless of the body's angle of rotation. Only the vertices of the convex hull may become rocking vertices. If any other point of the body was considered as a rocking vertex, then at least one of the vertices of the convex hull would penetrate the support medium, violating the constraints of this model.

The vertices of the body belonging to its convex hull will be denoted as q_i and are ordered from 1 to N_c in a counterclockwise manner about the body. The edges of the convex hull E_i are defined as the line segments connecting each convex hull vertex to its adjacent vertices. The body, when in a rocking pattern which will be introduced in Section 2.4.1, will only make an impact with the support surface when an edge E_i is parallel to the support surface with a zero Y-coordinate along the entire edge. The angles $\theta_{q_i q_{i+1}}$ between the E_i and the X-axis are calculated for the initial orientation of the body. Figure 2.6 shows how these angles are defined for an irregular body. Every E_i has a $\theta_{q_i q_{i+1}}$ associated with it.

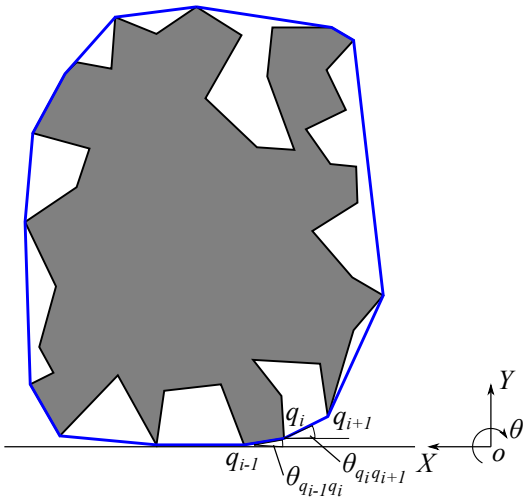


Fig. 2.6. An irregular body with its convex hull shown and its angles with the horizontal defined.

The $\theta_{q_i q_{i+1}}$ are calculated as:

$$\theta_{q_i q_{i+1}} = \text{atan}\left(\frac{y_{q_i q_{i+1}}}{x_{q_i q_{i+1}}}\right) \tag{2.5}$$

where atan is the four-quadrant inverse tangent based on the coefficients of adjacent convex hull vertices. Matlab's atan2 command is used to find these angles on the closed interval $[-\pi, \pi]$ (104). To detect events involving impact, $\theta_{q_i q_{i+1}}$ are then converted to angles on the interval $[0, 2\pi]$. $\theta_{q_i q_{i+1}}$ are compiled into a matrix $\boldsymbol{\theta}_m$ representing the angles at which impact could occur for the body. To allow for the body to undergo more than a full rotation if desired, the angles matrix is expanded:

$$\boldsymbol{\theta}_{m,final} = \boldsymbol{\theta}_m \pm 2\pi n \tag{2.6}$$

where n is a set of any desired integers and $\boldsymbol{\theta}_{m,final}$ is the matrix used to detect impacts.

2.4 Equations of Motion

To determine the motion of an irregular body, the equations of motion must be formulated and solved. Five patterns of motion are defined to model the response of the system, each with its own kinematic constraints. The patterns can be separated into groups with one, two, or no vertices in contact with the support medium (free flight).

2.4.1 Rocking Patterns

Figure 2.7 shows an irregular rigid body where only point q_i is in contact with the support surface. In such a case, the body is defined to be in a rocking pattern. The support medium reactions F_x and F_y, horizontal and vertical respectively, act at point q_i as shown, in addition to the external forces f_x and f_y and the force of gravity mg acting at the centroid of the body. The forces F_x, F_y, f_x, and f_y are shown in the positive direction and this convention is applied to all figures in this thesis. In the case of the support accelerations studied in this chapter, f_x and f_y are D'Alembert forces defined as:

$$f_x = -m\ddot{x}_g \qquad\qquad f_y = -m\ddot{y}_g \tag{2.7}$$

where $\ddot{x}_g$ and $\ddot{y}_g$ are the horizontal and vertical support accelerations respectively.

Without further assumptions about the constraints that have generated the constraint forces F_x and F_y, the equations of motion for this body are given in (2.8).

$$m\ddot{X}_{oc} - F_x = f_x \qquad m\ddot{Y}_{oc} - F_y = f_y - mg \qquad I_c\ddot{\theta} + Y_{cq_i}F_x - X_{cq_i}F_y = 0 \tag{2.8}$$

The above system of equations has five unknowns: $\ddot{X}_{oc}$, $\ddot{Y}_{oc}$, $\ddot{\theta}$, F_x, and F_y. Two additional equations are thus required to solve the equations of motion. The constraints necessary to solve equation (2.8) will be defined later in Section 2.4.4.

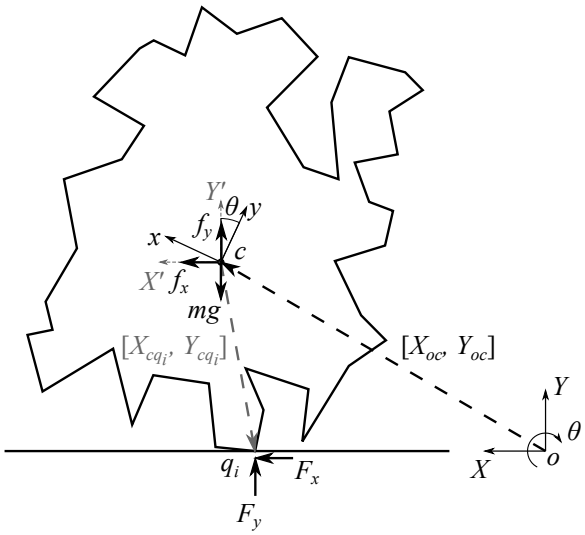


Fig. 2.7. The forces acting on a rocking rigid body.

2.4.2 Patterns with Multiple Vertices Contacting Support Medium

The trajectory of the studied system also involves patterns where at least two vertices, q_i and q_{i+1}, are in contact with the support medium as shown in Figure 2.8.

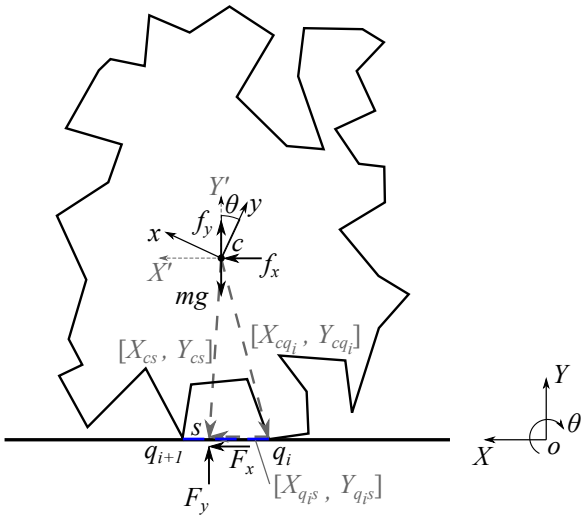


Fig. 2.8. The vectors and forces relevant to a rigid body in the static pattern or pure sliding with an edge of the convex hull contacting the support surface.

The body could be concave between q_i and q_{i+1}, in which case those are the only points in contact with the support, or it could be a straight edge in which case all the points of the corresponding edge E_i are in contact with the support as represented by the blue dashed

line in Figure 2.8. In either case, the resultant vertical reaction force F_y is applied at a point s between the two vertices q_i and q_{i+1}. The horizontal Cartesian coordinate of point s is defined by X_{cs} as:

$$X_{cs} = X_{cq_i} + dX_{q_i q_{i+1}} \tag{2.9}$$

where $d \in [0, 1]$ because the support is assumed to be incapable of providing tensile stresses.

Due to the sixth variable, d, being added for such cases, the equations of motion for these patterns differ from (2.8). The modified equations of motion are:

$$m\ddot{X}_{oc} - F_x = f_x \qquad m\ddot{Y}_{oc} - F_y = f_y - mg \qquad I_c\ddot{\theta} + Y_{cs}F_x - X_{cs}F_y = 0 \tag{2.10}$$

The above system has six unknowns: $\ddot{X}_{oc}, \ddot{Y}_{oc}, \ddot{\theta}, F_x, F_y$, and d, requiring three constraint equations for the unknowns to be determined, which again, are dependent on the pattern of motion and are introduced in Section 2.4.4.

2.4.3 Pattern without Contact Points

Figure 2.9 shows a pattern with no contact between the body and the support medium. In such cases, F_x and F_y are set to zero and the body is only acted on by gravity, f_x, and f_y.

2.4.4 The Patterns of Motion and Their Constraints

There are five possible patterns of motion, as shown in the following Figure 2.10: the static pattern (SP), pure sliding (PS), pure rocking (PR), slide rocking (SR), and free flight (FF). A different set of independent degrees of freedom (DOFs) is selected for each pattern. This section provides the constraints for each pattern.

As can be seen in Figure 2.10a, the static pattern occurs when a body has at least two of its convex hull vertices in contact with the support by a pin in one point (either of the two)

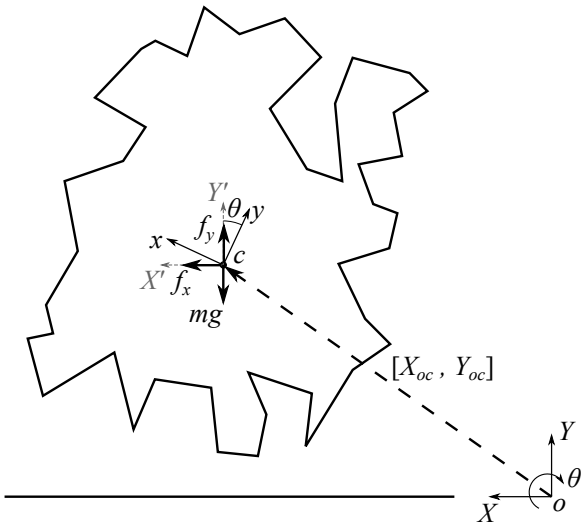
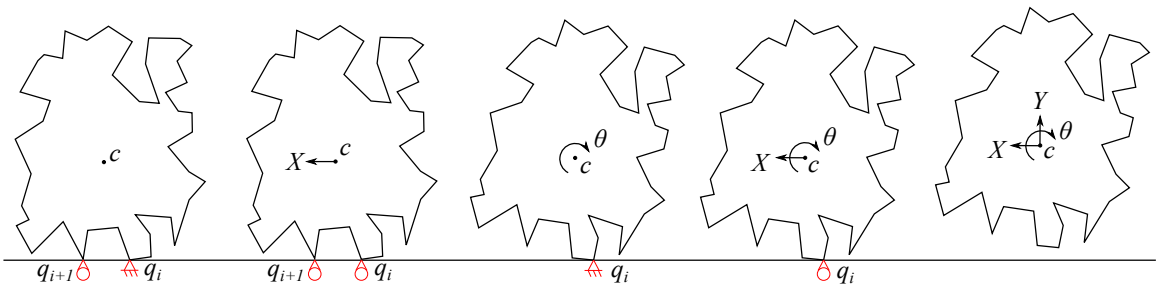


Fig. 2.9. An irregular body without contact with the support medium and reactions set to zero.



a. Static Pattern b. Pure Sliding c. Pure Rocking d. Slide Rocking e. Free Flight

Fig. 2.10. The five patterns of motion with their independent DOFs and constraints specified. (a) the static pattern with pin and roller contacts; (b) pure sliding with two rollers; (c) pure rocking with one pin; (d) slide rocking with one roller; (e) free flight with no contact with the support.

and a roller in the other. The kinematic constraints of the static pattern are:

$$\dot{X}_{oq_i} = \ddot{X}_{oq_i} = 0 \qquad \dot{Y}_{oq_i} = \ddot{Y}_{oq_i} = 0 \qquad \dot{Y}_{oq_{i+1}} = \ddot{Y}_{oq_{i+1}} = 0 \tag{2.11}$$

The velocity constraints in (2.11) can be integrated to find the additional displacement equations for the static pattern:

$$X_{oq_i} = X_{oq_i}(t_0) \qquad Y_{oq_i} = Y_{oq_i}(t_0) \qquad Y_{oq_{i+1}} = Y_{oq_{i+1}}(t_0) \tag{2.12}$$

where t_0 is the first time instance the body is in the current static pattern. Likewise, t_0 is defined as the first time instance the body is in the other patterns and is updated for each new instance of each pattern. These equations show that X_{oq_i}, Y_{oq_i}, and $Y_{oq_{i+1}}$ remain constant throughout the static pattern.

In pure sliding as in Figure 2.10b, the body has at least two vertices in contact with the support and slides along the support. The constraints for pure sliding are:

$$F_x + \text{sgn}(\dot{X}_{oq_i})\mu F_y = 0 \qquad \dot{Y}_{oq_i} = \ddot{Y}_{oq_i} = 0 \qquad \dot{Y}_{oq_{i+1}} = \ddot{Y}_{oq_{i+1}} = 0 \tag{2.13}$$

where the first of the above equations is the Coulomb friction law where μ is the coefficient of friction between the body and the support surface and sgn() is the signum function. It should be noticed that $\dot{X}_{oq_i} = \dot{X}_{oq_{i+1}}$. The velocity constraints in (2.13) can be integrated to obtain the additional pure sliding displacement equations:

$$Y_{oq_i} = Y_{oq_i}(t_0) \qquad Y_{oq_{i+1}} = Y_{oq_{i+1}}(t_0) \tag{2.14}$$

Pure rocking occurs when only one vertex is in contact with the support and does not slide along the support surface. Two constraint equations are derived from the rocking vertex q_i being restricted from translating in the horizontal and vertical directions (a pinned joint). The kinematic constraints are:

$$\dot{X}_{oq_i} = \ddot{X}_{oq_i} = 0 \qquad \dot{Y}_{oq_i} = \ddot{Y}_{oq_i} = 0 \tag{2.15}$$

The velocity constraints in (2.15) can be integrated to find the additional pure rocking displacement equations:

$$X_{oq_i} = X_{oq_i}(t_0) \qquad Y_{oq_i} = Y_{oq_i}(t_0) \tag{2.16}$$

During slide rocking, the body rotates about a rocking vertex q_i while the same vertex is also permitted to slide along the support surface as shown in Figure 2.10d. The constraints for slide rocking are:

$$F_x + \text{sgn}(\dot{X}_{oq_i})\mu F_y = 0 \qquad \dot{Y}_{oq_i} = \ddot{Y}_{oq_i} = 0 \tag{2.17}$$

The velocity constraint equation in (2.17) can be integrated to determine the additional slide rocking displacement equation:

$$Y_{oq_i} = Y_{oq_i}(t_0) \tag{2.18}$$

While in free flight, the body has no contact with the support and the support reactions are set to zero:

$$F_x = 0 \qquad F_y = 0 \tag{2.19}$$

2.4.5 The Degrees of Freedom and the Equations of Motion

The unconstrained DOFs $\mathbf{\Phi}$ and the unconstrained six states, the displacements and velocities for each DOF of the system, $\boldsymbol{Q}$, are:

$$\mathbf{\Phi} = \left[X_{oc},\ Y_{oc},\ \theta\right]^T \qquad \boldsymbol{Q} = \left[X_{oc},\ \dot{X}_{oc},\ Y_{oc},\ \dot{Y}_{oc},\ \theta,\ \dot{\theta}\right]^T \tag{2.20}$$

Due to the constraints mentioned in the previous section, only a subset of $\mathbf{\Phi}$ and $\boldsymbol{Q}$ are independent for each pattern. The independent DOFs and the independent states selected to fully describe each pattern are denoted by $\mathbf{\Phi}_a$ and $\boldsymbol{Q}_a$ respectively and are summarized in Table 3.1. The vectors $\mathbf{\Phi}_b$ and $\boldsymbol{Q}_b$ represent the remaining dependent DOFs and states of $\mathbf{\Phi}$ and $\boldsymbol{Q}$ respectively. Some of the patterns have multiple possible selections for $\mathbf{\Phi}_a$ and those shown in Table 3.1 were selected for their simplicity. The reduction from $\mathbf{\Phi}$ to the

$\mathbf{\Phi}_a$ and their derivatives is necessary to avoid numerical drift during integration and ensure the integration of the equations of motion is computationally efficient.

Table 2.1. Independent Degrees of Freedom and States for Each Pattern

Pattern	Degrees of Freedom, $\mathbf{\Phi}_a$	States, $\boldsymbol{Q}_a$
Rest	None	None
Pure Sliding	X	X, $\dot{X}$
Pure Rocking	θ	θ, $\dot{\theta}$
Slide Rocking	X, θ	X, $\dot{X}$, θ, $\dot{\theta}$
Free Flight	X, Y, θ	X, $\dot{X}$, Y, $\dot{Y}$, θ, $\dot{\theta}$

The kinematic equations (2.2)-(2.4) are substituted into the constraint equations (2.11)-(2.19) as necessary for each pattern. A system of equations is then created for each pattern combining the equations of motion, (2.8) or (2.10) depending on the pattern, and the constraint equations with kinematics substituted. This system has the vector of unknowns:

$$\mathbf{V} = \left[\ddot{\mathbf{\Phi}}, \boldsymbol{Q}_b, F_x, F_y, d\right]^T \tag{2.21}$$

where d is only defined for the static pattern and pure sliding. Solving this system of equations results in equations for each of the dependent states $\boldsymbol{Q}_b$ and the reaction variables F_x, F_y, and d.

Thus, the constrained equations of motion for each of the five patterns are formulated symbolically for each of the independent DOFs using Matlab's Symbolic Math Toolbox (75). These results are summarized by the following equations:

$$\begin{aligned} \ddot{\mathbf{\Phi}}_a &= h(\boldsymbol{Q}_a, m, g, \mu, I_c, x_{cq_i}, y_{cq_i}, \ddot{x}_g, \ddot{y}_g) \\ [F_x, F_y, d] &= j(\boldsymbol{Q}_a, m, g, \mu, I_c, x_{cq_i}, y_{cq_i}, \ddot{x}_g, \ddot{y}_g) \\ \boldsymbol{Q}_b &= k(\boldsymbol{Q}_a, m, g, \mu, I_c, x_{cq_i}, y_{cq_i}, \ddot{x}_g, \ddot{y}_g) \end{aligned} \tag{2.22}$$

where h, j, and k are the general forms of the non-linear functions occurring after the above process is completed. The right side of these equations are converted to automatically-

generated scripts using matlabFunctions (74) with the left side as the outputs.

k in (2.22) is the general form of the function that calculates $\boldsymbol{Q}_b$ for any time instance and j is the general form of the function that is used to calculate F_x, F_y, (and d where necessary), for any time instance during integration. The equations of motion for each pattern from (2.22) are brought into state-space form using the independent DOFs and states for each pattern:

$$\dot{\boldsymbol{Q}}_a = \begin{bmatrix} \dot{\boldsymbol{\Phi}}_a \\ \ddot{\boldsymbol{\Phi}}_a \end{bmatrix} \tag{2.23}$$

This reduces the differential equation h of (2.22) from second-order to first-order. $\boldsymbol{Q}_a$ is then found through integration and $\boldsymbol{Q}_b$ is found post-integration with k. The details of numerical integration are discussed in Section 2.6.

F_x, F_y, and d are used to determine transitions between patterns, which are discussed in Section 2.5.1. Each pattern thus has different symbolic expressions for the equations in (2.22) as $\boldsymbol{Q}_a$ is different for each pattern, but the same method is used for all patterns to determine $\boldsymbol{Q}_a$ and then calculate $\boldsymbol{Q}_b$ post-integration using matlabFunctions. This automated method using Matlab's symbolic toolbox reduces the likelihood of errors in the resulting formulation and allows for a single approach which is easily expanded to any number of objects with any geometry.

To illustrate the above process for the static pattern: the kinematic equations (2.2)-(2.4) are substituted into the constraint equations (2.11) and (2.12). These are then combined with the equations of motion (2.10) to create a system of twelve equations with twelve unknowns: $\ddot{\boldsymbol{\Phi}}$, X_{oc}, Y_{oc}, θ, $\dot{X}_{oc}$, $\dot{Y}_{oc}$, $\dot{\theta}$, F_x, F_y, and d. The solution of this system gives $\dot{\boldsymbol{\Phi}} = \ddot{\boldsymbol{\Phi}} = \mathbf{0}$ and $\boldsymbol{\Phi} = \boldsymbol{\Phi}(t_0)$. The same procedure is completed for the other four patterns which results in unique formulations of the equations of motion for each pattern.

2.5 Transitions Between Patterns

Transitions between the above-described patterns occur during the trajectory of the system. They are separated in the following discussion between transitions with impact and without impact.

2.5.1 Transitions Without Impact

Transitions between patterns can occur without impact in several ways which can be summarized by the following transitions: i) contact vertices transitioning between stick, i.e. the horizontal velocity of support contacts equal to zero, and slide; ii) a pattern with at least two vertices in contact with the support moving to a single-contact pattern; and iii) the body lifting off the support into free flight.

Transitions from stick to slide occur when the horizontal support reaction tends toward exceeding Coulomb's friction law:

$$|F_x(t^*)| = \mu F_y(t^*) \tag{2.24}$$

where t^* is the exact time the transition occurs. The opposite transition, from a sliding pattern to a non-sliding pattern, occurs at time t^* when:

$$\dot{X}_{oq_i} = 0 \tag{2.25}$$

where q_i is a vertex in contact with the support medium. However, for the body to transition to stick, Coulomb's criterion must further be satisfied at t^*:

$$|F_x(t^*)| \leq \mu F_y(t^*) \tag{2.26}$$

If the support contact(s) have zero horizontal velocity, $F_x(t^*)$ is calculated by the

equations of the corresponding stick pattern after transition, i.e. either the static pattern or pure rocking. If (2.26) is not met at t^*, then the sliding pattern is continued with $\text{sgn}(\dot{X}_{oq_i})$ set to a value dependent on F_x. This is discussed later along with the transition from stick to slide. This situation is not common, however, and does not occur in any of the examples provided.

The second category of transitions without impact, from multiple contact points to a single contact point, occurs if s, the point of application of the vertical support reaction F_y, coincides with either outer vertex defining the edge E_i in contact with the support. This transition occurs at the first time instance that either of the following are true:

$$d = 0 \qquad \text{or} \qquad d = 1 \tag{2.27}$$

Finally, for transitions to free flight, the positive F_y becomes zero:

$$F_y = 0 \tag{2.28}$$

Based on the previous descriptions, the following transition between patterns can occur without impacts: the static pattern can transition to pure sliding, pure rocking, and free flight. Pure sliding can transition to the static pattern, slide rocking, and free flight. Pure rocking can transition to slide rocking and free flight. And finally, slide rocking can transition to pure rocking and free flight.

When a stick pattern transitions to a sliding pattern without impact at time t^* or (2.26) is not met during a sliding pattern, $\dot{X}_{oq_i}(t^*) = 0$. This causes a problem in using the equations of motion at the first time instance of the sliding pattern. To avoid the ill-definition of $\text{sgn}(\dot{X}_{oq_i}(t^*))$, the following procedure explained for the transition from pure rocking to slide rocking is followed: Let F_{xPR} be the horizontal reaction predicted by the pure rocking pattern at the time instance of transitioning to slide rocking similar to F_x shown in Figure 2.7. Note that at the exact time instance of the transition both the pre-transition pattern and

slide rocking are applicable. A new variable s_f is defined as

$$s_f = -\text{sgn}(F_{xPR}) \tag{2.29}$$

The $\text{sgn}(\dot{X}_{oq_i})$ in the relevant equations for pure sliding (2.11) or, in this case, for slide rocking (2.17) must be replaced by s_f at time t^*. It is assumed that the motion of the body will cause q_i to move in the opposite direction of the insufficient horizontal friction force last acting on the rocking vertex during pure rocking. The equivalent procedure is followed for the transition from the static pattern to pure sliding.

2.5.2 Transitions with Impact

When a body rocks on one vertex or moves through the air during free flight, another of its vertices q_i will likely make contact with the support medium with $\dot{Y}_{oq_i} < 0$. As the support medium will not allow the point to penetrate its surface, an impact occurs. Capturing the effects of such an impact on the trajectory of a rocking body is an important part of this rocking model. Because the support medium and the body are both considered to be rigid, this impact will be a hard impact, i.e., it will be infinitesimal in duration. At the instance of impact, at least two vertices of the body will be in contact with the support surface when the pre-impact pattern is rocking. For a pre-impact pattern of free flight, only one vertex will be in contact with the support at impact as long as θ is not equal to any of the elements of $\boldsymbol{\theta}_{m,final}$ as defined in (2.6).

For a pre-impact rocking pattern, an impact occurs when θ is equal to any of the elements of $\boldsymbol{\theta}_{m,final}$ from equation (2.6) which will hereon be referred to as impact angles. Figure 2.6 shows how the impact angles are defined for an irregular body. Thus, an impact occurs during rocking when θ is equal to any of the impact angles. Each angle has two possible events associated with it, one for each direction of $\dot{\theta}$. When an impact angle is reached during integration, the post-impact rocking vertex i and its location are automatically determined

depending on $\dot{\theta}$. For free flight, the impact event occurs when $Y_{oq_i} = 0$, i.e., at the negative zero-crossing for Y_{oq_i}, for any vertex q_i of the body's convex hull.

Without any loss of generality, the upper diagrams of Figure 2.11 shows an impact occurring from a pre-impact rocking pattern where the body is shown immediately before, during, and immediately after the impact (from left to right). Initially, the body rocks about p, then impacts at i and begins rocking about i. The pre-impact velocities are denoted by the superscript $^-$ and the post-impact velocities by the superscript $^+$. During the impact, a horizontal impulse J_x and a vertical impulse J_y are applied by the support medium to the body at a point u between the pre- and post-impact rocking vertices p and i respectively. For the case of pre-impact free flight shown in the lower diagram of Figure 2.11, the object begins in free flight then impacts the support at i which must be the same as u due to it being the only point in contact with the support.

The vector $\mathbf{r}_{cu}$ defines the location of u:

$$\mathbf{r}_{cu} = \mathbf{r}_{ci} + \lambda \mathbf{r}_{ip} \tag{2.30}$$

where λ is a scalar. Due to the inability of the support medium to provide tensile stresses J_y must be applied between i and p, i.e., $\lambda \in [0, 1]$, with $\lambda = 0$ and $\lambda = 1$ corresponding to J_y being applied to i and p respectively. For rectangular blocks and pure rocking, $\lambda \leq 0.5$ is necessary to avoid gain of energy during the impact as discussed in (31). For irregular bodies, there is no known explicit limit to λ as the slenderness and different options for pre- and post-impact patterns vary. However, this value can be calculated numerically from the condition that the overall energy of the system is not increased after impact. In the examples provided, the value of λ was monitored so that is does not result in an increase of energy.

For impacts where free flight is the pre-impact pattern, λ does not need to be defined because i and u must be coincidental. It is theoretically possible for an impact from free flight to happen with two or more vertices simultaneously impacting the support, but this

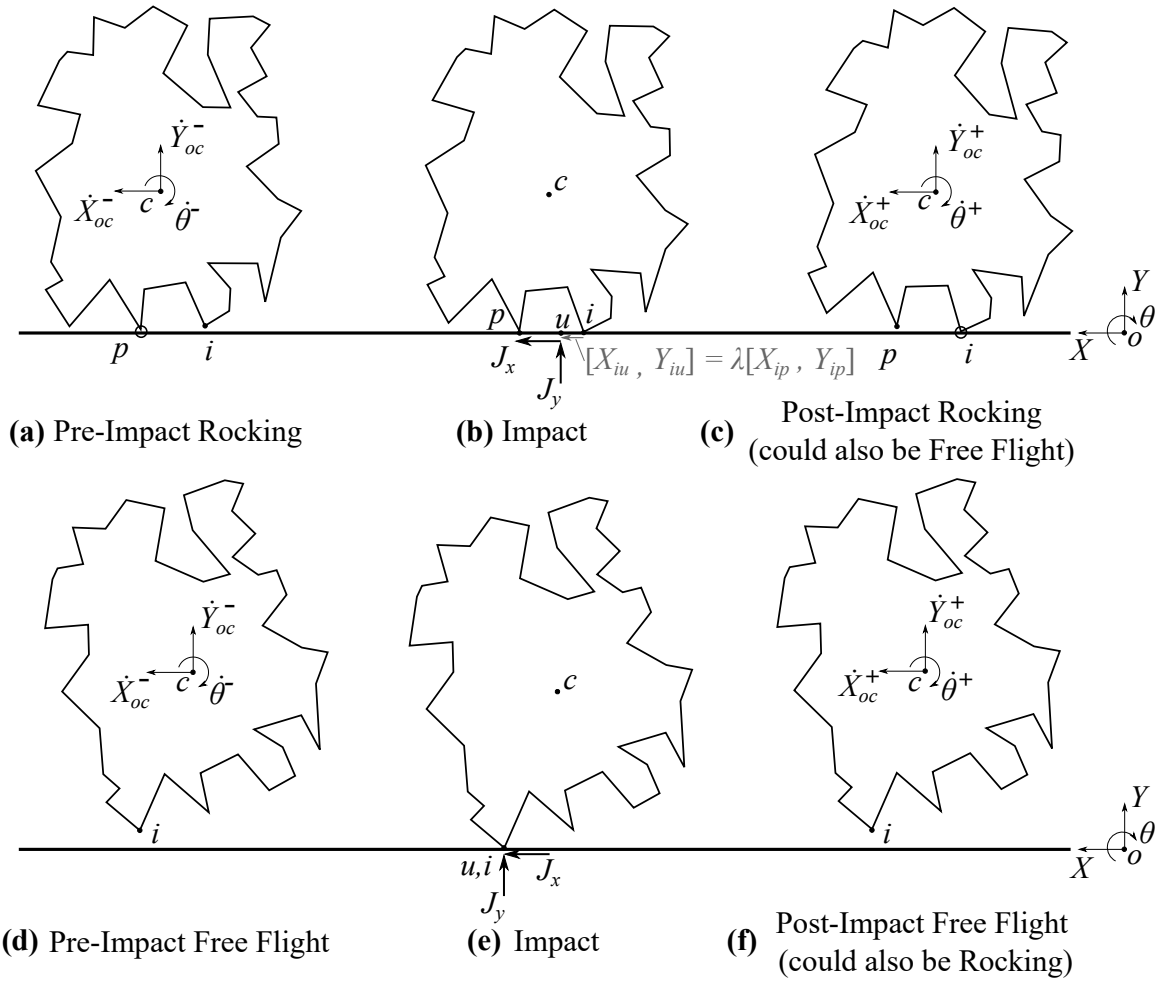


Fig. 2.11. Upper diagram: From left to right shows an irregular body rocking on p, impacting the support surface, and continuing to rock on i. The open circles indicate the rocking vertices. Lower diagram: From left to right shows an irregular body in free flight, impacting the support surface at i, and returning to free flight. Positive velocity conventions are shown.

is highly unlikely and does not appear in any examples presented in this thesis so is thus ignored. Thus, for an impact from free flight:

$$\mathbf{r}_{cu} = \mathbf{r}_{ci} \tag{2.31}$$

For any impact, four sets of impact conditions are possible. Each of the options places a restriction on the impacting vertex i immediately post-imapct. The four impact conditions are: "pure rocking" where i is restricted from moving in X and Y, "slide rocking" where i

may slide but not uplift from the support, "free flight without sliding" where i may uplift from the support but must have $\dot{X}_{oi}^{+} = 0$, and "free flight without restriction" where i may uplift from the support and move horizontally. This model assumes, as (95) does, that the support will cause X_{oi}^{+} and Y_{oi}^{+} to be zero if possible. The model thus has the following order of preference for the impact conditions: pure rocking, slide rocking, free flight without sliding, and free flight without restriction. These assumptions are necessary because more than one post-impact pattern may be applicable, with free flight typically being a valid pattern.

The equations of momentum for any body at impact are:

$$m\dot{X}_{oc}^{+} = m\dot{X}_{oc}^{-} + J_x \qquad m\dot{Y}_{oc}^{+} = m\dot{Y}_{oc}^{-} + J_y \qquad I_c\dot{\theta}^{+} = I_c\dot{\theta}^{-} - Y_{cu}J_x + X_{cu}J_y \tag{2.32}$$

Therefore, there are six unknowns in three equations: $\dot{X}_{oc}^{+}, \dot{Y}_{oc}^{+}, \dot{\theta}^{+}, J_x, J_y$, and λ. λ arises from $X_{cu} = X_{ci} + \lambda X_{ip}$ and must be assumed to reduce the number of unknowns to five. The unknowns in (2.32) are solved for by using two constraint equations for each post-impact pattern. The constraint equations for impact change depending on the post-impact pattern similar to the constraints for the equations of motion. In all cases, the two post-impact constraints, which are given in (2.33)-(2.36) below, and the equations of momentum (2.32) are combined to create a system with five equations and five unknowns. The system of equations is created and solved in the order of preference described above. The post-impact velocities and impulses obtained for each pattern must then be checked to ensure the solution to the impact is valid as discussed in the following Section 2.5.3. If one of the post-impact patterns is valid, the rest of the patterns are not checked and the velocities immediately after impact are defined as the initial conditions for the integration of the post-impact pattern.

For post-impact pure rocking, the constraint equations are:

$$\dot{X}_{oi}^{+} = 0 \Rightarrow \dot{X}_{oc}^{+} = Y_{ci}\dot{\theta}^{+} \qquad\qquad \dot{Y}_{oi}^{+} = 0 \Rightarrow \dot{Y}_{oc}^{+} = -X_{ci}\dot{\theta}^{+} \tag{2.33}$$

The constraint equations for post-impact slide rocking are:

$$J_x = -\text{sgn}(\dot{X}_{oi}^+)\mu J_y \qquad\qquad \dot{Y}_{oi}^+ = 0 \Rightarrow \dot{Y}_{oc}^+ = -X_{oi}\dot{\theta}^+ \tag{2.34}$$

The constraint equations for post-impact free flight without sliding are:

$$\dot{X}_{oi}^+ = 0 \Rightarrow \dot{X}_{oc}^+ = Y_{oi}\dot{\theta}^+ \qquad\qquad \dot{Y}_{oi}^+ = -\epsilon\dot{Y}_{oi}^- \tag{2.35}$$

where ϵ is a coefficient of restitution defining the ratio of $\dot{Y}_{oi}^+$ to $\dot{Y}_{oi}^-$. Finally, the constraint equations for free flight without restriction are:

$$J_x = -\text{sgn}(\dot{X}_{oi}^+)\mu J_y \qquad\qquad \dot{Y}_{oi}^+ = -\epsilon\dot{Y}_{oi}^- \tag{2.36}$$

The acceptable values for ϵ in the above equations theoretically lie on the interval $[0, 1]$ though the upper bound of 1 may be reduced by the requirement that there be no increase in the body's energy at impact. The energy before and after impact must be checked numerically after each impact. The negative sign in front of ϵ ensures that $\dot{Y}_{oi}^+$ is in the opposite direction of $\dot{Y}_{oi}^-$.

2.5.3 Validity Conditions for Post-Impact Patterns

The set of conditions required for a valid impact vary for each potential post-impact pattern. For all post-impact patterns the following condition must be true as the support is tensionless and J_y as shown in Figure 2.11 must therefore be positive:

$$J_y \geq 0 \tag{2.37}$$

Other conditions are only necessary for certain post-impact patterns. For post-impact rocking from a pre-impact rocking pattern to be valid, $\dot{\theta}^+$ must have the same sign as $\dot{\theta}^-$ or

be equal to zero:

$$\text{sgn}(\dot{\theta}^+) = \text{sgn}(\dot{\theta}^-) \qquad \text{or} \qquad \dot{\theta}^+ = 0 \tag{2.38}$$

If $\text{sgn}(\dot{\theta}^+) \neq \text{sgn}(\dot{\theta}^-)$ for a pre-impact rocking pattern going to a post-impact rocking pattern, a second impact would follow immediately after the first impact without time passing between the two impacts. A very specific value of λ depending on the body geometry would be required to cause $\dot{\theta}^+ = 0$. Its discussion is provided here for mathematical completeness. This is not possible as was also observed in (95). However, if the pre-impact pattern is free flight, condition (2.38) is not necessary. The sign of $\dot{\theta}$ can change after impact from free flight. Instead of this condition, for pre-impact rocking to post-impact free flight the following condition is necessary:

$$\dot{Y}_{op}^+ \geq 0 \tag{2.39}$$

as a negative vertical velocity would cause an impact immediately after the initial impact which is not permitted.

Finally, if the post-impact pattern does not permit sliding, i.e., in the case of post-impact pure rocking and free flight with $\dot{X}_{oi}^+ = 0$, Coulomb's inequality applied to the impulses must be valid during the impact:

$$|J_x| \leq \mu J_y \tag{2.40}$$

Otherwise, sliding will occur during impact and as a result $\dot{X}_{oi} \neq 0$. The effect of violating equation (2.40) is that a pure rocking post-impact pattern is replaced by slide rocking, and a free flight pattern with $\dot{X}_{oi} = 0$ is replaced by free flight with $\dot{X}_{oi} \neq 0$.

Table 2.2 displays the options for post-impact patterns and the conditions which must be met for each pattern to be valid.

Table 2.2. Conditions for Each Post-Impact Pattern

Condition	PR	SR	FF without Sliding	FF
$J_y \geq 0$	✓	✓	✓	✓
$\text{sgn}(\dot{\theta}^+) = \text{sgn}(\dot{\theta}^-)$ or $\dot{\theta}^+ = 0$ (for pre-impact rocking only)	✓	✓		
$\dot{Y}_{op}^+ \geq 0$ (for pre-impact rocking only)			✓	✓
$\lvert J_x \rvert \leq \mu J_y$	✓		✓	

Each of the post-impact patterns are checked in the order presented above. If any of the validity conditions for the pattern are not met, the post-impact pattern is deemed invalid and the next pattern is checked. If at any point, one of the post-impact patterns fulfill all its validity conditions, that pattern is selected as the post-impact pattern and the other less restrictive options are not checked.

Note the introduction of $\text{sgn}(\dot{X}_{oi}^+)$ in the friction constraint of equations (2.34) and (2.36). The value of $\text{sgn}(\dot{X}_{oi}^+)$ is unknown prior to solving the momentum equations and therefore requires a guess, $\text{sgn}(\dot{X}_{oi}^+)_{guess}$, and a check with the resulting value after solving, $\text{sgn}(\dot{X}_{oi}^+)_{actual}$. The condition:

$$\text{sgn}(\dot{X}_{oi}^+)_{guess} = \text{sgn}(\dot{X}_{oi}^+)_{actual} \tag{2.41}$$

is checked for post-impact slide rocking or free flight with sliding during impact. If equation (2.41) is not satisfied after the first attempt, $\text{sgn}(\dot{X}_{oi}^+)_{guess}$ is changed to $\text{sgn}(\dot{X}_{oi}^+)_{actual}$ and tested again. If equation (2.41) is still invalid, it does not necessarily constitute an error but it is unknown what value $\text{sgn}(\dot{X}_{oi}^+)$ should be set for this model. This is a situation beyond the limits of the assumed impulse version of the Coulomb friction model but does not occur commonly in practice. In the examples presented later, this scenario does not occur. If the post-impact slide rocking fails to meet equation (2.41) twice, the model could be stopped or the free flight checks could be carried out.

Transitions occurring at impacts are explained through the flowchart in Figure 2.12. This

flowchart summarizes the programmatic flow of the model to solve impacts, displaying the order of preference for post-impact patterns. The flowchart also details the conditions needed to validate each post-impact pattern which are dependent on the pre-impact pattern.

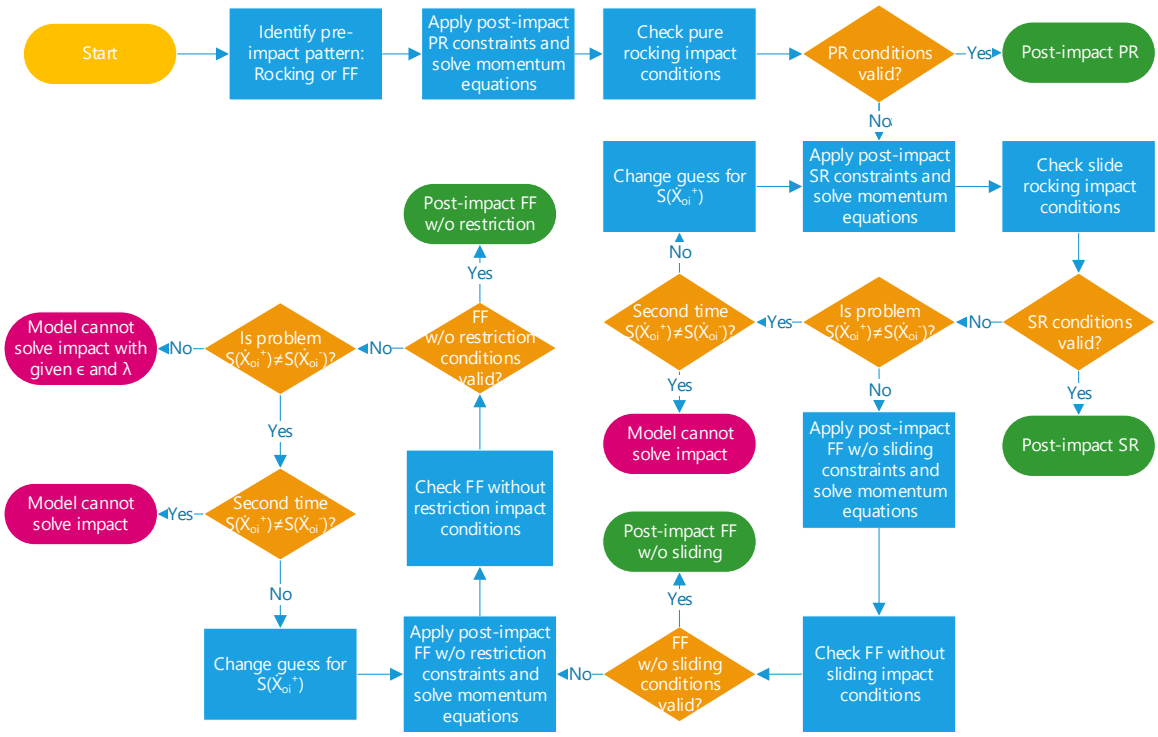


Fig. 2.12. A flowchart displaying how impacts are handled where PR = Pure Rocking, SR = Slide Rocking, and FF = Free Flight.

If the algorithm reaches free flight, the last post-impact pattern checked, and the results are still invalid, then the model is not capable of solving that particular impact with the given values of ϵ and λ. Changing the location of the impulse defined by λ changes the post-impact velocities and thus the post-impact pattern can also be affected. Additionally, ϵ can affect the validity of post-impact free flight.

There is a small subset of impacts, depending on the geometry and velocities of the body, where the pre-impact rocking vertex p in a pre-impact rocking pattern violates condition (2.39) upon solving the equations of momentum. This may occur more frequently for bodies where, at the instance of impact, $|X_{ip}|$ is greater than $|Y_{ic}|$. In this case, there is a problem with either the location of j dictated by λ, the coefficient of restitution ϵ, or the combination

of the two as they are arbitrarily defined. Alternate values for λ and/or ϵ can be selected so that $\dot{Y}_{op}^{+} > 0$. Nevertheless, impacts that require a change in ϵ and/or λ are very rare for reasonable initial selections of ϵ and λ and they do not occur in the examples provided.

2.5.4 Energy-Based Transitions

Energy is lost during each impact, through the corresponding momentum equations. However, the energy of the body never becomes zero even after an infinite number of impacts. Numerically, there will be situations where some of the states of interest have practically become very small numbers. A common occurrence is for the magnitude of $\dot{\theta}$ to become very small which leads to the instance of the body experiencing multiple consecutive impacts over a very small time period. To determine the relative magnitude of $\dot{\theta}$, the rotational velocity that would be required for the body to move from stable equilibrium to unstable equilibrium with the smallest change in potential energy is determined. Dividing the current $\dot{\theta}$ by the value obtained from above gives a dimensionless quantity for which a value of 0.01 or less would generally be considered small, signifying that the body has one hundredth of the rotational velocity required for the body to topple from its current position. Eventually, the decay of energy will lead to $\dot{\theta}$ attaining a value that is comparable to the machine tolerance. If such values are used in the momentum equations, precision errors will be induced potentially leading to an artificial increase of energy in the system and a numerical instability. Instead, it is clear that $\dot{\theta}$ would become zero shortly after this situation is met. To avoid this issue, a reasonably chosen minimum value for $|\dot{\theta}^{+}|$ is selected and if $|\dot{\theta}^{+}|$ falls below the minimum value, the two rocking vertices which were impacting the support are both placed on the support with zero velocity in the static pattern. The same can be true for a slide rocking body, only when $|\dot{\theta}^{+}|$ is negligible, the body is instead forced to pure sliding on the two engaged rocking vertices.

The transition from repeated free flight impacts to a rocking pattern faces the same difficulty as the transition from rocking to a multi-contact pattern. In some cases the same

point i will repeatedly impact the support and $\dot{Y}_{oi}^{+}$ will become smaller and smaller until it reaches the machine tolerance. To avoid this, a reasonably chosen minimum value for $\dot{Y}_{oi}^{+}$ is selected and if $\dot{Y}_{oi}^{+}$ is less than this value the impacting point is transitioned from free flight and placed on the support in a rocking pattern. The new rocking pattern may be either pure or slide rocking, depending on $\dot{X}_{oi}^{+}$ when the transition occurs. If $\dot{X}_{oi}^{+} \neq 0$ the object will enter slide rocking; otherwise it will enter pure rocking.

2.5.5 Summary of Transitions

A summary of the permitted non-impact and energy-based transitions between patterns is shown in Figure 2.13. The criteria that must be met for one pattern to transition to another is provided along each path between patterns.

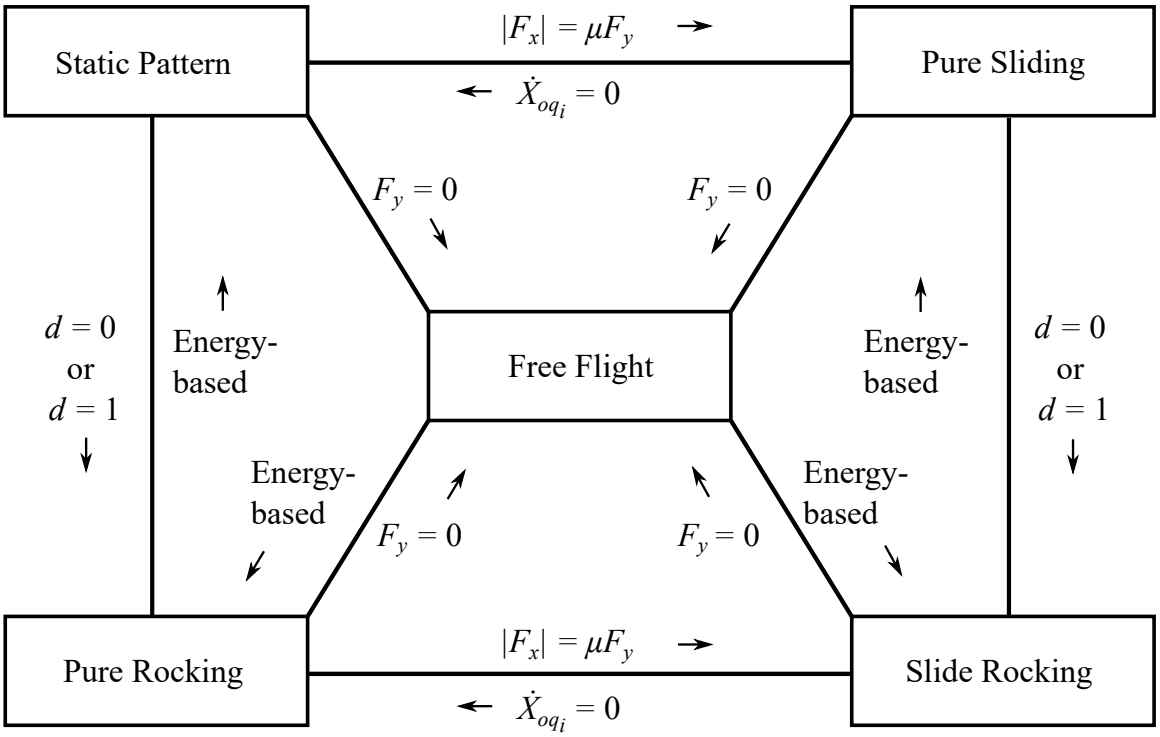


Fig. 2.13. Diagram showing the non-impact and energy-based transitions between the five patterns of motion.

2.6 Numerical Integration of the Equations of Motion

The equation (2.23) is numerically integrated over time using Matlab's ode45 function. Ode45 uses an explicit Runge-Kutta (4, 5) Dormand-Prince pair (RKDP) to solve the system of first-order ordinary differential equations given the differential equation or system of equations, the time span including the start and end times, and the initial conditions of the differential equations (94). An advantage of using a variable time stepping RKDP is the ability to detect events.

Transitions between patterns and impacts are detected using Matlab's ODE event location option. An event function runs simultaneously with ode45 and stops integration when an event occurs. Determining when an event occurs programmatically is strictly necessary to enable accurate solution. During integration, the event function triggers ode45 to stop integration of a given pattern when the criteria for transition to another pattern or impact are met. If the event is an impact, the equations of momentum are then solved to determine the post-impact velocities. If the event is a non-impact transition derived from equations (2.24), (2.25), (2.27), or (2.28), the equations of momentum are not evaluated and the required states are sent to the next pattern's integration.

A numerical model is introduced using the methods described above. In addition, a subset of the full model is designed that prohibits sliding or free flight. The model follows the structure found in Figure 2.14.

2.7 Examples of the Planar Rocking Behavior of Bodies with Irregular Geometry

2.7.1 Example 1: Shelving Unit Subjected to Sinusoidal Pulses

Figure 2.15 shows an example of a shelving unit that would be found in a warehouse or in a residential or office setting on a smaller scale.

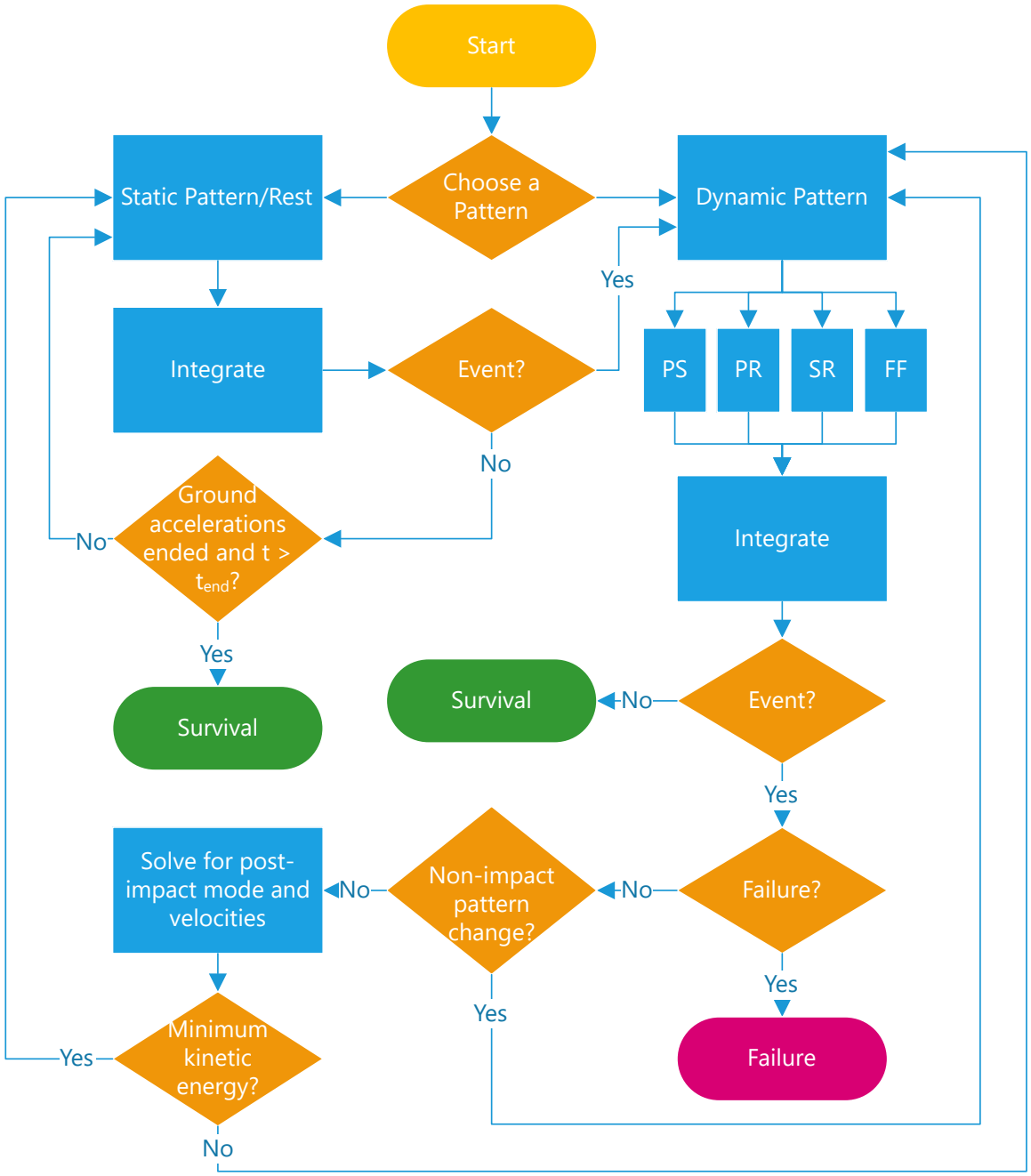


Fig. 2.14. Flowchart showing the overall structure of the code.

The shelving unit has a uniform geometry in the Z-direction extending for 3 meters. A steel unit of this size would present a life safety and property damage risk even without additional content on its shelves if exposed to support accelerations and rocking motion. Four different base configurations are provided to test which configurations offer better stability from support accelerations. The flat base of Figure 2.15a is the typical rocking

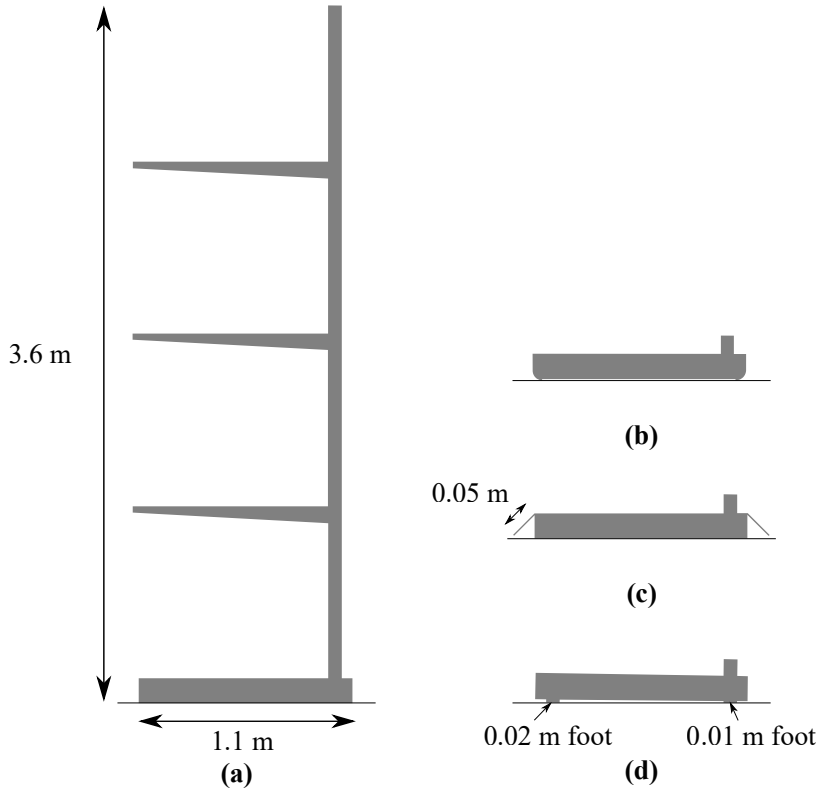


Fig. 2.15. A shelving unit with several base configurations. a) Flat base. b) Quarter circle feet. c) Extensions on either side. d) Uneven feet.

configuration in most rocking studies with two potential rocking vertices. The flat base will be tested with both $\lambda = 0$ and $\lambda = 0.3$ to show the importance of considering this parameter. The other base configurations provided are those that cannot be studied by previous models as they have more than two rocking vertices. The other base configuration use $\lambda = 0$ for simplicity, unless noted otherwise. Figure 2.15b shows a base with quarter circle feet which are slightly lower than the rest of the base to ensure they are the only part of the base to contact the support. Figure 2.15c has 5 cm extensions on either side of the base at 45° angles to the horizontal that will contact the support if the shelving rotates by about 10° in either direction. Finally, Figure 2.15d shows the common situation of two slightly uneven rectangular feet on either side of the unit. The foot on the left is 1 cm while that on the right is 2 cm. This results in a slightly askew unit which would make impacts with four vertices on the feet and two additional vertices at the extremities of the base. The STL files for each

of these units are provided in the supplementary material: STL File S2.1, flat base; STL File S2.2, quarter circle feet; STL File S2.3, with extensions; STL File S2.4, uneven feet.

The horizontal support accelerations applied to the shelving unit, $\ddot{x}_g$, has the form of a sinusoidal pulse of exactly one cycle:

$$\ddot{x}_g = \begin{cases} A\sin(2\pi f t), & \text{if } 0 \leq t \leq \frac{1}{f} \\ 0, & \text{if } t > \frac{1}{f} \end{cases} \tag{2.42}$$

where A is the amplitude of the pulse in terms of g, and f is the linear frequency of the pulse in Hz. The vertical support acceleration, $\ddot{y}_g$, is zero throughout the simulations.

For any excitation applied, the occurring time histories of the six states of the system are found. The angles at which the body fails by toppling, were selected to be -1.5 rad and 1.5 rad, indicating toppling failure. The positive and negative failure limits are referred to as clockwise and counterclockwise failure respectively in the following discussion. If θ never exceeds the failure angles during the pulse and for a reasonable amount of time after the pulse has ended, the body is deemed to have survived the pulse.

To test the broad likelihood of survival or failure for the shelving units, a range of sinusoidal pulses were applied to each of the models, varying A from $0.01g$ to $3g$ and f from 0.1 to 5 Hz. The result of each pulse is recorded as either survival or failure. The boundaries between survival and failure can then be compiled for each of the configurations into stability diagram such as those shown in Figure 2.16, one for each direction of the pulse.

The boundaries between survival and failure in a stability diagram are sensitive to the exact type of waveform used as shown in (86). The results obtained from the stability diagrams cannot be generalized to any other excitation, and hence, only allow for qualitatively discussing the importance of various effects on the response. For these simulations, $\mu = 0.55$ and $\epsilon = 0.1$, but any value may be chosen for these parameters. Additionally, the horizontal axis of Figure 2.16 gives the frequency in Hz of the sinusoidal pulse and the

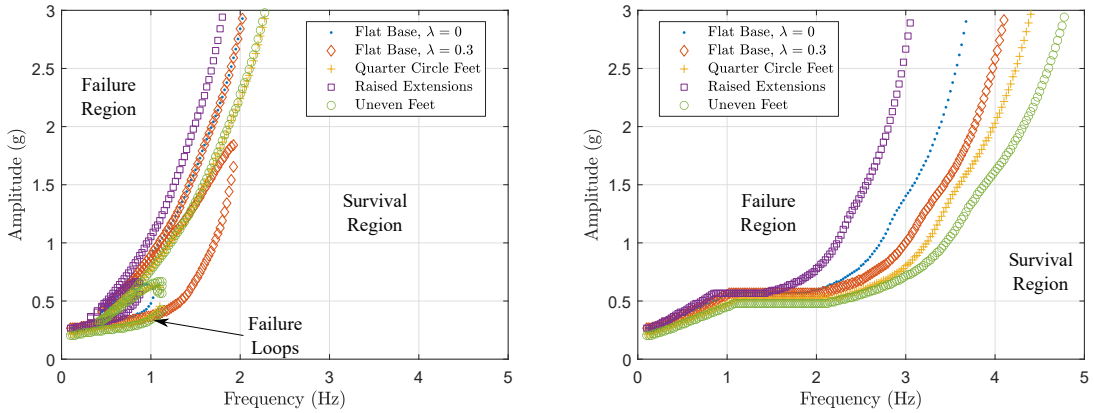


Fig. 2.16. Stability diagrams with boundaries between survival and failure marked. a) Initial positive (left) support acceleration. b) Initial negative (right) support acceleration.

vertical axis gives the amplitude in g.

Several important conclusions can be drawn from this example. First, the direction of the pulse matters due to the geometry of the object and its consequent location of c and moment of inertia. An initial negative support acceleration results in many more (f, A) pairs ending in failure compared to the opposite pulse direction. Another, important observation is that each base configuration has a noticeably different stability diagram. Overall, the bases with uneven feet and quarter circle feet have the most pulses for which they fail while the base with raised extensions fails for the least number of pulses. The difference in the minimum failure amplitude between different bases becomes more pronounced as the frequency increases.

The difference between the flat base with $\lambda = 0$ and $\lambda = 0.3$ is clear for both directions of the pulse, but particularly noticeable in the failure loops of Figure 2.16a where the loop for $\lambda = 0.3$ contains many more (f, A) pairs of failure than the loop for $\lambda = 0$. This is due to less energy being taken out of the base with $\lambda = 0.3$ and thus a greater amount of overturning when the pulse is reversed and the base impacts the support. As λ cannot be expected to be zero for a flat base, it is important to consider $\lambda = 0.3$ as a potential value for the body.

Finally, for either direction of pulse, the base with raised extensions proves to be most stable for sinusoidal pulses. This is presumed to be due to effectively widening the base through these extensions and creating an additional impact that assists in reducing the energy of the body. The common uneven feet of the object prove to be least stable and thus should be avoided and potentially replaced with a base that utilizes extensions or other means to increase the base width and limit rotation of the body.

2.7.2 Example 2: Shelving Unit Subjected to Earthquake

The model can handle any form of support acceleration including earthquakes. Thus, the earthquake accelerations shown in Figure 2.17 were applied to the shelving unit with raised extensions and with uneven feet.

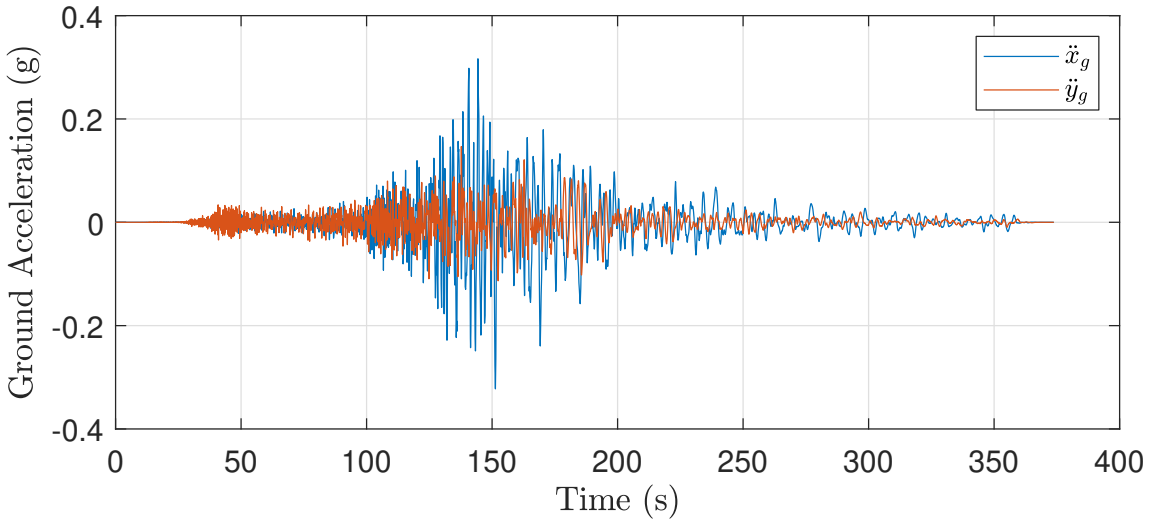


Fig. 2.17. Earthquake acceleration time history for the Chiapas, Mexico earthquake from 2017. The accelerations shown are scaled to 35% of those recorded.

These accelerations are derived from the 2017 Chiapas, Mexico earthquake. Since the original earthquake was very strong (magnitude 8.2), the accelerations have been scaled to 35 percent of the original to more easily identify differences in the response of the shelving unit with different bases. Figure 2.18 shows the time history of the unit with uneven feet and Figure 2.19 shows the time history for the unit with raised extensions.

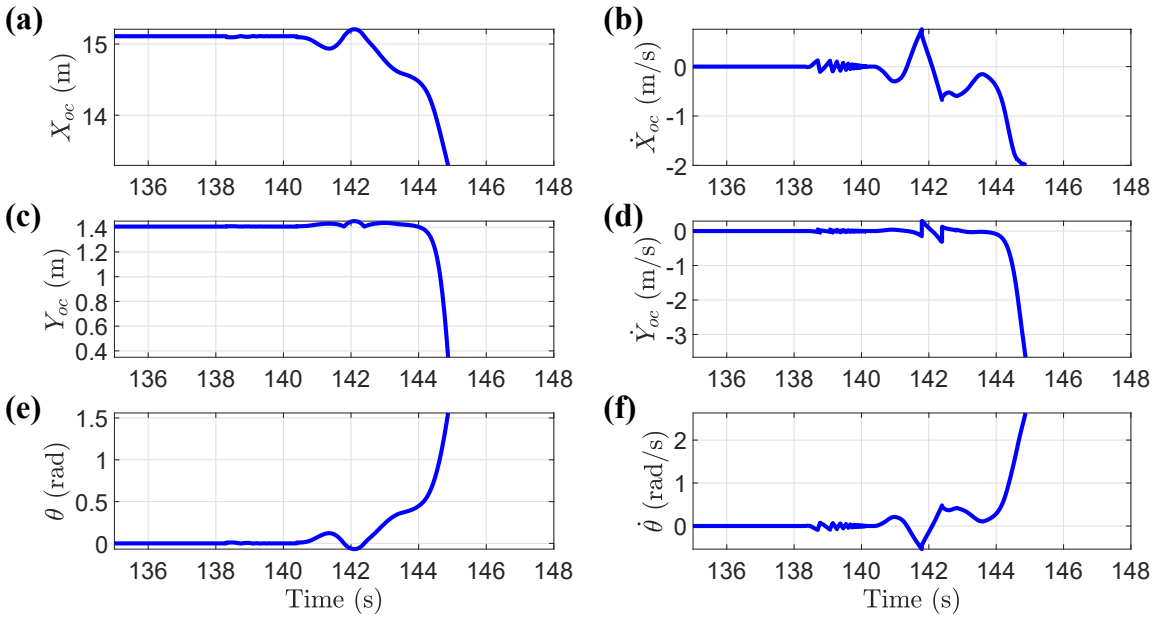


Fig. 2.18. Each of the six states of the shelving unit with uneven feet when exposed to the Chiapas earthquake resulting in toppling failure.

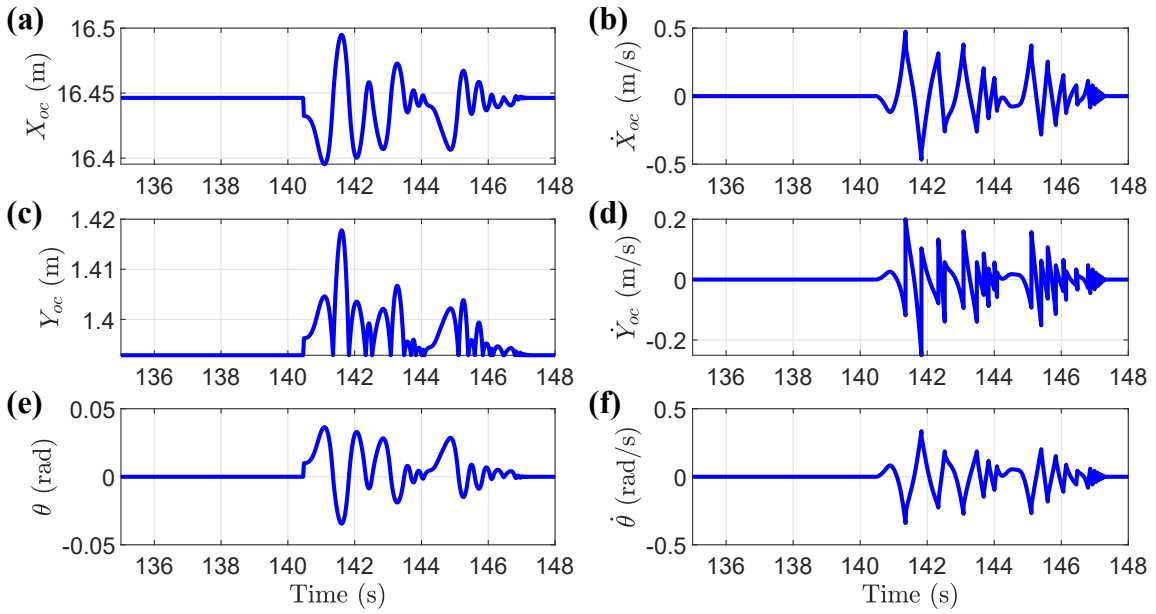


Fig. 2.19. Each of the six states of the shelving unit with raised extensions when exposed to the Chiapas earthquake resulting in survival.

These two figures show survival and failure for different base configurations under the same pulse. The unit with uneven feet begins rocking around 138 seconds into the earthquake and within five seconds topples clockwise. The unit with raised extensions rocks for about

six seconds before returning to the static pattern and surviving the earthquake. Videos of the motion for the unit with uneven feet and raised extensions are provided in Video S2.5 and Video S2.6 respectively. The closeup of the time history of θ for both units is shown in Figure 2.20.

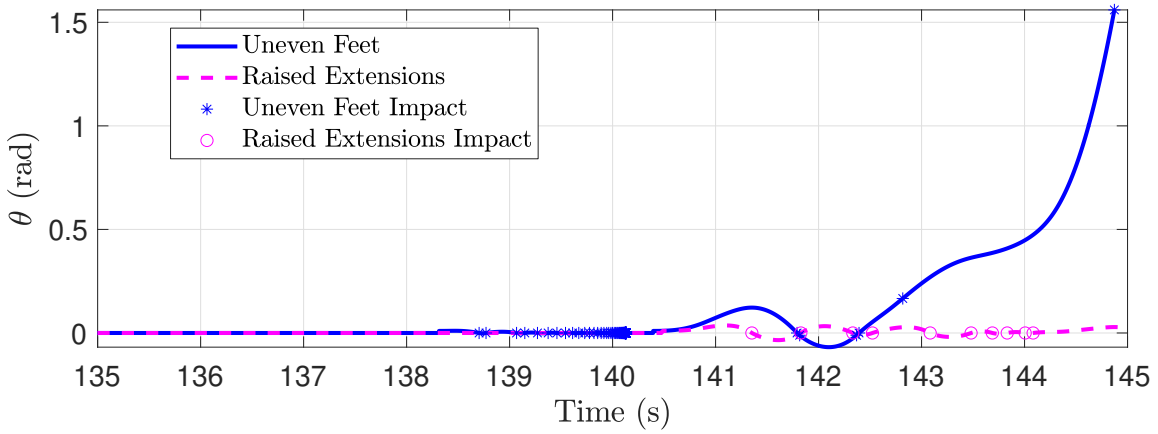


Fig. 2.20. The time history of θ and impact times for the shelving units with uneven feet and raised extensions when exposed to the Chiapas earthquake.

Several important points are derived from this figure. First, the unit with uneven feet begins rocking several seconds before the unit with raised extensions (after 138 seconds versus after 141 seconds). This difference is due to the difference in base width of either unit. The base with raised extensions is wider and results in later movement. Further, after movement begins, it is clear that the unit with uneven feet has a greater change in its rotation. This may be due to the smaller distance between impacting vertices which reduces the energy of the unit less than that for the unit with raised extensions which makes impacts between its initial contact vertices but actually does not engage its extensions in this example. This fact indicates that the width of the base, in addition to the impact created by the extensions, are important in stabilizing the object. The results in Figure 2.16 show that the extensions still assist compared to the flat base which further justifies them.

2.7.3 Example 3: Precariously Balanced Rock Subjected to Sinusoidal Pulses

Figure 2.21 shows an even more irregular body: a scaled-down planar approximation of a PBR known colloquially as *Balanced Rock* located in Colorado (58). This rock was selected to show the model's potential to handle any irregular geometry and number of rocking vertices. The real rock is nearly 11 meters tall, and has been scaled down so that experiments can be carried out in the future. An STL model of this rock was extruded in the Z-direction and input to the planar rocking model for analysis. The STL for this body is provided in STL File S2.7 of the online supplementary material. The support of the real PBR has been simplified to be horizontal to focus on the effect of the support accelerations on the system. Throughout this example it is assumed that $\lambda = 0$.

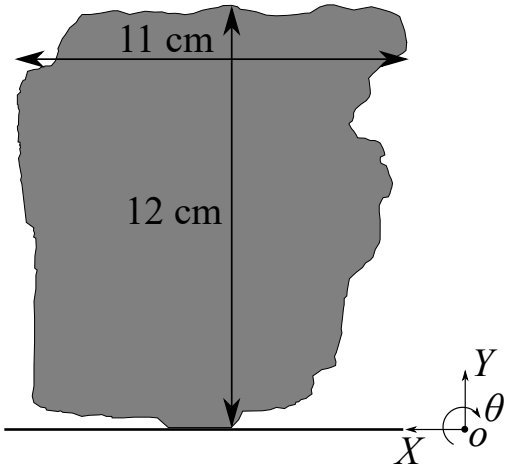
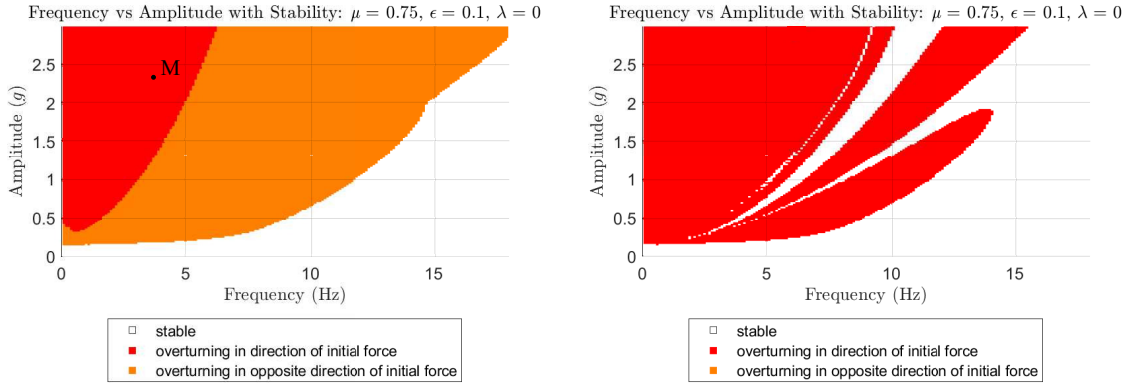


Fig. 2.21. A diagram showing the shape, dimensions, and coordinate system for the PBR studied.

In a similar manner as that for the shelving units, sinusoidal pulses are applied to the PBR to examine the frequencies and amplitudes for which it survives and fails. For the PBR the angles -1.27 rad and 1.64 rad are selected to represent toppling in either direction.

Sinusoidal pulses varying A from $0.01g$ to $3g$ and f from 0.1 to 18 Hz were applied to the PBR. The survival and failure for each combination of the amplitude and frequency

is converted into colored stability diagrams shown in Figure 2.22. For these simulations, $\mu = 0.75$ and $\epsilon = 0.1$. The red points correspond to pairs of (f, A) that result in overturning in the direction that the D'Alembert force acts for the first half of the pulse, f_{x0}, orange corresponds to failure in the opposite direction of the D'Alembert force, $-f_{x0}$, and white indicates survival for the pulse. The red, orange, and white regions will be referred to as failure A, failure B, and survival regions, respectively, through the rest of this chapter.



(a) **(b)**

Fig. 2.22. Stability diagrams for the PBR. (a) the results for an initial negative support acceleration; (b) the results for an initial positive support acceleration.

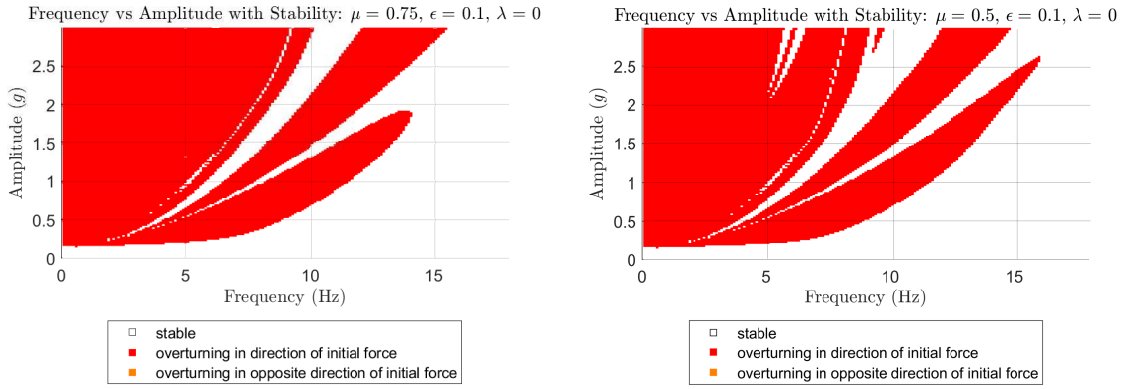
Figure 2.22a gives the results for an initial negative (right) support acceleration applied when the PBR is in the orientation shown in Figure 2.21 with the bottom edge flat on the support surface. The failure A region at low frequencies and high amplitudes shows failure by counterclockwise overturning. The failure B region that exists for all frequencies and only larger amplitudes as the frequency is increased, indicates clockwise toppling of the body. Finally, the survival region beneath a certain low amplitude indicates that the PBR does not overturn when the amplitude is below a minimum threshold. This survival region extends upward for higher frequencies where the effect of the larger amplitudes is gradually undermined by the shorter duration of the pulse.

Figure 2.22b shows the stability results for an initial positive (left) support acceleration. As can be seen in the plot, the PBR either topples clockwise or survives. There are no

counterclockwise failures when f_x initially acts to the right. Again, there is a minimum threshold for the amplitude below which the PBR does not fail that also extends upward as the frequency increases. Further, the solid failure A region for low frequencies and the lower failure A region that extends from the low frequencies upward are shapes analogous to stability diagrams produced for rectangular bodies. But alternating bands of survival and failure A are also visible for the PBR in Figure 2.22b. These bands result from the irregular geometry of the body and are not present for symmetric rectangular blocks under single-cycle support acceleration pulses (119).

Comparing Figures 2.22a and 2.22b proves the importance of geometry to the rocking response. Due to the shape of the PBR, it is much more likely to fail with clockwise rotation as large areas of (f, A) pairs show this type of failure. This result is significant because it shows that pulses with identical frequency and amplitude applied to the same object can produce drastically different results when the pulse direction is changed.

In addition to the geometry, another important factor that contributes to the rocking response of the object is the value of μ. The following Figure 2.23 shows two stability plots for the PBR with a positive (left) initial support acceleration and all parameters the same except for μ.



(a) **(b)**

Fig. 2.23. Stability diagrams for the PBR with initial positive (left) support acceleration for different coefficients of friction μ. (a) $\mu = 0.75$; (b) $\mu = 0.5$.

The results for each μ are similar in that toppling only occurs in the clockwise direction and that similar areas of survival or failure are observed in both. It is important to note that for some frequencies nearing 15 Hz, the minimum amplitude which causes failure actually decreases for lower values of μ for which more sliding occurs. This corroborates the findings in (33) and is an important result as ignoring sliding is often incorrectly assumed as a conservative assumption.

Figure 2.24 shows the time histories of the PBR for the pulse indicated by point M (f = 3.5 Hz, $A = 2.33g$) shown in Figure 2.22a.

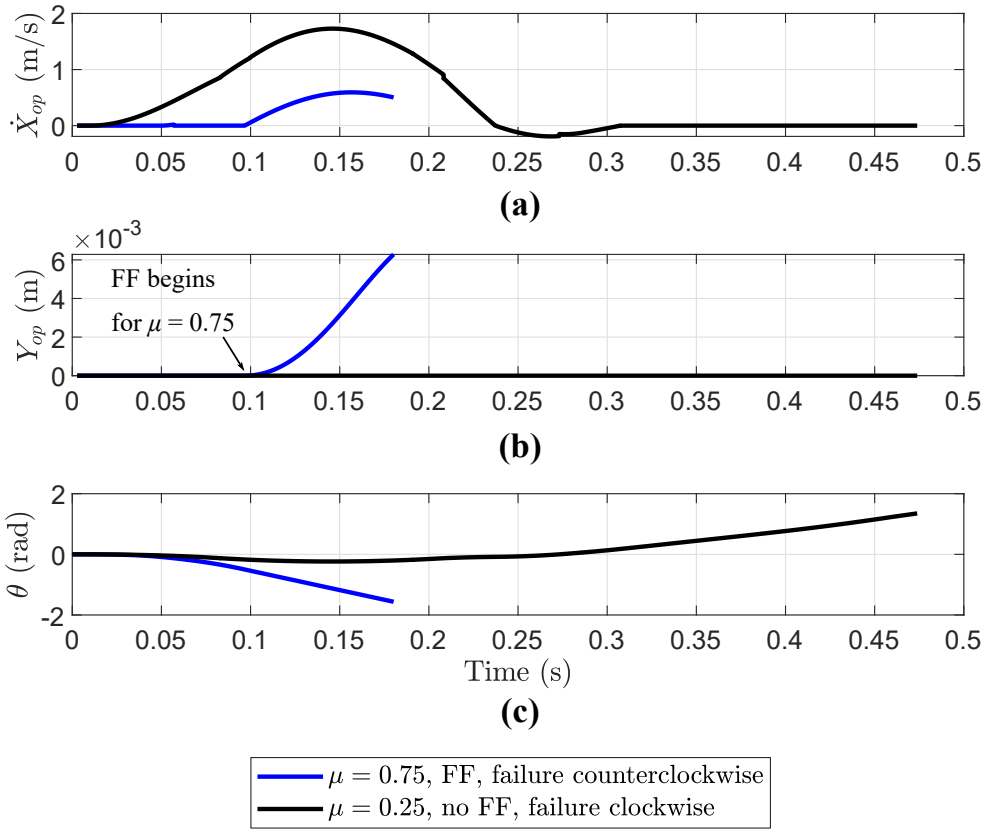


Fig. 2.24. Time histories of $\dot{X}_{op}$, Y_{op}, and θ for the PBR with the same pulse applied (point M from Figure 2.22a) but different μ. (a) The horizontal velocity $\dot{X}_{op}$ of the active rocking vertex. (b) The vertical position Y_{op} of the active rocking vertex (or the last rocking vertex in the case of free flight). (c) The angle θ of the body.

Two simulations were run to obtain the results of Figure 2.24. The blue line shows the counterclockwise toppling failure of the PBR with μ = 0.75. This is the time history

indicated by point M in Figure 2.22a. The black line shows clockwise toppling failure for the same pulse and PBR, but for $\mu = 0.25$. A number of important observations are derived from these results. First, when μ is reduced from 0.75 to 0.25 the body exhibits a large amount of slide rocking as shown by $\dot{X}_{op}$ in Figure 2.24a: non-zero $\dot{X}_{op}$ indicates sliding of the rocking vertex for the black line. However, when the body has a higher μ, it experiences free flight. The lifting from the support can be seen in Figure 2.24b, showing the Y-position of the active rocking vertex. During intervals of free flight, this corresponds to the rocking vertex of the previous pattern. For $\mu = 0.75$ this vertex leaves the support at around 0.1 seconds. The body then fails as another corner hits the support. Note that the PBR with $\mu = 0.25$ does not exhibit free flight and fails in the opposite direction. This highlights the importance of considering both free flight and slide rocking in the model as a simple change of the coefficient of friction can result in free flight and a different type of failure. The motion of the PBR with $\mu = 0.75$ cannot be accurately described if free flight was ignored as a possible pattern. While this example shows that free flight occurs for the higher of the two μ considered, this is not always the case and often slide rocking is coupled with free flight as shown by (30). Additionally, while the examples of this chapter do not show free flight occurring after an impact, this is also possible in which case the assumed value of ϵ would influence the response. Videos showing the movement of the PBR for these simulations are provided in the supplementary material. Videos for $\mu = 0.75$ at full speed and slow motion are provided in Video S2.8 and Video S2.9 respectively. Full speed and slow motion videos for $\mu = 0.25$ are provided in Video S2.10 and Video S2.11.

These results for the PBR show the importance of taking into account the object's irregular geometry, sliding, and free flight in a rocking model. One direction of the pulse can be more critical than its opposite for an irregular object and a lower μ, which results in more frequent occurrences of sliding, can lead to more frequent failure. Finally, changes in the coefficient of friction can result in free flight and much different trajectories.

2.7.4 Example 4: The *David* Sculpture Subjected to an Earthquake

Michelangelo's famous Renaissance sculpture *David* was selected for a case study involving an earthquake. The sculpture is located in Florence, Italy which is an area of high seismicity as demonstrated recently by the Galliano earthquake of December 2019. STL files of the sculpture were created in AutoCAD by drawing lines over the outline of an image of the sculpture (76). The STL files are a 2-D extrusion in the Z-direction with the face of the extrusion representing the front face of the sculpture. Two geometries are considered as shown in Figure 2.25, with and without a rectangular pedestal on the base of the sculpture denoted by points a, b, c, and d in the figure. Several pedestal configurations: solid, hollow, chamfer, and solid with feet are created to test the effect of the pedestal's mass and the number of rocking vertices engaged. STL files for each configuration of the *David* studied are provided in the supplemental material for this thesis as follows: no pedestal: STL File S2.12; solid pedestal: STL File S2.13; hollow pedestal: STL File S2.14; chamfered pedestal: STL File S2.15; and solid pedestal with feet: STL File S2.16. Note that the triangular feet added to the solid pedestal have negligible size and mass and this base configuration practically responds the same as the solid pedestal with $\lambda = 0$. These files were imported into Matlab to test the response of the bodies to the support accelerations recorded during an earthquake that struck Rocchetta, Italy in October 2016. The support accelerations for this earthquake were downloaded from the Orfeus Engineering Strong Motion Database (70) and the file was trimmed to include the data points numbered 6336 to 10334. The resulting accelerations are plotted in Figure 2.26.

The sculpture was modelled as 5.2 meters from bottom of foot to top of head, corresponding to the real dimensions of the sculpture. The pedestal is 1.7 meters by 0.35 meters. $\mu = 0.5$ to model the marble sculpture in contact with a marble support and the density of the sculpture is set to the density of marble, 2711 kg/m^3. The vertical accelerations and the horizontal accelerations from one of the horizontal directions of the earthquake were applied to each of the sculptures.

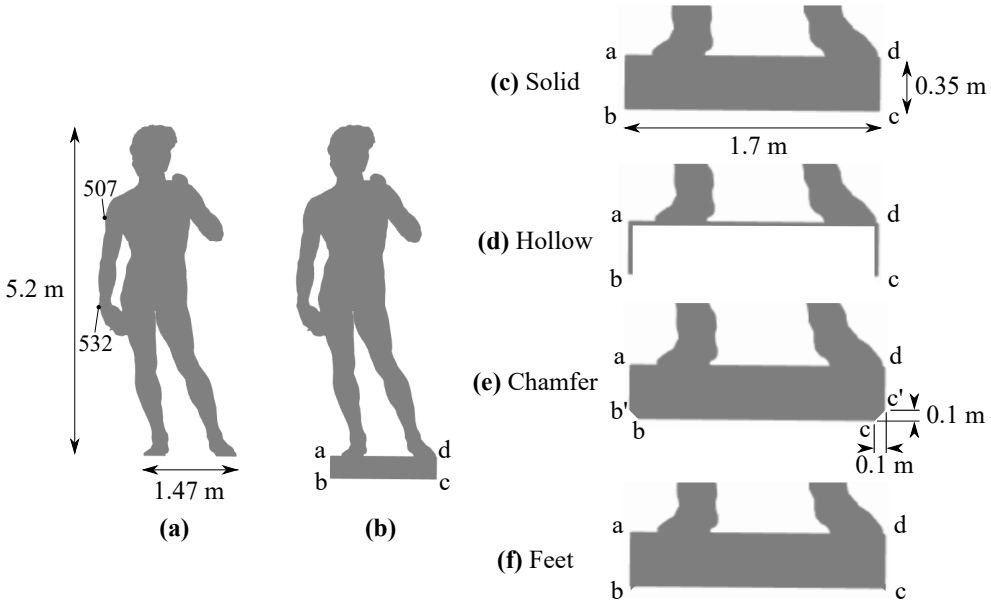


Fig. 2.25. Representations of Michelangelo's *David*. (a) The sculpture without a pedestal; (b) the sculpture with a solid pedestal; (c) a detail of the solid pedestal; (d) a detail of the hollow pedestal; (e) a detail of the chamfered pedestal; (f) a detail of the solid pedestal with small triangular feet at b and c.

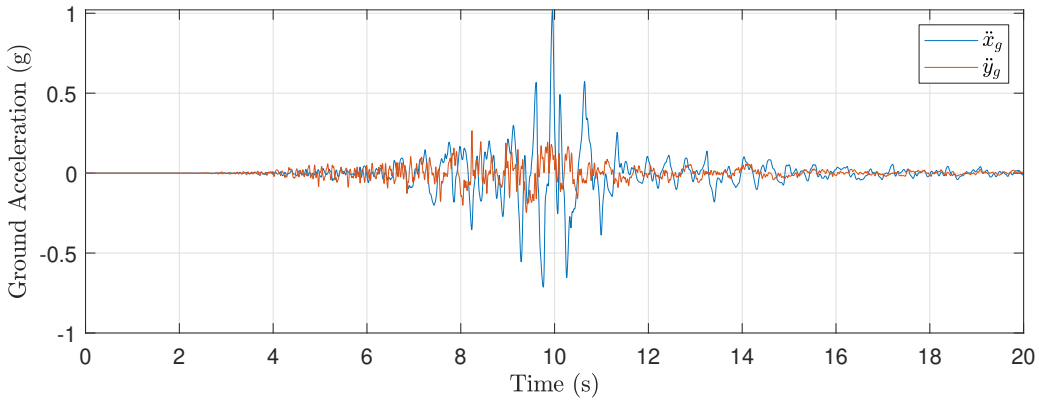


Fig. 2.26. Support accelerations from the Rocchetta, Italy earthquake in October 2016.

Figure 2.27 shows the time histories after six seconds, as the body remains in the static pattern before this, for each state in $\boldsymbol{Q}$ of the *David* without any pedestal and $\lambda = 0$ when subjected to the earthquake. The object fails by counterclockwise rotation after making many impacts (denoted by red circles in Figure 2.27) and a transition from pure rocking to slide rocking just before failure (indicated by the red asterisk and "SR" label). The model produces results for all states but the time history for θ is most informative as failure is

defined by two angles of θ. A video of the dynamics of the *David* without a pedestal during the Rocchetta earthquake is provided in Video S2.17 in the supplementary material.

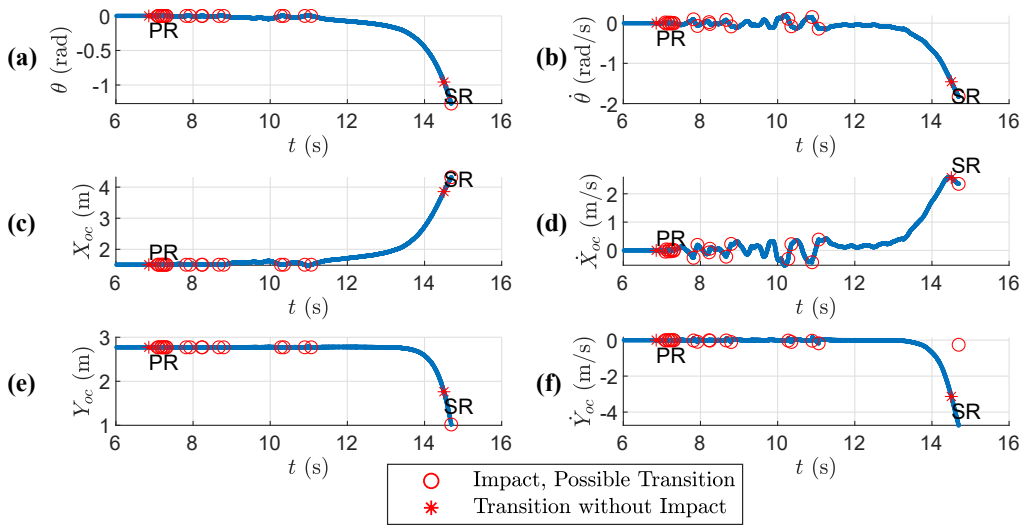


Fig. 2.27. The time histories of each state of $\boldsymbol{Q}$ for the *David* without a pedestal and $\mu = 0.5$, $\epsilon = 0.1$, and $\lambda = 0$. (a) θ; (b) $\dot{\theta}$; (c) X_{oc}; (d) Y_{oc}; (e) $\dot{X}_{oc}$; (f) $\dot{Y}_{oc}$. The labels PR and SR on the time histories correspond to the beginning of pure rocking and slide rocking, respectively.

The responses of different base configurations are tested under the same Rochetta earthquake. Figure 2.28 shows the time history after six seconds for θ for the configurations with no pedestal, the solid pedestal with $\lambda = 0$, and the hollow pedestal. For both pedestal configurations, the body is fixed on the pedestal and the pedestal is free-standing on the support medium.

The sculpture with the solid pedestal survives the Rocchetta earthquake while the sculpture with the hollow pedestal fails in a similar manner as the sculpture with no pedestal. Thus, the addition of the solid pedestal might affect the response of such a body significantly during the earthquake. The survival of the sculpture with the solid pedestal is attributed to the lowering of the center of mass of the object by the addition of mass on the base of the sculpture. The sculpture with the hollow pedestal results in failure in the same direction and around the same time as the sculpture without a pedestal. This shows that increasing the width of the base and overall height of the sculpture does not keep the

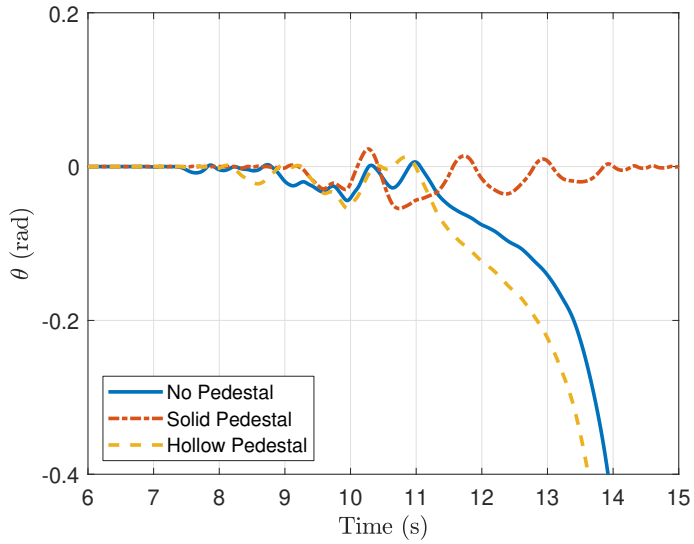


Fig. 2.28. The time histories of θ for the *David* with no pedestal, the solid pedestal with $\lambda = 0$, and the hollow pedestal.

sculpture from overturning as an addition of mass to the base does. Given the stochastic nature of earthquake accelerations, another time history with different record properties could yield a different result when applied to the same base configurations of the David and might even result in overturning failure where survival occurs for another earthquake. In light of this, a full analysis of the seismic risk of irregular objects such as sculptures would require a study with a number of earthquakes to accurately determine their risk of overturning (50).

2.7.5 Example 5: The *David* Sculpture Subjected to Sinusoidal Pulses

Figure 2.29 shows the stability diagram boundaries for sinusoidal pulses for the five configurations of the *David* shown in Figure 2.25: without any pedestal, with the solid pedestal and $\lambda = 0$, with the solid pedestal and $\lambda = 0.15$, with the chamfered pedestal and $\lambda = 0$, and with the hollow pedestal and $\lambda = 0$. When the body has a concave portion between its rocking vertices as the hollow pedestal does, $\lambda = 0$ is most appropriate. However, if there is a solid portion between the rocking vertices as for the solid pedestal, λ may be greater than zero and thus two values of λ are tested in this example. The chamfered pedestal could

also reasonably have $\lambda > 0$ but this study examines the effect of a change in the number of rocking vertices by way of the chamfered pedestal and keeps $\lambda = 0$ so that the responses for different pedestals are more easily compared to each other.

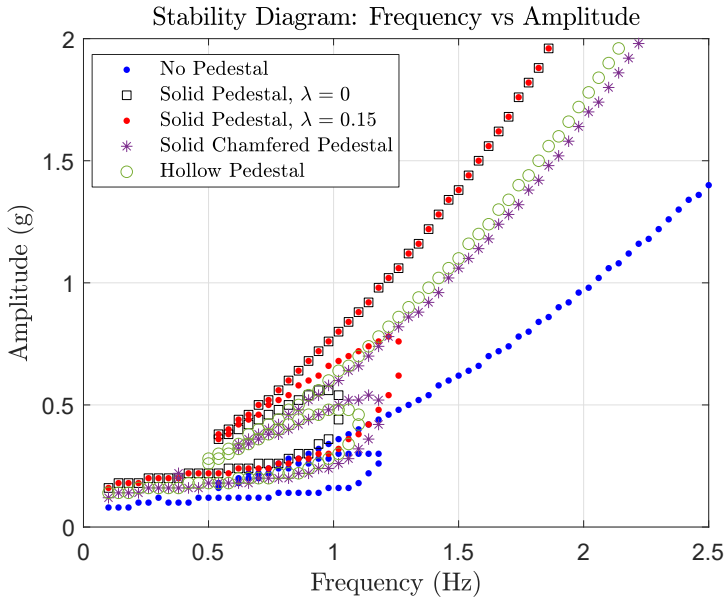


Fig. 2.29. A diagram showing the survival and failure boundaries for the various base conditions of the *David* sculpture.

As demonstrated in Figure 2.29, when λ is increased, the sculpture topples more frequently after impact. Each base configuration exhibits an overturning "loop" where the sculpture's base experiences impacts with the support before failing. This loop for $\lambda = 0.15$ in Figure 2.29 is considerably larger than that for the solid pedestal with $\lambda = 0$, but the boundary between survival and failure outside of the loop is identical regardless of λ because the body topples without impact between its initial support contacts, thus making λ inapplicable for those pulses. Because the pedestal with $\lambda = 0.15$ results in failure for pairs of (f, A) for which the body would have survived with the solid pedestal with $\lambda = 0$, assuming $\lambda = 0$ is not conservative as also shown in (31).

There are clear differences between the stability diagrams without the pedestal and with the pedestal. The sculpture without its pedestal has a much lower minimum threshold for failure amplitude at all frequencies with the difference increasing as f increases. The solid

pedestals are beneficial in preventing the toppling of the sculpture. As shown in the previous example, this is due to the extra mass on the bottom of the sculpture which lowers the center of mass of the sculpture and also slightly increases the distance between the sculpture's support contacts, thus also increasing the moment arm that must be overcome to topple the sculpture.

The results for the hollow pedestal show an intermediate result between the two solid pedestal configurations. The failure amplitude is less for the hollow pedestal for all frequencies when compared to the solid pedestal with $\lambda = 0$, but the relationship is more complicated when compared to $\lambda = 0.15$. In this case, the hollow pedestal generally fails at a lower amplitude except for a region around 1.1 to 1.3 Hz. The hollow pedestal still has better resistance to overturning than no pedestal in all instances. Thus, adding a pedestal to the body despite it raising the body's center of mass, even if the pedestal is hollow, can increase the object's resistance to overturning but this configuration still performs poorly compared to a solid pedestal, particularly when $\lambda = 0$, which can be obtained in practice by placing small "feet" at the rocking vertices of the pedestal to ensure the impulse is applied at the vertex. A flat pedestal without feet should conservatively be assumed to have $\lambda \geq 0.15$.

Finally, the sculpture with the chamfered pedestal has an interesting result when compared to the other configurations. The chamfered pedestal generally provides better resistance to overturning compared to no pedestal but has a larger region of (f, A) pairs which result in failure. The chamfered pedestal with $\lambda = 0$ shows less resistance to overturning compared to the solid pedestal with $\lambda = 0$ which indicates that the chosen chamfered geometry does not improve the overturning stability. This is most likely due to the narrower base of the chamfered pedestal and the fact that X_{oc} is not bounded by the X-coordinates of the vertices in contact with the support at impact. For example, X_{oc} is not bounded by X_{ob} and $X_{ob'}$ when the body rotates to impact at b′ as shown in Figure 2.25 thus making the body unstable at this rotation. However, it is possible that there is an optimal chamfer angle and width that would result in greater rocking stability if the energy of the body can be reduced

through this additional impact and the centroid kept above the outer vertices of the base.

These results show that using a solid pedestal with the minimum value of $\lambda = 0$ for an irregular body is most preferable for rocking stability. This value for λ can be achieved practically by the implementation of feet on the outer edges of the body's pedestal to limit the components of the vertical impulse on portions of a flat pedestal between the support contacts. The addition of feet drastically reduces the area of (f, A) pairs resulting in failure when compared to the solid pedestal with a reasonable $\lambda = 0.15$. The addition of feet also increases the minimum failure amplitude for many pulses. However, if a solid pedestal cannot be obtained, the addition of a hollow pedestal can still improve the object's resistance to overturning.

2.7.6 Example 6: 3-D Terracotta Warrior Sculpture Constrained to Rotate in Plane and Subjected to Sinusoidal Pulses

In addition to objects extruded uniformly in the Z-direction, this model is effective for determining the response of a body such as the terracotta warrior shown in Figure 2.30 provided that the Z-coordinate for the centroid of the body is the same as the Z-coordinate of the centroid of the rectangular pedestal on which the sculpture is placed and the accelerations applied to the body are in the XY plane. The second condition can be replaced by the condition that the pedestal has a sufficiently large length along the Z-direction to prevent out-of-plane rocking. If these conditions are met, such as they are for the objects shown in Figure 2.1, the dynamic response of the body can be determined using this planar rocking model. The object studied here fulfills these requirements to be tested using this model. This model focuses on the effect of using an accurate mass moment of inertia for this object, opposed to the moment of inertia for an approximate rectangular block, and studies the effects of the geometry, sliding and free flight in the planar rocking response of this object.

An STL file (102) of one of the terracotta warriors from the Terracotta Army in Shaanxi, China (shown in Figure 2.30a and 2.30b) was selected for testing. The model of the body

has approximate dimensions of 3.5 m high by 1.2 m wide by 1.2 m deep at its greatest sections while the pedestal is a rectangular prism with dimensions 0.8 m by 0.8 m by 0.1 m. The densities of both the body and pedestal are equal. The centroid (and geometric center consequently) of the pedestal is initially aligned with the centroid of the body without the pedestal and they are rigidly fixed to each other. The moment of inertia is calculated about c. The actual sculpture rests on soil and $\mu = 0.5$ is selected to approximate the contact between terracotta and soil while the soil is assumed to be sufficiently rigid. The effect of an eccentric base configuration is tested for this model by moving the base in the positive X-direction relative to the body of the sculpture by 1% of the total base width (0.008 m) as depicted in Figure 2.30c. This causes the overall centroid of the rigid body to be slightly closer to the right vertex of the base. Stability diagrams for this object are provided in Figure 2.31.

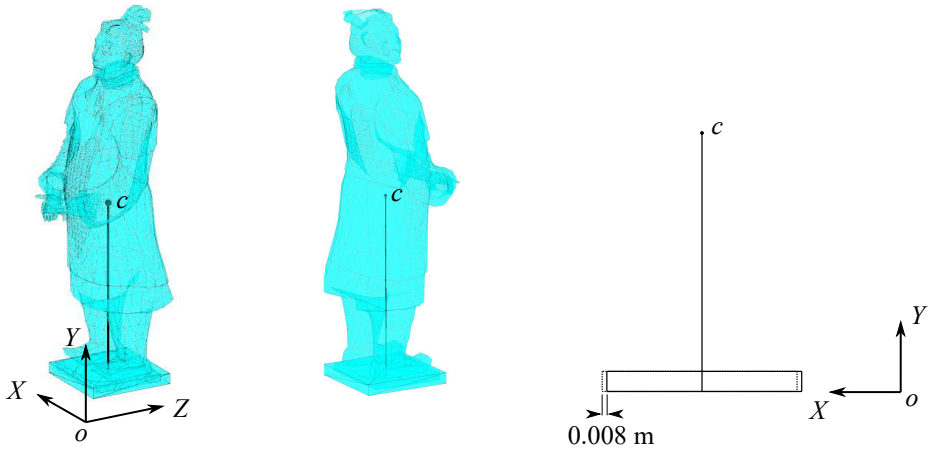


Fig. 2.30. An STL representation of a terracotta warrior from Shaanxi, China. (a) a front view of the sculpture with the body's centroid vertically aligned with the centroid and geometric center of the pedestal; (b) a rear view of the sculpture; (c) a depiction of the eccentricity of 0.008 m applied to the pedestal. The dashed and solid lines correspond to the outline of the centered and 0.008 m offset pedestal respectively.

Figure 2.31a shows the results of the centered pedestal with $\lambda = 0$. There is a large failure A region which does not extend past 4 Hz for all realistic amplitudes of acceleration. In addition, there is a small failure B region. Because the centroid is above the geometric

center of the pedestal in this case and the base of the body that contacts the support is symmetric about the centroid, sinusoidal pulses in the opposite direction yield the same stability diagram. On the other hand, Figure 2.31b and 2.31c shows the results for the body with the eccentric base.

The same pulses applied to the centered body in Figure 2.31a are applied for the eccentric base configuration where 2.31b and 2.31c correspond to positive and negative initial support accelerations respectively. Drastic changes in the stability diagram are observed in Figure 2.31b. The failure A region remains essentially the same, but the failure B region grows dramatically, signifying a much higher susceptibility to failure with impact due to the eccentricity of the body. The body experiences slide rocking and pure rocking and fails by overturning about the rocking vertex nearer the centroid as might be expected. As the body is asymmetric, pulses in the opposite direction reap a unique response as well. As the support acceleration now causes the body to rotate about the rocking vertex nearer the centroid before impact, the failure A region actually increases slightly, extending past 4 Hz where it did not previously. On the other side, the failure B region decreases in size, indicating greater safety if the object does not topple without impact. This is presumably due to the greater distance on the left side between the centroid and the rocking vertex which causes a greater reduction in energy than for the right side at impact. The right side also provides less resistance to overturning during integration of the post-impact rocking pattern due to the smaller effective width of the right side of the base compared to the left.

These results prove the critical importance of the location of the centroid in relation to the base geometry of the object. If the location of the body's centroid is changed by only 1% of the base width horizontally, the body's regions of survival and failure can change greatly. For pulses in one direction, there are many more pairs of amplitudes and frequencies that cause the body to fail compared to the body with its centroid at the geometric center, but for pulses in the opposite direction, the object has a slightly smaller failure A region. Overall, as the direction of seismic or other forms of support accelerations cannot be chosen by those

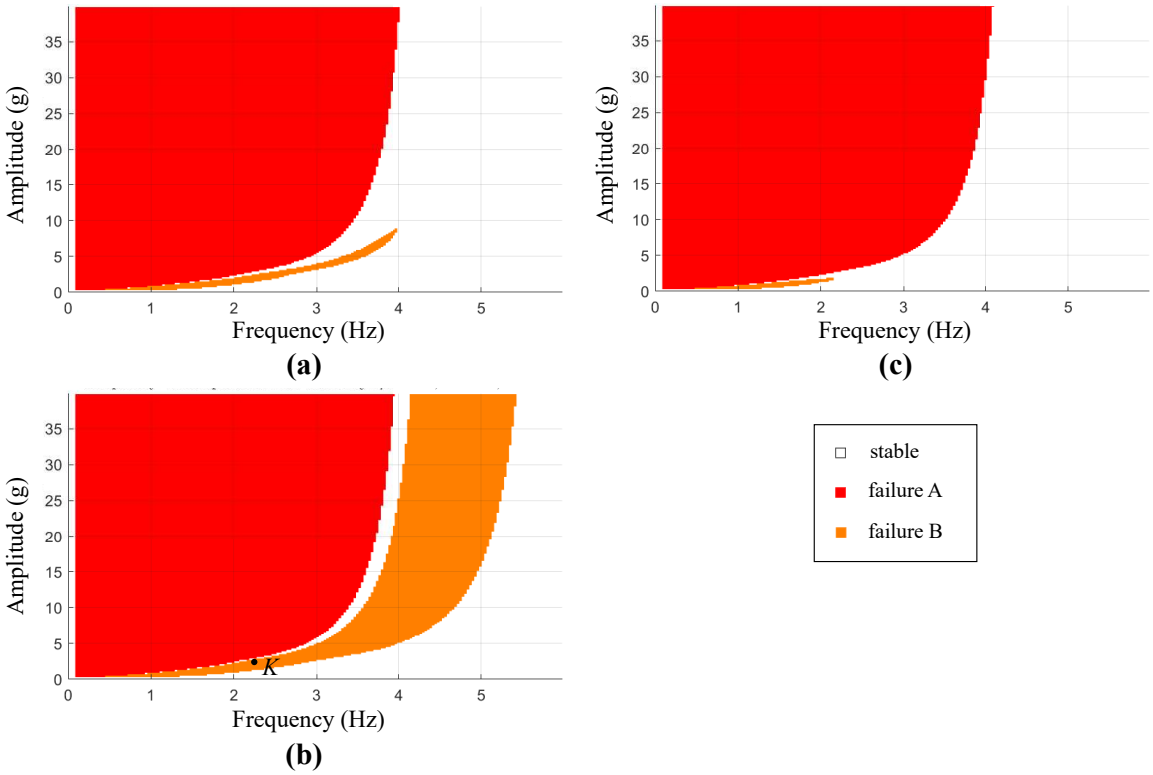


Fig. 2.31. Stability diagrams for the terracotta warrior sculpture with $\lambda = 0$. (a) no eccentricity; (b) 1% eccentricity and an initial positive support acceleration; (c) 1% eccentricity and an initial negative support acceleration.

with interest in protecting at-risk objects, the large increase in the failure region exhibited in Figure 2.31c makes any eccentricity in such objects more susceptible to failure than those with no eccentricity.

As in the case of the PBR in the first example, it is also important to note the importance of sliding in the dynamic response of the terracotta warrior during the sine pulses. The plot in Figure 2.32 shows X_{op} and $\dot{X}_{op}$ where p is the active rocking vertex, and the pulse applied is the (f, A) pair corresponding to point K from the stability diagram of Figure 2.31c. The non-zero values for $\dot{X}_{op}$ indicate that the object is in slide rocking before overturning. Slide rocking occurs for many pulses which result in failure in Figure 2.31. Point K is a mild example as many pulses result in drastic sliding even with a $\mu = 0.5$, which is normally considered as high. The instability arising from sliding is further evidence that neglecting sliding is not conservative for irregular objects in planar rocking.

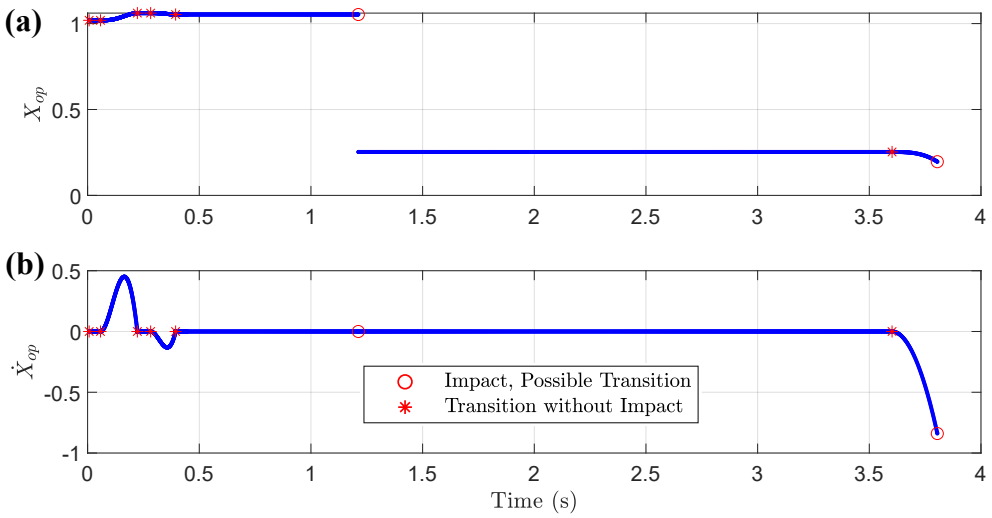


Fig. 2.32. The time history for the active rocking vertex horizontal position and velocity, X_{op} and $\dot{X}_{op}$, for point K from Figure 2.31 showing slide rocking leading to failure.

Further, as researchers have found the 3-D non-planar rocking of objects to be nonconservative (33; 120; 44), future studies should not be restricted to the planar motion of such objects.

2.8 Conclusions

A model for examining the planar rocking behavior of an irregular body with any polygonal geometry is introduced in this chapter. The model takes into account sliding, free flight, and the variable location of the impulse at impact defined by λ. It also allows for the examination of any rigid body given only the STL file defining the geometry of the body and the desired support accelerations to be applied to it. This new model allows for studying the response of a body with any geometry and any number of potential rocking vertices. Newtonian equations of motion for the non-linear system were formulated in an automated manner and solved using Matlab's symbolic toolbox, ode45, and ODE event location functionality. Equations of momentum for impacts were also formulated and solved taking into account sliding and free flight due to impact.

The examples and results presented show that the geometry of the body and its base configuration, the value of μ, the location of the vertical impulse defined by λ, the direction of the pulse, the presence of sliding and free flight, and the eccentricity of the centroid relative to its support contacts are all critical to determining the accurate rocking response of an irregular body. The example of the shelving units show that uneven feet, quarter circle feet, or a flat base with $\lambda = 0.3$ are undesirable compared to raised extensions that widen the base and act as additional rocking vertices. The studies on the shelving units and PBR also show the importance of using the full irregular geometry as different directions of failure are not equally common as for a rectangular block. Further, these studies verify past results where neglecting sliding is not a conservative assumption (30). The study on Michelangelo's sculpture with various base configurations shows the importance of accounting for a variable λ or trying to control it through modifying the base of the sculpture, showing that a solid pedestal with $\lambda = 0$, which can be achieved through small feet at the vertices, is most beneficial for the rocking stability of this sculpture. Finally, the terracotta warrior example shows the importance of minimizing the eccentricity between the centroid of the sculpture and geometric center of the base as well as the unstable nature of the object due to sliding. Particular findings of note are the abnormal shapes in the stability diagram that are not present for symmetric rectangular bodies subject to sine pulses and the finding that permitting more sliding by reducing μ does not result in a more stable body.

The software that utilizes this model is useful for studying the effects of earthquakes and other support accelerations on objects such as museum artifacts, PBRs, and other objects susceptible to rocking under conditions that would result in those objects experiencing planar rocking. The examples presented focus on irregular geometries that substantially deviate from a simple rectangular geometry; however, this model also enables the study of geometric defects of any shape or size. Finally, this chapter has demonstrated the importance of accounting for the irregular geometry of a rocking body but, as other researchers have shown, the geometry or excitation of many 3-D bodies would not result in planar rocking.

Thus, neglecting the 3-D nature of the response is not a conservative assumption (33; 120). As such, the extension of this model to 3-D is an important research step to take. This work, and the automated procedure suggested for formulating the equations of motion, defining the transitions between patterns, and solving the momentum equations, facilitates such an extension.

Chapter 3

The 3-D Pure Rocking Dynamics of Objects with Irregular Geometry

3.1 Introduction

Most objects, whether they have simple or irregular geometry, display 3-D rocking. Specific constraints would have to be applied for the body to display planar rocking. For objects with irregular geometry, these constraints may be even more difficult to meet than simple geometries and thus, a 3-D irregular geometry rocking model is necessary. Many museum artifacts, computers, glass bottles, and other delicate and valuable objects are prone to such 3-D rocking, among many other objects which may not be as delicate or valuable but which may be very large and present a safety risk or risk of damage to structures around them.

A discrete element method (DEM) approach using concentrated or continuous/Winkler springs in (33) could be extended to bodies of any geometry. But the potential for many vertices in the convex hull of a body with an irregular geometry results, even in the case of modeling the body using concentrated springs, in a significant computational cost. Further it is expected that neglecting the deformability of the body and the support may have smaller effects for smaller objects made of concrete, wood, stone, hard plastic, or metal resting on a

hard support. When using deformable models, some assumptions about the material of the body and the interface are required. To isolate the effect of the geometry from the specific material used, a rigid model can be used to offer qualitative results. Thus, a rigid body and support model, as for the planar model, is selected for greater computational speed and simplicity of results.

The choice between a general constraint method such as Lagrange multipliers and an analytical method which solves for independent DOFs must also be made. This choice is also necessary for the planar model. To eliminate numerical drift when integrating the equations of motion, the latter method will be utilized in this work. Thus, this chapter introduces the first model of its kind that robustly handles the 3-D pure rocking (PR) response (neglecting sliding and free flight) of a rigid body that has a general irregular geometry, The model takes into account the body's mass moment of inertia and any number of possible rocking vertices. Additionally, as argued in Chapter 2, a variable location for the vertical impulse at impact has a significant effect on the body's response and is also taken into account. To include all these effects, the model has different dynamic patterns that include up to three independent DOFs. Sliding and free flight are ignored in this model in order to focus on the irregular geometry of the objects and to lower the computational cost. Just as the planar model, the 3-D model uses an STL file to easily import the geometry of any object, but this geometry is not simplified but used without any modifications. Examples of rocking museum artifacts are provided which demonstrate the importance of considering the irregular geometry and full 3-D motion of the body.

This chapter extends the dynamics of the body from a planar to a 3-D response, and thus, the variables used in this chapter do not correspond directly with the variables used in the previous chapter and should generally be viewed as a separate set.

3.2 Generalized Coordinates

The rigid body shown in Figure 3.1 is an object of arbitrary geometry with mass m and volume V. For visualization purposes and without loss of generality, the following figures will make use of the geometry corresponding to a Roman reproduction of the *Doryphoros* currently exhibited at the Minneapolis Institute of Art (90; 47). However, the developed theory and model are applicable to a body of any geometry. Such a geometry can be defined, for example, through an STL file (79).

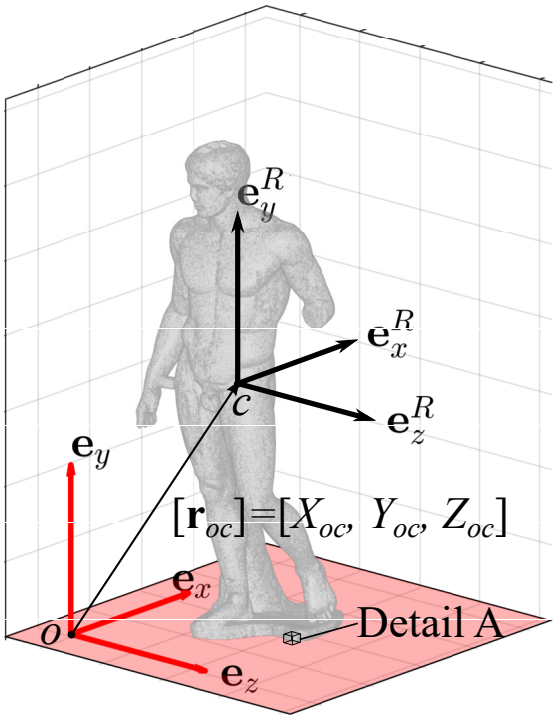


Fig. 3.1. An example of a rigid body with irregular geometry.

The object in Figure 3.1 has a mixture of convex and concave portions, holes in its geometry, and a very irregular base due to both its original design and subsequent damage. The Cartesian coordinate system S is defined from the origin o on the support surface as shown in Figure 3.1 by the X, Y, and Z axes which are fixed on the surface of the support medium and parallel to the unit vectors $\mathbf{e}_x$, $\mathbf{e}_y$, and $\mathbf{e}_z$ respectively. $\mathbf{e}_y$ is vertical and $\mathbf{e}_x$ and $\mathbf{e}_z$ are horizontal creating an orthonormal basis as shown in Figure 3.1. Additionally, a

coordinate system R that is fixed on the body, and hence rotates and translates with respect to base S is defined with its origin at the centroid c of the body with axes x, y, and z parallel to the unit vectors $\mathbf{e}_x^R$, $\mathbf{e}_y^R$, and $\mathbf{e}_z^R$ respectively. The Cartesian coefficients of a vector in base S from a point i to j, $\mathbf{r}_{ij}$, are denoted by the row vector $[\mathbf{r}_{ij}] = [X_{ij},\ Y_{ij},\ Z_{ij}]$, where the coefficients of the vector are uppercase. The coefficients for $\mathbf{r}_{ij}$ in base R are denoted by the row vector ${}^R[\mathbf{r}_{ij}] = [x_{ij},\ y_{ij},\ z_{ij}]$, where the coefficients of the vector are lowercase. Throughout this chapter the superscript preceding a vector of coefficients indicates that the coordinates are expressed in terms of the base suggested by the superscript. For example, the coefficients for $\mathbf{r}_{ij}$ in base W would be written ${}^W[\mathbf{r}_{ij}] = [{}^WX_{ij}, {}^WY_{ij}, {}^WZ_{ij}]$ unless noted otherwise. If no superscript prefix is present and it is not stated otherwise, the base should be considered to be S. Additionally, unless stated otherwise, the subscript ${}_x$, ${}_y$, or ${}_z$ refers to a coordinate along the corresponding unit vector of the base indicated by the leading superscript, or if no superscript is provided, base S. For example, ${}^R\omega_x$ refers to the component of $\boldsymbol{\omega}$ in the $\mathbf{e}_x^R$ direction. The mass moment of inertia tensor of the body with respect to c along the unit vectors of base R, will be denoted as ${}^R[\boldsymbol{I}]$. The coefficients of ${}^R[\boldsymbol{I}]$ when expanded are:

$$ {}^R[\boldsymbol{I}] = \begin{bmatrix} I_{xx} & I_{xy} & I_{xz} \\ I_{yx} & I_{yy} & I_{yz} \\ I_{zx} & I_{zy} & I_{zz} \end{bmatrix} \tag{3.1} $$

3.3 3-D Computational Geometry

A description of the geometry of the body to be studied must first be obtained. For simplicity, a stereolithography file (STL), which is common in 3-D printing and scanning, is used to store the geometry of objects for this model (79). STL files contain a triangulation of the external surface of the body and thus contain all the vertices that define the body and a connectivity matrix that defines all the triangular faces around the exterior of the body. STL

files are not limited in their ability to store different geometries and thus the body may have through holes, or openings that go all the way through the body, and multiple vertices that can act as rocking vertices.

The following Figure 3.2 shows Detail A from Figure 3.1.

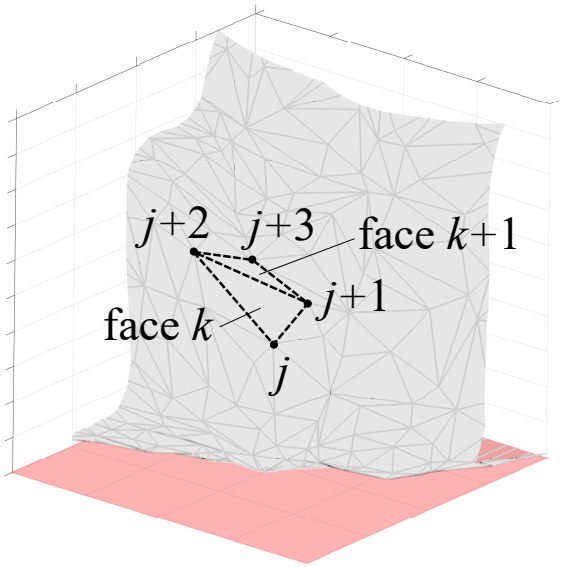


Fig. 3.2. Detail A of the *Doryphoros* as referenced in Figure 3.1, showing a cutout of the triangulation of the STL file and the vertices and edges for two faces highlighted.

The detail in Figure 3.2 shows a close-up view of the triangulation of the *Doryphoros* with two triangular faces of the STL labeled as face k and face $k+1$ and the vertices defining these two faces: j, $j+1$, and $j+2$ for face k, and $j+1$, $j+2$, and $j+3$ for face $k+1$. The STL file for this or any other object may be input to the model software using Matlab's stlread function (60) which creates an nx3 matrix $\mathbf{M}_v$ of the n vertex coordinates and an mx3 triangulation matrix $\mathbf{M}_f$ defining the m faces of the object. For example, from Figure 3.2, $\mathbf{M}_v$ would include the X, Y, and Z coordinates for vertices j, $j+1$, $j+2$, and $j+3$ and every other vertex on the body. Then, for face k, row k of $\mathbf{M}_f$ would include entries u, v, w which are the rows of face k's three vertices (j, $j+1$, and $j+2$) in $\mathbf{M}_v$.

The parameters $[\mathbf{r}_{oc}]$, ${}^{R}[\boldsymbol{I}]$, and V of the body are calculated using another Matlab function (93) by way of the divergence theorem (43) which is also used in the computation of volumes and centroids for the 3-D concentrated springs and Winkler models in (33)

and is further discussed there. If previously unknown, the mass of the body is calculated using the density of the material and V calculated above. To study a non-uniform density object, $[\mathbf{r}_{oc}]$ and m are calculated for each portion with a different density and the results are combined to find $[\mathbf{r}_{oc}]$ and ${}^{R}[\boldsymbol{I}]$ for the full body.

Finally, the 3-D convex hull of the body is calculated. The convex hull of a set of points K is the intersection of all convex sets containing K (114). The rigid body may only contact a rigid horizontal support at points on the convex hull and thus only the convex hull vertices need to be tracked for various events that are defined later, cutting computational costs. The ith vertex of the convex hull is denoted as u_i. Figure 3.3 shows the convex hull of the *Doryphoros* with one of the u_i vertices labeled.

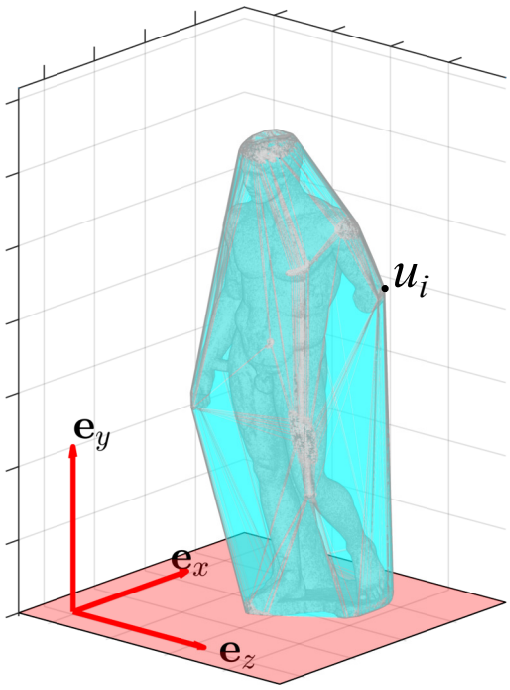


Fig. 3.3. The *Doryphoros* with its convex hull triangulation superimposed.

3.4 The Equations of Motion

3.4.1 Degrees of Freedom

To obtain the unconstrained equations of motion for a rigid body in three dimensions, a total of six DOFs are required. The three translational DOFs are defined by $[\mathbf{r}_{oc}]$: X_{oc}, Y_{oc}, and Z_{oc} as shown in Figure 3.1. The additional three DOFs are rotational. To model the 3-D rotations of the body, three sequential Euler angles ψ, θ, ϕ are utilized as shown in Figure 3.4.

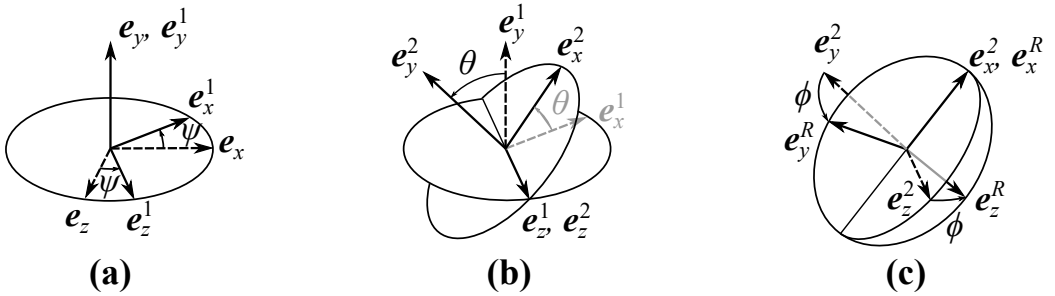


Fig. 3.4. The three sequential Euler angles forming a 2-3-1 combination. (a) ψ about $\boldsymbol{e}_y$. (b) θ about $\boldsymbol{e}_z^1$. (c) ϕ about $\boldsymbol{e}_x^2$.

Before rotating the unit vectors, a new base S^1 is created by translating base S from o to c. Then, the first Euler angle rotation ψ rotates the Cartesian base S^1 about $\mathbf{e}_y$ resulting in the base $\mathbf{e}_x^1$, $\mathbf{e}_y^1$, $\mathbf{e}_z^1$. The second Euler angle rotation is by angle θ about the $\mathbf{e}_z^1$ vector which results in the base $\mathbf{e}_x^2$, $\mathbf{e}_y^2$, $\mathbf{e}_z^2$. Finally, the last Euler angle rotation is by the angle ϕ about the $\mathbf{e}_x^2$ vector resulting in the base R fixed at c on the body and defined by unit vectors $\mathbf{e}_x^R$, $\mathbf{e}_y^R$, $\mathbf{e}_z^R$. The transformations for each of these rotations are defined by the rotation matrices

$\mathbb{R}_\psi$, $\mathbb{R}_\theta$, $\mathbb{R}_\phi$:

$$\begin{Bmatrix} \mathbf{e}_x^1 \\ \mathbf{e}_y^1 \\ \mathbf{e}_z^1 \end{Bmatrix} = \mathbb{R}_\psi \begin{Bmatrix} \mathbf{e}_x \\ \mathbf{e}_y \\ \mathbf{e}_z \end{Bmatrix} \qquad \begin{Bmatrix} \mathbf{e}_x^2 \\ \mathbf{e}_y^2 \\ \mathbf{e}_z^2 \end{Bmatrix} = \mathbb{R}_\theta \begin{Bmatrix} \mathbf{e}_x^1 \\ \mathbf{e}_y^1 \\ \mathbf{e}_z^1 \end{Bmatrix} \qquad \begin{Bmatrix} \mathbf{e}_x^R \\ \mathbf{e}_y^R \\ \mathbf{e}_z^R \end{Bmatrix} = \mathbb{R}_\phi \begin{Bmatrix} \mathbf{e}_x^2 \\ \mathbf{e}_y^2 \\ \mathbf{e}_z^2 \end{Bmatrix}$$

$$\mathbb{R}_\psi = \begin{bmatrix} \cos(\psi) & 0 & -\sin(\psi) \\ 0 & 1 & 0 \\ \sin(\psi) & 0 & \cos(\psi) \end{bmatrix} \quad \mathbb{R}_\theta = \begin{bmatrix} \cos(\theta) & \sin(\theta) & 0 \\ -\sin(\theta) & \cos(\theta) & 0 \\ 0 & 0 & 1 \end{bmatrix} \quad \mathbb{R}_\phi = \begin{bmatrix} 1 & 0 & 0 \\ 0 & \cos(\phi) & \sin(\phi) \\ 0 & -\sin(\phi) & \cos(\phi) \end{bmatrix} \tag{3.2}$$

To transform from base S^1 to base R, the product of the rotation matrices $\mathbb{R}_\phi \mathbb{R}_\theta \mathbb{R}_\psi$ defined more concisely as $\mathbb{R}_{\phi\theta\psi}$ is used. The resulting rotation matrix is defined as follows:

$$\begin{Bmatrix} \mathbf{e}_x^R \\ \mathbf{e}_y^R \\ \mathbf{e}_z^R \end{Bmatrix} = \mathbb{R}_{\phi\theta\psi} \begin{Bmatrix} \mathbf{e}_x \\ \mathbf{e}_y \\ \mathbf{e}_z \end{Bmatrix} \tag{3.3}$$

$$\mathbb{R}_{\phi\theta\psi} = \begin{bmatrix} \mathrm{c}(\psi)\mathrm{c}(\theta) & \mathrm{s}(\theta) & -\mathrm{c}(\theta)\mathrm{s}(\psi) \\ \mathrm{s}(\phi)\mathrm{s}(\psi) - \mathrm{c}(\phi)\mathrm{c}(\psi)\mathrm{s}(\theta) & \mathrm{c}(\phi)\mathrm{c}(\theta) & \mathrm{c}(\psi)\mathrm{s}(\phi) + \mathrm{c}(\phi)\mathrm{s}(\psi)\mathrm{s}(\theta) \\ \mathrm{c}(\phi)\mathrm{s}(\psi) + \mathrm{c}(\psi)\mathrm{s}(\phi)\mathrm{s}(\theta) & -\mathrm{c}(\theta)\mathrm{s}(\phi) & \mathrm{c}(\phi)\mathrm{c}(\psi) - \mathrm{s}(\phi)\mathrm{s}(\psi)\mathrm{s}(\theta) \end{bmatrix} \tag{3.4}$$

where s and c represent the sine and cosine functions respectively.

Since the ${}^R[\mathbf{r}_{cp_i}]$ are known, the Cartesian coordinates of any vertex p_i can be obtained by:

$$\left[X_{op_i},\ Y_{op_i},\ Z_{op_i}\right] = \left[X_{oc},\ Y_{oc},\ Z_{oc}\right] + \left[x_{cp_i},\ y_{cp_i},\ z_{cp_i}\right] \mathbb{R}_{\phi\theta\psi} \tag{3.5}$$

The Cartesian velocity and acceleration of a vertex p_i can also be obtained by differen-

tiating equation (3.5) with respect to time:

$$\begin{aligned}\left[\dot{X}_{op_i},\ \dot{Y}_{cp_i},\ \dot{Z}_{cp_i}\right] &= \left[\dot{X}_{oc},\ \dot{Y}_{oc},\ \dot{Z}_{oc}\right] + \left[x_{cp_i},\ y_{cp_i},\ z_{cp_i}\right]\dot{\mathbb{R}}_{\phi\theta\psi} \\ \left[\ddot{X}_{op_i},\ \ddot{Y}_{cp_i},\ \ddot{Z}_{cp_i}\right] &= \left[\ddot{X}_{oc},\ \ddot{Y}_{oc},\ \ddot{Z}_{oc}\right] + \left[x_{cp_i},\ y_{cp_i},\ z_{cp_i}\right]\ddot{\mathbb{R}}_{\phi\theta\psi}\end{aligned} \tag{3.6}$$

where $(\dot{})$ and $(\ddot{})$ represent the first and second derivatives with respect to time respectively. The coordinates $[x_{cp_i},\ y_{cp_i},\ z_{cp_i}]$ do not vary over time as the vector $\mathbf{r}_{cp_i}$ is on the rigid body. Further, the coefficients of the velocities in base S will be denoted: $[\mathbf{v}_{oc}] = [\dot{X}_{oc}, \dot{Y}_{oc}, \dot{Z}_{oc}]$.

3.4.2 Angular Velocity of the Body

The angular velocity $\boldsymbol{\omega}$ of base R with respect to base S is generally

$$\boldsymbol{\omega} = \dot{\psi}\mathbf{e}_y + \dot{\theta}\mathbf{e}_z^1 + \dot{\phi}\mathbf{e}_x^2 \tag{3.7}$$

where $\dot{\psi}$, $\dot{\theta}$, and $\dot{\phi}$ are the first derivatives of the Euler angles with respect to time. The angular velocity can also be expressed in base R coordinates as follows:

$${}^R[\boldsymbol{\omega}] = \left[\dot{\phi} + \dot{\psi}\sin(\theta),\ \dot{\psi}\cos(\theta)\cos(\phi) + \dot{\theta}\sin(\phi),\ -\dot{\psi}\cos(\theta)\sin(\phi) + \dot{\theta}\cos(\phi)\right] \tag{3.8}$$

3.4.3 Single Degree of Freedom Rocking Formulation

An alternative transformation from base S to base R is derived for a body which is rocking about one of its edges E_{ij}, which is a motion that requires a single DOF and will be discussed in detail beginning in Section 3.5. The following formulation is necessary to reduce the DOFs of the system to one. At some time t^*, the body begins rocking about an edge $E_{p_1p_2}$. t^* is the first time instance for which this edge becomes the only part of the body in contact with the support. Note that the geometry surrounding this "edge" may be either concave or convex. An example of a concave rocking edge is shown in Figure 3.5. After time t^*, the

motion of the object rocking about its edge can be defined by a single independent DOF γ, which is the rotation about a unit vector $\hat{\mathbf{n}}$ parallel to $\mathbf{r}_{p_1p_2}$.

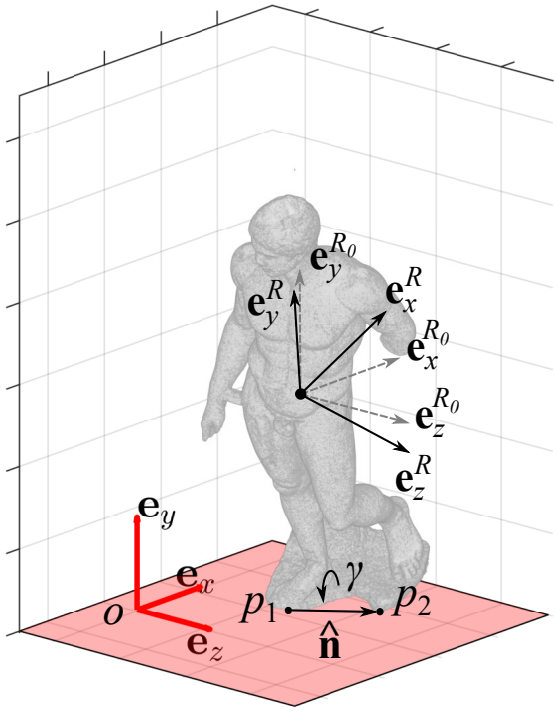


Fig. 3.5. *The Doryphoros* rotating about $\hat{\mathbf{n}}$ parallel to $E_{p_1p_2}$. Base R had the orientation shown by the $\mathbf{e}_x^{R_0}$, $\mathbf{e}_y^{R_0}$, $\mathbf{e}_z^{R_0}$ unit vectors when it began rocking about $E_{p_1p_2}$ at time t^* and subsequently rotated by γ about $\hat{\mathbf{n}}$ to give the base R unit vectors shown.

Let ϕ_0, ψ_0, θ_0 correspond to the values of ϕ, ψ, θ at time t^*. A new base R_0 is defined by the unit vectors $\mathbf{e}_x^{R_0}$, $\mathbf{e}_y^{R_0}$, $\mathbf{e}_z^{R_0}$ which coincide with the unit vectors of base R at time t^*. The R_0 vectors will remain fixed over time relative to the support medium, irrespective of the body's movement for $t > t^*$, unlike the vectors of base R which remain fixed on the body. To transform from base S^1 as defined above to base R_0, the following expression may be used:

$$\begin{Bmatrix} \mathbf{e}_x^{R_0} \\ \mathbf{e}_y^{R_0} \\ \mathbf{e}_z^{R_0} \end{Bmatrix} = \mathbb{R}_{\phi_0\theta_0\psi_0} \begin{Bmatrix} \mathbf{e}_x \\ \mathbf{e}_y \\ \mathbf{e}_z \end{Bmatrix} \tag{3.9}$$

where $\mathbb{R}_{\phi_0\theta_0\psi_0}$ is the rotation matrix $\mathbb{R}_{\phi\theta\psi}$ with $\phi = \phi_0$, $\psi = \psi_0$, $\theta = \theta_0$.

After time t^*, the body begins rocking with a single DOF about $E_{p_1p_2}$. Base M is defined through the unit vectors $\mathbf{e}_x^M$, $\mathbf{e}_y^M$, $\mathbf{e}_z^M$ which at time t^* are aligned and collocated with the unit vectors of base R_0 but remain fixed on the body. Both the body and base M are permitted to rotate by angle γ about the unit vector $\hat{\mathbf{n}}$, with initial condition $\gamma = 0$ at $t = t^*$. Base M is identical to base R; the only difference is the sequence of operations that are used to generate the two bases. The rotation that results in basis M from R_0 is different from previous Euler angle rotations as it is done about a vector that is not necessarily parallel to any of the unit vectors of R_0. The following equation describes this transformation:

$$\begin{Bmatrix} \mathbf{e}_x^M \\ \mathbf{e}_y^M \\ \mathbf{e}_z^M \end{Bmatrix} = \mathbb{R}_\gamma \begin{Bmatrix} \mathbf{e}_x^{R_0} \\ \mathbf{e}_y^{R_0} \\ \mathbf{e}_z^{R_0} \end{Bmatrix} \tag{3.10}$$

$$\mathbb{R}_\gamma = \begin{bmatrix} (1-\mathrm{c}(\gamma))\left({}^R n_1\right)^2 + \mathrm{c}(\gamma) & {}^R n_3 \mathrm{s}(\gamma) - {}^R n_1 {}^R n_2 \left(\mathrm{c}(\gamma) - 1\right) & -{}^R n_2 \mathrm{s}(\gamma) - {}^R n_1 {}^R n_3 \left(\mathrm{c}(\gamma) - 1\right) \\ -{}^R n_3 \mathrm{s}(\gamma) - {}^R n_1 {}^R n_2 \left(\mathrm{c}(\gamma) - 1\right) & (1-\mathrm{c}(\gamma))\left({}^R n_2\right)^2 + \mathrm{c}(\gamma) & {}^R n_1 \mathrm{s}(\gamma) - {}^R n_2 {}^R n_3 \left(\mathrm{c}(\gamma) - 1\right) \\ {}^R n_2 \mathrm{s}(\gamma) - {}^R n_1 {}^R n_3 \left(\mathrm{c}(\gamma) - 1\right) & -{}^R n_1 \mathrm{s}(\gamma) - {}^R n_2 {}^R n_3 \left(\mathrm{c}(\gamma) - 1\right) & (1-\mathrm{c}(\gamma))\left({}^R n_3\right)^2 + \mathrm{c}(\gamma) \end{bmatrix} \tag{3.11}$$

where the unit vector $\hat{\mathbf{n}}$ is defined in base R_0 or R (as they are identical at time t^* and $\hat{\mathbf{n}}$ does not move while the edge is in contact with the support) as ${}^R[\hat{\mathbf{n}}] = [{}^R n_1,\ {}^R n_2,\ {}^R n_3]$, and s and c are the sine and cosine functions respectively. The transformation from base S^1 to M is thus:

$$\begin{Bmatrix} \mathbf{e}_x^M \\ \mathbf{e}_y^M \\ \mathbf{e}_z^M \end{Bmatrix} = \mathbb{R}_\gamma \mathbb{R}_{\phi_0\theta_0\psi_0} \begin{Bmatrix} \mathbf{e}_x \\ \mathbf{e}_y \\ \mathbf{e}_z \end{Bmatrix} \tag{3.12}$$

where $\mathbb{R}_\gamma \mathbb{R}_{\phi_0\theta_0\psi_0}$ is the product of $\mathbb{R}_\gamma$ and $\mathbb{R}_{\phi_0\theta_0\psi_0}$. As previously described, the two bases

M and R are identical. To ensure this, the Euler angles ψ, θ, ϕ that produce the same orientation as the sequence of rotations ψ_0, θ_0, ϕ_0, γ is sought. Thus, the rotation matrix $\mathbb{R}_\gamma \mathbb{R}_{\phi_0\theta_0\psi_0}$ is named with elements R_{ij} for $i = j = 1, 2, 3$ where i is the row and j is the column of the element:

$$\mathbb{R}_\gamma \mathbb{R}_{\phi_0\theta_0\psi_0} = \mathbb{R}_{\phi\theta\psi} = \begin{bmatrix} R_{11} & R_{12} & R_{13} \\ R_{21} & R_{22} & R_{23} \\ R_{31} & R_{32} & R_{33} \end{bmatrix} \tag{3.13}$$

A set of Euler angles, ϕ, ψ, and θ, can be selected to give the same orientation defined by γ, ϕ_0, ψ_0, and θ_0 by equating corresponding entries in the rotation matrices $\mathbb{R}_{\phi\theta\psi}$ and $\mathbb{R}_\gamma \mathbb{R}_{\phi_0\theta_0\psi_0}$. Each of ϕ, θ, ψ can thus be solved in turn by the following equations from (97):

$$\begin{aligned} \sin(\theta) = R_{12} &\Rightarrow \theta = \arcsin(R_{12}) \\ -\tan(\psi) = \frac{R_{13}}{R_{11}} &\Rightarrow \psi = \operatorname{arctan2}\left(-\frac{R_{13}}{\cos(\theta)}, \frac{R_{11}}{\cos(\theta)}\right) \\ -\tan(\phi) = \frac{R_{32}}{R_{22}} &\Rightarrow \phi = \operatorname{arctan2}\left(-\frac{R_{32}}{\cos(\theta)}, \frac{R_{22}}{\cos(\theta)}\right) \end{aligned} \tag{3.14}$$

Note that arctan2 is the four-quadrant inverse tangent function with the resulting angle on the interval $[-\pi, \pi]$. Including the $\cos(\theta)$ terms ensures that the signs of the arguments for arctan2 are correct. There exist two unique sets of 2-3-1 sequential Euler angles for every orientation of the body but it is only necessary to calculate one set of angles.

These equations give ϕ, ψ, θ in terms of known variables $\hat{\mathbf{n}}$, ϕ_0, ψ_0, θ_0, and γ. Determining these angles in the opposite direction is simpler as ϕ_0, ψ_0, θ_0 are equal to ϕ, ψ, θ at time t^* and $\gamma = 0$ at t^*.

For rocking about an edge, $\boldsymbol{\omega}$ can be simply expressed as:

$$\begin{aligned} \boldsymbol{\omega} &= \dot{\gamma}\hat{\mathbf{n}} \\ {}^M[\boldsymbol{\omega}] = {}^R[\boldsymbol{\omega}] &= [\dot{\gamma}^R n_1, \dot{\gamma}^R n_2, \dot{\gamma}^R n_3] \end{aligned} \tag{3.15}$$

Because bases R and M are fixed on the body, the coefficients of $\boldsymbol{\omega}$ and $\hat{\mathbf{n}}$ are equal in these two bases. Further, the coefficients of $\boldsymbol{\omega}$ and $\hat{\mathbf{n}}$ are equal in base R_0 and R. The most efficient means of equating the coefficients of $\boldsymbol{\omega}$ from the route defined by ψ, θ, ϕ to the route defined by ψ_0, θ_0, ϕ_0, $\hat{\mathbf{n}}$, γ is to use the base R coefficients for both routes. Equating corresponding terms from equation (3.8) with those from equation (3.15) results in three equations with three unknowns: $\dot{\phi}$, $\dot{\psi}$, and $\dot{\theta}$:

$$\begin{aligned}
{}^R\omega_x &\Rightarrow \dot{\phi} + \dot{\psi}\sin(\theta) = \dot{\gamma}\,{}^R n_1 \\
{}^R\omega_y &\Rightarrow \dot{\psi}\cos(\theta)\cos(\phi) + \dot{\theta}\sin(\phi) = \dot{\gamma}\,{}^R n_2 \\
{}^R\omega_z &\Rightarrow -\dot{\psi}\cos(\theta)\sin(\phi) + \dot{\theta}\cos(\phi) = \dot{\gamma}\,{}^R n_3
\end{aligned} \tag{3.16}$$

These equations are solved analytically for $\dot{\phi}$, $\dot{\psi}$, and $\dot{\theta}$, resulting in equations that contain each of the Euler angles as well as $\dot{\gamma}$ and ${}^R[\hat{\mathbf{n}}]$. ϕ, ψ, and θ can be replaced by the expressions from equations (3.14) to produce the following:

$$[\dot{\phi}, \dot{\psi}, \dot{\theta}] = f(\gamma, \dot{\gamma}, {}^R[\hat{\mathbf{n}}], \phi_0, \psi_0, \theta_0) \tag{3.17}$$

where f is a general non-linear function relating the variables on the right of the equal sign to those on the left.

Equations (3.16) are then differentiated with respect to time to obtain:

$$\begin{aligned}
&{}^R\dot{\omega}_x \Rightarrow \sin(\theta)\ddot{\psi} + \ddot{\phi} + \cos(\theta)\dot{\psi}\dot{\theta} = \ddot{\gamma}\,{}^R n_1 \\
&{}^R\dot{\omega}_y \Rightarrow \sin(\phi)\ddot{\theta} + \cos(\phi)\dot{\theta}\dot{\phi} + \cos(\phi)\cos(\theta)\ddot{\psi} - \cos(\theta)\sin(\phi)\dot{\psi}\dot{\phi} - \cos(\phi)\sin(\theta)\dot{\psi}\dot{\theta} = \ddot{\gamma}\,{}^R n_2 \\
&{}^R\dot{\omega}_z \Rightarrow \cos(\phi)\ddot{\theta} - \sin(\phi)\dot{\theta}\dot{\phi} - \cos(\theta)\sin(\phi)\ddot{\psi} - \cos(\phi)\cos(\theta)\dot{\psi}\dot{\phi} + \sin(\phi)\sin(\theta)\dot{\psi}\dot{\theta} = \ddot{\gamma}\,{}^R n_3
\end{aligned} \tag{3.18}$$

These equations are linear in terms of $\ddot{\phi}$, $\ddot{\psi}$, and $\ddot{\theta}$ and can thus be solved in terms of the other variables. ϕ, ψ, θ, $\dot{\phi}$, $\dot{\psi}$, and $\dot{\theta}$ can then be replaced with γ, $\dot{\gamma}$, ϕ_0, ψ_0, θ_0, and ${}^R[\hat{\mathbf{n}}]$

using equations (3.14) and (3.17) resulting in:

$$[\ddot{\phi}, \ddot{\psi}, \ddot{\theta}] = g(\gamma, \dot{\gamma}, \ddot{\gamma}, {}^{R}[\hat{\mathbf{n}}], \phi_0, \psi_0, \theta_0) \tag{3.19}$$

where g is the general non-linear equation that relates the terms on the right to those on the left. Thus expressions for the accelerations of the three Euler angles can be expressed in terms of the single DOF γ and its derivatives.

Additionally, the three translational DOFs: X_{oc}, Y_{oc}, and Z_{oc}, and their time derivatives must also be expressed in terms of γ. This is achieved by deriving three constraints for one of the support contacts p_1 that will not move throughout the single DOF motion:

$$\begin{aligned}
\left[X_{op_1},\ Y_{op_1},\ Z_{op_1}\right] &= [X_{oc},\ Y_{oc},\ Z_{oc}] + \left[x_{cp_1},\ y_{cp_1},\ z_{cp_1}\right] \mathbb{R}_{\phi\theta\psi} \\
\left[\dot{X}_{op_1},\ \dot{Y}_{op_1},\ \dot{Z}_{op_1}\right] &= \left[\dot{X}_{oc},\ \dot{Y}_{oc},\ \dot{Z}_{oc}\right] + \left[x_{cp_1},\ y_{cp_1},\ z_{cp_1}\right] \dot{\mathbb{R}}_{\phi\theta\psi} = [0,\ 0,\ 0]
\end{aligned} \tag{3.20}$$

where $[X_{op_1},\ Y_{op_1},\ Z_{op_1}]$ is known and remains constant throughout the single DOF motion. The second equation above when differentiated with respect to time gives:

$$\left[\ddot{X}_{oc},\ \ddot{Y}_{oc},\ \ddot{Z}_{oc}\right] = -[x_{cp_1},\ y_{cp_1},\ z_{cp_1}]\ddot{\mathbb{R}}_{\phi\theta\psi} \tag{3.21}$$

The resultant expressions for $\ddot{X}_{oc}$, $\ddot{Y}_{oc}$, and $\ddot{Z}_{oc}$ in terms of ϕ, ψ, θ, and their time derivatives can be substituted in terms of γ and its derivatives by means of equations (3.14), (3.17), and (3.19). The above process allows for the transformation of the six unconstrained DOFs to one DOF, γ, and will be used for rocking about an edge in this model as will be explained in more detail below.

3.4.4 Lagrange's Equations of Motion

With the six unconstrained DOFs of the system defined, the governing equations of motion for the unconstrained body can be derived. A Langrangian formulation for the system is

utilized, and is first derived for the unconstrained 6-DOF object using Lagrange's equation:

$$\frac{d}{dt}\left(\frac{\partial {}^{S}T}{\partial \dot{q}_j}\right) - \frac{\partial {}^{S}T}{\partial q_j} = Q_j \tag{3.22}$$

where q_j is the jth DOF, Q_j is the generalized force for q_j, and ${}^{S}T$ is the kinetic energy of the body in base S.

3.4.4.1 Kinetic Energy of the Body

By utilizing quantities defined above, the kinetic energy may be written as

$${}^{S}T = \frac{1}{2}m[\mathbf{v}_{oc}]^2 + \frac{1}{2}{}^{R}[\boldsymbol{\omega}]^{R}[\boldsymbol{I}]^{R}[\boldsymbol{\omega}]^{T} \tag{3.23}$$

As ${}^{R}[\boldsymbol{I}]$ is known, the expression for ${}^{R}[\boldsymbol{\omega}]$ from equation 3.8 is used to find the rotational kinetic energy of the body. The kinetic energy defined in equation (3.23) is the relative kinetic energy of the body with respect to the support medium, which may be translating with respect to a fixed observer but is not rotating.

3.4.4.2 Generalized Forces

Figure 3.6 shows a body with a force $\mathbf{F}_i$, where$i = 1, ..., N$ acting at point p_i, which is one of N forces acting on the body where N is the total number of external forces present.

The generalized force Q_j with respect to the generalized coordinate q_j acting on this body can be obtained by the following summation with the N external forces $\mathbf{F}_i$:

$$Q_j = \sum_{i=1}^{N} [\mathbf{F}_i] \frac{\partial [\mathbf{r}_{op_i}]^T}{\partial q_j} \tag{3.24}$$

Applying equation (3.22) by using each of the six DOFs as the generalized coordinate results in six equations of motion that define the movement of the unconstrained body. The constraints, associated constraint forces, and corresponding independent DOFs change

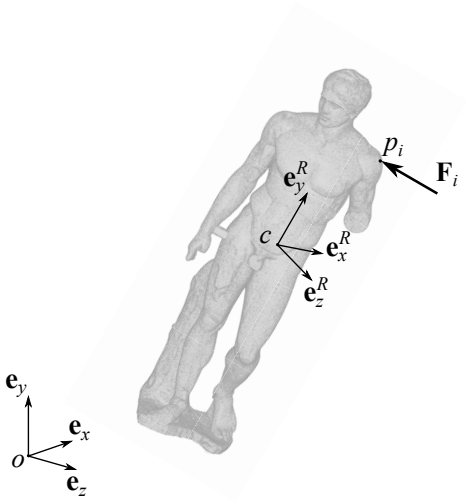
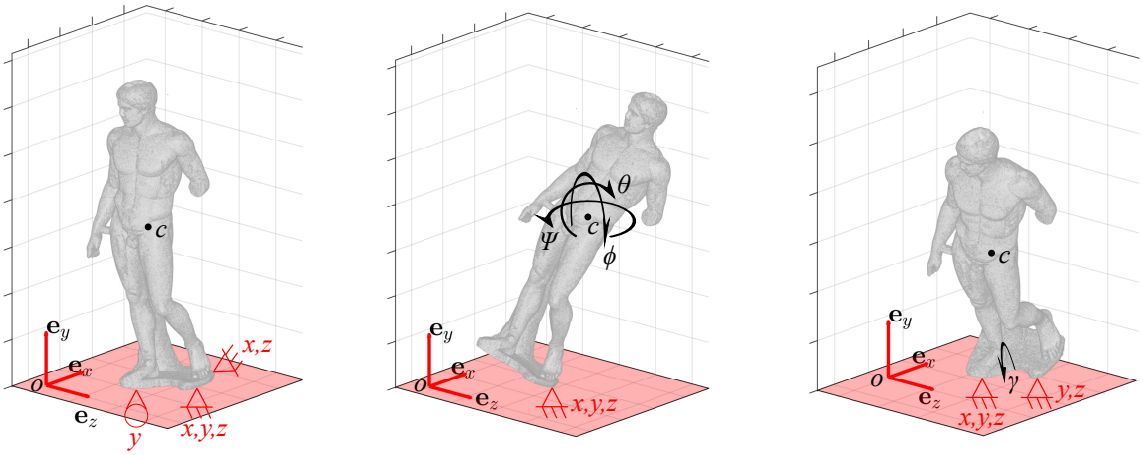


Fig. 3.6. A rigid body with generalized force $\mathbf{F}_i$ acting at p_i.

based on the pattern of motion which are discussed in detail below.

3.5 3-D Patterns of Motion

The motion of the object under the assumption of pure rocking can be classified with three patterns of motion which are depicted in Figure 3.7.



(a) **(b)** **(c)**

Fig. 3.7. Diagrams of the three patterns of motion. a) SP, b) PR1, and c) PR2 with their kinematic constraints and DOFs shown.

As seen in Figure 3.7, these patterns are the static pattern (SP), pure rocking with one

support contact (PR1), and pure rocking with two support contacts (PR2, or rocking about an edge as formulated in Section 3.4.3). SP requires that a face of the convex hull is in contact with the support and that the body does not move relative to the support. SP has a minimum of three support contacts, or vertices which are in contact with the support. PR1 has one support contact and does not move relative to it, but the body may pivot with respect to that vertex, and hence its motion can be described by three independent rotational DOFs: ϕ, ψ, θ. PR2 has an edge $E_{p_1p_2}$, or minimum of two support contacts, that does not move relative to the support about which the body may rotate, resulting in one DOF: γ.

Each pattern has a unique set of independent DOFs $\boldsymbol{\Phi}_a$: none for SP; ϕ, ψ, θ for PR1; and γ for PR2. Each pattern also has a set of independent states $\boldsymbol{Q}_a$ taken from the full set of unconstrained states $\boldsymbol{Q} = [X_{oc}, \dot{X}_{oc}, Y_{oc}, \dot{Y}_{oc}, Z_{oc}, \dot{Z}_{oc}, \phi, \dot{\phi}, \psi, \dot{\psi}, \theta, \dot{\theta}]$. The dependent DOFs and states which complement $\boldsymbol{\Phi}_a$ and $\boldsymbol{Q}_a$ are denoted by $\boldsymbol{\Phi}_b$ and $\boldsymbol{Q}_b$ respectively. $\boldsymbol{Q}_a$ consists of the displacement and velocity of each element in $\boldsymbol{\Phi}_a$. Both $\boldsymbol{\Phi}_a$ and $\boldsymbol{Q}_a$ are summarized in Table 3.1.

Table 3.1. Degrees of Freedom for Each Pattern

Pattern	Degrees of Freedom, $\boldsymbol{\Phi}_a$	Required States, $\boldsymbol{Q}_a$	Dependent States, $\boldsymbol{Q}_b$
Static Pattern	None	None	$X_{oc}, \dot{X}_{oc}, Y_{oc}, \dot{Y}_{oc}, Z_{oc}, \dot{Z}_{oc}, \phi, \dot{\phi}, \psi, \dot{\psi}, \theta, \dot{\theta}$
Pure Rocking 1	ϕ, ψ, θ	$\phi, \dot{\phi}, \psi, \dot{\psi}, \theta, \dot{\theta}$	$X_{oc}, \dot{X}_{oc}, Y_{oc}, \dot{Y}_{oc}, Z_{oc}, \dot{Z}_{oc}$
Pure Rocking 2	γ	$\gamma, \dot{\gamma}$	$X_{oc}, \dot{X}_{oc}, Y_{oc}, \dot{Y}_{oc}, Z_{oc}, \dot{Z}_{oc}, \phi, \dot{\phi}, \psi, \dot{\psi}, \theta, \dot{\theta}$

Though this pure rocking model omits them, one-contact slide rocking (SR1) and free flight (FF) are easily formulated. The additional patterns of pure sliding (PS) and multi-contact slide rocking (SR2), however, are more difficult to formulate as they require additional assumptions. The mechanical constraints for SR1 and FF are provided below for reference.

SR1 requires that one vertex of the body p is in contact with the support surface and

that it may slide horizontally across the surface while the body rocks about that point. The constraints for SR1 are thus:

$$\dot{Y}_{op} = \ddot{Y}_{op} = 0 \qquad\qquad F_H = -S(v_H)\mu|F_y| \tag{3.25}$$

where v_H is the horizontal velocity of p defined by $\sqrt{\dot{X}_{op}^2 + \dot{Z}_{op}^2}$.

During FF the body simply has no contact with the support surface and thus has no support reactions:

$$F_x = 0 \qquad\qquad F_y = 0 \qquad\qquad F_z = 0 \tag{3.26}$$

3.6 Forces Acting on Body

The support experiences translational accelerations $\ddot{x}_g$, $\ddot{y}_g$, $\ddot{z}_g$ in the $\mathbf{e}_x$, $\mathbf{e}_y$, $\mathbf{e}_z$ directions respectively. As the Cartesian axes are fixed on the moving support medium, to obtain the body's response relative to the support, the D'Alembert forces f_x, f_y, and f_z are applied at c parallel to $\mathbf{e}_x$, $\mathbf{e}_y$, and $\mathbf{e}_z$ respectively as shown in Figure 3.8 with magnitudes:

$$f_x = -m\ddot{x}_g \qquad\qquad f_y = -m\ddot{y}_g \qquad\qquad f_z = -m\ddot{z}_g \tag{3.27}$$

From the constraints shown for the SP in Figure 3.7a, an equivalent set of support reaction forces $\mathbf{F}_x = F_x\mathbf{e}_x$, $\mathbf{F}_y = F_y\mathbf{e}_y$, and $\mathbf{F}_z = F_z\mathbf{e}_z$ are applied at points r_x, r_y, and r_z respectively on the base of the body. These reactions are the resultant of the forces in each Cartesian direction produced by the constraints. PR1 has the same three reaction forces but they are applied at a single point p. PR2 has a total of five reaction forces analogous to the constraints shown in Figure 3.7: $\mathbf{F}_{x1} = F_{x1}\mathbf{e}_x$, $\mathbf{F}_{y1} = F_{y1}\mathbf{e}_y$, and $\mathbf{F}_{z1} = F_{z1}\mathbf{e}_z$ applied at p_1 and $\mathbf{F}_{y2} = F_{y2}\mathbf{e}_y$ and $\mathbf{F}_{z^*2} = F_{z^*2}\mathbf{e}_{z^*}$ applied at p_2. The z^* subscript indicates that $\mathbf{F}_{z^*2}$ may act in any horizontal direction as long as it is not parallel to $E_{p_1p_2}$, not necessarily the

Z-direction. The forces for each pattern are shown in Figure 3.8.

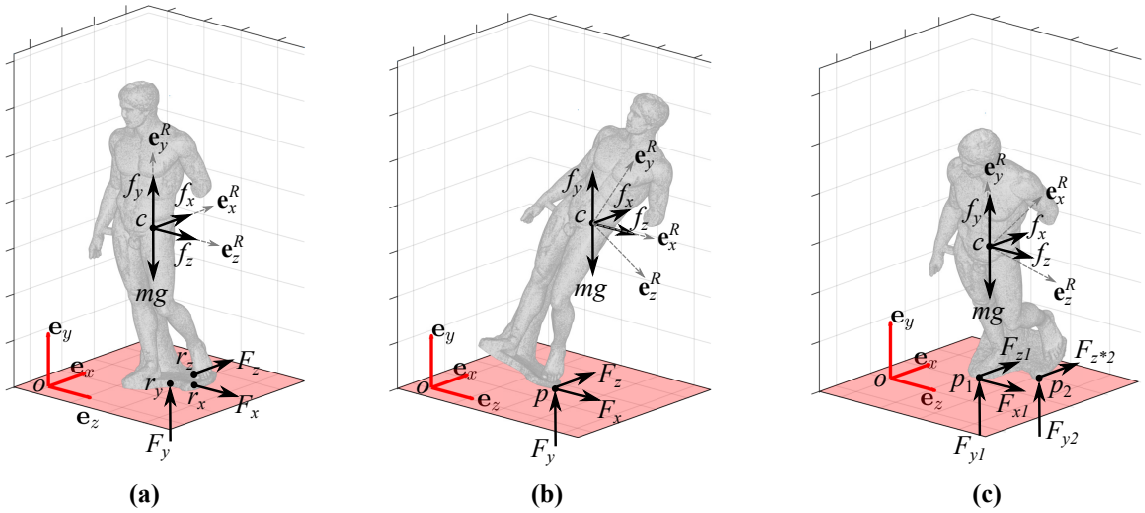


Fig. 3.8. Diagrams depicting the forces acting on the *Doryphoros* in each pattern. (a) SP. (b) PR1. (c) PR2.

In SP, the configuration of r_x, r_y, and r_z must result in the body not accelerating with respect to the support medium. Thus, these points may move over time due to support accelerations or external forces acting on the body. Figure 3.9 shows a plot of the base vertices for an irregular body with the locations of c, r_x, r_y, and r_z shown.

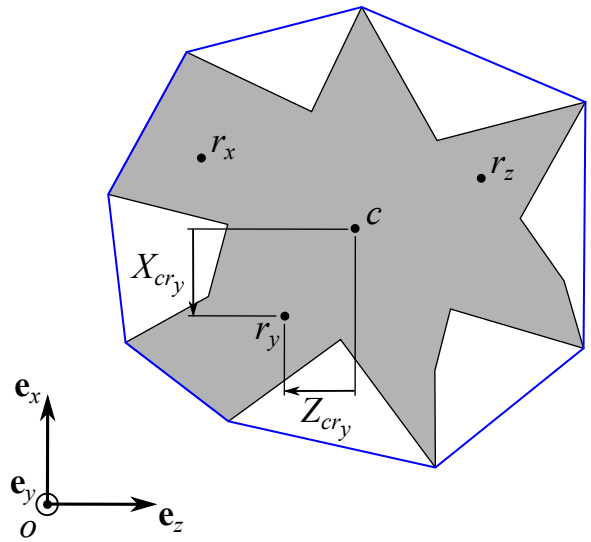


Fig. 3.9. The base of an irregular body during SP showing its convex hull (blue line) and the location of r_x, r_z, and r_y, which is defined by X_{cr_y} and Z_{cr_y}.

F_y may be applied anywhere within the 2-D convex hull of the support contact points and

its location will be defined by the Cartesian coordinates (X_{cr_y}, Z_{cr_y}) as shown in Figure 3.9. The other reaction force components F_x and F_z may be located using the coordinates (X_{cr_x}, Z_{cr_x}) and (X_{cr_z}, Z_{cr_z}) respectively. The two horizontal reactions may take any position to ensure the torque T about the vertical axis is null: $T = Z_{cr_x}F_x - X_{cr_z}F_z = 0$. Thus, there are five non-trivial unknowns for SP: F_x, F_y, F_z, X_{cr_y}, and Z_{cr_y}.

3.7 Kinematic Constraints for Each Pattern

Each pattern has a set of kinematic constraints that define the motion of the body while that pattern is engaged. SP can be described as having one support contact, p_i, pinned in all directions, another support contact, p_{i+1}, with a roller prohibiting uplift, and a final support contact, p_{i+2}, with its movement restricted in any horizontal direction. The contact vertices p_i, p_{i+1}, p_{i+2} must not be collinear. This results in the following constraint equations:

$$\begin{aligned} &\dot{X}_{op_i} = \ddot{X}_{op_i} = 0 && \dot{Y}_{op_i} = \ddot{Y}_{op_i} = 0 && \dot{Z}_{op_i} = \ddot{Z}_{op_i} = 0 \\ &\dot{X}_{op_{i+1}} = \ddot{X}_{op_{i+1}} = 0 && \dot{Y}_{op_{i+2}} = \ddot{Y}_{op_{i+2}} = 0 \end{aligned} \tag{3.28}$$

which restrict the body from moving with respect to the support medium during SP. Integrating the velocity constraints from (3.28) results in the additional displacement equations:

$$\begin{aligned} &X_{op_i} = X_{op_i}(t_0) && Y_{op_i} = Y_{op_i}(t_0) && Z_{op_i} = Z_{op_i}(t_0) \\ &X_{op_{i+1}} = X_{op_{i+1}}(t_0) && Y_{op_{i+2}} = Y_{op_{i+2}}(t_0) \end{aligned} \tag{3.29}$$

where t_0 is the first time instance of SP. These equations show that all displacements during SP remain constant. t_0 is likewise defined as the first time instance for each occurrence of the patterns defined in the following lines.

For PR1, a single vertex p is pinned to the support and not permitted to move in any

direction which results in the equations:

$$\dot{X}_{op} = \ddot{X}_{op} = 0 \qquad \dot{Y}_{op} = \ddot{Y}_{op} = 0 \qquad \dot{Z}_{op} = \ddot{Z}_{op} = 0 \tag{3.30}$$

Integrating the velocity equations in (3.30) results in the additional displacement equations for PR1:

$$X_{op} = X_{op}(t_0) \qquad Y_{op} = Y_{op}(t_0) \qquad Z_{op} = Z_{op}(t_0) \tag{3.31}$$

For PR2, the edge $E_{p_1p_2}$, as shown in Figure 3.7, is restricted from moving relative to a still observer. In order to constrain the body to rotate about the edge defined by these points, a total of five kinematic constraints are placed on points p_1 and p_2. p_1 is pinned restricting motion in all directions and p_2 is pinned in two directions: the vertical and in any arbitrary horizontal direction that is not parallel to the edge in contact with the support. Two of these constraints were previously used in the formulation provided in Section 3.4.3 by way of restrictions on $\boldsymbol{\omega}$. The three remaining constraints are:

$$\dot{X}_{op_1} = \ddot{X}_{op_1} = 0 \qquad \dot{Y}_{op_1} = \ddot{Y}_{op_1} = 0 \qquad \dot{Z}_{op_1} = \ddot{Z}_{op_1} = 0 \tag{3.32}$$

Integrating the velocity constraints in (3.32) results in the additional displacement constraints for PR2:

$$X_{op_1} = X_{op_1}(t_0) \qquad Y_{op_1} = Y_{op_1}(t_0) \qquad Z_{op_1} = Z_{op_1}(t_0) \tag{3.33}$$

3.8 Solving the Equations of Motion

For each pattern, the kinematic equations (3.5) and (3.6) and the constraint equations from Section 3.7 are combined with the unconstrained equations of motion (3.22) to create a

system of equations with the DOFs and reaction forces for each pattern as the unknowns. The equations take the following form:

$$\begin{aligned}\ddot{\boldsymbol{\Phi}}_a &= h(m, g, {}^R[\boldsymbol{I}], \boldsymbol{Q}_a, \boldsymbol{P}, \ddot{x}_g, \ddot{y}_g, \ddot{z}_g) \\ \mathscr{F} &= j(m, g, {}^R[\boldsymbol{I}], \boldsymbol{Q}_a, \boldsymbol{P}, \ddot{x}_g, \ddot{y}_g, \ddot{z}_g) \\ \boldsymbol{Q}_b &= k(m, g, {}^R[\boldsymbol{I}], \boldsymbol{Q}_a, \boldsymbol{P}, \ddot{x}_g, \ddot{y}_g, \ddot{z}_g)\end{aligned} \tag{3.34}$$

where h, j, and k are the general forms of the non-linear functions that relate the variables on the right to the variables on the left. $\boldsymbol{P}$ is a vector of parameters relevant to the equations of motion for each pattern. For SP, $\boldsymbol{P}$ is empty, for PR1, $\boldsymbol{P} = {}^R[\mathbf{r}_{cp}]$, and for PR2, $\boldsymbol{P} = [{}^R[\hat{\mathbf{n}}], {}^R[\mathbf{r}_{cp_1}], {}^R[\mathbf{r}_{cp_2}], \phi_0, \psi_0, \theta_0]$. $\mathscr{F}$ is a vector of the reaction-related variables for each pattern as described in Section 3.6. A state-space vector is then created of the form:

$$\dot{\boldsymbol{Q}}_a = [\dot{\boldsymbol{\Phi}}_a, \ddot{\boldsymbol{\Phi}}_a]^T \tag{3.35}$$

which can be integrated over time using ode45 to obtain $\boldsymbol{\Phi}_a$ and $\dot{\boldsymbol{\Phi}}_a$. The details of numerical integration will be discussed in Section 3.11. The accelerations of the dependent DOFs, $\ddot{\boldsymbol{\Phi}}_b$, are not integrated to eliminate numerical drift. j is used to determine the times of transitions between patterns which will be discussed in Section 3.9. Then, the dependent states of the pattern, $\boldsymbol{Q}_b$, can be calculated post-integration. To easily calculate the left side of each equation (3.34), matlabFunctions (74) from Matlab's symbolic toolbox are used.

For SP, the solution of (3.34) gives $\dot{\boldsymbol{\Phi}} = \ddot{\boldsymbol{\Phi}} = 0$ and thus the equations of motion reduce to the static equilibrium equations: three force balance equations in the X, Y, and Z directions and three moment balance equations about c arising from $\Sigma\mathbf{M} = 0$ where the moment $\mathbf{M} = \mathbf{F}_i \times \mathbf{r}_{ci}$ about the X, Y, and Z axes. This results in six equations with the

following form:

$$\begin{aligned} F_x + f_x &= 0 & Z_{cr_y} F_y - Y_{cm} F_z &= 0 \\ F_y + f_y - mg &= 0 & T &= 0 \\ F_z + f_z &= 0 & Y_{cm} F_x - X_{cr_y} F_y &= 0 \end{aligned} \tag{3.36}$$

where $Y_{cm} = -Y_{oc}$. The force balance equations (the left column of equations (3.36)) can be solved for F_x, F_y, and F_z as their magnitudes are independent of X_{cr_y} and Z_{cr_y}. Then, X_{cr_y} and Z_{cr_y} can be solved using the three moment balance equations on the right column of equations (3.36) for each time instance the body is in SP.

For PR1, the above procedure results in a system of nine equations with nine linear unknowns: $\ddot{X}_{oc}$, $\ddot{Y}_{oc}$, $\ddot{Z}_{oc}$, $\ddot{\phi}$, $\ddot{\psi}$, $\ddot{\phi}$, F_x, F_y, F_z.

For PR2, the general equations (3.34) could be used, but using all the unconstrained DOFs would produce a highly complex, non-linear set of equations which would be difficult to integrate. Thus, ϕ, ψ, θ, and their derivatives in (3.22) are replaced with the expressions of γ and its derivatives as described in Section 3.4. Additionally, $\ddot{X}_{oc}$, $\ddot{Y}_{oc}$, and $\ddot{Z}_{oc}$ are replaced via (3.21) and (3.32). This results in six equations with six unknowns: $\ddot{\gamma}$, F_{x1}, F_{y1}, F_{z1}, F_{y2}, and F_{z^*2} which are linear in terms of the unknowns. Equation (3.34) for $\ddot{\boldsymbol{Q}}_a$ is integrated over time to obtain γ and $\dot{\gamma}$ which together comprise $\boldsymbol{Q}_a$, which is then used to find $\boldsymbol{Q}_b$, in terms of the six original DOFs and their velocities, using equations (3.14), (3.17), and (3.20).

3.9 Transitions Between Patterns

A key component of this rocking model is the occurrence of events, i.e., instances during integration that signify transitions from one pattern to another. Physical laws governing the transition between different patterns must be defined. The two main classes of transitions

are those with and without impact as defined in the following sections. Figure 3.10 provides a summary of the transitions permitted in this pure rocking model.

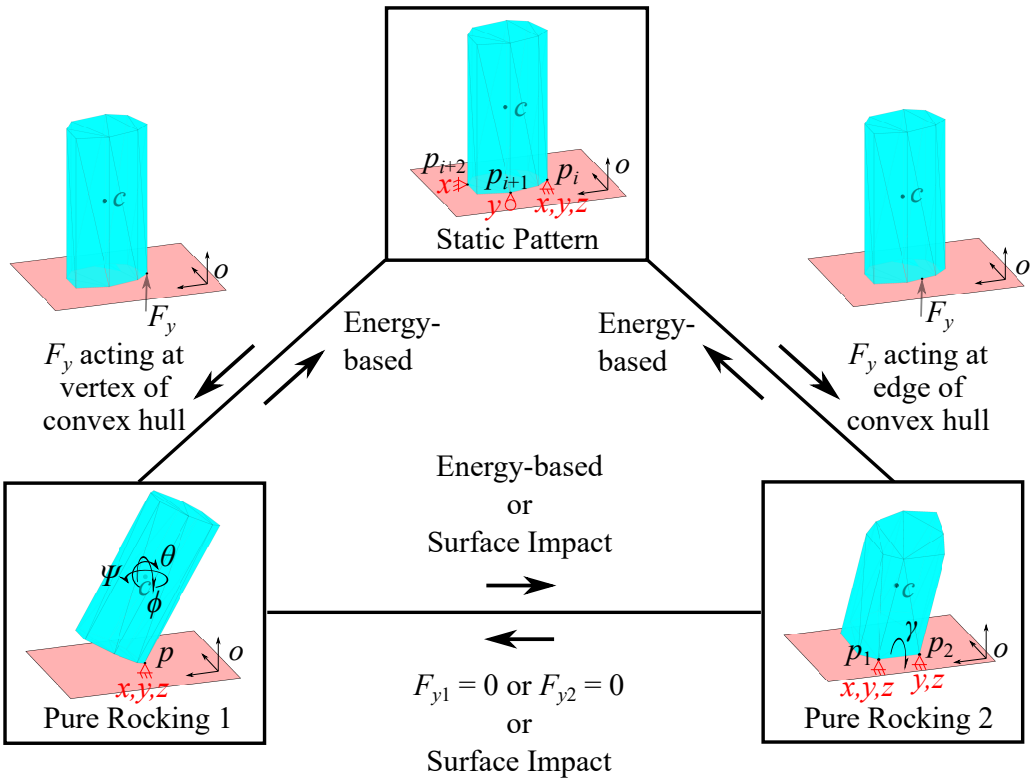


Fig. 3.10. A diagram showing the possible transitions between patterns in this pure rocking model.

3.9.1 Transitions Without Impact

SP may only transition to pure rocking. This is a transition that occurs without impact. As shown in Figure 3.10, SP may transition to pure rocking if r_y coincides with a vertex or edge of the 2-D convex hull of the support contact vertices. The coordinates of r_y (X_{cr_y}, Z_{cr_y}) are tracked during time integration from the solution to equations 3.36. Matlab's inpolygon function (53) determines whether r_y is inside or outside the convex hull of the contact vertices.

Figure 3.11 shows the base of an irregular rigid body in SP and three possible paths for the location of F_y over time. Assuming the object is in SP before the support accelerations

begin, F_y will act directly beneath c: $X_{oc} = X_{or_y}$ and $Z_{oc} = Z_{or_y}$. The geometry of the base is defined (in gray) as well as the convex hull of the base (in blue). If r_y moves to coincide with a vertex of the convex hull, as shown by the dotted Path 1 in Figure 3.11, the body would transition to PR1. However, if the path of r_y intersects the convex hull at a points between vertices, i.e., an interior point of an edge, as shown by the dashed Path 2 in Figure 3.11, it will transition to PR2 about that edge. The body must transition from SP to PR1 or PR2 when the path of r_y intersects the convex hull because if r_y is outside the convex hull, the support must apply tensile forces on the body which is not permitted in this model. The probability of a transition directly to PR1 is low as the accelerations must be very specific for the intersection to occur at exactly one of the vertices. In the numerical model, the object most commonly enters PR2 first and transitions to PR1 by a separate transition as necessary. It is also possible for r_y to never coincide with an exterior point of the convex hull of the body and thus remain in SP without transition as shown in the solid Path 3 of Figure 3.11.

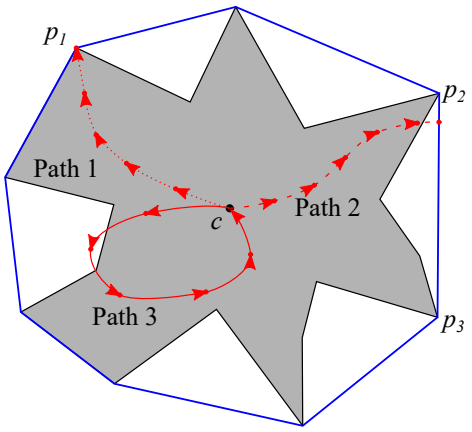
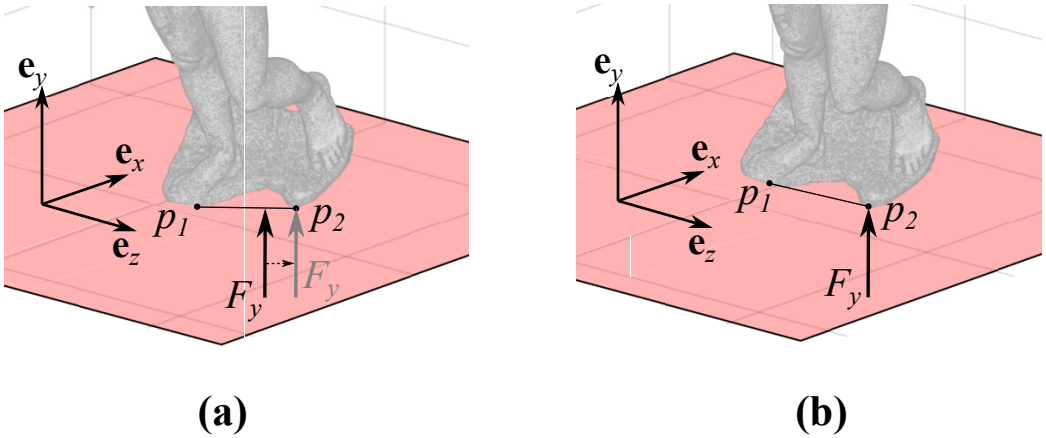


Fig. 3.11. The base of an irregular body in SP with its convex hull and three arbitrary paths showing possible paths of the location of F_y. Path 1 results in PR1 about point p_1, Path 2 results in PR2 about p_2 and p_3, Path 3 has no transition from SP.

It should be noticed that for transitions from SP to PR2, the geometry of the body between two convex hull points is inconsequential and will result in PR2 whether the geometry is a straight edge connecting the vertices or the body has concave geometry between the vertices

as shown in Figure 3.11.

The transition from PR2 to PR1 may occur without impact when either $F_{y1} = 0$ or $F_{y2} = 0$ from Section 3.6, corresponding to the resultant of the vertical reaction forces acting on the edge, $F_{y,tot} = F_{y1} + F_{y2}$, being directly beneath one of the rocking vertices as depicted in Figure 3.12. At the time that F_y is directly beneath p_1 or p_2 defining the rocking edge $E_{p_1p_2}$, the body will begin PR1 about that vertex.



(a) **(b)**

Fig. 3.12. A diagram showing (a) an object initially in PR2 with F_y between points p_1 and p_2 which define the edge. (b) at some time, F_y reaches point p_2 and the body begins PR1 about p_2.

Though patterns involving free flight and sliding are not included in this work, the time instances at which the body would transition without impact to either type of pattern can be determined. Using the forces calculated from (3.34), the transition from SP, PR1, or PR2 to sliding occurs when:

$$\sqrt{(F_{x,tot})^2 + (F_{z,tot})^2} > \mu F_{y,tot} \tag{3.37}$$

where $F_{x,tot}$, $F_{y,tot}$, $F_{z,tot}$ are the resultant of all reaction forces in each Cartesian axis and μ is the coefficient of friction between the body and the support. For PR2, where there may be multiple forces in a single direction, $F_{y,tot} = F_{y1} + F_{y2}$ and $\sqrt{(F_{x,tot})^2 + (F_{y,tot})^2} = F_H$ where F_H is the magnitude of the total horizontal force from combining F_{x1}, F_{z1}, and F_{z^*2}.

Transitions to FF may also occur from SP, PR1, or PR2 if $F_y = 0$ or $F_{y,tot} = 0$.

3.9.2 Transitions Involving Impact

When the body is in a PR pattern, it will likely impact the support medium. At these impacts the object may transition its pattern of motion from PR1 to PR2 or vice versa. A detailed discussion of impacts is given in Section 3.10.

3.10 Impacts

Impacts create a discontinuity in the integration of the body's motion. These impacts must be carefully considered to ensure an accurate model. As both the body and the support are rigid, all impacts are hard and infinitesimal in duration so that the displacements do not change during the impact. Two main types of impacts are possible in this model: line impacts and surface impacts. Line impacts occur when an edge of the 3-D convex hull impacts the support while surface impacts occur when a face of the convex hull impacts the support. This section also introduces a general model that allows for the variable location of the impulses at impact for objects of irregular geometry.

3.10.1 Momentum Equations

A new base P is defined for solving the equations of momentum. Base P is determined by the unit vectors $\mathbf{e}_x^P$, $\mathbf{e}_y^P$, $\mathbf{e}_z^P$, which occur from rotating $\mathbf{e}_x$, $\mathbf{e}_y$, $\mathbf{e}_z$, by an angle α about $\mathbf{e}_y$. This new base allows for consistent definition of the points of application of the impulses: $\mathbf{J}_x = {}^P J_x \mathbf{e}_x^P$ applied at j_x, $\mathbf{J}_y = {}^P J_y \mathbf{e}_y^P$ applied at j_y, and $\mathbf{J}_z = {}^P J_z \mathbf{e}_z^P$ applied at j_z. The coordinates of the new base P for $\mathbf{r}_{ij}$ are defined as: ${}^P[\mathbf{r}_{ij}] = [{}^P X_{ij},\ {}^P Y_{ij},\ {}^P Z_{ij}]$. The transformation from base S to base P is defined by the rotation matrix $\mathbb{R}_\alpha$:

$$\begin{Bmatrix} \mathbf{e}_x^P \\ \mathbf{e}_y^P \\ \mathbf{e}_z^P \end{Bmatrix} = \mathbb{R}_\alpha \begin{Bmatrix} \mathbf{e}_x \\ \mathbf{e}_y \\ \mathbf{e}_z \end{Bmatrix} \text{ where } \mathbb{R}_\alpha = \begin{bmatrix} \cos(\alpha) & 0 & -\sin(\alpha) \\ 0 & 1 & 0 \\ \sin(\alpha) & 0 & \cos(\alpha) \end{bmatrix} \tag{3.38}$$

Three translational and three angular momentum equations must be solved at each impact. The translational equations arise from the linear momentum balance in the $\mathbf{e}_x^P$, $\mathbf{e}_y^P$, $\mathbf{e}_z^P$ directions and the angular momentum equations are expressed in terms of the coefficients of the angular momentum vector $\mathbf{H}$, with respect to base R, ${}^R[\mathbf{H}]$ which may be expressed as:

$$ {}^R[\mathbf{H}] = {}^R[\omega]{}^R[\boldsymbol{I}] \tag{3.39} $$

as ${}^R[\boldsymbol{I}]$ is only known in base R. ${}^R[\mathbf{H}]$ can be transformed to base S using equation (3.3) and the result can be transformed to base P using equation (3.38) to obtain ${}^P[\mathbf{H}] = [{}^PH_x, {}^PH_y, {}^PH_z]$. The six momentum equations can then be formed in base P:

$$ \begin{aligned} m^P\dot{X}_{oc}^+ &= m^P\dot{X}_{oc}^- + {}^PJ_x \qquad & m^P\dot{Y}_{oc}^+ &= m^P\dot{Y}_{oc}^- + {}^PJ_y \qquad & m^P\dot{Z}_{oc}^+ &= m^P\dot{Z}_{oc}^- + {}^PJ_z \\ {}^PH_x^+ &= {}^PH_x^- + \Sigma^PM_x \qquad & {}^PH_y^+ &= {}^PH_y^- + \Sigma^PM_y \qquad & {}^PH_z^+ &= {}^PH_z^- + \Sigma^PM_z \end{aligned} \tag{3.40} $$

where the superscripts $^-$ and $^+$ signify the respective pre-impact and post-impact velocities and angular momenta of the body. The Σ^PM_i terms are the sum of the moments of the impulses with respect to c about the i axis. The Σ^PM_i terms from equations (3.40) can be expanded to:

$$ \begin{aligned} \Sigma^PM_x &= -{}^PZ_{cj_y}{}^PJ_y + {}^PY_{cj_z}{}^PJ_z \\ \Sigma^PM_y &= {}^PZ_{cj_x}{}^PJ_x - {}^PX_{cj_z}{}^PJ_z \\ \Sigma^PM_z &= -{}^PY_{cj_x}{}^PJ_x + {}^PX_{cj_y}{}^PJ_y \end{aligned} \tag{3.41} $$

where ${}^PY_{cj_z} = {}^PY_{cj_x} = -Y_{oc}$ at the instant of impact. The other moment arms, ${}^PZ_{cj_y}$, ${}^PZ_{cj_x}$, ${}^PX_{cj_z}$, and ${}^PX_{cj_y}$, will be defined later for the different types of impact. Different post-impact constraints and assumptions are applied to equations (3.40) for line and surface impacts to create a solvable system of equations in terms of the post-impact velocities and

resultant impulses whose solution will be discussed in the following sections.

3.10.2 Line Impacts

In the instance of a line impact as shown in Figure 3.13 the body begins in pre-impact PR1 about p^- (Figure 3.13a) and makes an impact so that $E_{p^-p^+}$ is instantaneously contacting the support surface (3.13b). The body then continues to rock about p^+ (3.13c). Figure 3.14 shows a closeup of the geometry of the *Doryphoros* during the infinitesimal-duration impact of Figure 3.13b.

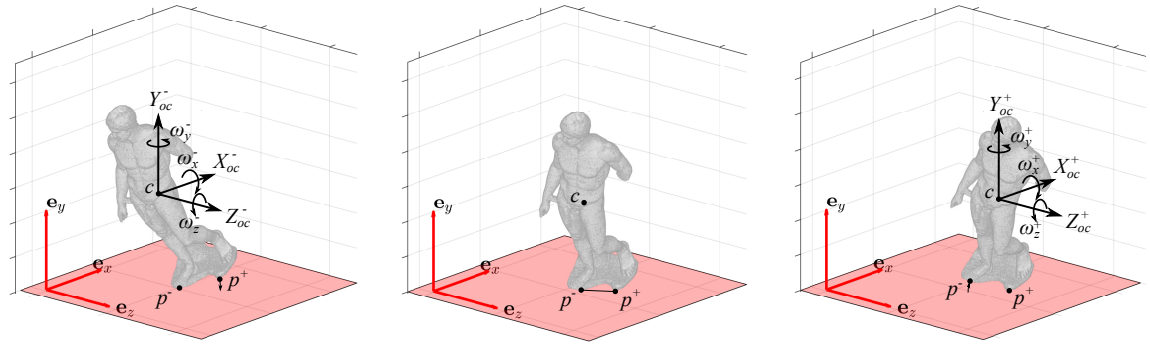


Fig. 3.13. A diagram of an irregular object experiencing a line impact: a) before impact the object rocks in PR1 about p^-, b) the object impacts the support at point p^+, and c) after impact the object rocks in PR1 about p^+.

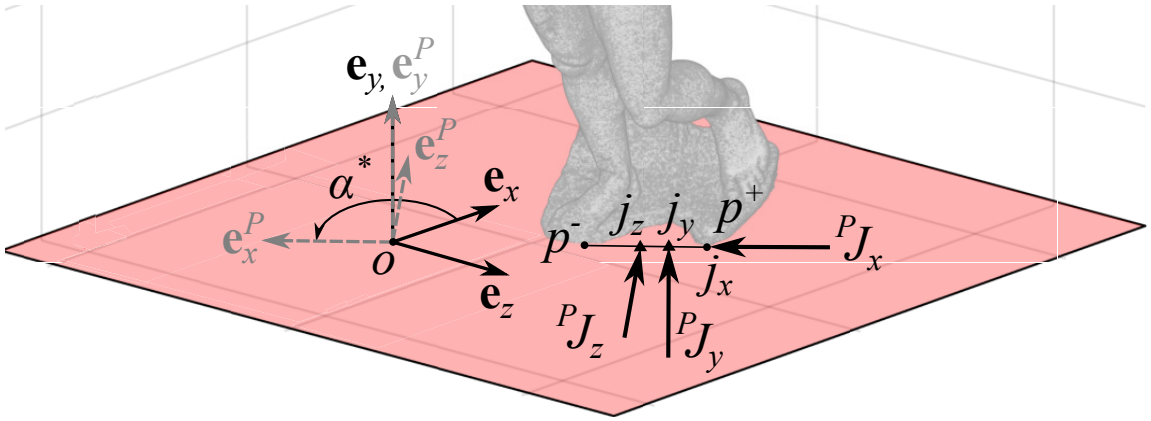


Fig. 3.14. The pre- and post-impact rocking vertices during a line impact with the impulses and bases S and P defined.

Base P is used to consistently and easily define the location of j_x, j_y, and j_z as shown in Figure 3.14. The angle α^* is the angle by which the base S unit vectors must be rotated so that $\mathbf{e}_x^P$ acts in the same direction as $\mathbf{r}_{p^+p^-}$. Due to how base P is defined, ${}^P[\mathbf{r}_{p^+p^-}] = [{}^PX_{p^+p^-}, 0, 0]$ and the coefficients in base P from p^+ to j_x, j_y, and j_z is defined by:

$$ {}^PX_{p^+j_x} = \lambda_{xx}\,{}^PX_{p^+p^-} \qquad {}^PX_{p^+j_y} = \lambda_{yx}\,{}^PX_{p^+p^-} \qquad {}^PX_{p^+j_z} = \lambda_{zx}\,{}^PX_{p^+p^-} \tag{3.42} $$

where λ_{xx}, λ_{yx}, and λ_{zx} are commonly denoted as λ_{ab} with the subscript a corresponding to the direction of the impulse component in base P as follows: x for $\mathbf{e}_x^P$, y for $\mathbf{e}_y^P$, and z for $\mathbf{e}_z^P$. The subscript b is similarly the base P unit vector about which the impulse of a creates a moment during impact. Note: $a \neq b$ for a given λ_{ab} to be relevant, making λ_{xx} inconsequential. The four yet-undefined moment arms from equations (3.41): ${}^PZ_{cj_y}$, ${}^PZ_{cj_x}$, ${}^PX_{cj_z}$, and ${}^PX_{cj_y}$ can now be determined using λ_{ab}.

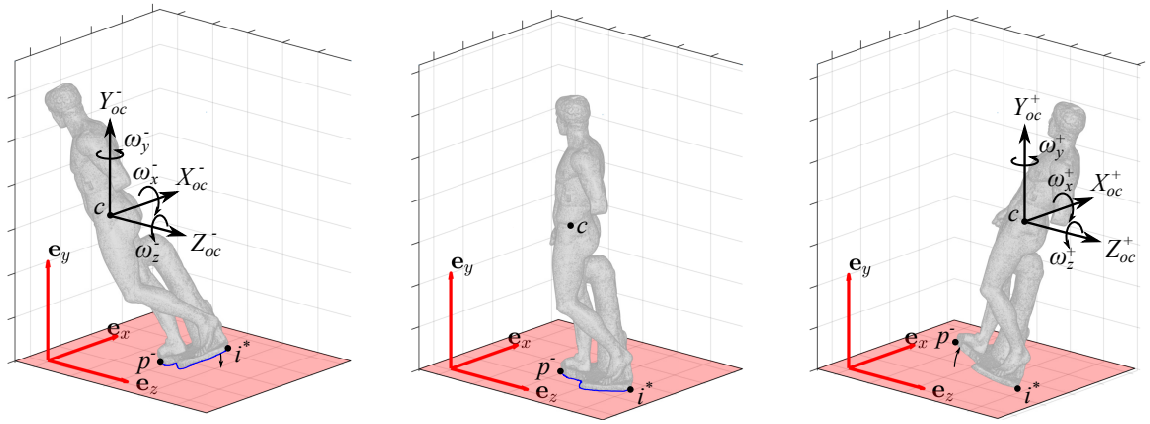
Line impacts are solved in the same way whether the edge impacting the support is straight or the object has concave geometry around it as the impact shown in Figure 3.14. ${}^PJ_y$ can theoretically be applied at any point between p^+ and p^-. ${}^PJ_z$ can be applied at any point along the line defined by p^+ and p^- and affects the post-impact velocities while ${}^PJ_x$ may be theoretically applied at any point along the line connecting the points with no effect on the post-impact velocities.

Several conditions must be checked to ensure the line impact is valid. These will be discussed after surface impacts are explained.

3.10.3 Surface Impacts

A surface impact occurs when a face of the body's convex hull impacts the support as depicted in Figure 3.15. When this occurs, there can be either one post-impact rocking vertex i^* for post-impact PR1, or a post-impact rocking edge defined by points i_1^* and i_2^* for

post-impact PR2. In Figure 3.15, a body is rocking about p^- (3.15a), then experiences a surface impact (3.15b), before continuing to rock about i^* (3.15c). All the vertices shown in blue Figure 3.15 come into contact with the support along with all vertices belonging to the same face, though many of these are not visible due to the opacity of the sculpture.



(a) **(b)** **(c)**

Fig. 3.15. The *Doryphoros* sculpture experiencing a surface impact. a) the body rocks about p^-, b) the body experiences a surface impact, and c) the body continues rocking about i^* after impact. The vertices impacting the support are shown by the blue line along the base of the sculpture.

Surface impacts must be treated differently from line impacts as the impulses act in a plane opposed to on a line. Figure 3.16 shows two additional depictions of the geometry of the impacting face of an irregular body during an impact. The body in Figure 3.16a was previously in PR2 about p_1^- and p_2^- while the body in Figure 3.16b was initially in PR1 about p^-. In both cases, the pre-impact angular velocity vector is indicated as $\boldsymbol{\omega}^-$. Each body has a number of vertices which were not in contact with the support during the pre-impact pattern, but are in contact with the support at the instant of the surface impact. These vertices will be called impacting vertices and the vertices comprising their convex hull are labeled as i_k, i_{k+1}, etc., with each being a possible post-impact rocking vertex.

In a similar manner as for line impacts, a new base P is defined for the body at impact so that the location of the impulses can be defined in a consistent manner. However, the convention used for surface impacts is more complicated due to the greater variability

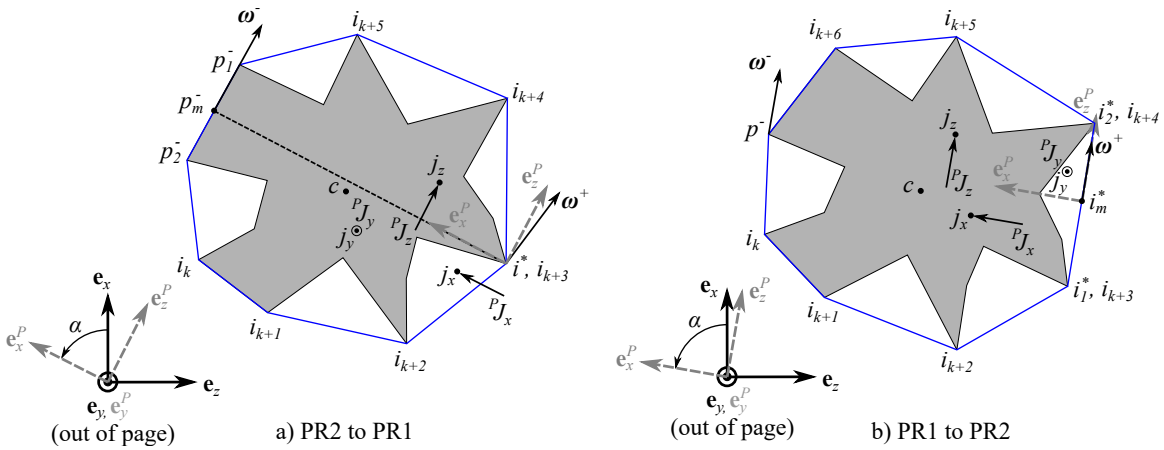


Fig. 3.16. Two examples of a surface impact. a) shows an object initially in PR2 transition to PR1 after impact and b) shows an object initially in PR1 transition to PR2 after impact. The locations of the impulses j_x, j_y, and j_z are shown along with the pre- and post-impact rocking vertices.

allowed in the locations of the impulses. The points p_m^- and i_m^* are defined as the midpoints of the pre- and post-impact rocking edge when the body is in pre- and post-impact PR2 respectively. For surface impacts, the $\mathbf{e}_x^P$ axis is aligned with $\mathbf{r}_{i^*p^-}$ for pre-impact PR1 to post-impact PR1 and with $\mathbf{r}_{i^*p_m^-}$ for pre-impact PR2 to post-impact PR1. If the post-impact pattern is PR2, the $\mathbf{e}_x^P$ axis is aligned so that it is perpendicular to the potential post-impact rocking edge $E_{i_1^* i_2^*}$ and pointing inward on the convex hull as shown in Figure 3.16b.

These axes will be used later to define the locations of the impulses at impact. Note that the other two surface impacts listed in Table 3.2, PR1→PR1 and PR2→PR2, are not included in Figure 3.16 but can be fully realized by the concepts depicted in Figure 3.16.

3.10.3.1 Location of Impulses

There is no unique arrangement of j_x, j_y, and j_z for a surface impact. Considering the conditions for a valid impulse as described in detail below, some impacts have theoretically infinite allowable combinations of locations for the impulses. Four λ_{ab} variables are used

in order to define the location of the impulses for surface impacts:

$$ {}^{P}Z_{i^*j_x} = \lambda_{xz}\,{}^{P}X_{i^*p^-} \quad {}^{P}X_{i^*j_y} = \lambda_{yx}\,{}^{P}X_{i^*p^-} \quad {}^{P}Z_{i^*j_y} = \lambda_{yz}\,{}^{P}X_{i^*p^-} \quad {}^{P}X_{i^*j_z} = \lambda_{zx}\,{}^{P}X_{i^*p^-} \quad (3.43) $$

In the same way as for line impacts, the above expressions can be used with ${}^{P}X_{ci^*}$ and ${}^{P}Z_{ci^*}$ in equations (3.41) to obtain the moment arms about c. Note that i^* can be replaced by i^*_m in equation (3.43) for post-impact PR2. When all $\lambda_{ab} = 0$ the impulses act at i^* or i^*_m.

The horizontal impulses ${}^{P}J_x$ and ${}^{P}J_z$ are permitted to lie outside the convex hull of the impacting vertices as they represent the resultant of the horizontal impulse distribution during impact. However, the vertical impulse ${}^{P}J_y$ cannot act outside of the convex hull of the impacting face as the support cannot provide any tensile force. Thus, if this occurs, the corresponding combination of λ_{ab} variables for ${}^{P}J_y$ are deemed invalid and must be adjusted to produce a valid location of ${}^{P}J_y$.

The five impact scenarios discussed above are summarized in Table 3.2.

Table 3.2. Classification of 3-D Impacts

Pre-Impact Pattern	Post-Impact Pattern	Type of Impact	Number of λ_{ab} Required
PR1	PR1	Line	2
PR1	PR1	Surface	4
PR1	PR2	Surface	4
PR2	PR1	Surface	4
PR2	PR2	Surface	4

3.10.4 Post-Impact Kinematic Constraints

In order to solve the equations of momentum for each impact, the kinematic constraints for the post-impact pattern must be applied.

3.10.4.1 Post-Impact PR1

For post-impact PR1, arising from either a line or surface impact, the relevant constraints are:

$$ {}^{P}\dot{X}^{+}_{op^{+}} = 0 \qquad {}^{P}\dot{Y}^{+}_{op^{+}} = 0 \qquad {}^{P}\dot{Z}^{+}_{op^{+}} = 0 \tag{3.44} $$

indicating that the post-impact rocking vertex p^{+} is restricted from moving in any direction. p^{+} may be replaced by i^{*} as necessary for surface impacts. Equations (3.44) when combined with equations (3.40) result in nine total equations which can be solved for nine unknowns: the six post-impact velocities and the three impulses. Thus, the system can be solved for a line impact only if λ_{zx} and λ_{yx} from equations (3.42) are assumed. For a surface impact, λ_{zx}, λ_{yx}, λ_{yz}, and λ_{xz} must all be assumed in order to solve the equations of momentum.

3.10.4.2 Post-Impact PR2

When PR2 is the post-impact pattern, five kinematic constraints must be added to equations (3.40) to ensure pure rocking about the edge defined by i^{*}_{1} and i^{*}_{2}:

$$ {}^{P}\dot{X}^{+}_{oi^{*}_{1}} = 0 \qquad {}^{P}\dot{Y}^{+}_{oi^{*}_{1}} = 0 \qquad {}^{P}\dot{Z}^{+}_{oi^{*}_{1}} = 0 \qquad {}^{P}\dot{Y}^{+}_{oi^{*}_{2}} = 0 \qquad {}^{P}\dot{Z}^{+}_{oi^{*}_{2}} = 0 \tag{3.45} $$

Therefore, there are 11 equations for post-impact PR2 and 13 unknowns: six post-impact velocities, three impulses, and four λ_{ab}. Thus, only two of the four λ_{ab} can be solved; the other two must be assumed. It can be shown that you must assume one of the pair of coordinates defining j_y, ${}^{P}X_{cj_y}$ or ${}^{P}Z_{cj_y}$, and one from the pair of coordinates defining j_x and j_z, ${}^{P}X_{cj_z}$ or ${}^{P}Z_{cj_x}$. For this thesis, the coordinates ${}^{P}X_{cj_y}$ and ${}^{P}Z_{cj_x}$ are assumed while the others are calculated. The products of variables P_1 and P_2:

$$ P_1 = {}^{P}Z_{cj_y}\,{}^{P}J_y \qquad P_2 = {}^{P}X_{cj_z}\,{}^{P}J_z \tag{3.46} $$

are created in order to eliminate the nonlinear product of the impulses and their coordinates and allow for a linear solution. The equations can then be solved for ${}^{P}J_x$, ${}^{P}J_y$, ${}^{P}J_z$, P_1, and P_2 directly. The unknown λ_{ab} from equations (3.43) can then be solved making use of the relationship between P_1 and P_2 and the impulses ${}^{P}J_y$ and ${}^{P}J_z$. Once equations (3.40) and the relevant constraint equations are solved for unknowns in base P, they are converted to base S by use of equation (3.38).

3.10.5 Verification of Impact Validity

At each impact, whether line or surface, a set of conditions must be met for it to be valid. Line and surface impacts both have the following minimum conditions:

$$T^- \geq T^+ \qquad\qquad J_y > 0 \tag{3.47}$$

where T^- and T^+ are the pre- and post-impact kinetic energies. The first condition comes from the observation that for most commonly-used materials, a system cannot gain energy from an impact. An exception to this was demonstrated in (86) for the case of rotating support media, which is not the case described in this thesis. Also, $J_y < 0$ forces the support to provide tensile impulses on the body which breaks the tensionless support requirement of this model.

Additionally, for a line impact:

$$\dot{Y}^+_{op^-} > 0 \tag{3.48}$$

where $\dot{Y}^+_{op^-}$ is the post-impact vertical velocity of the pre-impact rocking vertex p. Surface impacts have a similar restriction:

$$\dot{Y}^+_{oi_k} > 0 \tag{3.49}$$

where $\dot{Y}^+_{oi_k}$ represent the post-impact vertical velocities of the k vertices that defined the impacting face, including the pre-impact rocking vertex or vertices but excluding the post-impact rocking vertex for PR1 or the vertices of the post-impact rocking edge for PR2. If any of the velocities from equations (3.48) and (3.49) are negative, this indicates that that vertex or vertices are "burying" in the support post-impact which is not possible for a rigid support medium.

For surface impacts, equation (3.49) creates a restriction on the direction of the post-impact angular velocity $\boldsymbol{\omega}^+$. This restriction is equivalent to the requirement that $\boldsymbol{\omega}^+$ must lie between the vectors $\mathbf{r}_{i^*i_{ccw}}$, the vector connecting i^* to the nearest potential rocking vertex moving counterclockwise about the convex hull of the body, and $-\mathbf{r}_{i^*i_{cw}}$, the opposite vector connecting the nearest potential rocking vertex moving clockwise about the body as shown in Figure 3.17. If $\boldsymbol{\omega}^+$ is in the same direction as $\mathbf{r}_{i^*i_{ccw}}$, the body would rotate about $E_{i^*i_{ccw}}$ in PR2 and if $\boldsymbol{\omega}^+$ moved any further counterclockwise it would cause $\dot{Y}_{oi_{ccw}} < 0$ breaking the condition (3.49). The same issue occurs if $\boldsymbol{\omega}^+$ moved clockwise past $-\mathbf{r}_{i^*i_{cw}}$.

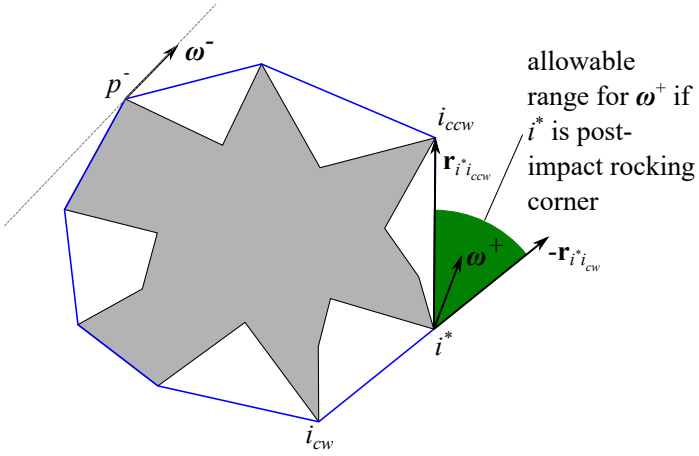


Fig. 3.17. An example of a surface impact with an object entering post-impact PR1 with the allowable range for $\boldsymbol{\omega}^+$ shown.

Finally, J_y must also lie inside, or on the edge, of the convex hull of the impacting face. If any of conditions (3.47) or (3.49) are not true at impact, the solution to the impact is not accepted. In the instance that a surface impact is invalid, a different post-impact rocking vertex i^* or edge $E_{i^*_1 i^*_2}$ can be tested if available, or the locations of the impulses can be

changed by varying λ_{ab}.

3.10.6 Algorithmic Procedure for Surface Impacts

When a surface impact occurs, more than one of the impacting vertices, i_k, or edges, $E_{i_k i_{k+1}}$, could be a valid post-impact rocking vertex or edge depending on the selection of λ_{ab}. Thus, the following procedure is followed to determine the valid post-impact scenarios.

At each surface impact, all the potential post-impact rocking vertices, i_k, are assigned as i^* in turn to see if any are valid in post-impact PR1, and each of the potential rocking edges, $E_{i_k i_{k+1}}$, are also checked for post-impact PR2 validity. If only one vertex or rocking edge is valid, it is accepted as the post-impact rocking vertex or edge. If two or more vertices or edges are valid, the result is flagged as the solution is not unique. If no vertices or edges are valid, the surface impact does not have a solution with the parameters provided.

Some impacts may not meet the post-impact requirements for any post-impact rocking vertex or edge for a given set of λ_{ab}. In this case, a new set of λ_{ab} may be checked following the same procedure as above. If a suitable set of λ_{ab} cannot be found, this PR model is overstretched as the body would most likely slide or uplift during impact. For the model used in this chapter, the object will be set to SP when the initial set of λ_{ab} does not result in a valid surface impact for any vertex or edge. This will be achieved by setting all velocities to zero and the position states to their values at impact, similar to (32; 99). However, in most of the examples presented here, this situation does not arise as the impacts are solved with their initial λ_{ab} variables. The few exceptions to this are noted in the examples below. Figure 3.18 shows a flowchart for the solution of impacts in this irregular geometry model.

3.10.7 Energy-Based Transitions

A rigid body rocking model must take into account energy-based changes of pattern from one pattern to a more restrictive pattern as the numerical code would continue integration infinitely even after many impacts, leading eventually to numerical instability. These

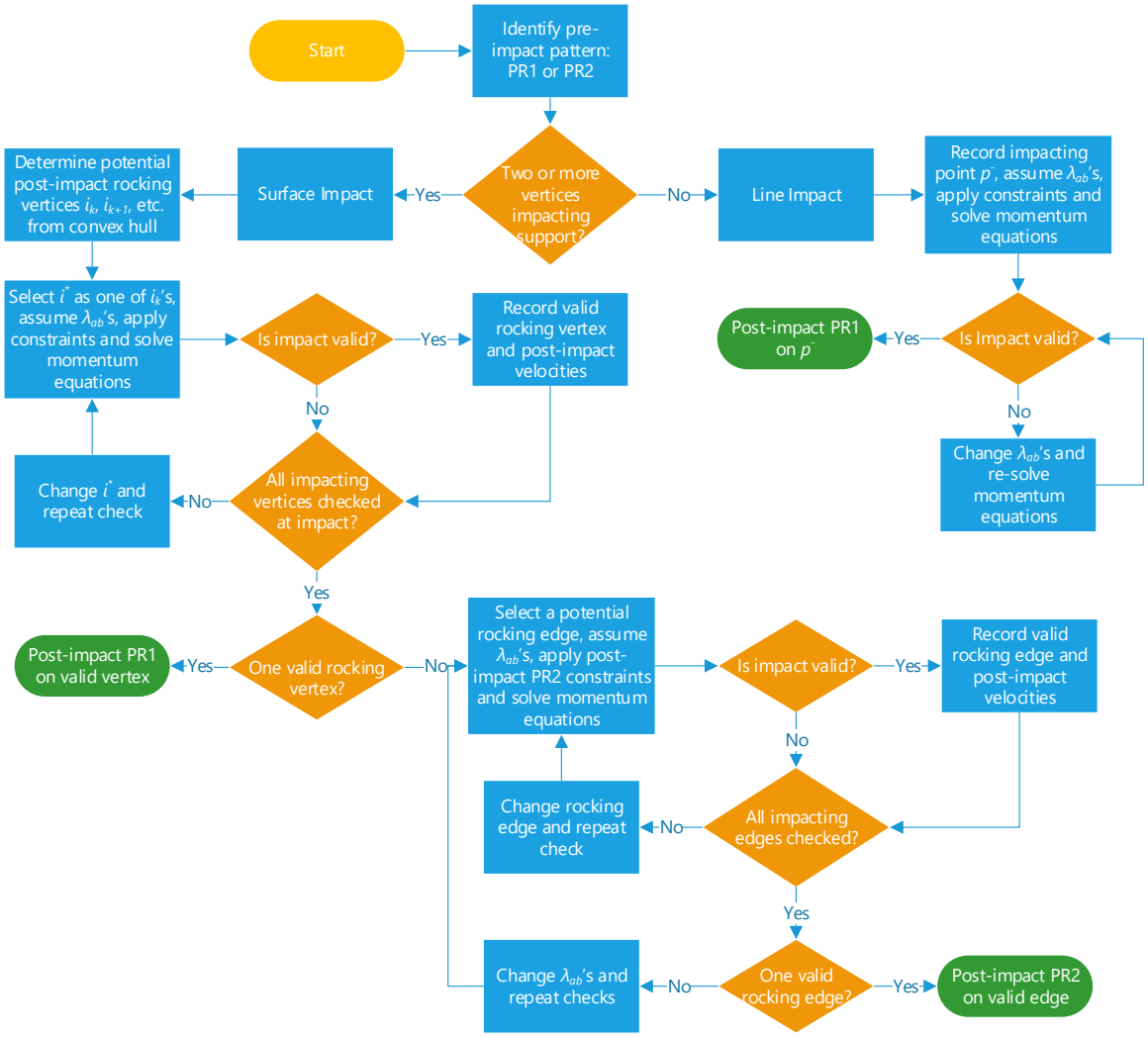


Fig. 3.18. A flowchart showing the iterations and program flow for line and surface impacts in the irregular geometry model.

transitions are not mentioned in previous studies (120) yet are necessary to solve for the full dynamic response of a rocking object. At some time t^*, some or all components of $[\omega^+]$ fall below the floating precision of the computer and thus numerical errors are introduced. The three energy-based transitions permitted in this pure rocking model are PR1 to SP, PR2 to SP, and PR1 to PR2 as diagrammed in Figure 3.10.

When in PR1, after external forces have ceased, the body may continue sequential impacts from one vertex to another about one of the body's faces. At some point, ${}^{S}T$ falls below a reasonably chosen threshold. At this time, the body may be placed into the SP by

means of an energy-based transition as it is assumed the body would not topple but come to rest. This is simply a way to shorten the integration of the equations of motion.

A similar transition may occur when an object with two parallel edges (such as a rectangular prism) repeatedly exhibits surface impacts going from PR2 to PR2 on the parallel edges. In this case, ${}^{S}T$ and the magnitude of $\boldsymbol{\omega}^{+}$ are checked and if either falls below a reasonably chosen threshold the body will be transitioned to SP.

Finally, the most complicated but important energy-based transition in this model is that from PR1 to PR2 through line impacts. There are instances such as the case shown in Figure 3.13 where, after the impact shown, the body would rock about i, impact and rock about p and repeat the process. The two vertices i and p alternate as rocking vertices in PR1. At some time, these vertices alternate impacts but have a negligible component of $\boldsymbol{\omega}^{+}$ perpendicular to the impacting edge, or about $\mathbf{e}_z^P$, as can be visualized in Figure 3.14. If $\boldsymbol{\omega}^{+}$ about $\mathbf{e}_z^P$ falls below a reasonably chosen threshold, the body will transition to PR2 by an energy-based transition by placing points i and p on the support and giving them zero velocities while $\dot{\gamma} = {}^{P}\omega_x$ is set as the initial condition in the integration of PR2.

3.11 Numerical Time Integration

With the basic physical parameters of the object ascertained and the patterns and equations of motion defined, the equations of motion for each pattern described in Section 3.8 are integrated over time to obtain $\boldsymbol{Q}_a$ using Matlab's ode45, which is a Runge-Kutta (4, 5) Dormand-Prince pair, with the desired support accelerations applied (40; 94). Matlab's event location functionality is used during integration to detect impacts and transitions from one pattern to another. The dependent states $\boldsymbol{Q}_b$ are then calculated using $\boldsymbol{Q}_a$ and the appropriate equations for each pattern as described in Section 3.8.

Figure 3.19 shows a flowchart for the full model.

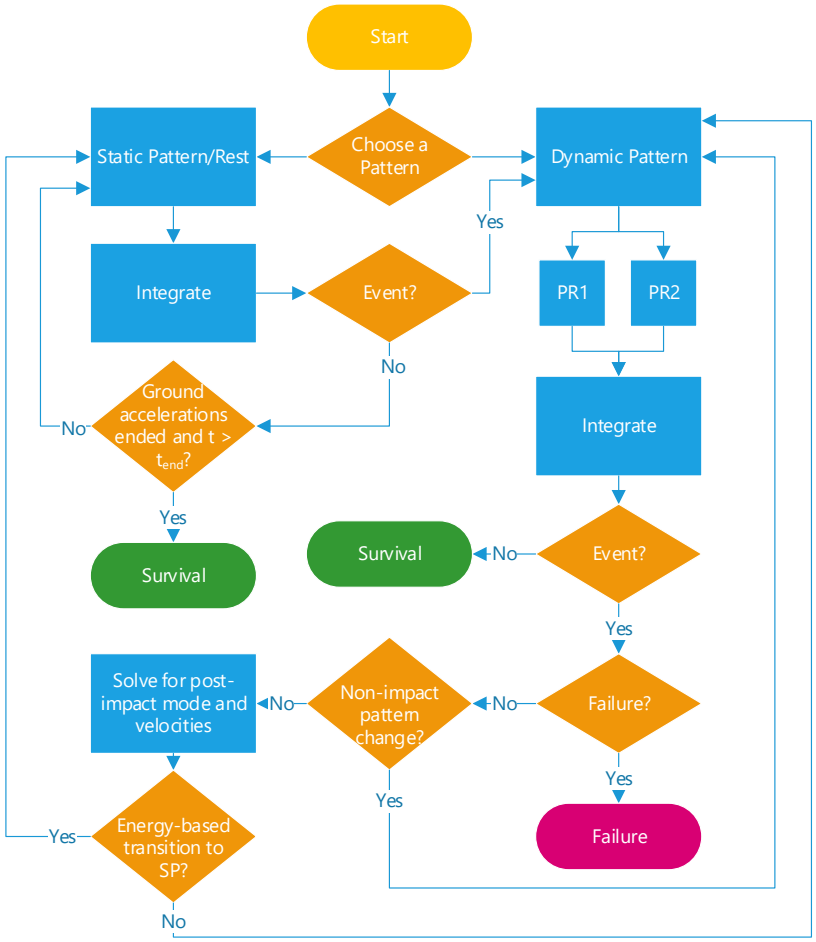


Fig. 3.19. A flowchart showing the program flow for the full 3-D irregular geometry model.

3.12 Examples of 3-D Pure Rocking Dynamics

The following examples show the use of this irregular geometry model in determining the dynamic response of two museum artifacts: the *Doryphoros* introduced previously and the *Discobolus*, another ancient sculpture. These museum artifacts are selected as they exhibit irregular geometry and many more than four possible rocking vertices around their bases. Furthermore, they also represent some of the most valuable objects of irregular geometry at risk of toppling and damage due to rocking. The model is not limited to museum artifacts but could be applied to many other objects such as computers, bottles or other delicate objects made of glass, and even children's toys such as a rocking horse. For example, the model has previously been applied to extruded polyhedral solids resembling cylinders in

(27).

3.12.1 Example 1: The *Doryphoros* Sculpture Subjected to an Earthquake

The *Doryphoros* sculpture from Figure 3.1 offers an insightful case study into the capability of this irregular geometry model and the importance of considering the geometry in seismic studies. The *Doryphoros* sculpture shows a highly irregular geometry. Its base has multiple vertices that can act as rocking vertices, there are portions of the body that are clearly concave, and the body clearly cannot be accurately represented as a rectangular prism as it does not possess any sort of symmetry. Finally, the projection of the centroid of the body on the support medium is not collocated with the geometric centroid of the face of the body in contact with the support when the body is in its initial equilibrium position. The STL file for this sculpture (47) is provided in STL File S3.1 as part of the online supplementary material. Figure 3.20 shows the initial orientation of the *Doryphoros* before the earthquake with approximate dimensions of 0.31 m, 0.36 m, and 1.30 m in the X, Y, and Z directions respectively.

To examine the seismic response of the *Doryphoros* sculpture, the unscaled accelerations obtained from the Kobe Japan Meteorological Agency station during the Kobe, Japan earthquake of 1995 is applied to the body (1). The support accelerations applied are shown in Figure 3.21.

The results of the Euler angles and displacement of c over time for the earthquake are shown in Figure 3.22. The displacement of c is defined as $[\mathbf{r}_{oc}] - [\mathbf{r}_{oc0}]$ where $[\mathbf{r}_{oc0}]$ describes the initial position of c.

As can be seen in Figure 3.22, for the first seven seconds of the earthquake the sculpture remains in SP as the excitations do not reach the level at which F_y reaches the edge of the convex hull of the base. The trajectory of the location of F_y during that period is shown in Figure 3.23. The black points represent the actual vertices of the sculpture in contact

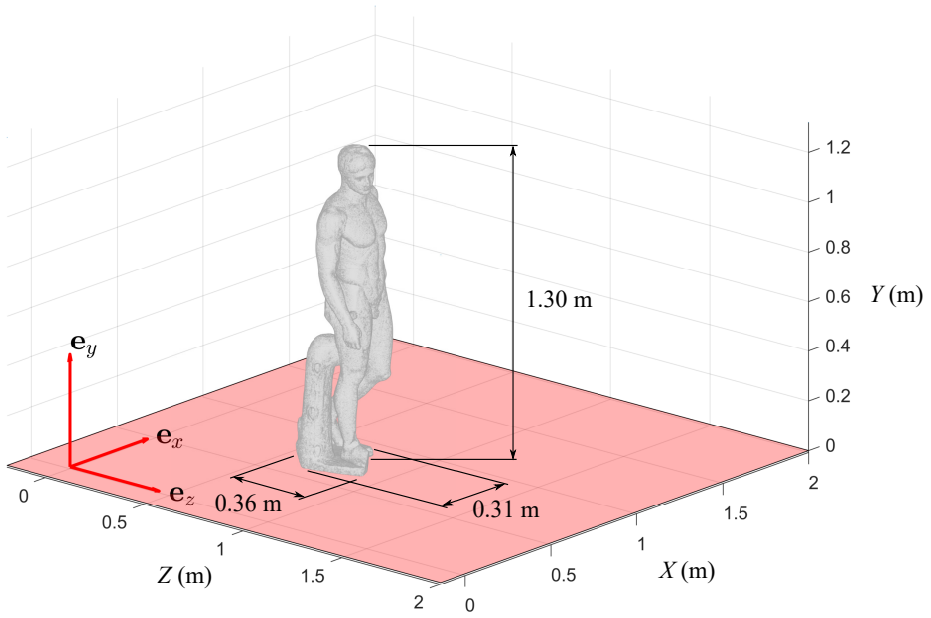


Fig. 3.20. The orientation of the *Doryphoros* sculpture at the beginning of the Kobe, Japan earthquake.

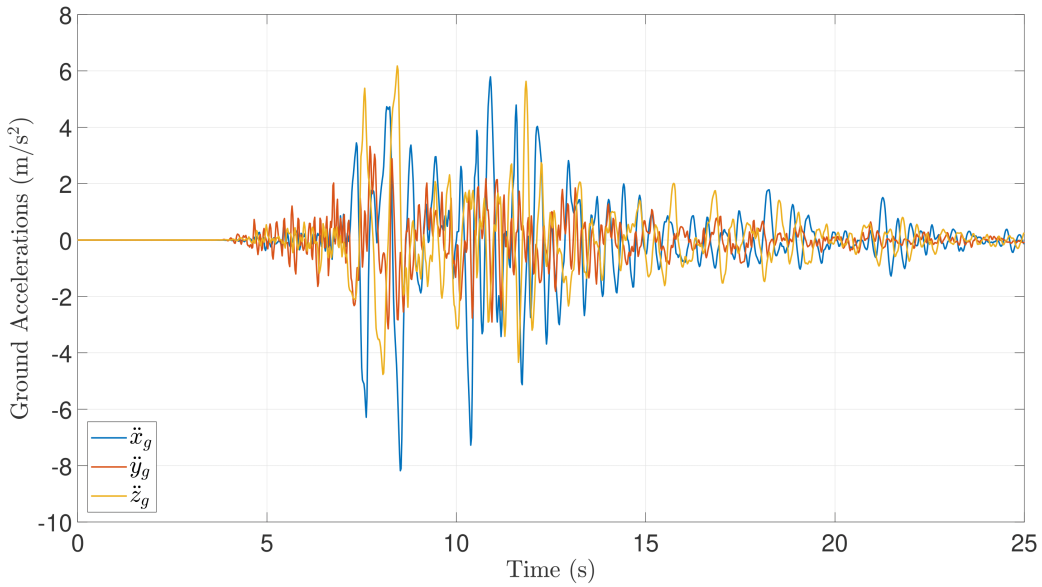


Fig. 3.21. The support acceleration time history for the Kobe, Japan earthquake of 1995.

with the support. At some locations the density of black points in a given area makes them appear continuous in the plot. The red line is the convex hull of the support contacts, the large black point is the projection of the centroid on the support surface, and the blue line shows the location of F_y during the first seven seconds of the earthquake until it reaches

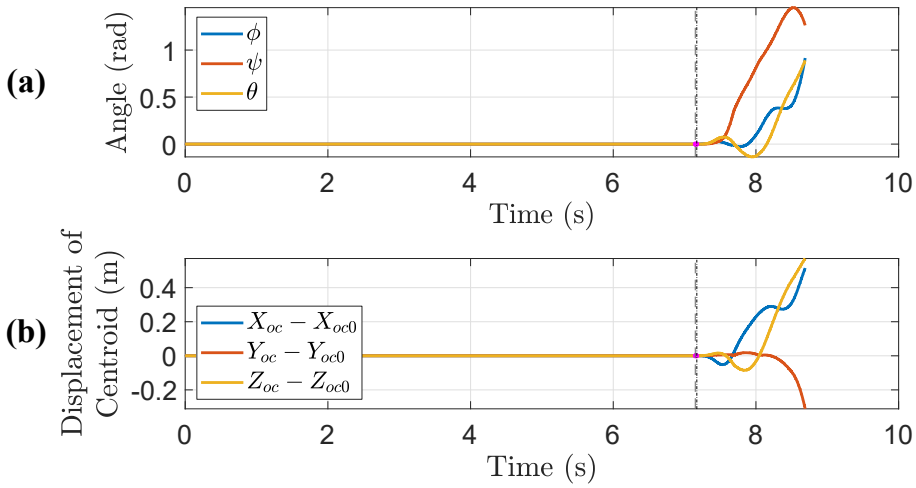


Fig. 3.22. Plots of (a) the Euler angles and (b) the displacement of the centroid over time for the *Doryphoros* sculpture during the Kobe, Japan earthquake of 1995.

the edge of the convex hull of the base. The location of F_y changes over that period but the body remains in SP until F_y reaches an edge of the convex hull.

At this instance the body enters PR2; this is depicted by the first (leftmost) dashed line in Figure 3.22. Less than 0.1 seconds after the body transitions to PR2, F_{y1} tends to zero. Thus, the body transitions to PR1 which is shown by a second dashed line in Figure 3.22. After this transition, the sculpture remains in PR1 while making a series of line impacts and changing rocking vertices until failure. Notice the 3-D motion with each of the three Euler angles changing significantly during PR1. The sculpture twists and "walks" about its vertices, particularly from time 7.75 to 8.20 seconds, until it topples. The walking motion can be defined as rocking in PR1 about a vertex p_i that results in the body predominantly twisting about a vertical axis and impacting the support on another vertex p_{i+1}, entering PR1 on the impacting vertex, and continuing this pattern by rocking between those vertices or neighboring vertices while moving forward. This motion can be seen in Video S3.2 and Video S3.3, corresponding to a real-time video and a video where the time has been slowed down to 25% of real-time respectively, which are provided in the online supplementary material. This walking motion of the sculpture cannot be described by planar rocking

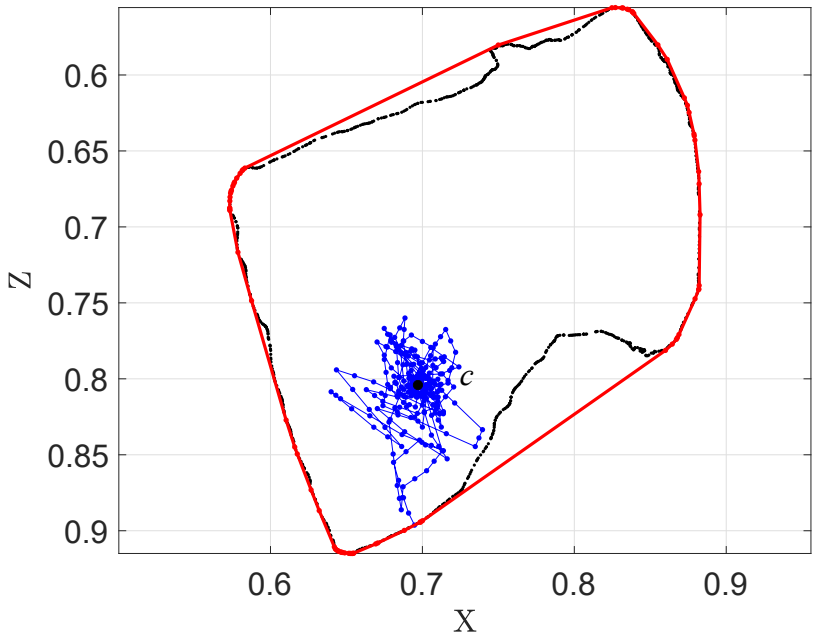


Fig. 3.23. A plot of the *Doryphoros* support contacts and location of F_y for the first seven seconds of the Kobe, Japan earthquake. The small black points are the support contacts of the sculpture, the large black point is the projection of c on the base, the red line is the convex hull of the support contacts, and the blue line and points are the location of F_y over time.

models yet it is clearly important to the response and in this example leads to toppling of the sculpture. Further, the irregular geometry of the sculpture and its base results in a dynamic response which is much different than the response of a rectangular block even in 3-D as many more than four rocking vertices are engaged during the sculptures motion.

Thus, this irregular geometry rocking model has been shown to be vital in considering the motion of this object as it is excited from the SP and rocks until failure. The many rocking vertices that contact the support and the "walking" motion of the sculpture cannot be described by planar rocking or rectangular approximations and thus this model offers an important tool to study such motions. A museum may also consider placing a sculpture such as the *Doryphoros* on a different mount or pedestal with a different shape than its actual base. Any desired pedestal shape or size can be handled by simply inputting a new STL to the model.

3.12.2 Example 2: The *Doryphoros* Subjected to Sinusoidal Acceleration Pulses

In both of the previous investigations, the body was assumed to have a specific orientation with respect to the axes of the earthquake. However, as a certain alignment of a body to earthquake axes cannot be chosen, other orientations must be investigated. To demonstrate that, the relationship between the orientation of the *Doryphoros* and its stability when subjected to support accelerations was tested by applying sinusoidal acceleration pulses in varying horizontal directions. The angle β represents a rotation about the negative $\mathbf{e}_y$ axis measured from the positive $\mathbf{e}_x$ axis. The support experiences a horizontal sinusoidal acceleration pulse of exactly one cycle in the direction defined by β. The pulse's amplitude A and frequency ω are varied:

$$\ddot{x}_g = \begin{cases} A \sin \omega t \cos(\pi - \beta), & \text{if } 0 \leq t \leq \frac{1}{f} \\ 0, & \text{if } t > \frac{1}{f} \end{cases} \qquad \ddot{z}_g = \begin{cases} A \sin \omega t \sin(\pi - \beta), & \text{if } 0 \leq t \leq \frac{1}{f} \\ 0, & \text{if } t > \frac{1}{f} \end{cases} \tag{3.50}$$

The minimum failure amplitude (MFA), or the minimum A in g for which the body topples for a specific f, is recorded for varied β for pulses with $f = 0.5$ Hz. The MFA for every value of β are plotted in blue in the polar plot of Figure 3.24. Additionally, the base vertices and convex hull of the base of the *Doryphoros* are plotted in black and red respectively to show the orientation of the base with respect to the angle β of pulse applied. The radial scale of the plot is in g for the blue line and scaled to 1:1.18 m for the red and black points indicating the orientation of the body's base to scale. The base vertices are provided to aid visualization. STL File S3.1 can be examined for details of the base geometry.

This polar plot shows an irregular distribution of the MFA for the *Doryphoros*. The minimum of the MFAs for all angles ($0.140g$) occurs around $\beta = 60°$ (shown by green

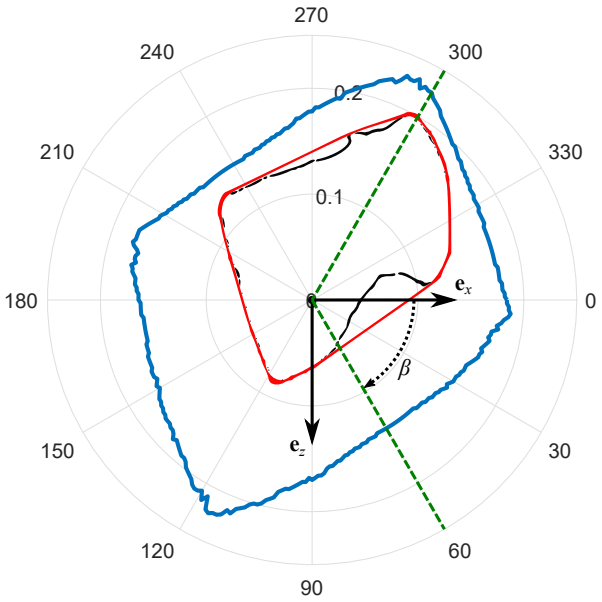


Fig. 3.24. Blue line: the minimum failure amplitude in g of the *Doryphoros* for sinusoidal pulses applied at various angles with frequency 0.5 Hz. Red line: the convex hull of the contact vertices showing the orientation of the base relative to the pulses. Black points: the actual contact vertices for the *Doryphoros*. Green dashed lines: two angles of β for which stability diagrams are made. The angle β is positive in the direction shown in the figure while the base is oriented with the centroid over o as shown by the unit vectors $\mathbf{e}_x$ and $\mathbf{e}_z$.

dashed line). The maximum of the MFAs for all angles ($0.232g$) occurs near $\beta = 300°$ and is more than 65% greater than the minimum of the MFAs and thus shows a large variation in the MFA depending on the angle of the support acceleration. The base of the sculpture is near its widest in the $\beta = 120°, 300°$ direction and near its narrowest in the $\beta = 60°, 240°$ direction. However, result that the base width and MFA are directly proportional as would be assumed for planar rocking does not hold for all β. Figure 3.24 only shows the MFA for $f = 0.5$ Hz. The MFA curve would change as the frequency of the examined pulse changes. In order to understand the more complete response of β on the stability of the body, two angles ($\beta = 60°$ and $\beta = 300°$, as shown by the green dashed lines in Figure 3.24) were selected to create stability diagrams which provide an image of the stability of the body for various f on the horizontal axis and A on the vertical axis. Pulses for which the body topples and survives are marked in red and green respectively.

Figure 3.25 shows stability diagrams for $\beta = 60$ and $\beta = 300°$. These plots are markedly different from each other though they are produced from the same pulses on the same object with the only difference being β.

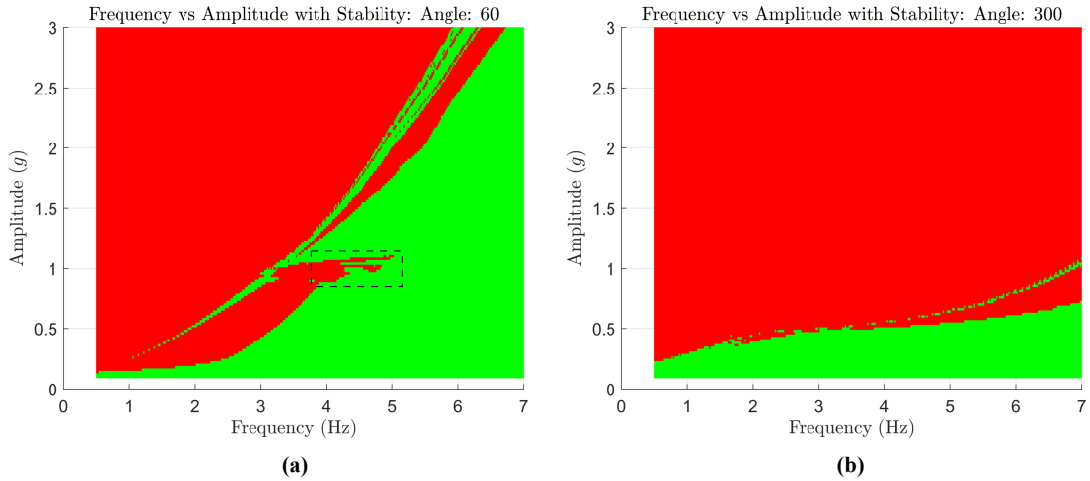


Fig. 3.25. Stability diagrams for the *Doryphoros* under sinusoidal pulse support accelerations where red indicates failure by overturning and green indicates survival of the pulse. (a) $\beta = 60°$. (b) $\beta = 300°$.

Even though $\beta = 300°$ offers a much higher MFA for pulses of 0.5 Hz, the stability diagrams show that for nearly all pulses with frequency greater than 3 Hz, the MFA for $\beta = 60°$ is greater than that for $\beta = 300°$. The difference in MFA is pronounced for many frequencies. For some frequencies $\beta = 60$ has more than three times the MFA as $\beta = 300°$, e.g. 6 Hz, showing that the width of the base and the MFA are not directly proportional. In this case, the lower MFA is due to out-of-plane motion whereby the body rotates about an axis defined by the line at $\beta = 300°$. Examples of out-of-plane motion were seen in the earthquake examples for the *Doryphoros* and the *Discobolus*. These results would not be predicted based on the common assumption that the greatest risk of overturning occurs due to planar rocking perpendicular to a vector defined by β for which the base width is minimum (10). These results show that it is important not only to consider polar stability plots or estimates of the stability in a given direction based on the width of the base in that direction, but also to consider the effect of 3-D irregular geometry and a range of both

frequencies and amplitudes for different β about the entire body.

Another interesting observation from Figure 3.25 is the region enclosed by the dashed rectangle. The irregular shape and extension of this region from around 3.5 to 5 Hz cannot be explained by the planar inverted pendulum model. Thus, by using a 3-D rocking model that handles irregular geometry, the 3-D nature of the response for museum sculptures can be seen. The change in the stability diagrams as β is varied shows that the irregular geometry, particularly the base having more than four vertices, is influential on the rocking response and stability of the body. The 3-D irregular geometry and the presence of more than four rocking vertices cannot be studied with a rectangular approximation or common planar rocking assumptions. Thus, this 3-D irregular geometry model should be used in lieu of a planar rocking model or rectangular approximations. Further, the great difference in stability for different β also make a comprehensive study, i.e., for many β, of the stability of an irregular body such as the *Doryphoros* with a 3-D irregular geometry model necessary to determine the direction of rocking and MFA that would most likely cause failure.

The final example for the *Doryphoros* examines the effect of different λ_{ab} on the stability diagrams of the sculpture. As different λ_{ab} are assumed for both line impacts and surface impacts, the post-impact velocities change, resulting in a different trajectory of the system for the same support acceleration. Previous research has shown that λ_{ab} for rectangular blocks does not need to be zero (31; 108), and using $\lambda_{ab} = 0$ has been shown to be non-conservative for rectangular blocks during planar rocking (31). Different values of λ_{yx} are assumed and applied to the the *Doryphoros* to obtain stability diagrams. The other λ_{ab} variables other than λ_{yx} are set to zero for simplicity and to illustrate the significant effect of a single λ_{ab} on the stability of the body.

Thus, λ_{yx} is assigned values of 0, 0.15, and 0.30 and checked for $\beta = 60°$. The other assumed λ_{ab} are set to zero. A $\lambda_{yx} = 0.30$ for a line impact means that J_y is applied at 30% of the distance from the post-impact rocking vertex to the pre-impact rocking vertex whereas $\lambda_{yx} = 0$ means J_y is applied at the post-impact rocking vertex. For a surface

impact, $\lambda_{yx} = 0.3$ means that J_y is applied at 30% of the distance from either i^* or i_m^* to p^- or p_m^-, as described in Section 3.10.3, depending on the pre- and post-impact patterns. The results for $\lambda_{yx} = 0.15$ and $\lambda_{yx} = 0.30$ are shown in Figure 3.26 (the results for $\lambda_{yx} = 0$ were previously shown in Figure 3.25).

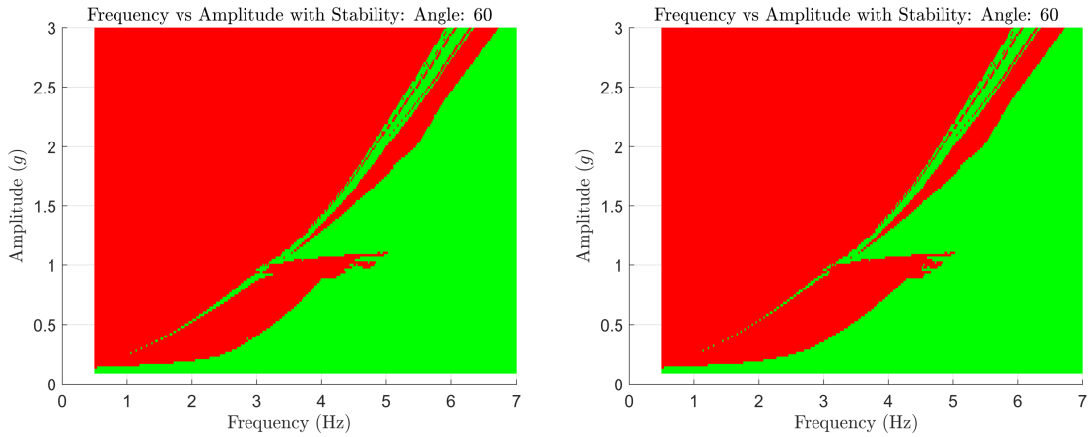


Fig. 3.26. Stability diagrams for the *Doryphoros* under single-cycle sinusoidal pulse support accelerations with $\beta = 60°$. (a) $\lambda = 0.15$. (b) $\lambda = 0.30$.

When compared to the result for $\lambda_{yx} = 0$ in Figure 3.25 and $\beta = 60°$, a larger failure loop at lower frequencies is observed. This region corresponds to failure after the pulse reverses direction and makes impacts with the support. This failure loop grows substantially in size resulting in a lower MFA for $\lambda_{yx} = 0.30$ for all pulses ranging from 2.5 to 4.5 Hz. As a non-zero λ_{yx} has been observed to be appropriate for rectangular blocks (31; 108), the same is assumed for irregular bodies and thus $\lambda_{yx} = 0$ is a non-conservative choice. There is also an upper limit to λ_{yx}, whereby the energy of the body increases at impact. It is presumed that this occurs around $\lambda_{yx} = 0.5$ as it does for rectangular blocks (31). However, the exact value of λ_{yx} for which the energy increases may vary for each impacting edge or face.

Because $\lambda_{yx} = 0.3$ produces greater instability in the body than a lower value, one option available to an engineer is to reduce the actual λ_{ab} that the body will exhibit at impact. For a sculpture as irregular and with as many rocking vertices as the *Doryphoros*, mechanically reducing λ_{ab} is difficult. For simpler objects such as those with rectangular bases, λ_{ab}

may be reduced by attaching "feet", or small base attachments that cause the impacting vertices to protrude from the rest of the body's geometry. As this is not easily achieved for a body such as the *Doryphoros*, another option is to change the base geometry to a simpler rectangular base where feet can more easily be implemented. This would require additional stability analysis for the body with the new base geometry. A different base cannot be attached to all objects, however, and thus the final option for those dealing with a rocking object with irregular geometry is to assume high λ_{ab} and perform stability analysis of the body as done above. If the risk of overturning after such analysis is deemed to be too great and the body must retain its irregular geometry, alternative options can be explored such as anchoring the body to its support. However, these alternatives provide a separate range of issues from rocking that requires more research.

3.12.3 Example 3: Investigating the Stability of the *Discobolus* Sculpture

An additional example is given of another sculpture, the *Discobolus*, which is a rough replica of the Townley Discobolus at the British Museum (78) and pictured in Figure 3.27. The STL file for this sculpture is provided in STL File S3.4 in the supplementary material (9). This sculpture also depicts a human form but has a much different shape and base compared to the *Doryphoros*. The base of the *Discobolus* is relatively similar to a rectangular of 0.86 m by 0.53 and the sculpture has a total height of 1.86 m. Due to its geometry, the body is expected to be more prone to rocking in the plane defined by the short side and the vertical axis. It will nonetheless be shown that the length of the body's base and its curved irregular geometry are not sufficient to prevent 3-D rocking.

Some researchers have assumed that museum sculptures such as the *Discobolus* would rock in a plane about a "critical" edge of the sculpture, most probably the longer edge as it appears to offer less resistance to overturning (10). The *Discobolus* was tested by applying the unscaled support accelerations from Figure 3.21 for the Kobe, Japan earthquake to

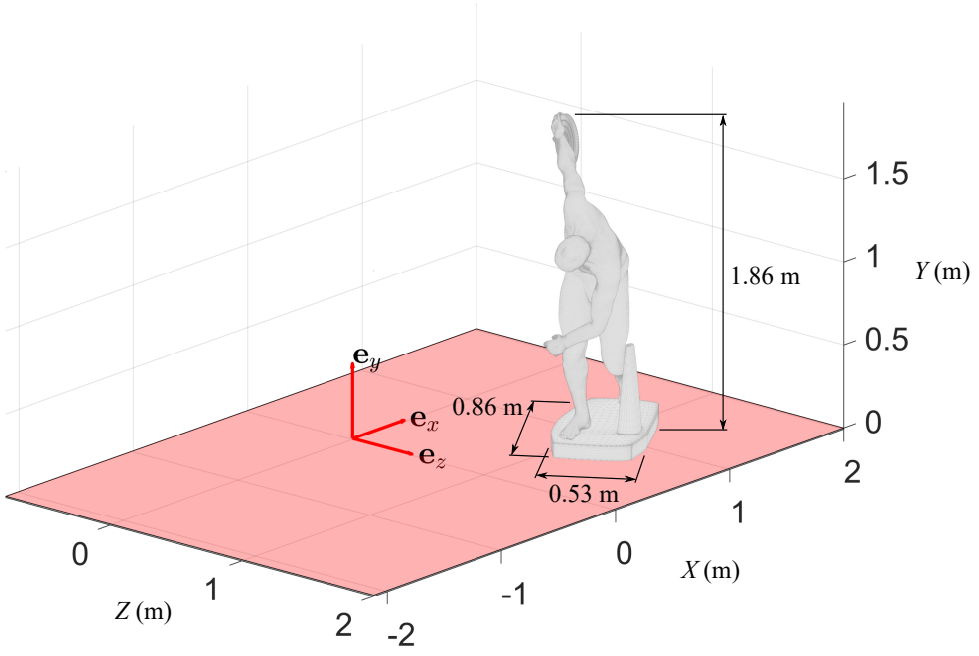


Fig. 3.27. The initial position of the *Discobolus* sculpture before being subjected to the Kobe, Japan earthquake.

compare its response with the *Doryphoros*. The rotation of either sculpture about the vertical axis is arbitrarily selected and a different response could be observed for any other selection. The effect of different orientations of the object to the same support acceleration will be examined later. The results of the body's movement for the "twist" selected, shown by its Euler angles and the position of its centroid over time, are given in Figure 3.28.

As can be seen in Figure 3.28, the *Discobolus* remains in SP longer than the *Doryphoros* due to its base being larger and the projection of c on the base being closer to the geometric center of the base. At about 8.0 seconds, however, the *Discobolus* enters pure rocking and continues rocking until it fails by toppling. Further, the larger and more rectangular base of the *Discobolus* does not keep it from failing due to the earthquake and the motion exhibited by the body during rocking has some similarities with the *Doryphoros*. The *Discobolus* also exhibits rocking about the rim of the statue after 8.5 seconds and no surface impacts occur for the duration of the motion. Only line impacts occur for this body, many of them occuring between vertices that are very close in proximity along the rim of the base. Due to the small

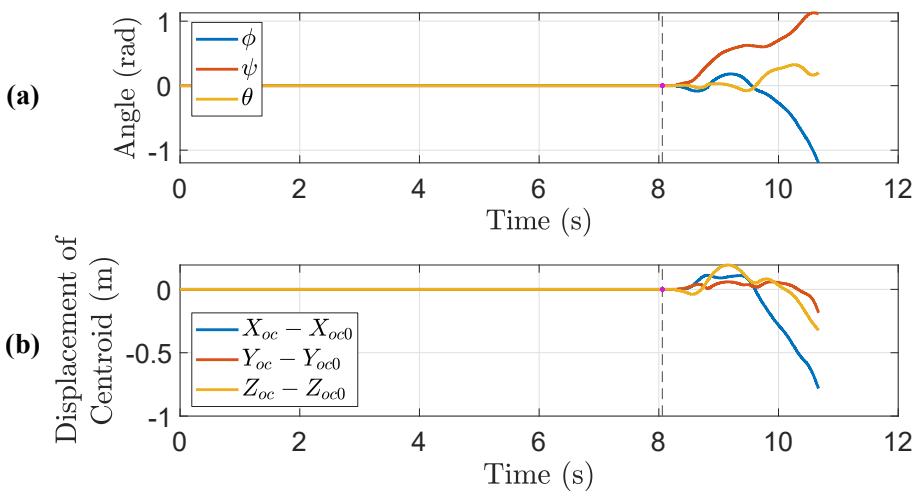


Fig. 3.28. Plots of (a) the Euler angles and (b) the location of the centroid c of the *Discobolus* for the support accelerations produced by the Kobe, Japan earthquake of 1995.

distance between these vertices, the body loses minimal energy at each impact and can rock about the full perimeter of the base. It appears that the sculpture almost experiences rolling about the perimeter of the base. This was also observed in (27) for the rolling of polygonal approximations of a cylinder. Videos of the motion of the *Discobolus* can be seen in full speed and 25% full speed in Video S3.5 and Video S3.6 in the supplementary material. The videos clearly show the twisting and rolling nature as many quick impacts about the rim of the base occur with small amounts of energy lost.

3.13 Conclusions

The model introduced in this chapter provides the ability to study the 3-D pure rocking response of a rigid body with any geometry under 3-D support accelerations. The model can analyze the motion of objects with any geometry in pure rocking in a fraction of the computational time required for models with deformable supports which utilize very stiff springs due to the high number of springs required in a deformable model for an irregular body. While the results would be expected to be similar for the rigid model and a deformable support model with high stiffness, the results will not align exactly because λ cannot be

selected for a springs model as it is for the rigid model. The examples above analyze the motion of some of the most irregular and valuable objects: ancient sculptures.

The results of both the *Doryphoros* and the *Discobolus* show the importance of considering the 3-D geometry of the object and its full 3-D motion. Neither of these objects, or any bodies like them with irregular bases and geometries, are naturally restricted to planar rocking in the presence of support excitations. Their dynamic response clearly has three non-zero independent DOFs and exhibits twisting and walking motions which cannot be realized by any model that makes planar rocking approximations or attempts to eliminate independent DOFs from PR1. The mode of failure is much more complicated than a simple rectangular prism rocking in PR2 about an edge until failure. The twisting motion of these bodies makes them more prone to toppling than for bodies that make surface impacts on their bases. The line impacts that these bodies exhibit promote continued rocking compared to surface impacts as each line impact generally causes less energy to be lost due to the smaller distance between pre- and post-impact rocking vertices.

Further, the sinusoidal pulse results show that the orientation of an object with an irregular base to a given pulse can make a large difference in the MFA that is not directly related to the width of the base in the direction of the pulse. The MFA for a pulse with a certain frequency can vary greatly for different β as the body experiences 3-D rocking rather than planar rocking about a plane, and thus, testing the stability of a body with pulses of various β should be done to obtain estimates of the lowest expected MFA. Additionally, changing the λ_{yx} value for a given object is shown to affect the stability of an irregular body. $\lambda_{yx} = 0$ has been shown to be non-conservative for irregular bodies just as it has been shown previously for rectangular blocks. The other λ_{ab} should be analyzed similarly to λ_{yx} for an irregular object and methods to reduce λ_{ab} should be adopted as necessary such as the addition of feet.

These factors prove that carefully studying the full 3-D motion and geometry of an irregular body is important to determine its dynamic response as the intricacies that occur

with more than four rocking vertices cannot be constrained to 2-D motion or be modeled by a rectangular block. Models considering simplified geometry, planar rocking, or the conservation of momentum about the post-impact rocking vertex are likely to result in non-conservative estimates and should be avoided and replaced by a 3-D model for irregular geometry. The model introduced here can also be used for many other objects with irregular geometry other than museum sculptures, including those with curved surfaces such as the cylindrical approximations shown in (27). The following chapter will show additional examples of this pure rocking model applied to other irregular geometries such as toy tops. Future study should also be aimed at modeling sliding and free flight for irregular objects.

Chapter 4

The Dynamics of Objects with Curved Surfaces

4.1 Introduction

The dynamics of rolling have captivated humans for millennia. At least since the invention of the wheel, humans have used rolling objects to their advantage. The academic study of rolling dynamics has thus been an important field of study for engineers for many years whether examining wheels, balls, disks, or more irregular rolling objects such as those shown in Figure 4.1.

Previous studies on curved objects are either experimental or simplify the object's curved geometry to an algebraic expression such as a circle, ellipse, or parabola in order to use a rolling model. As one can see, however, these objects can be sculpted, 3-D printed, or manufactured to take any curved geometry which does not conform to algebraic functions. Thus, the rolling models that require a specific geometry struggle to handle more complex curvatures such as those in Figure 4.1 or any deviations from a smooth curved surface which could occur in the theoretical description of an object or due to imperfections in the manufacturing process. Objects with such geometries have consequently been neglected in



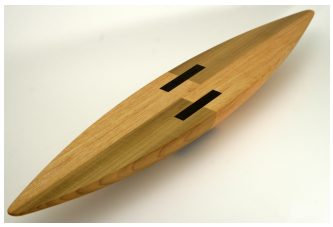
(a) Tippe top



(b) Gömböc



(c) Moai



(d) Rattleback

Fig. 4.1. Objects with curved surfaces that display rolling.

previous theoretical modeling of rolling dynamics. Rocking and rolling are fundamentally different models, yet this chapter investigates how rolling dynamics can be described by pure rocking.

As the pure rocking model considers a polyhedral approximation of a curve with any resolution desired (judged by the number of vertices), the full irregular geometry of any object can be considered regardless of the shape of the curve, and the dynamic results of the object on a horizontal support can be obtained under any desired forcing function. This chapter presents the results of the pure rocking model introduced in Chapter 3 when it is applied to various objects with curved geometry. Five types of curved objects and their motion will be discussed: cylinders and similar polyhedral solids, Euler's disk, the rattleback, the gömböc, and the tippe top. A literature review of these objects and the phenomena they exhibit follows.

Koh et al. initially studied the free rocking of a cylinder considering a rolling motion about the rim of the cylinder and defined patterns of nutation and rocking for the cylinder (63). Srinivasan and Ruina looked more closely at the free vibration of a cylinder, par-

ticularly when it is "flicked" from an unstable equilibrium point, so that the base of the cylinder impacts the ground and topples almost in the opposite direction of the initial tilt (100). Srinivasan and Ruina were particularly interested in determining why the cylinder does not overturn in exactly the opposite direction of the initial tilt as would be theoretically expected for a perfectly symmetric cylinder released with zero initial velocities. They derived models for both rolling and sliding contacts between the rim of the cylinder and the support to explain the asymmetric toppling of the cylinder. More recently, Vassiliou et al. have studied the rocking of a cylinder during an earthquake using constraints that allow for only two DOFs (110). But these constraints must be provided by mechanical constraints in addition to the cylinder being on a flat surface with sufficient sliding to prevent sliding. Similar work has been completed on the dynamics of polyhedra resembling cylinders by the author and supervisor of this thesis (27) which examines the dynamics of solids created by extruding polygons into "cylinders" that represent curves with different levels of resolution, i.e., different numbers of vertices, and models the motion of these "cylinders" with a pure rocking model.

Below a subjectively chosen height to diameter ratio, a cylinder is normally considered to be a disk. A disk of significance in previous dynamics research is Euler's disk, a toy disk known for its ability to spin for an extended period of time when placed on its edge and given an initial angular velocity about the vertical axis. It is, in essence, a stocky cylinder with a radius of 3.81 cm and thickness of 1.27 cm. Many researchers have studied the motion of a disk, though not necessarily Euler's disk (81; 101; 92; 35; 17; 18; 21). Additional researchers have studied Euler's disk more closely, focusing on several interesting aspects including its contact model (84), its energy dissipation mechanism and finite-time singularity at the end of its motion (77; 42; 66; 15), the sound the disk makes that increases in frequency toward the end of its motion (62; 91), and the details of its contact at the end of motion (22). Several of these studies will be examined in greater depth in the following examples.

The rattleback, also known as a celtic stone or wobblestone, is a peculiar object closest

in shape to a semiellipsoid that appears to defy the conservation of angular momentum. Rattlebacks come in various sizes and shapes but all of them exhibit the response that when they are spun about a vertical axis in a certain direction, they will initiate a rocking motion about their shorter horizontal axis and reverse their spin direction about the vertical axis. Most rattlebacks prefer one direction of spin, either counterclockwise or clockwise, but some are designed to reverse their spin regardless of its initial direction. Rattlebacks achieve this bizarre behavior through either asymmetric geometry or through asymmetric mass distribution over a symmetric base geometry. A number of researchers have studied the motion of rattlebacks (83; 20; 48; 28). However, the majority of these works only study rattlebacks with the geometry of an elliptic parabaloid or semiellipsoid, thus allowing for simpler analytical solutions. These solutions do not allow for study of rattlebacks that do not conform to the basic ellipsoidal geometry and thus the 3-D model which can handle any geometry will be shown to be useful.

Another object of interest for its rolling and rocking motion is the gömböc, a convex homogeneous body that has only one point of stable equilibrium and one point of unstable equilibrium, termed a mono-monostatic body (109). The geometry of the gömböc is such that no matter the initial position it is released from on a flat, horizontal support, the body will come to rest with the same point of equilibrium. Many mono-monostatic objects exist but the gömböc is the first known mono-monostatic object that has both convex geometry and homogeneity of material (107; 39). The exact shape of the gömböc is not unique but all gömböcs have a similar form. The dynamics of the gömböc as it moves from an unstable position to its stable point of equilibrium will be examined.

Finally, the tippe top, a toy that exhibits another peculiar motion on a horizontal support, has been the subject of study by a number of researchers (24; 103; 80; 55) and has even captured the fascinations of Wolfgang Pauli and Niels Bohr (34). The top is axially symmetric with uniform density and includes a bell portion approximately the shape of a sphere and a roughly cylindrical shaft. The tippe top displays a counterintuitive motion when

it is spun with an angular velocity about its shaft when its spherical portion is in contact with the support. If spun with sufficient angular velocity and under the right support contact conditions, the top will overturn and spin about its shaft. Previous researchers, cited above, have studied the tippe top and its reasons for overturning using continuous mathematical models considering a perfectly spherical lower component of the top. These models exclusively consider a continuously changing point of contact with the support either in rolling or sliding motion. In the 1950s, several researchers considered the dynamics of the tippe top. Synge considered a rolling friction model while Braams (24), Hugenholtz (55), and Parkyn (82) postulated that sliding friction was necessary to achieve the overturning effect seen in the top. Various models have been provided for the sliding friction model employed by the top (80; 34; 61). The motion of the top when considered by a pure rocking model will be presented to offer a new perspective to the study of this old toy.

4.2 Modeling Rolling Dynamics with Lagrange Multipliers

The following Figure 4.2 depicts a portion of a rigid body with curved surfaces that is permitted to roll on a horizontal plane.

When ignoring constraints, this body has six DOFs and six unconstrained equations of motion just as the rigid bodies considered in the last chapter. When taking into account constraints imposed by a pure rolling model, the body has a single point of contact p_i with the support and the relative velocity of the point of the body that coincides with the contact point is equal to zero in all three Cartesian directions. The point of the body in contact with the support may change continuously for a rolling model as indicated by the red dashed curve of Figure 4.2. In the alternative case, where the body is described by an external surface comprised of polygonal faces, the movement of the body would not be described by rolling, but by rocking. This geometry is shown in Figure 4.2 for a portion of the outer

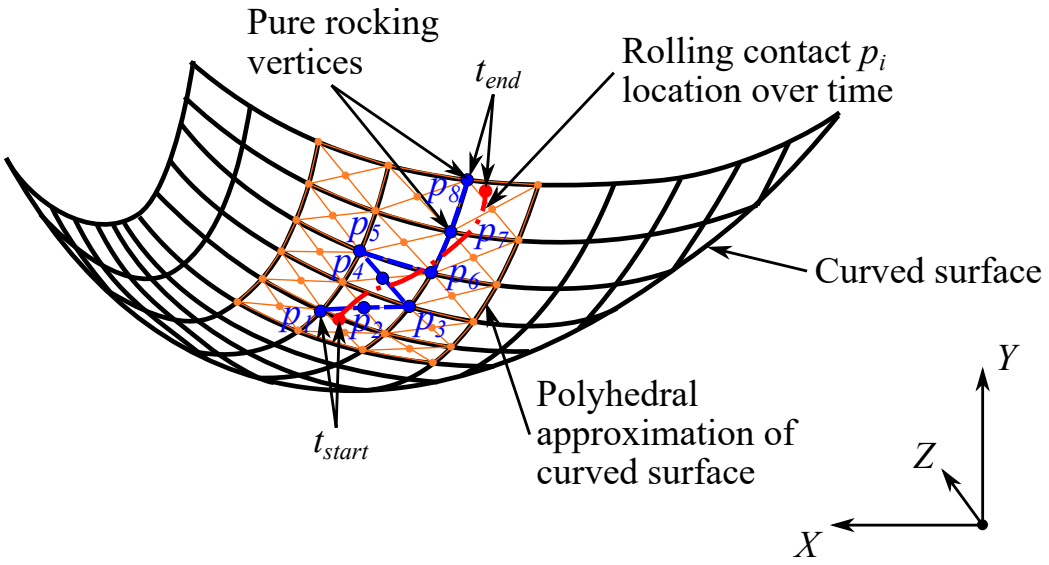


Fig. 4.2. A diagram showing a portion of a rigid body with a curved surface and the contact point p_i over time for pure rocking and rolling models from time t_{start} to t_{end}. Black lines: A smooth curved surface. Orange lines and points: a polyhedral approximation of the curved surface. Blue line and points: the movement of the pure rocking vertex over time from vertex p_1, p_2, ..., p_7. Red line and points: the movement of the rolling contact p_i.

surface of the body with the polygons indicated with orange lines. In pure rocking, the vertex in contact with the support changes discretely as shown by the blue points in Figure 4.2 and can be coincident with any of the vertices of the polyhedral faces. For each change in the rocking vertex, an impact occurs which causes a discontinuity in the velocities of the body.

The changing of a contact point involving impact can be visualized with the following Figure 4.3. The body in Figure 4.3 has three distinct portions where the external surfaces of the body are described by three different constraint equations: $g_1(x_{cp_i}, y_{cp_i}, z_{cp_i}) = 0$, $g_2(x_{cp_i}, y_{cp_i}, z_{cp_i}) = 0$, and $g_3(x_{cp_i}, y_{cp_i}, z_{cp_i}) = 0$ where x_{cp_i}, y_{cp_i}, and z_{cp_i} are the coordinates of a point belonging to the external surface of the body.

The body has its centroid at c as shown and the boundaries between surfaces described by a different constraint in Figure 4.3 correspond to lines that simultaneously satisfy the constraint equations of the surfaces around it. The constraint equations for the points of the outer surface of the body, $g_i(x_{cp_i}, y_{cp_i}, z_{cp_i}) = 0$, are in terms of their coordinates with

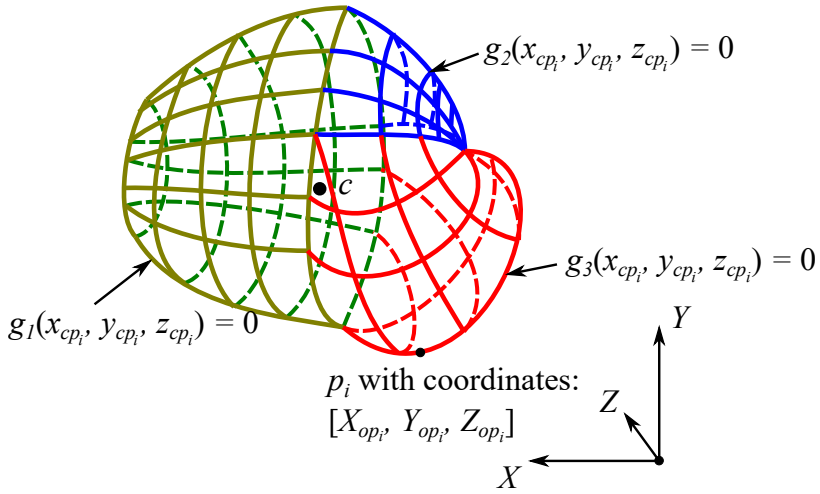


Fig. 4.3. A rigid body with three portions defined by three equations. Green surface: g_1, blue surface: g_2, and red surface: g_3.

respect to the system of axes fixed on the body, R. Given a translation and rotation of the rigid body, the kinematic equations of the body define the coordinates and velocities of any point on the body including those on the outer surface and are the general kinematic equations defined previously in Chapter 3: equations (3.5) and (3.6).

The following additional constraints must be placed on the contact point p_i:

$$[\dot{X}_{op_i}, \dot{Z}_{op_i}] = 0$$
$$Y_{op_i} = 0 \tag{4.1}$$

It should be observed that equations (4.1) are in terms of the Cartesian vertical coefficients Y_{op_i} and the Cartesian horizontal velocities, $\dot{X}_{op_i}$ and $\dot{Z}_{op_i}$. In contrast, the geometry constraints are functions of the body coordinates of a point x_{cp_i}, y_{cp_i}, and z_{cp_i}. To proceed, equations (3.5) and (3.6) need to be used to convert to a common coordinate system. The contact point is the only point on the body that satisfies the constraints (4.1) and one of the geometry constraints g_i, a system of equations that will be referred to collectively as g_r in the following discussion. When a simple surface such as a sphere or ellipsoid is studied, the constraints g_r can potentially be satisfied by making use of special generalized

coordinates that automatically satisfy them. In such cases, it is theoretically possible to define analytically the point of the body which is the contact point, and then determine a set of generalized coordinates that satisfy the kinematic constraints (4.1) for that point. However, the problem becomes substantially more complicated when the geometric constraint describing the surface of the body that the contact point belongs to changes. This case will be discussed in a later paragraph. However, even in the case that focuses on responses that would not result in the constraint equation g_i changing during the dynamic response of the system, the corresponding constraint equations would be more complicated as in the case of the bodies shown in Figure 4.1. When the constraint equations are more complicated, determining the contact point analytically and/or finding the set of generalized coordinates that automatically satisfy the constraints is not a straightforward process. In certain cases, a solution may not be achieved or may involve overly-complicated transformations.

Examples of the difficulties that occur in formulating and solving equations of motion when complicated constraints are applied can be found in (16). To overcome this problem, Lagrange multipliers are commonly used. The method is briefly explained below.

Consider a body with j generalized coordinates with m constraints applied. The constraints for this system are expressed generally as:

$$g_n(\mathbf{q}, \mathbf{q}) = 0 \tag{4.2}$$

where $\mathbf{q}$ and $\mathbf{q}$ are the vectors of the generalized coordinates q_k and their time derivatives $\dot{q}_k$ respectively for $k = 1, 2, ..., j$, and g_n is the nth constraint equation of g_r. The generalized forces Q_c arising from the constraints are expressed as

$$Q_c = \sum_{n=1}^{m} \Lambda_n \frac{\partial g_n}{\partial \Phi} \tag{4.3}$$

where Φ, for nonholonomic constraints, represents the generalized coordinates $\dot{q}_k$ for constraints on the contact point velocities and q_k for constraints on the coordinates. For

holonomic constraints, the equations for $\dot{q}_k$ must first be integrated over time to obtain the constraints in terms of the coordinates q_k which can then be replaced for Φ in equation (4.3). Λ_n $(n = 1, 2, ..., m)$ in equation (4.3) represents the Lagrange multipliers, one for each constraint equation. Using the generalized forces from the constraints, a modified form of Lagrange's equation of motion (3.22) may be obtained:

$$\frac{d}{dt}\left(\frac{\partial^S T}{\partial \dot{q}_k}\right) - \frac{\partial^S T}{\partial q_k} + \sum_{n=1}^{m} \Lambda_n \frac{\partial \mathrm{g}_n}{\partial \Phi} = Q_k \qquad k = 1, 2, ..., j \tag{4.4}$$

where the terms other than that with Λ_n are the same as those in (3.22) (16). After the modified equations of motion are derived, the system of the j equations of motion (4.4) and the m constraint equations (4.2) may be solved for the $j+m$ unknowns $q_1, q_2, ..., q_j, \Lambda_1, \Lambda_2, ..., \Lambda_m$ to obtain a set of differential-algebraic equations. The solution to this system of equations requires solving for every DOF and Lagrange multiplier and integrating the differential equations over time to obtain the states of all DOFs. However, this method retains all the DOFs of the system without any reduction to a set of independent generalized coordinates and while the states and Λ_n appearing in equation (4.4) may satisfy the system of equations, the original constraints may not necessarily be satisfied by the current realization of the states. This is due to the time integration of the equations which over time will likely result in undesired numerical drift. In some simple problems, one can intuitively eliminate that drift, but for a complicated geometry such corrections may not be possible or may introduce substantial sources of error resulting in the body's trajectory deviating from its ideal path.

The procedure just described assumes that the contact point changes smoothly. While it is possible to describe segments of the curved surfaces of irregular objects such as those in Figure 4.1 with continuous yet highly non-linear expressions as the states of the system evolve over time there will be situations where the contact point(s) on the body will need to transition from one surface described by one constraint g_k to another g_l. Figure 4.4 shows an example of another object with curved surfaces defined by functions g_1 and g_2, and two

different types of transition.

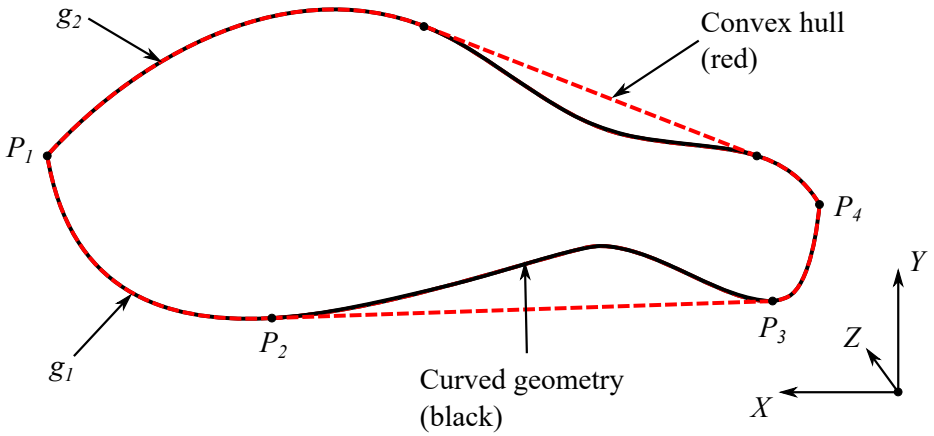


Fig. 4.4. A rigid body which depicts two curved surfaces defined by g_1 and g_2 in black, which connect at points P_1 and P_2. The convex hull of the body is shown with red dashed lines.

The two functions, g_1 and g_2, describe the black surfaces in Figure 4.4 which meet at points P_1 and P_4. Both g_1 and g_2 have have concave portions which cannot make contact with a rigid horizontal support. To consider only the points of the surfaces which are able to make contact with the support, the convex hull of the body in red dashed lines is used in order to detect transitions from the contact point, e.g., P_2 to P_3. In effect, the requirement that the concave portions of the body cannot make contact with the support means that the original function g_1 cannot actually describe all the surface contact points that may occur for the body. If the body moves so that it has contact point P_2 with the support and then transitions to point P_3, the body will experience an impact which creates discontinuous velocities for the body about two portions of g_1. A transition from g_1 to g_2, or vice versa, about points P_1 or P_4 would also result in an impact and a transition from one curve to another.

In other words, the outer surfaces of an object like the one shown in Figure 4.4 cannot be described by one smooth function of the coordinates of the points belonging to the surface. Even for a single smooth curve, e.g., g_1, the body may have concave portions such as those shown in Figure 4.4. These concave portions mean that a smooth curved object still may

experience impacts and thus an abrupt discrete change in its rocking vertex. This impact scenario, and the additional need for changes from one equation to another, e.g., g_1 to g_2 for the object in Figure 4.4, presents another problem for Lagrange multiplier methods as discontinuous impacts and changes from one curve to another must be handled by additional modeling considerations and assumptions. The problems that arise with multiple contacts are described in (65). When considering the motion of objects with curved surfaces, multiple contacts commonly occur during impacts or multi-contact patterns. The rigid body multiple contact problem is a major problem in mechanics. A variety of solutions to this problem have been offered with different assumptions. A review of these methods is provided in (25). The solution for the magnitude of reaction forces or impulses during a multi-contact pattern or during impact is not unique for rigid models. For example, at an impact, the multiple points of contact with the support have their own set of three impulses. This creates an indeterminate problem which requires assumptions to be placed on the impulses (25). These assumptions may be difficult to discern or compare with previous rocking models and experiments. Because it is desired to compare the model introduced in the last chapter to previous rocking models, this thesis uses a minimal set of assumptions which allows for easier comparison with previous studies. For impacts, the solution is manifest by λ_{ab}. As stated in (31) and (108), there is no unique choice for the λ_{ab} parameter. However, engineers have a better intuition about λ_{ab} compared to assuming the scaling of impulses on multiple simultaneous contact points. For the multiple contact patterns, SP and PR2, the problem with determining the individual reaction forces or impulses at each support contact are avoided by assuming pure rocking and the resultant of such reaction forces and impulses.

The pure rocking model described in the previous chapter can assist in modeling the dynamics of objects that macroscopically appear to have curved geometry, but may, in reality, consist of polygonal faces due to their manufacturing process or damage they have sustained. Common examples of such geometry are 3-D printed objects. The model could

also be used to approximate the motion of actual curved surfaces where the Lagrange multiplier method would be difficult to use or require undesired limitations or assumptions. The rocking model introduced in the previous chapter may be used with any geometry of body and does not require that the curved surfaces have simple algebraic expressions. Instead, as discussed in Chapter 3, any geometry described by a set of polygonal faces can be handled by the model. The equations of motion are reduced to a set of active DOFs eliminating drift, and the discontinuity between curved surfaces or concave portions of irregular bodies are automatically handled through the impacts and transitions between patterns described in the previous chapter.

4.3 Examples of the Dynamics of Objects with Curved Geometry

The following examples will consider the dynamics of various objects with curved surfaces to determine the accuracy by which their rolling motion can be described with a pure rocking model. New explanations for several interesting dynamic phenomena will be provided.

4.3.1 Example 1: Right Prisms with Regular Polygonal Bases Subjected to Sinusoidal Pulses

The first example examines the effect of the base geometry on the stability of right prisms with regular polygonal bases subjected to ground motions. Seven polyhedral solids resembling cylinders were considered with various bases consisting of regular polygons with $4n$ sides where n is any integer resulting, for this example, in shapes varying from square to 1024-gon. Figure 4.5 shows the different base configurations for each object. Every base was circumscribed by the same circle with diameter of 1 m and given a total height of 3 m. STL files for each of these geometries are provided in the supplemental material:

square: S4.1; octagon: S4.2; dodecagon: S4.3; 16-gon: S4.4; 20-gon: S4.5; 24-gon: S4.6; 1024-gon: S4.7. The support moves with a horizontal acceleration defined by the sinusoidal pulse of exactly one cycle with amplitude A and frequency ω:

$$\ddot{x}_g = \begin{cases} A \sin \omega t, & \text{if } 0 \leq t \leq \frac{2\pi}{\omega} \\ 0, & \text{if } t > \frac{2\pi}{\omega} \end{cases} \tag{4.5}$$

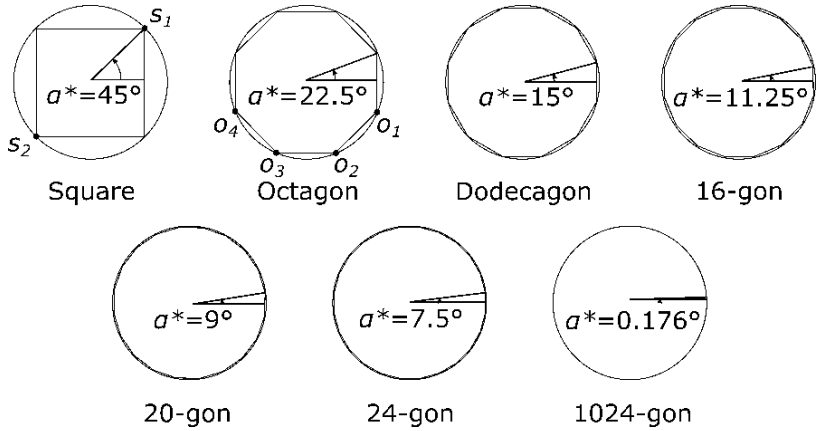


Fig. 4.5. Polygonal base configurations with α^* defined for bodies tested with ground accelerations.

4.3.1.1 Unidirectional Sinusoidal Pulses

For the first example, the support accelerates in a single horizontal direction that makes an angle α with the X-axis. The bodies are originally placed so that the axes fixed on the body are parallel to the Cartesian axes and the X-axis bisects an edge of the base at a right angle. The angle α^* for each base is the angle between the X-axis and the vector from the center of the circle to the nearest vertex of the polygon as shown in Figure 4.5.

Sinusoidal pulses with frequencies ranging 0.5 to 4.5 Hz and amplitudes ranging $0.1g$ to $6g$, where g is the acceleration of gravity, were applied to each of the objects at an angle defined by a fraction of α^*. Three general results can occur: the body can never exit SP and thus survive, the body can begin rocking but eventually come to rest with an SP

pattern which is also defined as survival, or the body can begin rocking and topple, i.e., one of the vertices initially above the centroid would impact the support, which is defined as failure. The results are presented in stability diagrams, where the frequency ω is varied in the horizontal axis and the amplitude A in the vertical axis. For each pair of (ω, A) the survival of failure of the body is recorded. In Figure 4.6, points that correspond to the limits between the areas of survival and failure are indicated with a scatter mark. For $A = 0$ the body always survives.

Figure 4.6 shows the results for the ground translating in the directions $\alpha = 0$, $\alpha = \alpha^*$, and $\alpha = 0.99\alpha^*$. As all of these polyhedra have symmetry about every plane connecting the midpoints of diametrically opposite edges of their base, when $\alpha = 0$ the force applied is exactly perpendicular to an edge of the body. When the force is strong enough to induce rocking, this results in PR2 about this edge which will either result in direct toppling or a surface impact when the body falls back to its initial orientation. In the latter case, the edge parallel to the initial rocking edge on the opposite side of the base is then engaged in PR2. Thus, this pulse results in planar rocking about these two edges for every polyhedron up to the 1024-gon. From Figure 4.6a, it can be seen that the stability diagrams essentially converge for a 24-gon compared to a 1024-gon for $\alpha = 0$. This is expected as the distance between the rocking edges increases at a much slower rate as the number of sides in the polygon increases and approaches the diameter of the circle at 1 m.

A similar symmetry exists for $\alpha = \alpha^*$ as it does for $\alpha = 0$ as the object also has symmetry about the vertical plane connecting any vertex to its antipodal vertex. An example of such a plane would makes the angle $\alpha = \alpha^*$ with the X-axis. As a result, for $\alpha = \alpha^*$ the body will still experience planar rocking. The results for the square and 24-gon for $\alpha = \alpha^*$ are provided on Figure 4.6a and converge to the result of the 1024-gon at $\alpha = 0$. However, note that for the square the distance between the antipodal points, s_1 and s_2 in Figure 4.5, is significantly larger than the distance between the midpoints of the opposite edges with respect to which the body rocks when $\alpha = 0$, and the inertial properties of the body

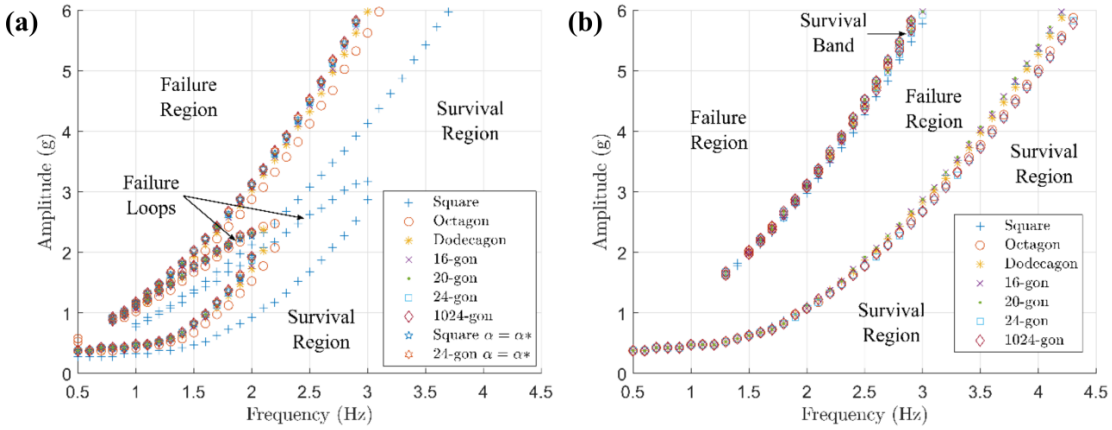


Fig. 4.6. Stability diagrams for various base configurations and angles of application α. a) $\alpha = 0$ with selected $\alpha = \alpha^*$. b) $\alpha = 0.99\alpha^*$.

perpendicular to the rocking plane are also different. Those differences become smaller when the number of vertices is increased.

Figure 4.6b shows the results when a pulse is applied at $0.99\alpha^*$. It should be noticed that the results between Figure 4.6a and Figure 4.6b are significantly different. Notice in this instance that there is a much greater area of (ω, A) pairs that correspond to failure for each of the polyhedra. The upper scatter marks labeled "Survival Band" in Figure 4.6b correspond to a narrow band of pulses for which the object survives the pulse. All other regions above the lower line of scatter marks result in failure for the object. The primary difference between the $\alpha = 0$ or $\alpha = \alpha^*$ cases compared to the $\alpha = 0.99\alpha^*$ cases is the presence of 3-D rocking motion. The 1% change in angle results in 3-D rocking rather than planar rocking and does not result in a surface impact which would require all base points to impact the support simultaneously. Instead, the body impacts from PR1 with a line impact that involves its nearest vertex. This pattern is repeated again in later impacts with the body appearing to roll about its rim making successive line impacts from one vertex to the next. This can be visualized by the octagon in Figure 4.5 where successive impacts would be made on points o_1 to o_4 along the rim. These PR1 impacts resulting from rolling motion cause much less energy to be lost than surface impacts due to the smaller effective width measured by the distance between the pre- and post-impact rocking vertices. This results in

the body overturning for many more pairs of amplitude and frequency as Figure 4.5 shows. This rolling motion corroborates Srinivasan and Ruina (100) who also noted the rolling, about the rim of a cylinder's base.

These results show the importance of considering a 3-D rocking motion for these objects opposed to 2-D. The results for $\alpha = 0$ and $\alpha = \alpha^*$ are a special case in which the body remains in a planar motion. However, this requires a unidirectional pulse that is perfectly aligned with an axis of symmetry for the body; a more general bidirectional pulse, or a unidirectional pulse that is not perfectly aligned with a plane of symmetry would likely cause a body to rotate out of plane, and may lead to a less stable motion for a polyhedron with several vertices as shown on the right of Figure 4.6. As an earthquake ground record is not in practice purely unidirectional or perfectly aligned with the geometry of a body, it is vital to consider the less stable configuration of the body produced by considering 3-D motion.

4.3.1.2 Sinusoidal Pulses with Variable Direction

The nonconservative results of 3-D rocking motion compared to 2-D were demonstrated in the previous example where, for polygonal bases with a large number of vertices, planar rocking would be an unlikely scenario. This observation would also be applicable to objects with curved edges such as cylinders. Any deviation of the cylinder from the perfect axisymmetric form, e.g., machining the cylinder as a 1024-gon, or a deviation of the load from being perfectly uniaxial would result in rolling rather than rocking as demonstrated in Figure 4.6b.

The observation of rolling agrees with the findings in (100) for the case of free vibrations of a cylinder. Recently models for cylinders (110) have studied their response using only two independent DOFs, which would suggest that the problem can be described using only two independent generalized coordinates. To test this, a second set of examples was devised to test the response of the 1024-gon, representing a cylinder, subjected to a pulse

that changes direction over time. In this case, a sinusoidal ground acceleration pulse is again implemented with the same form as equation (4.5), but the direction of application of the pulse is changed linearly with time as $\alpha(t) = \frac{90^\circ}{\tau}t$ where t is the time since the start of the pulse in seconds and τ is the period of the pulse in seconds. This results in ground accelerations in the X and Z directions given by:

$$\ddot{x}_g = \begin{cases} A \sin \omega t \cos \alpha(t), & \text{if } 0 \leq t \leq \frac{2\pi}{\omega} \\ 0, & \text{if } t > \frac{2\pi}{\omega} \end{cases} \quad \ddot{z}_g = \begin{cases} A \sin \omega t \sin \alpha(t), & \text{if } 0 \leq t \leq \frac{2\pi}{\omega} \\ 0, & \text{if } t > \frac{2\pi}{\omega} \end{cases} \tag{4.6}$$

The pulse ends at $t = \tau$ when it reaches the 90° angle. In the following example, a pulse with frequency 4 Hz and amplitude 1.04g is applied to both the 1024-gon and the 24-gon which was circumscribed by the same circle in order to draw conclusions regarding the response of prisms with different numbers of vertices and edge widths. Both have the initial conditions $\alpha = \phi = \psi = \theta = 0$ and the 1024-gon has initial centroid location X_{oc} = -8.98 m, Y_{oc} = 1.5 m, and Z_{oc} = -2.4 m, while the 24-gon has X_{oc} = -7.95 m, Y_{oc} = 1.5 m, and Z_{oc} = -9.04 m.

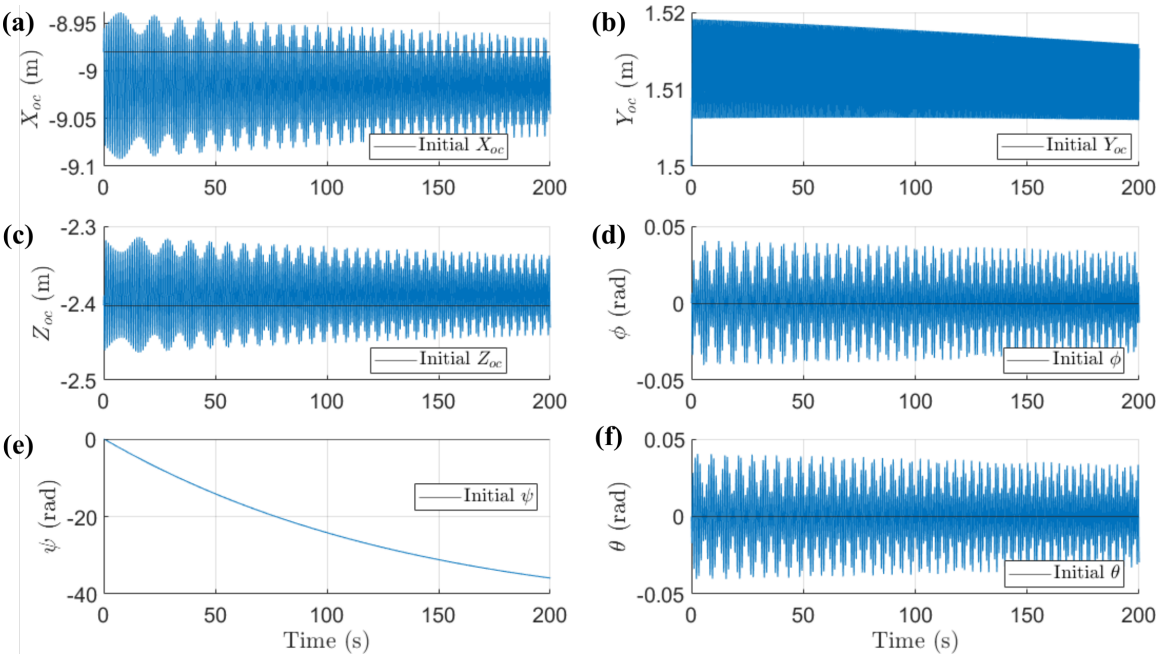


Fig. 4.7. Time history of 1024-gon with variable-direction sine pulse applied.

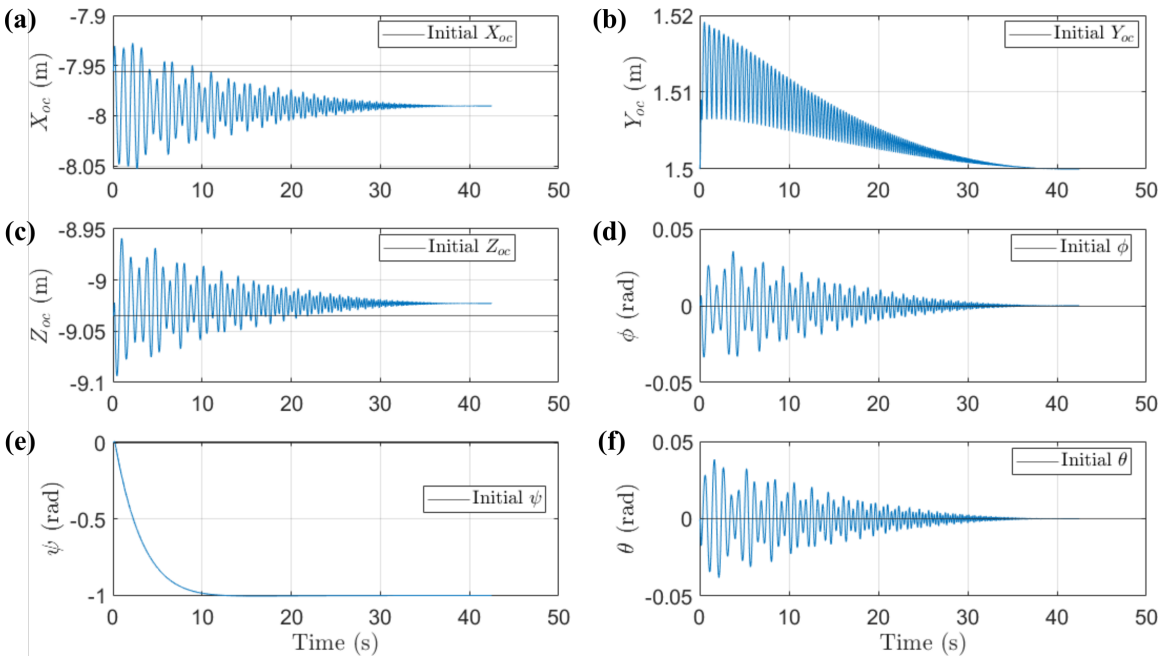


Fig. 4.8. Time history of 24-gon with variable-direction sine pulse applied.

Figure 4.7 shows the time history for the 1024-gon for the first 200 seconds of its motion and Figure 4.8 shows the time history of the 24-gon's motion as it survives the pulse, returning to rest on the same face in contact with the ground at $t = 0$. The 1024-gon is expected to survive the pulse as well but loses energy very slowly as the effective width between its vertices is much less than that for the 24-gon. Neglecting energy losses due to the cylinder or the ground being deformable and air resistance, a cylinder should not lose any energy during its motion and the result of the 1024-gon shows this trend toward no energy loss.

Even in these instances where the objects survive the pulse, the time history provides notable insight into the motion of the object. Of particular note is the time history for ψ which decreases over time for both objects and eventually attains its final value when the object comes to rest. The difference in the initial and final values of ψ represents a permanent twist that occurs for the body. Even when sliding is neglected in this model and the 1024-gon effectively rolls about its rim, it does not have equal final and initial values of ψ. Additionally, the final SP position of the object is different from its initial

position as seen from the residual displacements for X_{oc}, Z_{oc}, and ψ on the time histories on the left side of Figure 4.7 and Figure 4.8. Those findings agree with observations made about purely rolling cylinders in (100). Hence, the additional constraints assumed in (110), which would require that the twist of the body with respect to the vertical axis is zero and that the body must return to its original position when it comes to rest, are not satisfied. Such additional constraint equations would correspond to further mechanical constraints that would need to be applied to the cylinder and would not occur in the case of a cylinder rolling on a horizontal surface with an infinitely high coefficient of friction. Thus, the above time histories indicate an important result which proves the importance of studying the rocking motion of free-standing objects with three independent DOFs opposed to two, especially as it becomes easier for the object to roll about its rim such as in the case of a cylinder.

Thus, for free-standing rocking objects such as those studied here, the assumptions that they would only move with two independent DOFs and have no residual displacement for ψ are not valid. A model that fully considers 3-D motion should be used to study the dynamics of such objects due to earthquake or other forms of ground acceleration.

The planar motion for most of these polyhedra or a cylinder is a special and theoretical case that would be very unlikely to occur in practice. Thus, the motion of a cylinder, or even other more block-like geometries such as a rectangular prism with a square base, cannot, in reality, and should not, in modelling, be constrained to 2-D motion as this assumption is nonconservative.

Additionally, the similarity of the 24-gon to the results given by the 1024-gon, as far as their survival or failure of given pulses, shows the strong potential to adequately approximate the dynamics of bodies with curved geometries using polyhedral approximations of modest resolution and drastically decrease the computational time required to run simulations.

Finally, the results from the pulse with changing direction demonstrate that previously made assumptions, such as the cylinder returning to its original configuration after the

ground motion is over, would not be satisfied by only assuming high coefficients of friction, i.e., the body experiencing pure rocking or rolling on a horizontal surface, and therefore such a result would require additional mechanical constraints to be imposed. The residual displacements and twist prove the importance of considering their 3-D motion with three independent DOFs validating the observations made for cylinders in (100).

4.3.2 Example 2: Further Investigation of a Cylinder Under Free Vibration

In a similar manner as in (100), the motion of another cylinder will be examined when it is "flicked", or set into motion by hand from an unstable equilibrium such as that shown in Figure 4.9, so that the base of the cylinder impacts the ground and rotates in the approximately opposite direction of its initial tilt. Srinivasan and Ruina examined the motion of a cylinder which was released with only a ω_x component and showed that the cylinder has an out-of-plane response.

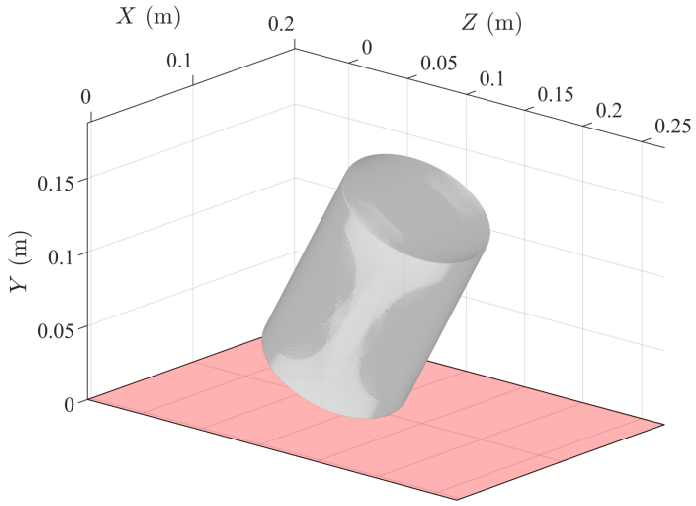


Fig. 4.9. The initial position of a solid cylinder with radius 0.051 m and height of centroid 0.069 m. Initial conditions: $\phi = \pi/6$ rad, $\psi = 0$, $\theta = 0.0812$ rad, $\dot{\phi} = -5$ rad/s, $\dot{\psi} = \dot{\theta} = 0$. (a) Euler angles in rad. (b) Displacement of centroid in m. (c) Euler angle time derivatives in rad/s. (d) Translational velocity of centroid in m/s.

To begin the study, an STL file of a solid "cylinder", derived from a 1024-gon inscribed

in a circle of 0.051 m and extruded to a height of 0.138 m, the same dimensions as the cylinder used in (100), was created using AutoCAD and imported into the model. The STL file of this cylinder is provided in STL File S4.8 in the supplemental material. The cylinder is given initial conditions: $\phi = 0.524$ rad, $\theta = 0.0812$ rad, and $\psi = 0$ rad as shown in Figure 4.9 and the velocities: $\dot{\phi} = -5$ rad/s and $\dot{\psi} = \dot{\theta} = 0$ so that ω_x tends to reduce ϕ. The initial velocities given to the cylinder are perpendicular to its expected plane of motion. The non-zero initial θ is given to signify the human error with which the object would initially be released in the experiments of (100). Due to the symmetry of the 1024-gon, if the initial θ is not given a slight difference from zero, the object would experience surface impacts and planar rocking due to its symmetric polyhedral geometry about the X-axis. This would lead to a faster loss of energy and greater overturning resistance as described in (27).

When the cylinder is released with these initial conditions, it results in the time history given in the following Figure 4.10.

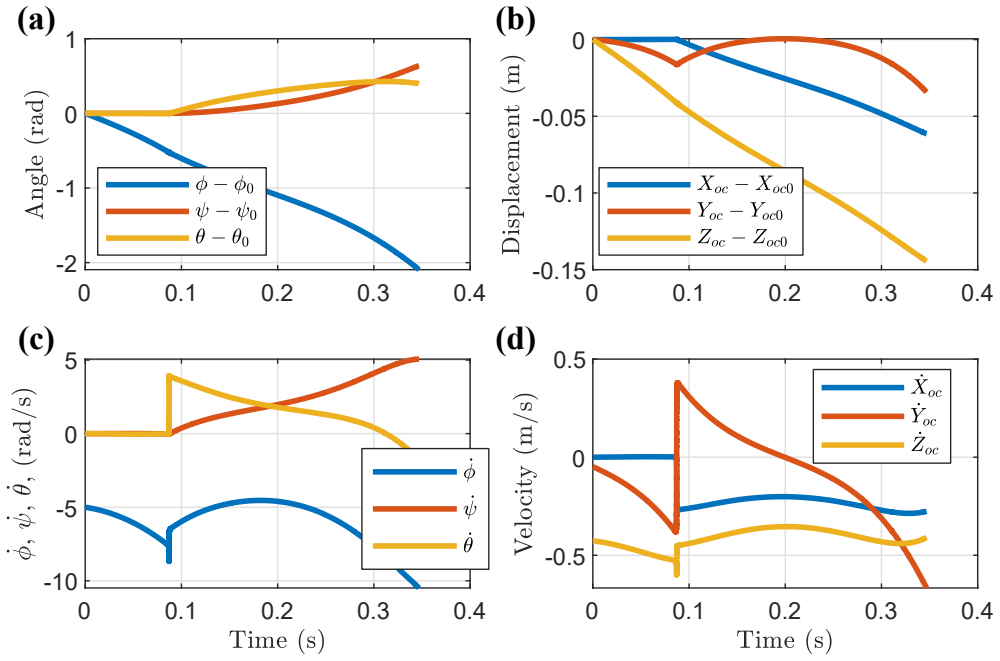


Fig. 4.10. The time history for a solid cylinder with radius 0.051 m and height of centroid 0.069 m. Initial conditions: $\phi = \pi/6$ rad, $\psi = 0$, $\theta = 0.0812$ rad, $\dot{\phi} = -5$ rad/s, $\dot{\psi} = \dot{\theta} = 0$. a) Euler angles in rad. b) Displacement of c in m. c) Time derivatives of Euler angles in rad/s. d) Velocity of c in m/s.

Videos of the cylinder's motion during this simulation are provided in full speed and slow motion in Video S4.9 and Video S4.10 respectively in the supplemental material. Both a side view and top view of the cylinder are included in these videos so the 3-D response of the cylinder can be easily visualized. The cylinder does not display a planar motion as would be expected for a cylinder that is macroscopically set in motion with an angular velocity perpendicular to its plane of motion, but instead shows significant out-of-plane motion. The centroid veers from its initial direction of motion as can be seen by X_{oc} and $\dot{X}_{oc}$ in Figure 4.10. Notice also the residual change in ψ, measured as the angle between the vector from the bottom to the top of the cylinder along its axis of symmetry and the vector $\mathbf{e}_z$, at toppling is 216.6° indicating an offset of 36.6° from the 180° one might expect for a perfect cylinder to experience. Further, after observing many simulations for θ on the interval [0, 0.0812 rad], the cylinder varies a maximum of 0.5° from 216.6° as long as the cylinder does not experience a surface impact. This reinforces the finding of (100) that the change in ψ is independent of the initial velocity of the cylinder.

Srinivasan and Ruina (100) predict residual angles of ψ for this cylinder as 202° for pure rolling and 220° for pure sliding. These predictions are derived from equations independent of the cylinder's exact initial conditions. As long as the cylinder displays the near surface impact behavior that it does here, its residual angle of ψ will be within 0.5° of that shown here. However, during experiments with the cylinder, Srinivasan and Ruina found a residual angle of 213° and 218° depending on whether the cylinder toppled to the left or right. This slight asymmetry is presumed to be caused by small geometric or mass deformities in the experimental cylinder. Interestingly, the residual angle resulting from the pure rocking model (216°) is within the ranges predicted by Srinivasan and Ruina and the tighter range of the experimental results. However, given apparent imperfections in the experiment, the accurate theoretical result of the cylinder's dynamics is not certain.

To better understand the motion of the cylinder and why it does not topple in the exact opposite direction of its initial motion, the location of the rocking vertex on the support

surface is considered. Figure 4.11 shows the location of the rocking vertex with line segments connecting successive rocking vertices.

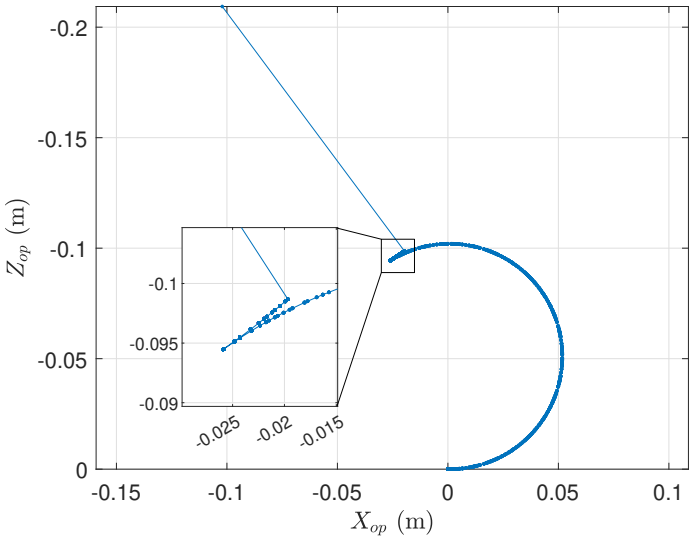


Fig. 4.11. The location of the rocking vertex throughout the motion of the solid cylinder with radius 0.051 m and height of centroid 0.069 m. Line segments connect successive rocking vertices. The initial rocking vertex is set to $X_{op} = Y_{op} = 0$. Initial conditions: $\phi = \pi/6$ rad, $\psi = 0$, $\theta = 0.0812$ rad, $\dot{\phi} = -5$ rad/s, $\dot{\psi} = \dot{\theta} = 0$.

Figure 4.11 clearly shows that the majority of the rocking vertex's locus is a circular arc of about 216°. The inset plot shows another surprising aspect of this motion. As the cylinder approaches its toppled position indicated by the longest line in the plot, the residual angle ψ, $\dot{\theta}$ changes sign. This change in sign can also be seen in the time history of Figure 4.10 around $t = 0.3$ seconds. This is interesting as the location of the rocking vertex is not restricted to that of the circular arc with a radius the same as that of the cylinder's base as is assumed in other models (110).

Thus, this pure rocking model provides a new method of studying the motion of the cylinder including showing its tendency to contact the support unrestricted by the circular arc with the same radius as its base. The model's prediction of the residual ψ is very similar to the findings of Srinivasan and Ruina (100). The additional ability to view videos of the motion (Video S4.9 and Video S4.10) and visualize the location of the rocking vertex adds additional information that cannot be garnered from an experiment for such a short but

surprisingly complex motion.

4.3.3 Example 3: Euler's Disk

A stocky cylinder, known as Euler's disk, is now considered. Previous studies of Euler's disk have used an analytical model of a perfectly cylindrical disk or a two-dimensional polygonal disk (81; 17; 21). Both of these methods have their own limitations when considering a disk of finite thickness and imperfect cylindrical geometry. The perfectly cylindrical disk model cannot model a slightly imperfect disk as one would find in reality and the two-dimensional disk model cannot handle impacts across the thickness of the disk which would commonly occur for a disk released with random initial conditions. To examine both the finite thickness and potential non-circular geometry of the disk, the STL files used to represent Euler's disk in this model contain polygonal bases of lower resolution than the cylinder. The disks studied in the following examples consist of a regular polygon inscribed in a circle of radius 3.81 cm that is extruded to create a solid disk with a thickness of 1.27 cm.

4.3.3.1 The Disk Set into Spinning Motion

For the first example, a polygon with 42 sides is used to create Euler's disk. The STL file for this 42-sided disk is available in STL File S4.11 in the supplemental material. To test the dynamic response of Euler's disk using the pure rocking model introduced in the last chapter, it was given the initial conditions: $\phi = 0.26$ rad, $\psi = 0$, $\theta = 0$, $\dot{\phi} = \dot{\theta} = 0$, $\dot{\psi} = 20$ rad/s. The initial position of the disk is shown in Figure 4.12 where it was set in a spinning motion from this nearly upright position.

Figure 4.13 shows the time history of the motion of Euler's disk when released with the initial conditions described above. A video of the motion of the disk can be viewed in Video S4.12 of the supplementary material. Figure 4.13(a) gives the Euler angles in rad, (b) shows the displacement of c in m, (c) shows the time derivatives of the Euler angles in rad/s, and (d) shows the velocity of c in m/s. The change in ψ in 4.13a indicates that the disk

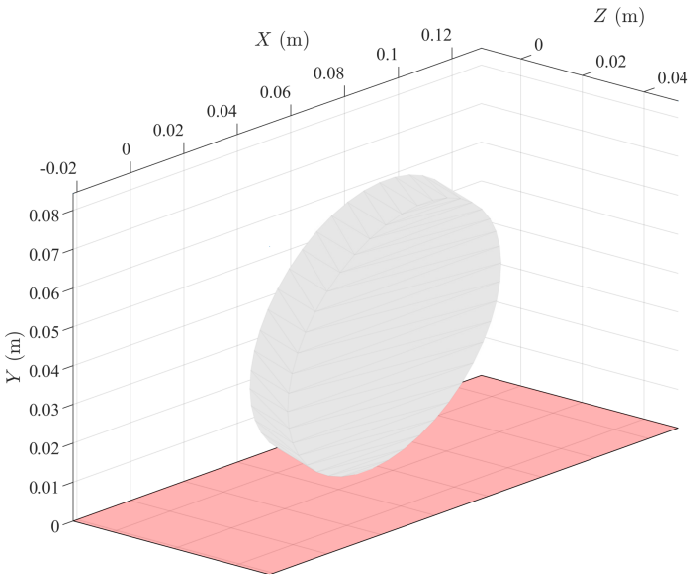


Fig. 4.12. The initial position of Euler's disk (made from a 42-gon) before being released. Initial conditions: $\phi = 0.26$, $\psi = 0$, $\theta = 0$, $\dot{\phi} = \dot{\theta} = 0$, $\dot{\psi} = 20$.

makes several complete spins just as would be expected in a rolling model or in observing an actual Euler's disk. The plot of Y_{oc} in Figure 4.13b also shows that the centroid of the disk moves toward the support over time finding its final position with its face flat on the support. From the plots for the time derivatives in Figures 4.13c and 4.13d, it can be seen that the disk all velocities converge to zero indicating that the disk loses energy over time. This reduction of energy is due to the impacts that the disk makes with the support and is an aspect of the model which cannot be examined through the perfect cylinder models described above.

Previous studies (77; 42) discussed the increasing precession rate that the disk experiences as its inclination angle with the horizontal decreases. Moffatt (77) defined this increase as a finite-time singularity, as the precession rate theoretically extends to infinity at the end of the disk's motion. This model offers a new perspective on this finite-time singularity which can be observed through the frequency of impacts experienced by the disk throughout its motion. Figure 4.14 represents each impact occurring at a specific instance by a vertical line drawn at that time instance. As the disk's centroid moves closer to the support surface, the frequency of impacts increases dramatically. The first impact occurs

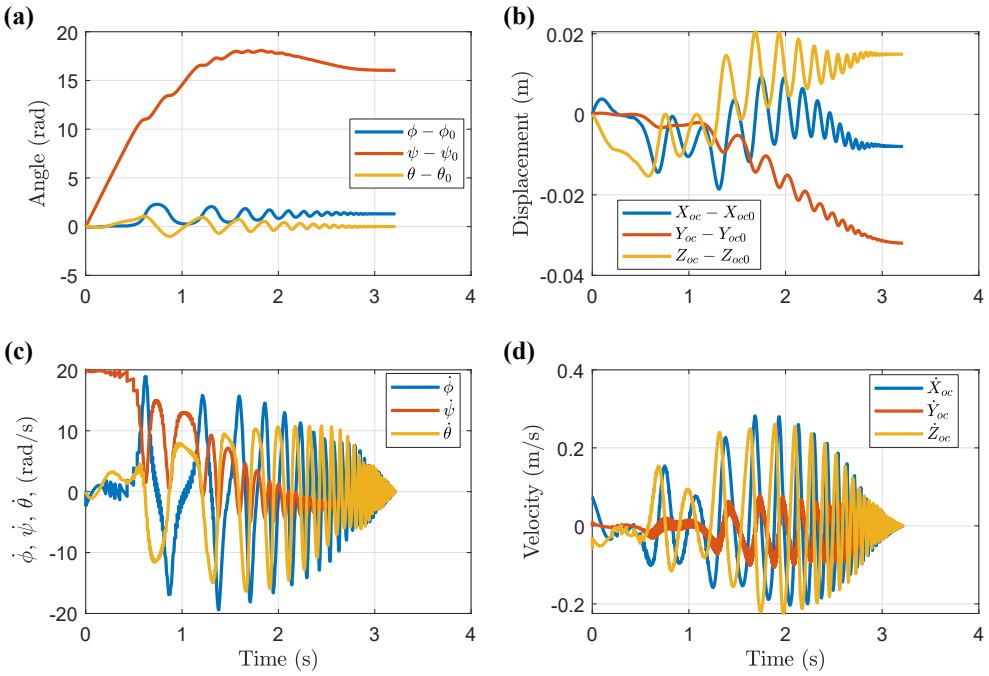


Fig. 4.13. The time history of the spinning motion of Euler's disk. Initial conditions: $\phi = 0.26$, $\psi = 0$, $\theta = 0$, $\dot{\phi} = \dot{\theta} = 0$, $\dot{\psi} = 20$. a) Euler angles in rad. b) Displacement of c in m. c) Time derivatives of Euler angles in rad/s. d) Velocity of c in m/s.

around 0.2 seconds and by 2.75 seconds, the impacts succeed each other so quickly that the gaps between them can no longer be distinguished in Figure 4.14. This dark region represents the finite-time singularity of rapid spinning motion that occurs at the end of the disk's motion as described by Moffatt (77) and Easwar et al. (42). Thus, this pure rocking model predicts a similar result as the rolling models for Euler's disk.

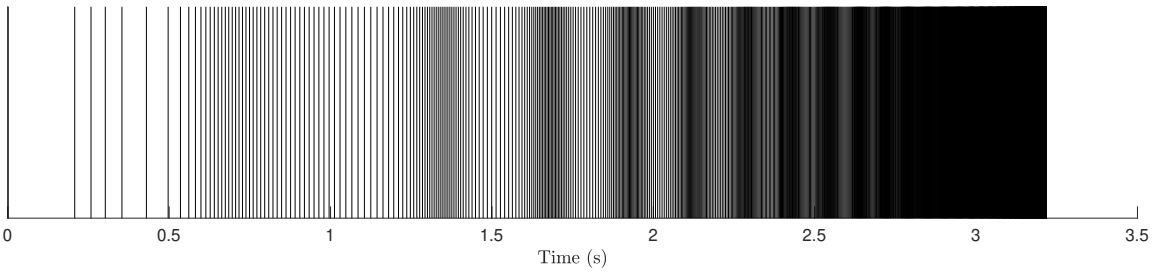
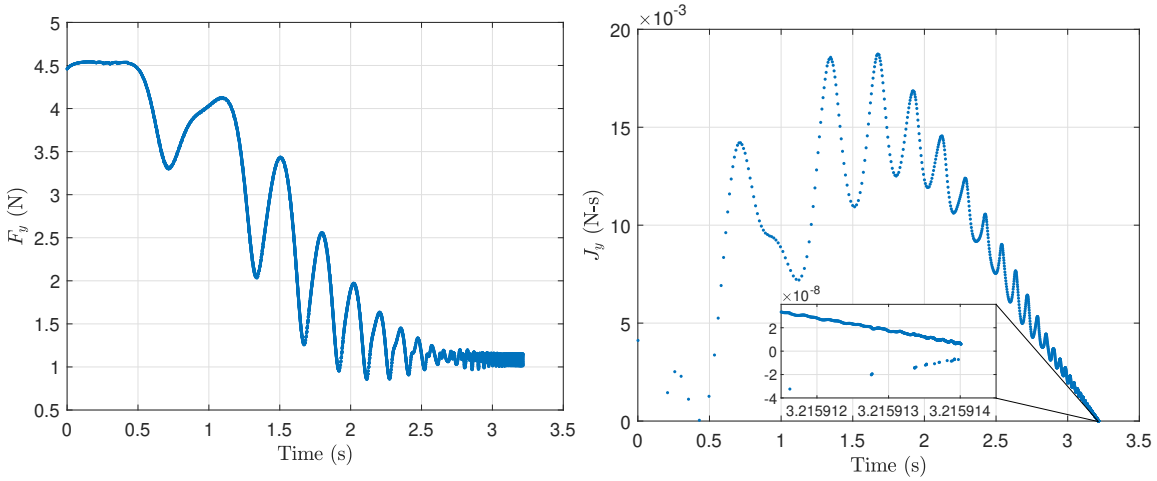


Fig. 4.14. A diagram showing the density of impacts for Euler's disk over time when released from rest. Each impact is drawn as a vertical line on the plot. Initial conditions: $\phi = 0.26$, $\psi = 0$, $\theta = 0$, $\dot{\phi} = \dot{\theta} = 0$, $\dot{\psi} = 20$.

In addition to the finite-time singularity, this pure rocking model also sheds light on

another notable aspect of Euler's disk. Borisov et al. (22) showed experimentally that, at the end of the disk's motion, the disk actually loses contact with the support (free flight) and that this may be integral in stopping its motion and breaking the finite-time singularity. No mathematical model for this loss of contact is provided by Borisov et al., but other researchers offer explanations for it. For example, Kessler and O'Reilly (62) posited that the disk enters free flight at a very small inclination angle due to deformations in the disk and the surface. To more closely examine the end of the motion and the disk's tendency to enter free flight, the vertical reaction force F_y and the vertical impulse J_y are recorded over time for each time instant of rocking and impact respectively. The results of these values are provided for F_y in Figure 4.15a and for J_y in Figure 4.15b.



(a) F_y during rocking

(b) J_y at each impact

Fig. 4.15. Plots of the vertical reaction force F_y and the vertical impulse J_y for the spinning Euler's disk.

The vertical force is initially similar to the weight of the disk, 4.55 N, but as it continues spinning, F_y slowly decreases in magnitude until it oscillates around 1.2 N (about 25% of the disk's weight) in its final stages of motion. Also, F_y and J_y do not reach their peak values at the same time. F_y is greatest at the beginning of its motion as the disk is nearly upright but J_y peaks as the norm of the translational velocity of c reaches its maxima as can be seen in Figure 4.13.

The inset of the last 3×10^{-8} seconds of motion shown in Figure 4.15b offers an explanation for the loss of contact observed in (22). J_y first becomes negative in the last moments of its motion, indicating that at this impact the disk would actually lift off the support into free flight. Because the pure rocking model prohibits free flight, rocking is forced to continue, and the frequency of impacts with $J_y < 0$ increases as the disk loses energy. At the time of these impacts, Y_{oc} is less than 1×10^{-9} m greater than it is when the disk is lying flat on the support and thus the position of the disk is very near its final position. At this crucial time, which is neglected by other rigid models, this rocking model shows the potential for the disk to enter free flight following an impact. The presence of negative J_y shows further that irregularities, or manufacturing that leads to the disk having polygonal faces, e.g., 3-D printing, can cause free flight. In the case of Euler's disk, it is only a matter of time before one of the impacts causes it to enter free flight, which has been postulated as the reason the disk abruptly halts its motion (62). Though this final pattern of free flight cannot be considered in more detail with a pure rocking model, it is hypothesized that free flight will cause a faster rate of energy loss potentially due to a non-adjacent vertex to the rocking vertex impacting the support.

Another interesting phenomenon of Euler's disk is the sound that it makes, particularly noteworthy due to its increase in frequency as its inclination angle with respect to the horizontal decreases. Several explanations have been offered as to what creates the sound. Saje and Zupan attribute it to a normal force that periodically increases and decreases (91). This is plausible given the oscillations of increasing and decreasing values of F_y from Figure 4.15a. Kessler and O'Reilly consider that the disk and the support surface are deformable and vibrate to create the sound (62). This chapter offers a new theory for the sound based on the frequency of impacts throughout the disk's motion, tying the sound of the disk to the increasing frequency of its precession rate in a new way. The audio of Video S4.12 was produced from Matlab's audiowrite function with sampling frequency of 23000 Hz. At the nearest sampled time instance to the instance of an impact, t_{im}, the value of the voltage

signal sent to the speakers is set to 1 volt. The audiowrite function then produces a file with a discrete impulse-like signal of 1 volt sent to the speakers at each impact time and no voltage at other times. The increasing frequency of the disk's spinning and consequent increasing speed of impact can be heard in the resulting sound data. Though it is not the same frequency or timbre as the actual sound produced by Euler's disk, it is qualitatively similar as it increases in frequency, particularly noticeable as the disk comes to the end of its motion. This offers a potential explanation for the sound produced by Euler's disk, if the disk is assumed to have non-smoothness due to imperfections in the manufacturing process or due to damage.

After many simulations for different initial conditions of the 42-sided disk are considered, it is clear the model of the disk comes to rest much quicker than an actual disk due to the rough polyhedral approximation and the loss of energy due to impacts. The 42-sided approximation of Euler's disk presented above comes to rest in only several seconds due to the energy dissipation mechanism tied to the impacts the disk makes. The greater the ratio of the distance between adjacent rocking vertices to the total height of the object, the more energy is lost in each impact and thus the faster the decay of energy for the disk. One of the defining features of a physical Euler's disk is its surprisingly long duration of motion when set in a spinning motion. The duration of the model's response can be extended to come closer to that of the actual disk by two means: increasing the number of vertices and changing the point of application of the impulse at impact.

To examine the relationship of the distance between vertices and the length of free vibration, STL files representing Euler's disk made from polygons of 32, 64, 128, and 256 vertices inscribed in a circle with a radius of 3.81 cm were created and released with the same initial conditions as the 42-sided disk ($\phi = 0.26$ rad, $\psi = \theta = 0$, $\dot{\phi} = \dot{\theta} = 0$, $\dot{\psi} = 20$ rad/s). The point of application of the impulses are also varied via λ_{ab}, and the dynamic response time, computational time, and time history are recorded for analysis. The simulations were run on an Intel(R) Core(TM) i7-7700 CPU @ 3.60 GHz with four cores.

Table 4.1 provides a summary of this data for each of the STL files. The STL files for each representation of the disk are provided in the supplementary material: 32 sides: STL File S4.13; 64 sides: STL File S4.14; 128 sides: STL File S4.15; 256 sides: STL File S4.16.

Table 4.1. Computational Time for Different STL Files

Number of Sides	λ_{ab}	Duration of Dynamic Response	Computational Time
32	0	2.1 s	1.7 min
32	0.40	10.8 s	9.6 min
32	0.43	15.3 s	14.9 min
32	0.45	20.8 s	23.9 min
64	0	4.2 s	8.1 min
128	0	8.4 s	36.0 min
256	0	16.8 s	196.3 min

From Table 4.1 it can be seen that for $\lambda_{ab} = 0$, meaning all impulses are applied at the post-impact rocking vertex, the number of vertices in the polygonal/polyhedral representation is directly proportional to the duration of the dynamic response. However, the computational time required for each run increases at a much greater rate. For each doubling of the number of vertices, the computational time to complete the run increases by a factor of more than four. To obtain a simulation where the disk continues its motion for a long duration with a lower computational cost, a disk with less vertices but different λ_{ab} is used. By increasing λ_{ab} to 0.43 for the disk with 32 sides, the duration of the dynamic response can be extended to be close to that of the 256-sided disk but keeps a computational time of less than 8% of the time for the 256-sided disk with $\lambda_{ab} = 0$. The increase in λ_{ab} reduces the effective distance between the rocking vertices during impact by moving the location of the impulse at impact, and thus causes less energy loss for each impact. The time histories of the six states are provided in Figures 4.16 and 4.17 for the 32-sided STL with $\lambda_{ab} = 0.43$ and the 256-sided STL with $\lambda_{ab} = 0$ respectively, showing the similarities and differences in the response of the two disks. Computer animations of the motion of the 32- and 256-sided disks with audio produced by the method described above are provided in Video S4.17 and Video S4.18 respectively. As can be seen from the videos, both STLs provide a visually

plausible motion, i.e., an observer would be unable to determine which motion is closer to that of a physical disk.

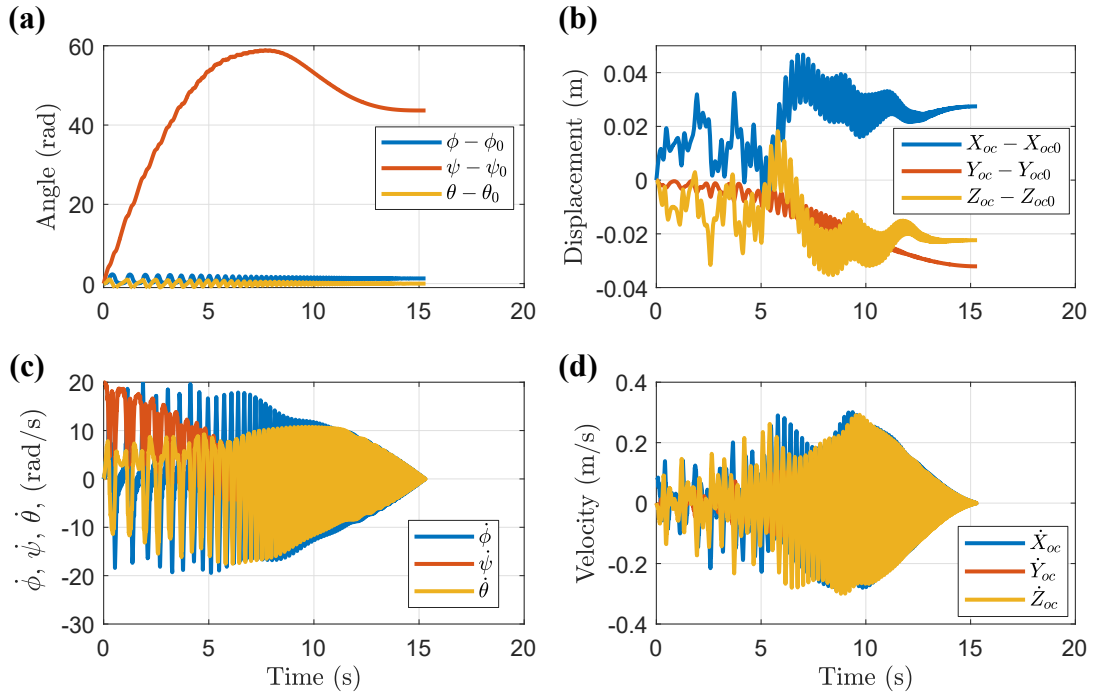


Fig. 4.16. A plot of the time history for the 32-sided STL of Euler's disk. Initial conditions: $\phi = 0.26$, $\psi = \theta = 0$, $\dot{\phi} = \dot{\theta} = 0$, $\dot{\psi} = 20$. a) Euler angles in rad. b) Displacement of c in m. c) Time derivatives of Euler angles in rad/s. d) Velocity of c in m/s.

Comparing Figure 4.16 and Figure 4.17, the 256-sided STL has a slightly longer dynamic response than the 32-sided STL with $\lambda_{ab} = 0.43$. This gap could be completely closed by further tuning λ_{ab} to match the duration of the 256-sided STL. Instead of trying to calculate the λ_{ab} that would result in the exact same duration of motion, the results of Figures 4.16 and 4.17 will be discussed as they are. The Euler angles and their velocities in Figures 4.16a, 4.16c, 4.17a, and 4.17c are similar throughout either disk's motion. The magnitudes of the translational velocities in Figures 4.16d and 4.17d are also similar, however, there is a slight difference in the horizontal trajectory of the centroid for each disk as seen by X_{oc} and Z_{oc} in Figures 4.16b and 4.17b. The two disks are on similar paths until somewhere in the range of 5 to 7 seconds, where X_{oc} increases over time for the 32-sided STL but decreases for the 256-sided STL. Z_{oc} also shows a similar divergence around this time, decreasing for

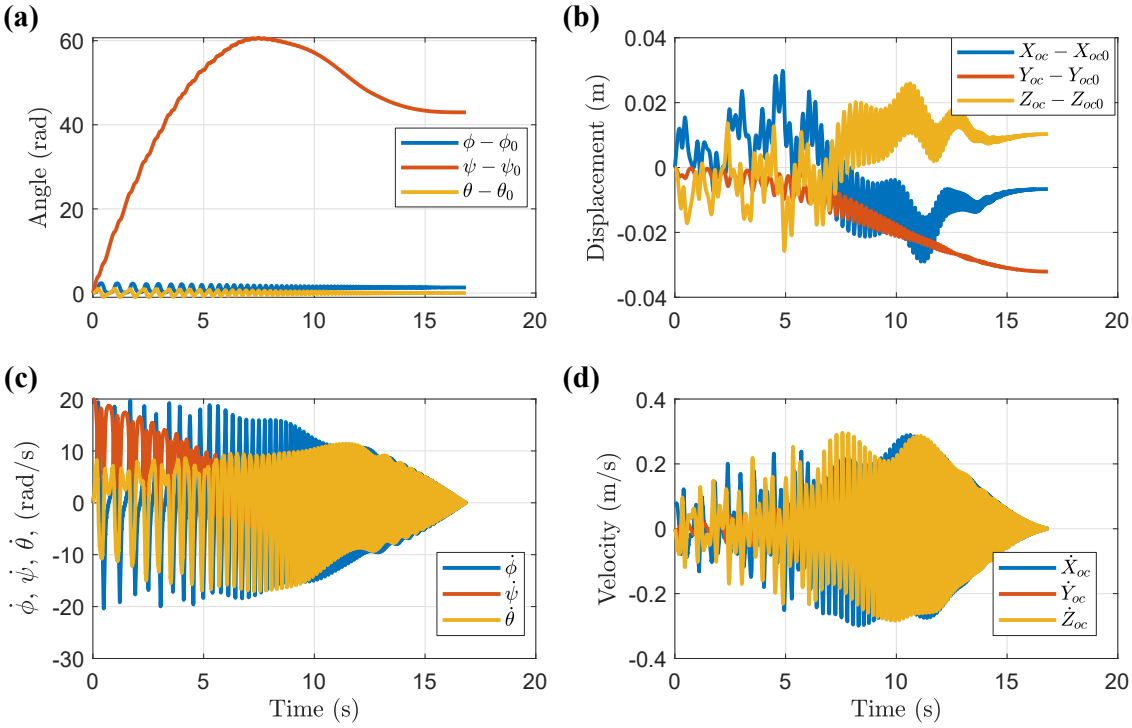


Fig. 4.17. A plot of the time history for the 256-sided STL of Euler's disk. Initial conditions: $\phi = 0.26$ rad, $\psi = \theta = 0$, $\dot{\phi} = \dot{\theta} = 0$, $\dot{\psi} = 20$ rad/s. a) Euler angles in rad. b) Displacement of c in m. c) Time derivatives of Euler angles in rad/s. d) Velocity of c in m/s.

the 32-sided STL but increasing for the 256-sided STL. This divergence can be attributed to the differing geometry between the STL files. Overall, the two responses of disks with substantially different numbers of vertices produce a qualitatively similar response and a similar duration of motion.

This example provides two important results. The first is the observed difference in the duration of the dynamic response for a disk with various numbers of sides when λ_{ab} remains constant. The second is the ability to tune the motion of a coarse representation of the disk to match that of a finer representation by increasing λ_{ab}. This has proven to be qualitatively possible and to offer the additional benefit of a 90%+ reduction in computational time. These findings could be exploited in computer animation to produce a visually accurate motion for a rolling or spinning object with irregular curved geometry at a lower computational cost than considering a much finer mesh or a deformable model.

4.3.3.2 The Disk Released from Rest

Like the cylinder presented previously, Euler's disk is also expected to display an out-of-plane response even when it released from rest in an unstable PR1 position so that an angular velocity perpendicular to its plane of symmetry is developed. The disk similarly experiences a near surface impact on the support like the cylinder. However, instead of the rocking vertex forming a circular arc of around 216°, the equations from (100) indicate that for a pure rolling model, the location of the disk's rocking vertices are expected to form a circular arc of more than 360° during each near surface impact it makes. To examine this motion using the model introduced in Chapter 3, the 42-sided STL is released with zero velocity from the initial position: $\phi = \pi/9$ rad, $\psi = 0$, $\theta = 0.01$ rad. This initial position is shown in Figure 4.18.

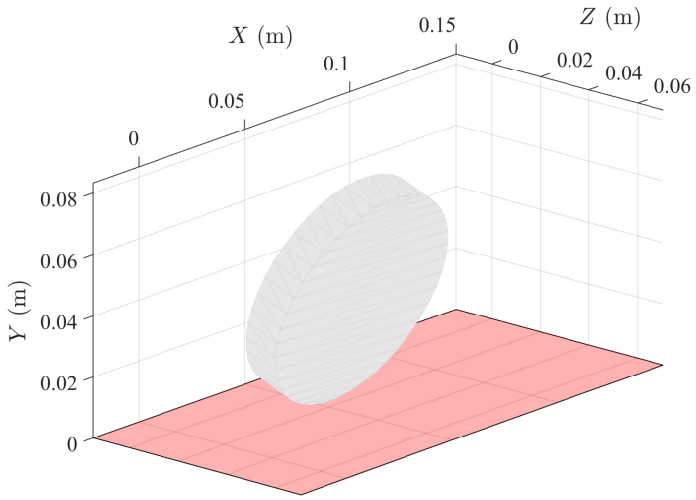


Fig. 4.18. The initial position of Euler's Disk before being released. Initial conditions: $\phi = \pi/9$ rad, $\psi = 0$, $\theta = 0.01$ rad, $\dot{\phi} = \dot{\psi} = \dot{\theta} = 0$.

After release from this position, the disk makes a series of near surface impacts on the support similar to those exhibited by the cylinder, whereby the rocking vertex changes rapidly over the short time duration of the quick succession of line impacts. The time history of the disk is shown in Figure 4.19.

As can be seen from the Euler angle time derivative plot in Figure 4.19c, the disk makes a series of impacts where these velocities change their sign rapidly and reach local maxima

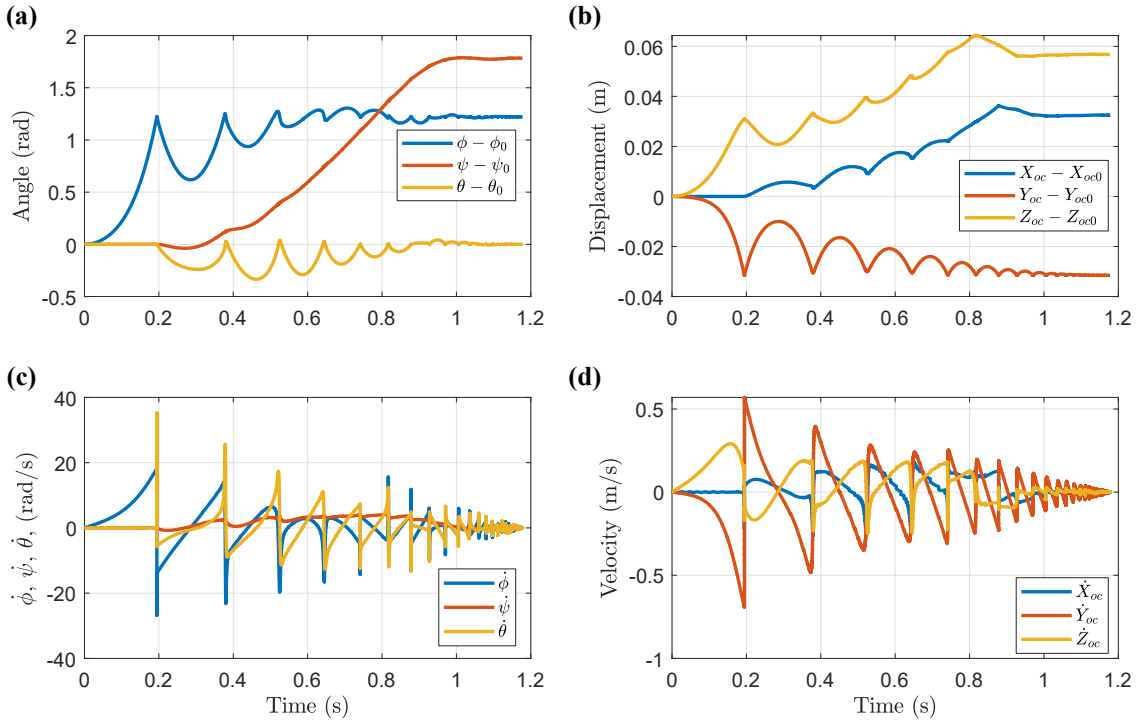


Fig. 4.19. The time history of Euler's Disk as it vibrates freely. Initial conditions: $\phi = \pi/9$ rad, $\psi = 0$, $\theta = 0.01$ rad, $\dot{\phi} = \dot{\psi} = \dot{\theta} = 0$. a) Euler angles in rad. b) Displacement of c in m. c) Time derivatives of Euler angles in rad/s. d) Velocity of c in m/s.

or minima due to the rapidly changing rocking vertex. Additionally, Figures 4.19c and 4.19d show that the magnitude of the velocities of the disk quickly decay to zero. This decay is much faster for the 42-gon than it would be for a disk with more sides as previously shown, e.g. the 1024-gon, due to the greater distance between its vertices. The 42-gon also appears to lose energy faster than an actual Euler's disk. An actual Euler's disk would be subjected to deformations in the disk and support which cause energy loss as well as impacts. Unlike some rigid body pure rolling models that would not allow for any energy loss, this pure rocking model allows for energy loss that can be tuned through the number of vertices used in the polyhedral approximation and λ_{ab}. A video of the disk's motion can be viewed in Video S4.19 of the supplemental material. The approximate motion of the disk can be visualized by casual experiment at home by releasing the cap of a large-mouth food container from a similar position. An example of such an experiment being conducted is provided in Video S4.20 and S4.21 in full speed and slow motion respectively. Note

that Video S4.20 shows instances of both the near surface impact response described in this example as well as an apparent surface impact which results in the cap losing energy much quicker which is similar to the surface impact and planar response described for the approximately cylindrical polyhedra discussed in Example 1 of this chapter.

As all the videos show, both simulation-based and experimental, the disk does not necessarily show planar rocking motion. Figure 4.20 shows the location of the rocking vertex during the first near surface impact of the disk on the support.

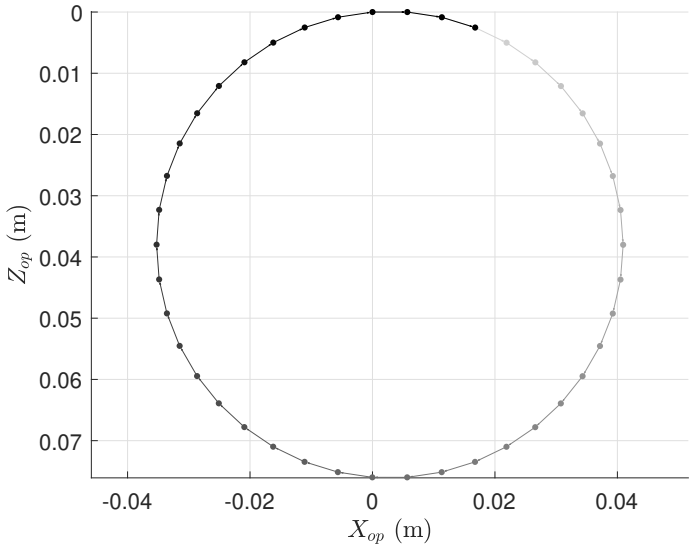


Fig. 4.20. The location of the rocking vertex for the initial near surface impact of Euler's disk around 0.2 seconds. Line segments connect successive rocking vertices and the first rocking vertex is set to $X_{op} = Z_{op} = 0$. The lines and points marking the rocking vertex locations are displayed as darker as time goes on. Initial conditions: $\phi = \pi/9$ rad, $\psi = 0$, $\theta = 0.01$ rad, $\dot{\phi} = \dot{\psi} = \dot{\theta} = 0$.

The first rocking vertex is set to $X_{op} = Z_{op} = 0$ and shows that the rocking vertex makes a full revolution around the rim of the disk and then continues for 26° for a total change of 386°. This movement of the rocking vertex by more than a full revolution can also be observed through casual experiment with the large-mouth cap in Video S4.21. Due to this 3-D response, the disk does not stay within the bounds of the circle visualized from its initial slapping motion but moves horizontally over time as illustrated in Figure 4.21.

This plot shows the movement of the disk as it initially increases both its X_{op} and Z_{op}

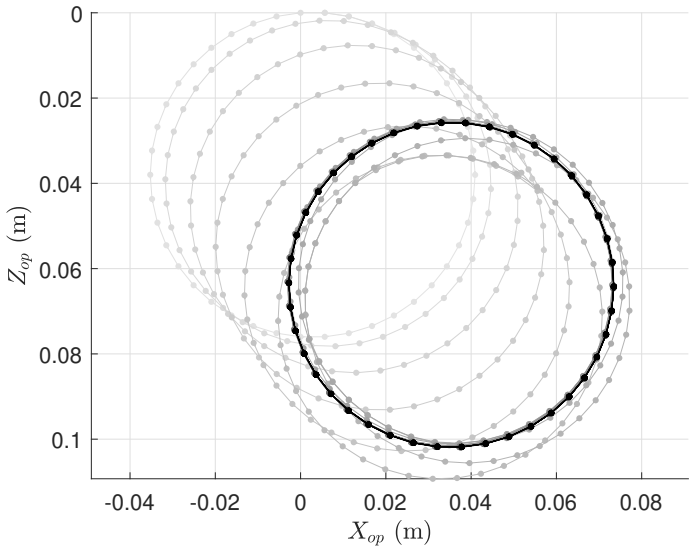


Fig. 4.21. The location of the rocking vertex for the motion of the Euler's Disk until its energy is spent. Line segments connect successive rocking vertices and the first rocking vertex is set to $X_{op} = Z_{op} = 0$. The lines and points marking the rocking vertex locations are displayed as darker as time goes on. Initial conditions: $\phi = \pi/9$, $\psi = 0$, $\theta = 0.01$, $\dot{\phi} = \dot{\psi} = \dot{\theta} = 0$.

coordinates before reversing its course and decreasing in both X_{op} and Z_{op} before coming to rest. The disk changes the direction of its movement in the horizontal plane around 0.79 seconds and this change also coincides with a reversal in the direction of the changing rocking vertex from clockwise to counterclockwise. The counterclockwise change in the rocking vertex can be seen in Figure 4.22.

The disk displays this reversal in the direction of the change of its rocking vertex at $t = 0.79$ seconds. Interestingly, this does not immediately result in $\dot{\psi}$ for the disk reversing direction but at the end of the motion, around 1.0 seconds, the direction of $\dot{\psi}$ does change briefly. It is surprising that the direction of the rocking vertex changes given the clear preference for clockwise movement at the beginning of the motion. The experimental verification of such a movement is difficult to achieve due to the speed with which the disk moves in its final stages of motion. The high velocity at which the rocking vertex changes can be illustrated through the plot in Figure 4.23 produced in the same manner as Figure 4.14.

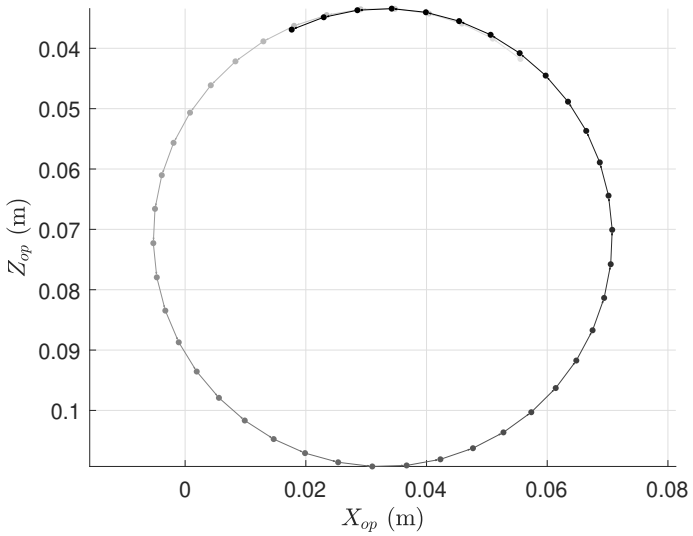


Fig. 4.22. The location of the rocking vertex of Euler's Disk from 0.79 seconds to 0.84 seconds. Line segments connect successive rocking vertices and the location of the rocking vertex at $t = 0.79$ seconds is set to $X_{op} = Z_{op} = 0$ and the lines and points marking the rocking vertex locations are displayed as darker as time goes on. Initial conditions: $\phi = \pi/9$, $\psi = 0$, $\theta = 0.01$, $\dot{\phi} = \dot{\psi} = \dot{\theta} = 0$.

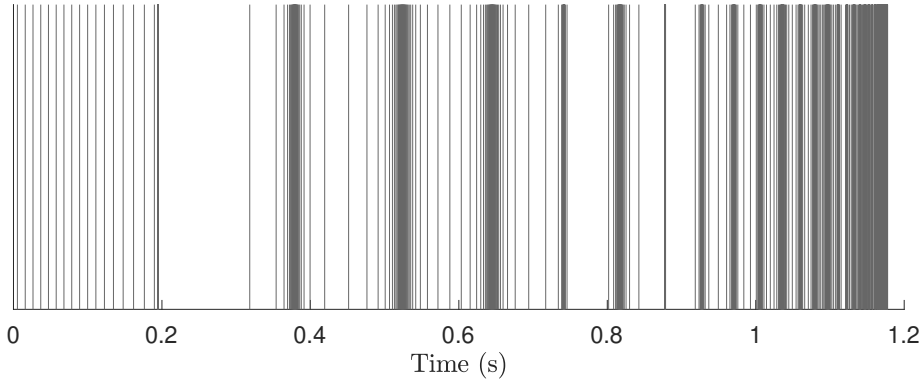


Fig. 4.23. A diagram showing the density of impacts for Euler's Disk over time when released from rest. Each impact is drawn as a vertical line on the plot. Initial conditions: $\phi = \pi/9$ rad, $\psi = 0$, $\theta = 0.01$ rad, $\dot{\phi} = \dot{\psi} = \dot{\theta} = 0$.

This plot reveals an undulating pattern of extremely fast succession impacts such as at 0.19 seconds and 0.37 seconds. Each of these thick bands represents more than 40 impacts. Notice that the first near surface impact at 0.19 seconds has a faster change in rocking vertex than most near surface impacts. An exception to this is the near surface impact occurring at 0.88 seconds. Also, the gap between successive near surface impacts decreases in duration as expected, until the gaps are indistinguishable and all that can be seen are successive

impacts shortly after 1.1 seconds showing that a disk released from rest displays a similar finite-time singularity as that shown for the disk with initial velocities as shown above.

This example shows the plausibility of a rocking and discrete impact model to describe the motion of Euler's disk. This model not only allows for rocking study of a disk, but also for the incorporation of non-cylindrical geometries which could have a significant effect on the object's motion. The model shows the ability to model the finite-time singularity for the disk and offers a new explanation for the sound produced during the motion of Euler's disk and the tendency for it to uplift from its support near the end of its motion. Finally, it has also been shown that the number of sides used to approximate the disk can be tuned through comparison with experiments so that the duration of its motion is similar to reality.

4.3.4 Example 4: The Rattleback

The rattleback, shown in Figure 4.24, has an irregular geometry which does not correspond to simple shapes such as parabaloids or ellipsoids. The geometry of this rattleback is provided in STL File S4.22 (59) which was designed in a CAD program with the purpose of being manufactured by a 3-D printer. Thus, the polyhedral geometry shown in the file is the polyhedral geometry which is theoretically produced when the rattleback is 3-D printed. While the rattleback could theoretically be studied using Lagrange multipliers as described in Section 4.2 the irregularities in the rattleback's geometry and associated constraint equations would be expected to cause significant issues with this method. To the best of the author's knowledge, previous studies of the dynamics of such an irregular geometry whether modeled with curved surfaces or polyhedra has not been conducted and is thus studied with a pure rocking model for the first time to determine whether a pure rocking model can model the reversal of the spin direction that the rattleback is known for.

The rattleback is released with the following initial conditions: $\dot{\psi} = 6$ rad/s, $\dot{\phi} = \dot{\theta} = 0$. Figure 4.25 shows the time history for the rattleback with this initial velocity.

Notice the change in sign of $\dot{\psi}$ in Figure 4.25c at around 1.5 seconds. At $t = 0$, $\dot{\phi}$ and $\dot{\theta}$

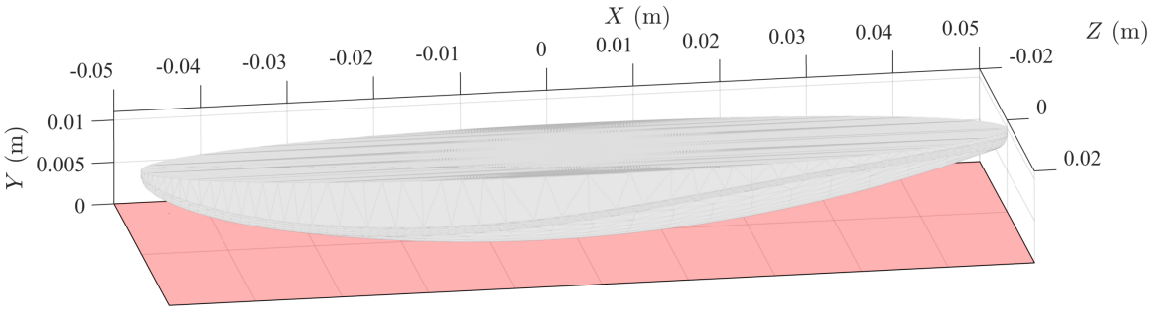


Fig. 4.24. The initial position of the rattleback when set in motion.

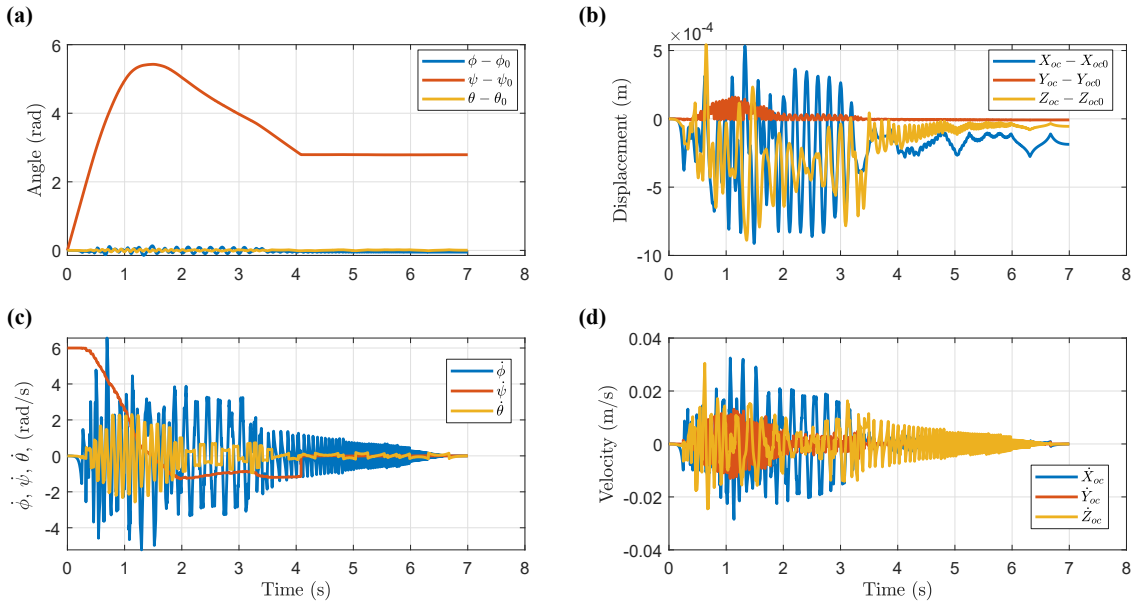


Fig. 4.25. The time history of the rattleback's motion with initial conditions $\dot{\psi} = 6$ and $\dot{\phi} = \dot{\theta} = 0$. a) Euler angles in rad. b) Displacement of c in m. c) Time derivatives of Euler angles in rad/s. d) Velocity of c in m/s.

are zero but as the object spins counterclockwise, $\dot{\phi}$ and $\dot{\theta}$ are excited and grow in magnitude with greater magnitude so that the rattleback displays rotations about horizontal axes until it reverses spin and the magnitudes of oscillation decrease until the rattleback comes to rest.

The following Figure 4.26 depicts the first 1.47 seconds of the rattleback's motion.

From Figure 4.26 the motion of the rattleback can be visualized. The rattleback's long axis is initially parallel to the X-axis and it is given an initial velocity that creates a counterclockwise motion. In the center of the diagram, the location of the rocking vertices can be visualized. Initially, the rocking vertex remains centered with respect to the

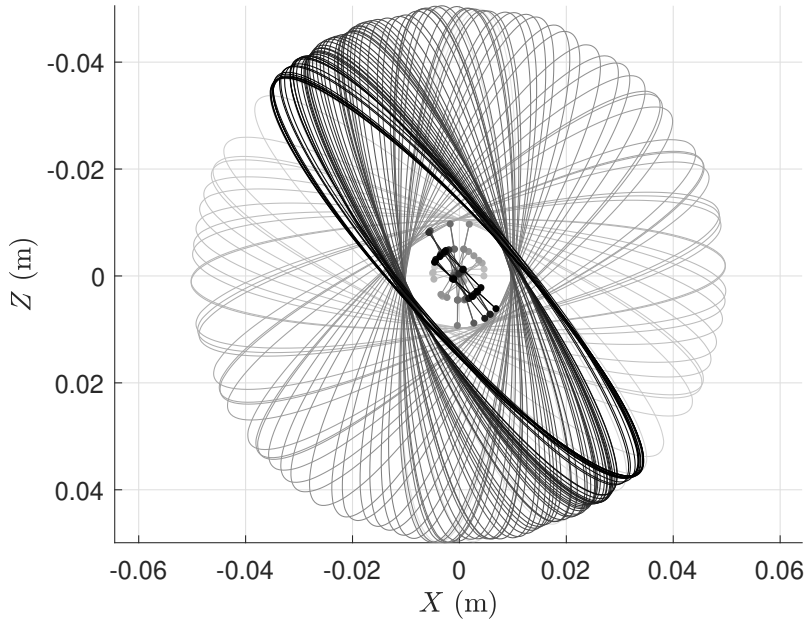


Fig. 4.26. The outline of the rattleback and its rocking vertices depicted by points and connected by line segments. The line and point color turns darker as time goes on. The initial rocking vertex is set to $X = Z = 0$.

rattleback's outline, but as time goes on, the geometry of the rattleback and its consequent mass distribution cause the rattleback's centroid to move so that it is not directly above the rocking vertex. This causes instability in the rattleback and other other rocking vertices are thus engaged. Many of these points can be visualized by the by the points 0.01 m radially from the point $X = Z = 0$ in Figure 4.26. These rocking vertices, as they are not directly underneath the centroid, cause a moment about the short axis of the rattleback which induces a rocking motion about this axis. As time goes on, the energy from the initial angular velocity of the body ω_y is converted into a velocity about the short axis of the body. Note that the darkest rocking vertices depicted in the center of the diagram show the greatest spread over space of the rocking vertices indicating the most violent rocking motion about the rattleback's short axis.

Eventually, the reaction forces cause the change in sign of $\dot{\psi}$ and the rattleback then rotates in a clockwise direction and continues to do so as the rocking vertex remains close to the horizontal projection of the centroid. The rattleback continues spinning clockwise

until its energy is spent due to impacts occurring between adjacent rocking vertices.

Videos of the rattleback's motion are provided in Video S4.23 (side view) and S4.24 (top view). Slow motion videos of the same motion are provided in Video S4.25 (side view) and Video S4.26 (top view). Finally, a video of a 3-D printed rattleback moving after being given similar initial conditions to those in the model is provided in Video S4.27. The side view videos labeled above show the rattleback with a black vertical vector extending from c in the direction of $\mathbf{e}_y$ and a blue vector from the rocking vertex in the direction of the support reaction force over time (the length of the force vector is scaled to correspond with the magnitude of the reaction over time). It can be seen that the reaction force is very close to the direction of the vertical for the first 0.5 seconds of motion but the mass distribution of the rattleback eventually causes the rocking vertex to change and the reaction force to change its direction. Video S4.24 and Video S4.26 provide more insight into the movement of the rocking vertex and the direction of the reaction force. These videos show the horizontal projection of the rocking vertex as a red point, the horizontal projection of the centroid as a black circle, and the direction of the horizontal reaction force by a blue line segment with its origin at the rocking vertex in red. The rocking vertex appears to move on a line roughly parallel to the long axis of the rattleback that runs through c and when the rocking vertex moves away from the centroid, the horizontal reaction force increases in magnitude creating a clockwise moment about c. The horizontal reaction force shown here explains the tendency of the rattleback to reverse its direction of spin.

This example again proves the versatility and ability of this model to describe the rocking dynamics of another fascinating object with irregular geometry. This model seamlessly handles the geometry of the rattleback and explains the movement of the rocking vertex and the reaction forces induced due to the object's geometry. The changing of the rocking vertex and the horizontal reaction forces explain the reversal of spinning motion of the rattleback.

4.3.5 Example 5: The Gömböc

Another object which describes a unique dynamic behavior on a horizontal support is the gömböc. Figure 4.27 shows an example of a gömböc.

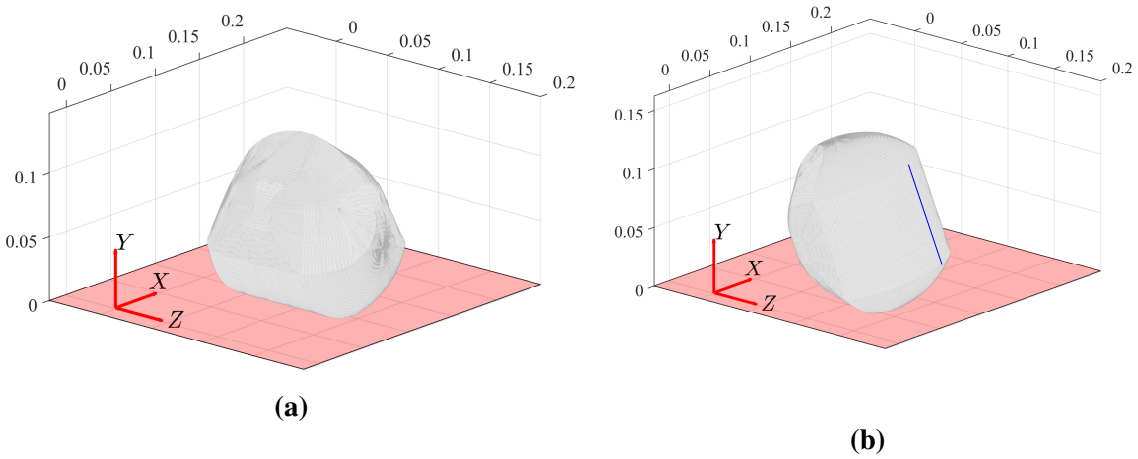


Fig. 4.27. Diagrams showing the geometry and orientation of the gömböc in (a) its stable equilibrium and (b) in its rotated state from which it is released for dynamic analysis.

The STL file of the gömböc shown in Figure 4.27 is provided in STL File S4.28 in the online supplementary material for this thesis. With reference to the axes in Figure 4.27a, the approximate maximum dimensions of the gömböc are 0.12 m in the X-direction, 0.13 m in Y, and 0.15 m in Z. To the best of the author's knowledge, there are no readily available rigid body models that can simulate the dynamics of a gömböc. Again, Lagrange multiplier solutions have major limitations.

It is desired to study the gömböc's behavior of returning to rest on the same point of equilibrium. Different gömböc's would have different manufacturing methods based on their material and precision. For example, they can be produced from metal with computer-controlled milling or plastic from 3-D printing. This example examines a gömböc which has a lower resolution than actual gömböcs, as the manufacturing requirements for an actual gömböc to return to rest are very stringent as any imperfections may not lead to the desirable single point of stable equilibrium. The gömböc studied here has a stable equilibrium represented by the edge marked in blue in Figure 4.27b, regardless of its initial

position. To examine the efficacy of the rocking model to analyze the motion of the polyhedral representation of a gömböc, the STL file was imported to Matlab and given an initial rotation (in radians) $\phi = 1.31$ rad, $\psi = 0$, $\theta = 3.32$ rad, and $\dot{\phi} = \dot{\psi} = \dot{\theta} = 0$ so that it was oriented in the configuration shown in Figure 4.27b. The gömböc was then released from this position and allowed to freely move. Time histories for all the states of the gömböc's motion are provided in Figure 4.28.

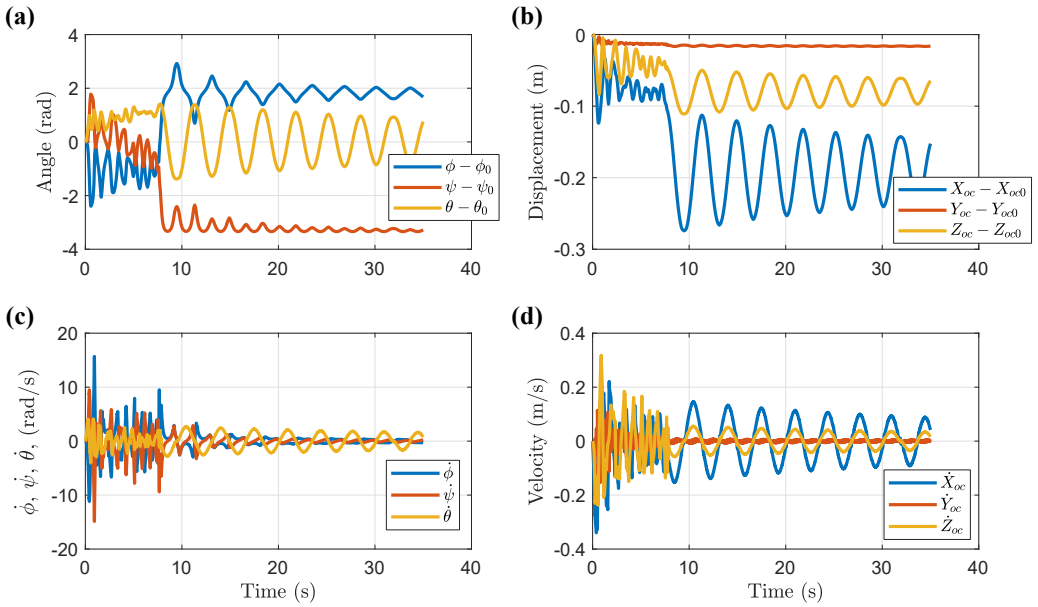


Fig. 4.28. Time histories for all states of the gömböc during free vibration when released from rest with initial conditions: $\phi = 5\pi/12$ rad, $\psi = 0$, $\theta = 3.32$ rad, $\dot{\phi} = \dot{\psi} = \dot{\theta} = 0$. a) Euler angles in rad. b) Displacement of c in m. c) Time derivatives of Euler angles in rad/s. d) Velocity of c in m/s.

A video of the gömböc's motion displayed in Figure 4.28 is provided in Video S4.29 of the supplemental material. This video should be viewed to better visualize the dynamics of the gömböc in the discussion that follows. Figure 4.28 shows several interesting aspects of the gömböc's dynamics. For about the first 10 seconds of motion, as seen in Figure 4.28, the gömböc undergoes a series of impacts and 3-D motion before transitioning to a planar motion after 10 seconds. This planar rocking motion is a decaying periodic which would generally be described as rolling and can be visualized in Figures 4.28a and 4.28b.

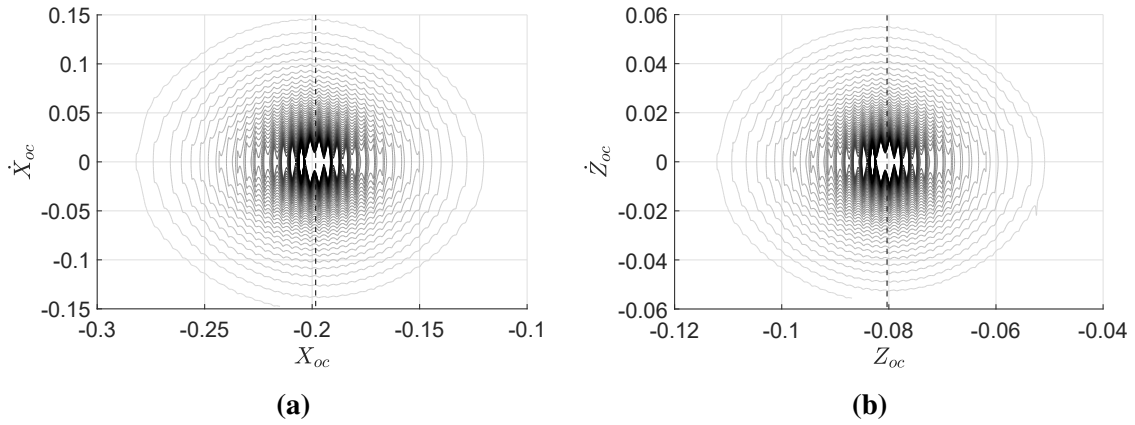
Thus, the gömböc transitions from a 3-D PR1 motion to a planar motion where the

body experiences PR2 rocking from one straight edge along the cylindrical curve of the lower portion of the gömböc to another. Instead of a continuously moving point of contact with the support, the gömböc experiences many successive surface impacts that transition from PR2 to PR2 on parallel edges. The gömböc remains in PR2 after each surface impact because the pre- and post-impact angular velocities are parallel to each other and the pre- and post-impact rocking edges. This planar PR2 motion could be modeled with less limitations, i.e., the allowing of sliding and free flight, by the planar model described in Chapter 2. Note that even this planar rocking motion could not be described by previous rocking models due to the presence of many rocking vertices/edges. However, the relatively small velocities of the body and the absence of external forces other than the support reactions for the gömböc lead one to believe that the gömböc would not likely begin sliding or free flight and that this 3-D pure rocking model is sufficient for modeling such motion. But the planar rocking model remains a novel possibility to combine the best of the two models presented in this thesis.

The gömböc continues this planar rocking motion for several minutes and thus the time histories are trimmed to include only the first 35 seconds of motion. The amplitudes of the gömböc's change in states continue to decay until the gömböc comes to rest at either face adjacent to the equilibrium edge shown in blue in Figure 4.27. The gömböc does not come to rest exactly on the equilibrium edge due to small imperfections in the numerical representation of the gömböc's geometry in the STL file.

After viewing other simulations of the gömböc's dynamic response for different initial conditions, it has been observed that the gömböc returns to the same point of equilibrium but the duration of motion for the simulations are longer than the duration of dynamic responses for an actual gömböc. This phenomenon represents the opposite end of the spectrum displayed by the low-resolution representations of Euler's disk. The very small distances between vertices for the gömböc cause a very slow loss of energy. Like Euler's disk, the number of vertices or λ_{ab} can be altered to change the duration of motion.

To examine the tendency of the gömböc to reach equilibrium at the same orientation, phase space diagrams for the two horizontal translational DOFs, X_{oc} and Z_{oc}, are produced. Figure 4.29 shows these phase space diagrams for the gömböc beginning after it displays the periodic rolling motion, from $t = 9$ seconds to $t = 182$ seconds.



(a) **(b)**

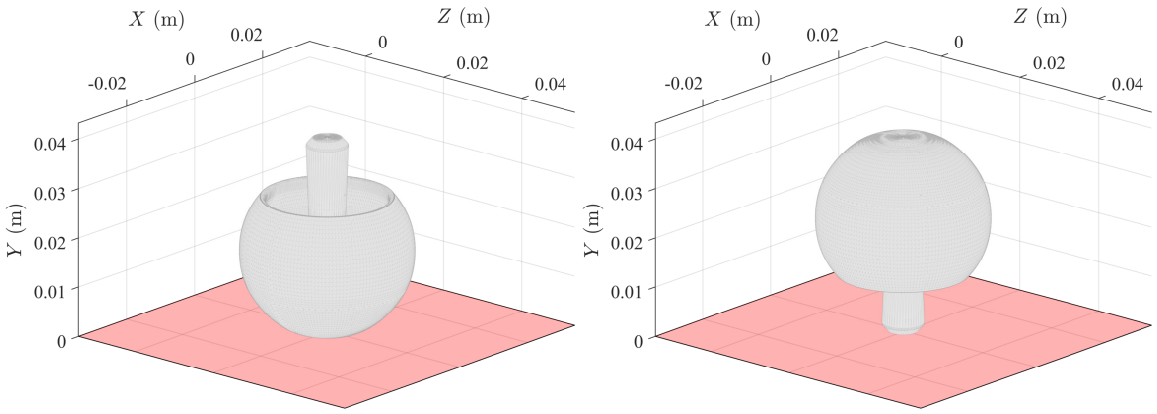
Fig. 4.29. Phase space diagrams for X_{oc} and Z_{oc}. Positions are plotted in m and velocities in m/s. The dashed line shows the value of the DOF for which equilibrium will occur.

Vertical dashed lines are drawn from the approximate maximum to approximate minimum velocities: $\dot{X}_{oc}$ and $\dot{Z}_{oc}$. The horizontal coordinates of these lines represent the value of X_{oc} and Z_{oc} at the gömböc's final location when it comes to rest: $X_{oc} = -0.08$ and $Z_{oc} = -0.2$. The gömböc begins orbiting this point at the beginning of its periodic motion from $t = 10$ seconds. The equilibrium values for the gömböc are the mean values of $X_{oc}(t)$ and $Z_{oc}(t)$ in Figure 4.28b after 10 seconds. Since the simulation of the gömböc can continue for a long duration, the phase space diagram and the point about which the gömböc orbits can be used to determine the final position of the gömböc and save computational resources. When the gömböc exhibits a periodic motion as shown by Figure 4.29, which is the most common motion that the gömböc displays as it nears its final state of rest, the values of the states at the times that the gömböc passes through its maximum velocities (the vertical dashed line in Figure 4.29) can be set as the final equilibrium position of the gömböc. This stop can be placed to save significant computational time after the gömböc has made as little as two revolutions of the phase portrait.

In conclusion, the model of the gömböc displays the expected behavior of returning to its single stable point of equilibrium. The duration of the dynamic response of this representation of the gömböc appears to be longer than that for an actual gömböc, but this could be adjusted in a similar manner as was achieved for Euler's disk. The gömböc displays a stable motion that can be visualized through its phase space diagram and exploited to realize the final equilibrium states of the gömböc. This pure rocking model thus provides the first dynamic modeling of the gömböc to the best of the author's knowledge.

4.3.6 Example 6: The Tippe Top

Finally, the tippe top also displays a counterintuitive motion whereby it inverts when spun with sufficient angular velocity about its axis of symmetry. The tippe top is studied in the 3-D pure rocking model of Chapter 3 to determine whether the model can properly model the inversion, rolling, and spinning dynamics of the tippe top. An STL of the tippe top shown in Figure 4.30 is provided in STL File S4.30 in the supplemental material.



(a) A tippe top with its spherical bell in contact with the support.

(b) A tippe top with its shaft contacting the support.

Fig. 4.30. Images of the tippe top with its initial and overturned orientations depicted.

While previous researchers argued the importance of sliding friction to the tipping motion of the top, this pure rocking model does not allow sliding but still offers a valuable perspective as it does not consider a constantly changing point of contact with the support

and can handle any geometry of tippe top. For this example, a relatively fine polyhedral approximation of the tippe top is used such as may be produced by a 3-D printer. The fineness of the mesh describing the tippe top can be adjusted to contain any desired number of vertices so that if an actual tippe top is deemed to be very smooth it could still be represented as a polyhedral body, as the actual tippe top displays non-smooth geometry at some scale (potentially as small as microscopic).

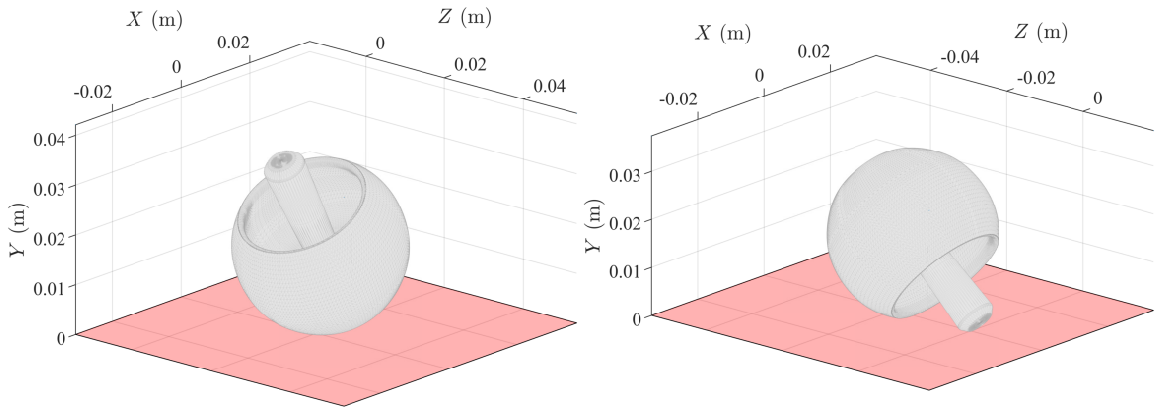
The tippe top was input to the pure rocking model of Chapter 3 to attempt an answer to several questions. First, does the pure rocking model provide a reasonable result for the top released from rest? The tippe tops has a similar property to the gömböc in that it has a stable point of equilibrium on its spherical bell which it will return to when released from another position. The question of whether the model provides a qualitatively similar response for a top given an initial spin about its axis of symmetry on a support will also be investigated. And finally, does the response of the tippe top derived from the pure rocking model corroborate the findings of previous researchers, particularly regarding the friction model and the top's qualitative behavior, i.e., tipping motion?

4.3.6.1 Release from Rest

To answer the first question above, the top was released from rest (all velocities initially zero) in two randomly-selected initial positions. The first simulation was given initial conditions: $\theta = 0.52$ rad and $\phi = \psi = 0$. The second was released with $\phi = 2.27$ rad and $\psi = \theta = 0$. The initial positions for both releases can be viewed in the following Figure 4.31. These two initial conditions were randomly selected to check that the model provides the expected response of the tippe top returning to rest on its stable point of equilibrium.

Figure 4.32 provides the time history for each of the tippe top's states when it is released from rest with initial conditions: $\theta = \pi/6$ rad and $\phi = \psi = 0$.

A video of the top's motion described by Figure 4.32 can be seen in Video S4.31 in the supplemental material. The top rocks about vertices on its lower spherical portion as its



(a) Initial conditions: $\theta = \pi/6$ rad, $\phi = \psi = 0$

(b) $\phi = 2.27$ rad, $\psi = \theta = 0$

Fig. 4.31. Diagrams of the initial position of the tippe top when released from rest with the initial rotations specified.

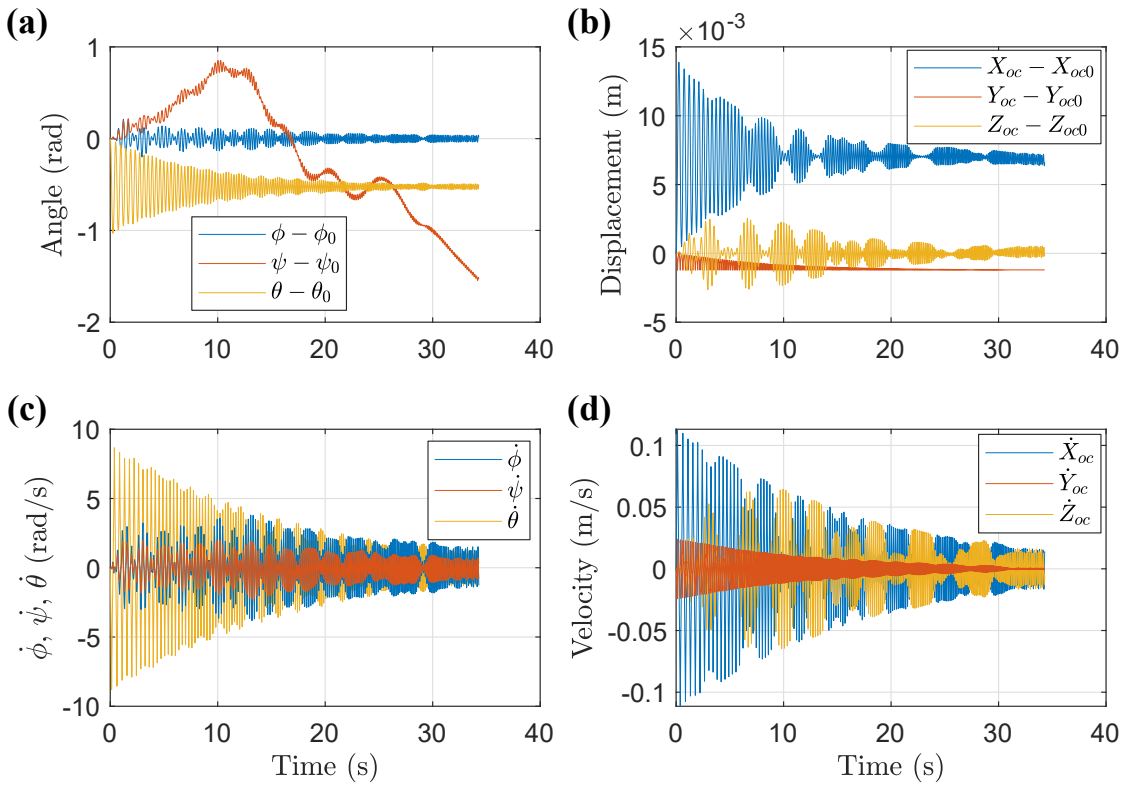


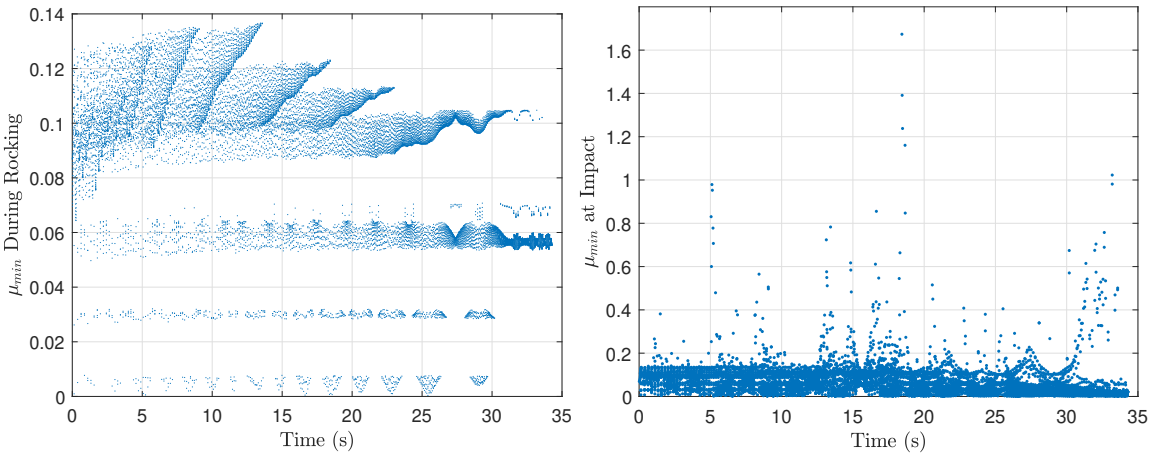
Fig. 4.32. A time history for the tippe top released with $\theta = 0.52$ rad and with all other angles and velocities initially zero. a) Euler angles in rad. b) Displacement of c in m. c) Time derivatives of Euler angles in rad/s. d) Velocity of c in m/s.

velocities decrease in magnitude (Figure 4.32c and 4.32d) so that its shaft is parallel to the vertical. From the Euler angle plot in 4.32a, notice the change in ψ over time representing

a twisting of the top about its axis of symmetry. As can be seen from the video of the tippe top, it displays a clear 3-D motion. To confirm that the top can be accurately modeled when sliding is ignored, the minimum coefficient of friction μ_{min} required to maintain pure rocking was calculated for each recorded time instance of rocking, and for each impact by the following equations:

$$\mu_{min,rock} = \frac{\sqrt{F_x^2 + F_z^2}}{F_y} \qquad \mu_{min,impact} = \frac{\sqrt{J_x^2 + J_z^2}}{J_y} \tag{4.7}$$

Figure 4.33 shows μ_{min} over time for both rocking (4.33a) and impacts (4.33b).



(a) $\mu_{min,rock}$ **(b)** $\mu_{min,impact}$

Fig. 4.33. μ_{min} over time for the top when released with initial condition: $\theta = \pi/6$ rad.

Figures 4.33a and 4.33b show that μ_{min} for both rocking and impacts is generally within the range of 0 to 0.15. During pure rocking (opposed to at impact), μ_{min} never exceeds 0.14. Given that the typical coefficient of kinetic friction between clean, dry, hard objects such as wood, metal, or glass is generally around 0.4, a pure rocking model is reasonable for this instance as a reasonable value of μ would not be exceeded during rocking (105). Note that during some impacts μ_{min} exceeds 0.4. It is expected that the top would transition to sliding at these impacts but because they are limited to less than 1% of the total impacts and another impact is expected to immediately succeed, they are assumed not to affect the

result shown.

When the tippe top is rotated by $\phi = 2.27$ rad its shaft is nearly in contact with the support as shown in Figure 4.31b and is released from rest, it shows a similar response to that for the first release and tends to orient its shaft upward. The time history for this initial condition is shown in the following Figure 4.34.

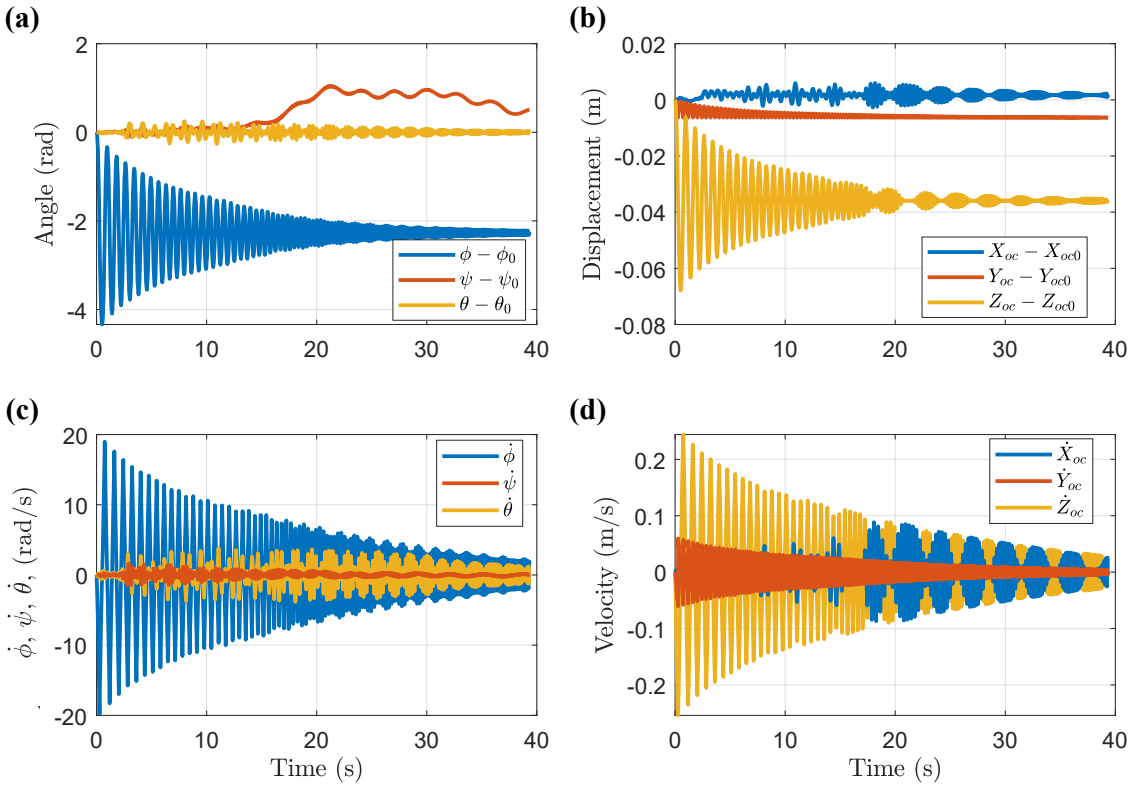


Fig. 4.34. A time history for the tippe top released with initial conditions: $\phi = 2.27$ rad and with all other angles and velocities initially zero. a) Euler angles in rad. b) Displacement of c in m. c) Time derivatives of Euler angles in rad/s. d) Velocity of c in m/s.

A video of the top's motion for the second release is available in Video S4.32 in the supplemental material. Figures 4.34c and 4.34d and Video S4.32 show, like the first release, the velocities of the body decaying over time. However, this release displays a longer duration of motion given the greater amplitude of the initial angle and the consequently greater maximum velocities in Figure 4.34c more than double the first release. Though the plots of the coefficient of friction are not repeated for the second release, $\mu_{min,rock}$ again does not exceed 0.2 during pure rocking and $\mu_{min,impact}$ exceeds 0.4 for a small number of

impacts. The rare occurrence of the high $\mu_{min,impact}$ is not expected to affect the overall dynamic result significantly as the tippe top displays its expected behavior and reaches equilibrium with its shaft vertical and spherical bell in contact with the support. Thus, this rocking model provides a realistic and accurate dynamic response for the tippe top released from rest and the tippe top moves to its stable point of equilibrium as expected.

4.3.6.2 Release with Non-zero Initial Velocity

The response of the tippe top was then tested for a release with an initial velocity about the top's axis of symmetry. Figure 4.35 shows the time history of the tippe top when released with initial conditions: $\theta = 0.035$ rad, $\phi = \psi = 0$, $\dot{\psi} = 100$ rad/s, and $\dot{\phi} = \dot{\theta} = 0$. The body is given an initial rotation from the vertical to ensure that a moment is introduced about a horizontal axis, as the top must rotate out of its axial symmetry in order to overturn as seen in videos of physical tippe tops.

A video of the tippe top model corresponding to Figure 4.35 is provided in Video S4.33 in the supplementary material. As seen in this video and Figure 4.35a, the angle ψ changes continuously over the duration of the motion showing that the spinning motion, i.e., where the top appears to primarily rotate about its axis of symmetry. This appears to be a rolling motion when viewed from a macroscopic perspective. A video of an actual tippe top spinning and overturning is provided in Video S4.34 in the supplementary material. This pure rocking model also provides an explanation for the decrease in velocities which is not readily available from a continuous spherical or circular rolling model. As can be seen in the Figures 4.35c and 4.35d, the velocities decrease over time and approach zero due to many impacts between the top and the support which cause small incremental energy loss at each occurrence.

Observing the trajectory of the top's centroid and rocking vertex over time can offer further insight into its dynamic response. Thus, the following Figure 4.36 shows the position of the centroid indicated by X_{oc} and Z_{oc} in Figure 4.36a and the position of the contact

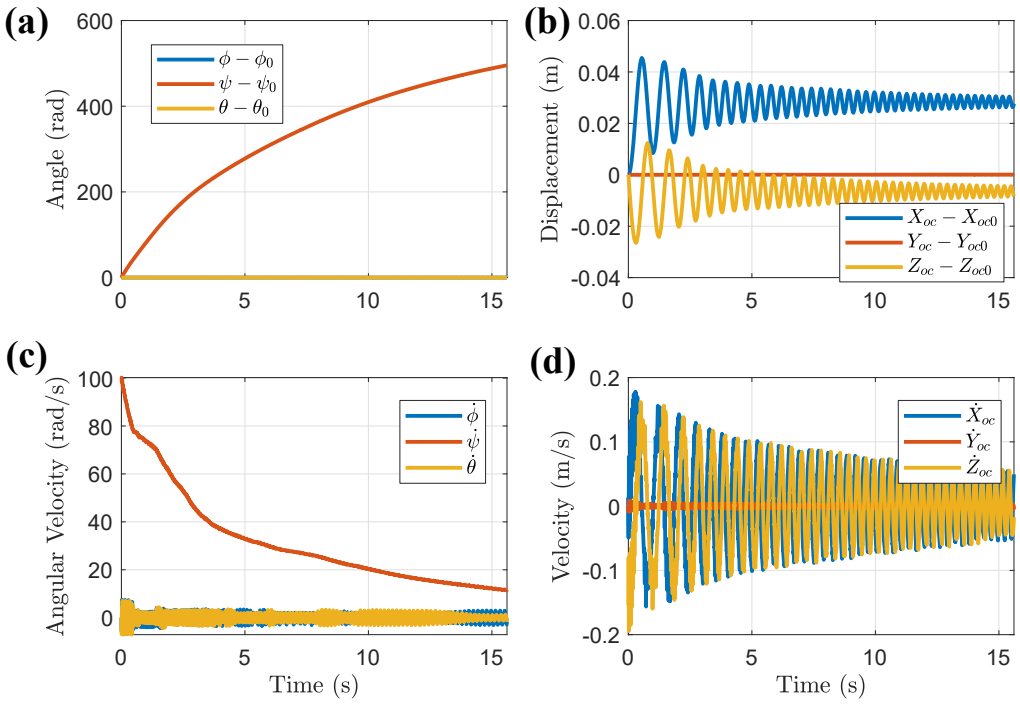
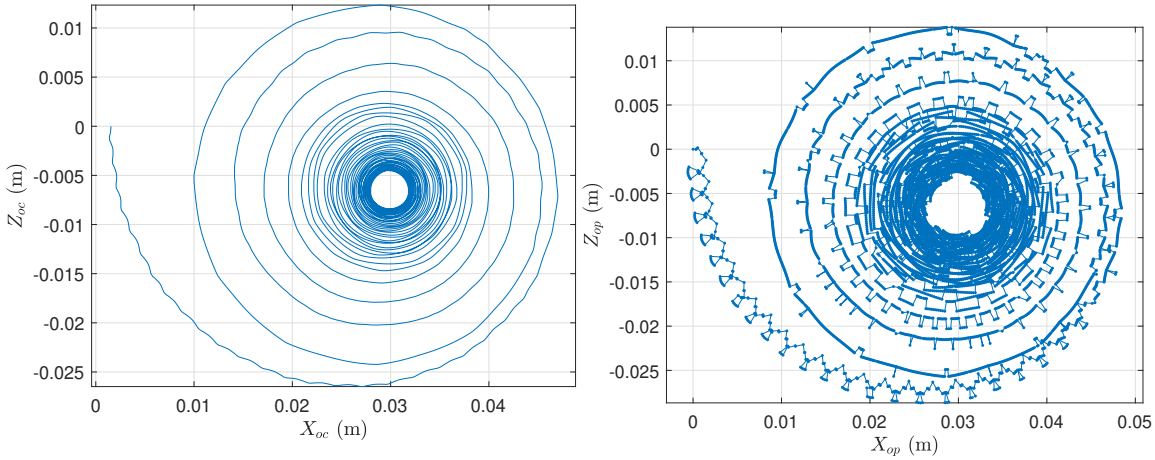


Fig. 4.35. A time history for the tippe top released with initial conditions: $\theta = 0.035$ rad and $\dot{\psi} = 100$ rad/s with all other angles and velocities initially zero. a) Euler angles in rad. b) Displacement of c in m. c) Time derivatives of Euler angles in rad/s. d) Velocity of c in m/s.

vertex defined by X_{op} and Z_{op} in Figure 4.36b over the course of the top's spinning.



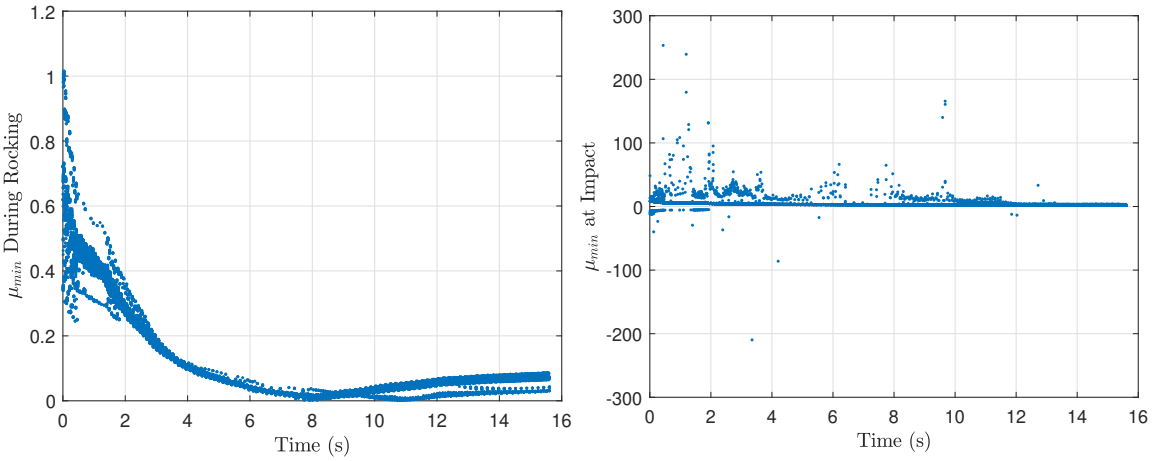
(a) The X_{oc} and Z_{oc} position of the centroid over time.

(b) The location of the rocking vertex over time.

Fig. 4.36. Plots of the location of the tippe top's centroid and rocking vertex over time.

Figure 4.36a shows the centroid of the top oscillate in a direction normal to the macroscopic spiral direction of the top's motion which is defined as the tangential direction in this case. This motion normal to the spiral is most obvious at the beginning of the top's motion on the left side of Figure 4.36a. However, unlike the actual tippe top, as shown in Video S4.34 (experiment), the centroid seems to correct itself to keep a similar horizontal coordinate as the rocking vertex as shown in Figure 4.36b. This figure shows the many different rocking vertices the top employs during its spinning motion signified by points with lines connecting successive rocking vertex locations.

From Video S4.33, and by examining the Euler angles of the body over time from Figure 4.35a, it is clear that the top does not overturn as it does in experiments. Further, after testing various initial conditions believed to be similar to those applied to an actual tippe top that overturns, the overturning of the tippe top in the model could not be obtained. To discern the effect that sliding friction might have on the overturning of the top, the minimum value for μ over time is calculated in the same way as in Figure 4.33. The result of μ_{min} for the top with non-zero initial velocity is provided in Figure 4.37.



(a) $\mu_{min,rock}$ **(b)** $\mu_{min,impact}$

Fig. 4.37. Plot of μ_{min} over time during rocking and at impacts while the tippe top is spinning.

The results for μ_{min} from Figure 4.37 are significantly different from Figure 4.33 for a release from rest. In Figure 4.37a, μ_{min} exceeds 1 and has many instances greater than

0.4 indicating that the top would slide if it and the support surface were hard, clean, and dry. This is an important observation as it shows the limitation of the pure rocking assumption to model the motion of the tippe top and any similar objects that would require high coefficients of friction to remain in rocking. The results of $\mu_{min,impact}$ are even more critical as $\mu_{min,impact}$ exceeds 250 for some impacts and has a minimum positive value of 5 for the first several seconds of motion. Unlike the releases from rest where most impacts have $\mu_{min,impact} < 0.4$, this result is critical as every impact displays $\mu_{min,impact} > 5$ that is incompatible with normal materials. Thus, sliding is an important pattern of motion to consider for the motion of the tippe top.

Another critical result for the spinning top is the existence of negative $\mu_{min,impact}$ for a number of impacts, particularly during the first 2 seconds of motion as shown in Figure 4.37b. These negative values occur due to a negative J_y at impact which is an indication that the top would lift off the support surface at these impacts and the support must provide a tensile impulse on the top in order to keep it from doing so. This shows the necessity of also considering free flight to appropriately model the response of the spinning tippe top, which has not been done to date.

The examples displayed for the tippe top show that this pure rocking model offers a viable dynamic analysis for a tippe top released with certain initial conditions, but there are other situations where free flight and sliding cannot be ignored. The pure rocking model introduced in this thesis does not accurately predict the response in the latter cases. This corroborates previous researchers' findings that the sliding friction of tippe tops is critical to their overturning and raises the question of how important free flight is to the overturning of the tippe top.

4.4 Conclusions

This chapter shows that the irregular geometry pure rocking model may be used to study the movement of a variety of irregular curved objects and scenarios with relative ease and low computational cost compared to many previous dynamic models. The capability of the model to take an object with any geometry as an input and output dynamic results with any desired support accelerations or initial conditions allows for insightful study of objects that were previously very difficult to study numerically or had to be idealized to be studied analytically with simplified models. This model shows that an object that appears to experience rolling may actually experience pure rocking if it is considered to have a polyhedral geometry, which is commonly the case for 3-D printed and other manufactured objects.

Examples of the motion of various irregular objects with curved surfaces have been presented here that corroborate previous studies and offer new perspectives and tools to study the dynamics of these objects. The pure rocking model has been shown to be viable for studying the motion of a cylinder and disk and shows the out-of-plane motion that such objects display even with seemingly symmetric geometry and initial conditions. The model has also provided insights into the sound produced by Euler's disk, the uplift of the disk from its support in the final stages of its motion, and the ability to reduce computational time for the disk's motion by reducing the number of vertices used in its STL. This great reduction of computational time can be exploited for use in computer graphics and animation to realistically simulate countless objects and their dynamics when the details of the accurate dynamic response are not necessary. Additionally, the motion of the gömböc and the rattleback were captured by the pure rocking model and offer a novel ability to study any detailed geometry of gömböc or rattleback. This model allows a researcher to consider material imperfections or different geometry ad libitum and thus offers a powerful tool for anyone interested in studying a wide array of dynamic problems. Finally, the study of the tippe top shows from a new perspective the importance of sliding and free flight to the

tipping motion of the top.

The findings developed here have strong potential uses in computer animation, education, and manufacturing. The use of the model is not limited to the study of the objects shown here but can be applied as desired to nearly any object in a variety of dynamic scenarios. The findings of further study can then be applied to improve computer animation, educate students of many levels about physics, engineering, and dynamics, and offer insight into the tolerances that should be accepted for the manufacturing of objects designed to move on a horizontal support.

Chapter 5

Conclusions

Chapter 2 introduced a new planar rocking model for irregular geometry and showed the importance of considering irregular geometry, the direction of the support acceleration, the location of the centroid relative to the rocking vertices, sliding, free flight, and a variable location for the impulse at impact for planar rocking motion. The different dynamic response displayed by the shelving units and PBR depending on the direction of pulse and the body's geometry, proves the importance of considering the irregular geometry of the object. The counterintuitive effect of a reduction in the coefficient of friction causing failure at lower amplitude sinusoidal pulses for some frequencies was also observed for bodies with irregular geometry in this work, as had previously been observed for blocks in (30). The PBR example also shows the importance of including free flight in a rocking model, and for any object that experiences support accelerations as free flight can lead to more dramatic or abrupt failure.

The findings presented in Chapter 2 also show the advantages that can be reaped from using different base configurations for objects with irregular geometry. The inclusion of a pedestal that widens the base of the sculpture has been shown to be beneficial for the rocking stability of the sculptures as well as the addition of extensions that widen the base and create additional rocking vertices as shown in the shelving unit example. Additionally,

the inclusion of “feet" on the outer vertices of the base of a pedestal effectively allow for ensuring smaller values of λ which can be assumed to be sufficiently close to zero, leading to greater rocking stability. The examples in Chapter 2 demonstrate how other base configurations can easily be taken into account. While not explicitly shown in Chapter 2, the model also allows for approximating curved edges through polygonal or polyhedral segments as discussed in Chapter 4. Overall, this enables the study of any possible type of base that a museum mount-maker may consider manufacturing for supporting a museum artifact. It has been shown that adding mass to the pedestal is also effective in reducing its overturning failure tendency, but this is not strictly necessary given other options such as widening the base and adding feet to the outer vertices.

The planar rocking model of Chapter 2 is also capable of modeling the dynamics of a 3-D irregular body that experiences planar motion due to its specific geometric and mechanical constraints. The model thus offers an upgrade to the study of planar rocking as it enables the study of 3-D objects with non-prismatic geometries and their consequent mass moments of inertia. This planar rocking model can also be extended to handle more complex objects such as those with heterogeneous materials or multiple objects in contact with each other. It can be used to produce a basic understanding of the motion of objects prone to rocking, particularly when those objects have mechanical constraints that would prevent them from out-of-plane rocking. The model can further be used for computer graphics and animation for simple planar animations of motion.

Chapter 3 introduced a new 3-D pure rocking model for irregular geometry. The model patches several gaps previously existent in the study of rocking and offers new insights on these points. Chapter 3 shows the importance of allowing for more than four rocking vertices, considering both line and surface impacts, allowing for a variable location for the impulse at impact, considering the post-impact situations that can arise for irregular objects, using a robust impact and pattern transition detection mechanism such as Matlab’s ode45 and event functions, and ensuring the numerical results of the model are accurate by

using analytical formulations of the equations of motion and only integrating the minimum number of DOFs necessary to wholly determine the motion of the body. Each of these inclusions has been shown to be a valuable component of studying the motion of irregular rocking objects through the examples of the *Doryphoros* and the *Discobolus*.

The model allows for the study of various objects of irregular geometry, including museum sculptures. Examples of sculptures subjected to an earthquake were provided which prove the importance of considering the irregular geometry including the vertices of the base in detail along with allowing three DOFs. These findings show that the use of planar rigid body rocking models or models that only consider rectangular prisms are inappropriate for the study of irregular bodies. It was shown that even for unidirectional sinusoidal pulses, irregular 3-D bodies do not rock in a plane. Further, different orientations of the same body to a given pulse can result in large differences in the minimum failure amplitude of the body for sinusoidal pulses. It is clear that the width of the base in the direction of the pulse does not necessarily predict the stability of the body, and thus, simplified planar rocking models that attempt to discern a critical plane of rocking are misjudged. A smaller width of the base in the direction of the pulse can result in lower amplitudes of failure when compared to a much wider portion of the base due to its irregular geometry.

Chapter 3 shows that the 3-D geometry and motion of rocking objects important to consider in a dynamic model with no less than three DOFs. The location of the impulses applied at impact is also an important aspect of considering the motion of these objects. Finally, a full analysis of the rocking response of such objects in various orientations has been shown to be necessary in order to understand the risk of failure. The model introduced in Chapter 3 is thus valuable for studying the motion of various objects including museum artifacts, PBRs, computers, and more.

Chapter 4 applies the 3-D pure rocking model introduced in Chapter 3 to irregular objects with curved surfaces that macroscopically display rolling motions. This pure rocking model offers a new ability to study objects that may resemble curves, but in reality actually consist

of polygonal faces such as 3-D printed objects or objects manufactured with vertices, even if they appear to be smooth. Instead of a rolling model, a pure rocking model is more appropriate to model the motion of such objects. Examples of the motions of various objects, including cylinders, disks, rattlebacks, gömböcs, and tippe tops, has been shown. Surprisingly, the pure rocking model can handle the motion of many of these rolling objects and can even offer new insight on their motions.

The results provided for prisms with a polygonal base subjected to unidirectional sinusoidal pulses show that when a 3-D rocking response is initiated, the body is much more susceptible to overturning failure than planar rocking. Further, as the number of vertices for the polygonal base change from four (a square) toward 1,024 to approximate a circle, the body exhibits a greater likelihood of 3-D motion and the engagement of many vertices as rocking vertices. This proves the importance of considering the 3-D rocking response for various objects as well as an appropriate number of vertices for curved objects such as cylinders. The results of Srinivasan and Ruina for cylinders given an initial "flick" have been corroborated from the perspective of pure rocking opposed to rolling about the rim, proving that both models give similar results that show 3-D motion opposed to planar rocking.

Several important findings have been demonstrated for Euler's disk. A plausible explanation for the sound exhibited by the disk has been shown to be due to the impacts between the disk and the support. The tendency of the disk to uplift from its support at the very end of its motion has been shown by negative vertical impulses. Additionally, Chapter 4 demonstrated the potential to reduce the computational time and produce a qualitatively similar result by using a disk with a reduced number of vertices but a greater λ. This finding presents potentially great advantages for computer animation algorithms.

Additionally, the ease by which irregular objects such as the rattleback and gömböc can be studied by the new model has been shown and the dynamic response provided by these models proves qualitatively similar to the results of casual experiments. The tippe top and its failure to exhibit its tipping motion when modeled with pure rocking corroborates previous

findings that show the sliding of the tippe top with respect to the support is necessary to allow its overturning. More so, the coefficient of friction can be calculated throughout the motion of the tippe top and thus offers new insight into how it develops over time.

Chapter 4 examines whether objects that macroscopically appear to roll could actually be engaged in pure rocking. The results of each of the examples presented shows that the apparent rolling behavior of these objects can indeed be described by a pure rocking model. This is an important result, particularly for the study of objects which may look curved but actually have polyhedral geometry such as 3-D printed objects.

Overall, this thesis provides new models for the 2-D and 3-D rocking and rolling motions of objects with irregular geometry. The comprehensive nature of the models provides for a wide array of conclusions to be drawn based on dynamic simulation results of various objects. This thesis can be further expanded and applied to countless problems in engineering dynamics, museum conservation, paleoseismology, computer animation, and manufacturing and is thus a significant and valuable contribution to human knowledge.

5.1 Directions for Future Work

The family of rigid body, rigid support rocking models can be further expanded by adding both sliding and free flight to the 3-D model presented here. This step can be completed using the algorithms and formulations presented in this thesis. This expansion will allow for broader applicability of the model to problems in this space, including the study of various objects and their risk of failure due to sliding and free flight. However, this thesis has indicated that considering these added effects will require further assumptions related to how the reaction forces are distributed along an edge or surface in contact with the support. Such assumptions may not be perfect as the issues of rigid algorithms with simultaneous multiple contact points are already known. In such cases, such phenomena might be included through extending DEM approaches such as that presented in (33). Studying the

effect of areas of the body with different materials and densities is another route to expand rocking knowledge which is closely related to this work. The models described in this thesis can again be easily adapted to consider the inertia properties of heterogeneous rigid bodies. Finally, an expansion to multiple objects and their interactions with each other offers another fertile field of knowledge to be harvested. The 3-D model provided here can act as a building block for more advanced models with multiple objects and the effect of their interactions.

The work of this field should be further expanded to compare experiments on irregular geometries to that produced by these models. This will allow for greater understanding of the accuracy of such a model and for further study on the risk related to rocking for various museum artifacts and other sculptures. To further ease the study of objects via this model, automated processes for obtaining and importing geometries to the model should also be developed. These will conceivably include ways to easily 3-D scan objects using smartphones or other common cameras.

Other work on deformable bodies and deformable supports will continue to develop in complexity and these upgrades are of course welcomed, though the computational cost of such models will be much larger than that for the rigid models provided herein. The rigid body rocking model family may have an important role to play in efficiently filtering out irrelevant objects and motions so that greater computational resources are not squandered by deformable or finite element models.

Bibliography

[1] Pacific earthquake engineering research center (peer). https://ngawest2.berkeley.edu/.

[2] *FEMA E-74 Reducing the Risks of Nonstructural Earthquake Damage—A Practical Guide, Fourth Edition*, December 2012.

[3] H. A. Abadi, V. Paton-Cole, E. Gad, N. Lam, and V. Patel. Rocking behavior of irregular free-standing objects subjected to earthquake motion. *Journal of Earthquake Engineering*, 23(5):793–809, sep 2017.

[4] S. Acikgoz and M. J. DeJong. The interaction of elasticity and rocking in flexible structures allowed to uplift. *Earthquake Engineering & Structural Dynamics*, pages 1–18, mar 2012.

[5] S. Acikgoz and M. J. DeJong. The rocking response of large flexible structures to earthquakes. *Bulletin of Earthquake Engineering*, 12(2):875–908, nov 2013.

[6] M. S. Agbabian, W. S. Ginell, S. F. Masri, and R. L. Nigbor. Evaluation of earthquake damage mitigation methods for museum objects. *Studies in Conservation*, 36(2):111, may 1991.

[7] J. J. Ajrab, G. Pekcan, and J. B. Mander. Rocking wall–frame structures with supplemental tendon systems. *Journal of Structural Engineering*, 130(6):895–903, jun 2004.

[8] R. H. Allen, I. J. Oppenheim, A. R. Parker, and J. Bielak. On the dynamic response of rigid body assemblies. *Earthquake Engineering & Structural Dynamics*, 14(6):861–876, nov 1986.

[9] G. Amila. Discobolus thrower statue 3d model. *Turbosquid by Shutterstock*, 2021.

[10] C. Arredondo, M. A. Jaimes, and E. Reinoso. A simplified model to evaluate the dynamic rocking behavior of irregular free-standing rigid bodies calibrated with experimental shaking-table tests. *Journal of Earthquake Engineering*, 23(1):46–71, may 2017.

[11] M. Aslam, D. T. Scalise, and W. G. Godden. Earthquake rocking response of rigid bodies. *Journal of the Structural Division, Vol. 106, Issue 2, Pg. 377-392*, 1980.

[12] E. Avgenakis and I. N. Psycharis. Modeling of rocking elastic flexible bodies under static loading considering the nonlinear stress distribution at their base. *Journal of Structural Engineering*, 143(7):04017051, jul 2017.

[13] E. Avgenakis and I. N. Psycharis. An integrated macroelement formulation for the dynamic response of inelastic deformable rocking bodies. *Earthquake Engineering & Structural Dynamics*, 49(11):1072–1094, jun 2020.

[14] J. A. Bachmann, M. F. Vassiliou, and B. Stojadinovic. Rolling and rocking of rigid uplifting structures. *Earthquake Engineering & Structural Dynamics*, 48(14):1556–1574, aug 2019.

[15] T. Baranyai and P. L. Várkonyi. Imperfections, impacts, and the singularity of euler's disk. *Physical Review E*, 96(3):033005, sep 2017.

[16] H. Baruh. *Analytical Dynamics*. McGraw-Hill international editions : engineering mechanics series. WCB/McGraw-Hill, 1999.

[17] M. Batista. Integrability of the motion of a rolling disk of finite thickness on a rough plane. *International Journal of Non-Linear Mechanics*, 41(6-7):850–859, jul 2006.

[18] M. Batista. Steady motion of a rigid disk of finite thickness on a horizontal plane. *International Journal of Non-Linear Mechanics*, 41(4):605–621, may 2006.

[19] L. Berto, T. Favaretto, A. Saetta, F. Antonelli, and L. Lazzarini. Assessment of seismic vulnerability of art objects: The "galleria dei prigioni" sculptures at the accademia gallery in florence. *Journal of Cultural Heritage*, 13(1):7–21, jan 2012.

[20] H. Bondi. The rigid body dynamics of unidirectional spin. *Proceedings of the Royal Society of London. A. Mathematical and Physical Sciences*, 405(1829):265–274, jun 1986.

[21] A. V. Borisov, A. A. Kilin, and Y. L. Karavaev. Retrograde motion of a rolling disk. *Physics-Uspekhi*, 60(9):931–934, sep 2017.

[22] A. V. Borisov, I. S. Mamaev, and Y. L. Karavaev. On the loss of contact of the euler disk. *Nonlinear Dynamics*, 79(4):2287–2294, nov 2014.

[23] R. Boroschek and D. Romo. Overturning criteria for non-anchored non-symmetric rigid bodies. In *Proceeding of the 13th world conference on earthquake engineering*, pages 1–6, 2004.

[24] C. Braams. On the influence of friction on the motion of a top. 18(8-9):503–514, aug 1952.

[25] B. Brogliato, A. ten Dam, L. Paoli, F. Ge´not, and M. Abadie. Numerical simulation of finite dimensional multibody nonsmooth mechanical systems. *Applied Mechanics Reviews*, 55(2):107–150, mar 2002.

[26] J. Brune, M. Purvance, and A. Anooshehpoor. Gauging earthquake hazards with precariously balanced rocks. *American Scientist*, 95(1):36, 2007.

[27] M. D. Burton and M. N. Chatzis. Investigating the rocking dynamics of rigid right prisms with regular polygonal bases. In *17th World Conference on Earthquake Engineering, 17WCEE, Sendai, Japan*, 2021.

[28] W. Case and S. Jalal. The rattleback revisited. *American Journal of Physics*, 82(7):654–658, jul 2014.

[29] M. N. Chatzis and A. W. Smyth. Three-dimensional dynamics of a rigid body with wheels on a moving base. *Journal of Engineering Mechanics*, 139(4):496–511, apr 2013.

[30] M. Chatzis and A. Smyth. Robust modeling of the rocking problem. *Journal of Engineering Mechanics*, 138:247–262, 03 2012.

[31] M. Chatzis, M. G. Espinosa, and A. Smyth. Examining the energy loss in the inverted pendulum model for rocking bodies. *Journal of Engineering Mechanics*, 143(5):04017013, 2017.

[32] M. Chatzis, M. Garcia Espinosa, C. Needham, and M. Williams. Energy loss in systems of stacked rocking bodies. *Journal of Engineering Mechanics*, 144, 07 2018.

[33] M. Chatzis and A. Smyth. Modeling of the 3d rocking problem. *International Journal of Non-Linear Mechanics*, 47(4):85–98, 2012.

[34] R. J. Cohen. The tippe top revisited. 45(1):12–17, jan 1977.

[35] R. Cushman and J. Duistermaat. Nearly flat falling motions of the rolling disk. *Regular and Chaotic Dynamics*, 11(1):31, 2006.

[36] G. Deierlein, H. Krawinkler, X. Ma, M. Eatherton, J. Hajjar, T. Takeuchi, K. Kasai, and M. Midorikawa. Earthquake resilient steel braced frames with controlled rocking and energy dissipating fuses. *Steel Construction*, 4(3):171–175, aug 2011.

[37] E. G. Dimitrakopoulos and M. J. DeJong. Revisiting the rocking block: closed-form solutions and similarity laws. *Proceedings of the Royal Society A: Mathematical, Physical and Engineering Sciences*, 468(2144):2294–2318, apr 2012.

[38] E. G. Dimitrakopoulos and T. S. Paraskeva. Dimensionless fragility curves for rocking response to near-fault excitations. *Earthquake Engineering &amp Structural Dynamics*, 44(12):2015–2033, feb 2015.

[39] G. Domokos, A. Sipos, T. Szabó, and P. Várkonyi. Pebbles, shapes, and equilibria. *Mathematical Geosciences*, 42(1):29–47, oct 2009.

[40] J. Dormand and P. Prince. A family of embedded runge-kutta formulae. *Journal of Computational and Applied Mathematics*, 6(1):19–26, mar 1980.

[41] V. Drosos and I. Anastasopoulos. Shaking table testing of multidrum columns and portals. *Earthquake Engineering & Structural Dynamics*, 43(11):1703–1723, mar 2014.

[42] K. Easwar, F. Rouyer, and N. Menon. Speeding to a stop: The finite-time singularity of a spinning disk. *Physical Review E*, 66(4):045102, oct 2002.

[43] D. Eberly. Polyhedral mass properties (revisited) (https://www.geometrictools.com/documentation/documentation.html). 2009.

[44] A. D. Egidio, D. Zulli, and A. Contento. Comparison between the seismic response of 2d and 3d models of rigid blocks. *Earthquake Engineering and Engineering Vibration*, 13(1):151–162, mar 2014.

[45] F. Esmonde-White. Patch slim (patchslim.m). *MATLAB Central File Exchange*, 2011.

[46] A. O. Espinoza. *Seismic Performance of Reinforced Concrete Bridges Allowed to*

Uplift During Multi-Directional Excitation. PhD thesis, University of California, Berkeley, 2011.

[47] J. Fisher. Doryphoros at the minneapolis institute of art. *MyMiniFactory*, 2016.

[48] A. Garcia and M. Hubbard. Spin reversal of the rattleback: theory and experiment. *Proceedings of the Royal Society of London. A. Mathematical and Physical Sciences*, 418(1854):165–197, jul 1988.

[49] M. Garcia Espinosa. *Risk Estimation of Rocking Components Subjected to Ground Motions*. PhD thesis, University of Oxford, 2018.

[50] M. Garcia Espinosa, M.; Chatzis. A preliminary investigation of methods for estimating theprobability of failure for rocking bodies. In *16th World Conference on Earthquake, 16WCEE 2017*, 2017.

[51] F. Gelagoti, R. Kourkoulis, I. Anastasopoulos, and G. Gazetas. Rocking isolation of low-rise frame structures founded on isolated footings. *Earthquake Engineering & Structural Dynamics*, 41(7):1177–1197, nov 2011.

[52] G. Godin, J.-A. Beraldin, J. Taylor, L. Cournoyer, M. Rioux, S. El-Hakim, R. Baribeau, F. Blais, P. Boulanger, J. Domey, and M. Picard. Active optical 3d imaging for heritage applications. *IEEE Computer Graphics and Applications*, 22(5):24–35, sep 2002.

[53] K. Hormann and A. Agathos. The point in polygon problem for arbitrary polygons. *Computational Geometry*, 20(3):131–144, nov 2001.

[54] G. W. Housner. The behavior of inverted pendulum structures during earthquakes. *Bulletin of the Seismological Society of America*, 53(2):403–417, 1963.

[55] N. Hugenholtz. On tops rising by friction. 18(8-9):515–527, aug 1952.

[56] H. W. S. III. Criteria for initiation of slide, rock, and slide-rock rigid-body modes. *Journal of Engineering Mechanics*, 122(7):690–693, jul 1996.

[57] Y. Ishiyama. Motions of rigid bodies and criteria for overturning by earthquake excitations. *Earthquake Engineering & Structural Dynamics*, 10(5):635–650, 1982.

[58] W. H. Jackson. Balanced rock, garden of the gods, colorado (https://www.dia.org/art/collection/object/balanced-rock-garden-gods-87825). Detroit Publishing Co., 1908.

[59] jasay. Rattleback20101216-ccw. MakerBot Thingiverse, 2010.

[60] E. Johnson. Stl file reader. *MATLAB Central File Exchange*, 2011.

[61] T. R. Kane and D. A. Levinson. A realistic solution of the symmetric top problem. *Journal of Applied Mechanics*, 45(4):903–909, dec 1978.

[62] P. Kessler and O. O'Reilly. The ringing of euler's disk. *Regular and Chaotic Dynamics*, 7(1):49, 2002.

[63] A.-S. Koh and G. Mustafa. Free rocking of cylindrical structures. *Journal of Engineering Mechanics*, 116(1):35–54, jan 1990.

[64] A.-S. Koh, P. D. Spanos, and J. M. Roesset. Harmonic rocking of rigid block on flexible foundation. *Journal of Engineering Mechanics*, 112(11):1165–1180, nov 1986.

[65] P. R. Kraus, A. Fredriksson, and V. Kumar. Modeling of frictional contacts for dynamic simulation. In *Proceedings of IROS 1997 workshop on dynamic simulation: Methods and applications*, volume 28, pages 1–10. Citeseer, 1997.

[66] R. I. Leine. Measurements of the finite-time singularity of the euler disk. 2009.

[67] Y.-W. Li, Y.-Z. Wang, and Y.-B. Wang. Application of seismic resilient energy-dissipative rocking columns with HSS tension braces in steel frames. *Engineering Structures*, 253:113812, feb 2022.

[68] S. A. Linde, D. Konstantinidis, and M. J. Tait. Rocking response of unanchored building contents considering horizontal and vertical excitation. *Journal of Structural Engineering*, 146(9):04020175, sep 2020.

[69] M. Lowry, B. Farrar, D. Armendariz, and J. Podany. Protecting collections in the j. paul getty museum from earthquake damage. *WAAC newsletter*, 29(3):16–23, 2007.

[70] L. Luzi, R. Puglia, E. Russo, and ORFEUS Working Group 5. Engineering strong motion database (esm), 2015.

[71] N. Makris and M. F. Vassiliou. Planar rocking response and stability analysis of an array of free-standing columns capped with a freely supported rigid beam. *Earthquake Engineering & Structural Dynamics*, 42(3):431–449, jun 2012.

[72] G. Manos and M. Demosthenous. The behavior of solid or sliced rigid bodies when subjected to horizontal base motion. In *Proc. 4th U.S. Nat. Conf. on Earthquake Engrg., Earthquake Engineering Research Instititute, 3, 41-50*, 1990.

[73] F. Masi, I. Stefanou, P. Vannucci, and V. Maffi-Berthier. ROCKING RESPONSE AND OVERTURNING OF MUSEUM ARTEFACTS DUE TO BLAST LOADING. In *Proceedings of the 7th International Conference on Computational Methods in Structural Dynamics and Earthquake Engineering (COMPDYN 2015)*. Institute of Structural Analysis and Antiseismic Research School of Civil Engineering National Technical University of Athens (NTUA) Greece, 2019.

[74] MathWorks. matlabfunction (https://www.mathworks.com/help/symbolic/matlabfunction.html). *MathWorks.com*, 2019.

[75] MathWorks. Symbolic math toolbox (https://www.mathworks.com/products/symbolic.html). *MathWorks.com*, 2019.

[76] Michelangelo. David (https://commons.wikimedia.org/wiki/file: Jorg Bittner Unna, Wikimedia Commons, 1501-1504.

[77] H. K. Moffatt. Euler's disk and its finite-time singularity. *Nature*, 404(6780):833–834, apr 2000.

[78] T. B. Museum. The townley discobolus.

[79] U. L. of Congress. Stl (stereolithography) file format, binary (https://www.loc.gov/preservation/digital/formats/fdd/fdd000505.shtml). *Sustainability of Digital Formats: Planning for Library of Congress Collections*, September 2019.

[80] A. C. Or. The dynamics of a tippe top. 54(3):597–609, jun 1994.

[81] O. M. O'Reilly. The dynamies of rolling disks and sliding disks. *Nonlinear Dynamics*, 10(3):287–305, jul 1996.

[82] D. G. Parkyn. The inverting top. *The Mathematical Gazette*, 40(334):260–265, dec 1956.

[83] M. Pascal. Asymptotic solution of the equations of motion for a celtic stone. *Journal of Applied Mathematics and Mechanics*, 47(2):269–276, jan 1983.

[84] D. Petrie, J. L. Hunt, and C. G. Gray. Does the euler disk slip during its motion? *American Journal of Physics*, 70(10):1025–1028, oct 2002.

[85] R. H. Plaut. Rocking instability of a pulled suitcase with two wheels. *Acta Mechanica*, 117(1-4):165–179, mar 1996.

[86] R. Plaut, W. Fielder, and L. Virgin. Fractal behavior of an asymmetric rigid block overturning due to harmonic motion of a tilted foundation. *Chaos, Solitons & Fractals*, 7(2):177–196, feb 1996.

[87] M. Priestley, R. Evison, and A. Carr. Seismic response analysis of structures free to rock on their foundations. *Bull. of the New Zealand Seismological Soc. for Earthquake Eng, 11(3), 141-150*, 1978.

[88] I. N. Psycharis and P. C. Jennings. Rocking of slender rigid bodies allowed to uplift. *Earthquake Engineering & Structural Dynamics*, 11(1):57–76, jan 1983.

[89] P. R. Lipscombe and S. Pellegrino. Free rocking of prismatic blocks. *Journal of Engineering Mechanics*, 119:1387–1410, 07 1993.

[90] U. Roman. The doryphoros. *Minneapolis Museum of Art*, 120-50 BC.

[91] M. Saje and D. Zupan. The rattling of euler's disk. *Multidiscipline Modeling in Materials and Structures*, 2(1):49–66, jan 2006.

[92] C. L. Saux, R. I. Leine, and C. Glocker. Dynamics of a rolling disk in the presence of dry friction. *Journal of Nonlinear Science*, 15(1):27–61, feb 2005.

[93] A. Semechko. Rigid body parameters of closed surface meshes (https://www.github.com/antonsemechko/rigid-body-parameters). *GitHub*, 2019.

[94] L. F. Shampine and M. K. Gordon. *Computer solution of ordinary differential equations: the initial value problem*. Freeman, San Francisco, CA, 1975.

[95] H. W. Shenton III and N. P. Jones. Base excitation of rigid bodies. i: Formulation. *Journal of Engineering Mechanics*, 117(10):2286–2306, 1991.

[96] B. Shi, A. Anooshehpoor, Y. Zeng, and J. N Brune. Rocking and overturning of precariously balanced rocks by earthquakes. *Bulletin of the Seismological Society of America*, 86, 10 1996.

[97] G. G. Slabaugh. Computing euler angles from a rotation matrix.

[98] P. D. Spanos and A.-S. Koh. Rocking of rigid blocks due to harmonic shaking. *Journal of Engineering Mechanics*, 110(11):1627–1642, nov 1984.

[99] P. D. Spanos, P. C. Roussis, and N. P. Politis. Dynamic analysis of stacked rigid blocks. *Soil Dynamics and Earthquake Engineering*, 21(7):559–578, oct 2001.

[100] M. Srinivasan and A. Ruina. Rocking and rolling: A can that appears to rock might actually roll. *Phys. Rev. E*, 78:066609, Dec 2008.

[101] A. Stanislavsky and K. Weron. Nonlinear oscillations in the rolling motion of euler's disk. *Physica D: Nonlinear Phenomena*, 156(3-4):247–259, aug 2001.

[102] STLFILESFREE. Terracotta army (https://cults3d.com/en/3d-model/art/terracotta-army). Web, November 2017. Cults.

[103] J. Synge. LXX. on a case of instability produced by rotation. *The London, Edinburgh, and Dublin Philosophical Magazine and Journal of Science*, 43(342):724–728, jul 1952.

[104] I. The Mathworks. *atan2*. https://uk.mathworks.com/help/matlab/ref/atan2.html.

[105] E. Toolbox. Friction - friction coefficients and calculator. *Available at: https://www.engineeringtoolbox.com/friction-coefficients-d_778.html*, 2004.

[106] W. K. Tso and C. M. Wong. Steady state rocking response of rigid blocks part 1: Analysis. *Earthquake Engineering & Structural Dynamics*, 18(1):89–106, 1989.

[107] P. Várkonyi and G. Domokos. Mono-monostatic bodies: The answer to arnold's question. *The Mathematical Intelligencer*, 2006.

[108] P. L. Várkonyi, M. Kocsis, and T. Ther. Rigid impacts of three-dimensional rocking structures. *Nonlinear Dynamics*, dec 2021.

[109] P. Varkonyi and G. Domokos. Static equilibria of rigid bodies: Dice, pebbles, and the poincare-hopf theorem. *Journal of Nonlinear Science*, 16(3):255–281, may 2006.

[110] M. F. Vassiliou, S. Burger, M. Egger, J. A. Bachmann, M. Broccardo, and B. Stojadinovic. The three-dimensional behavior of inverted pendulum cylindrical structures during earthquakes. *Earthquake Engineering & Structural Dynamics*, 46(14):2261–2280, apr 2017.

[111] M. F. Vassiliou, K. R. Mackie, and B. Stojadinović. Dynamic response analysis of solitary flexible rocking bodies: modeling and behavior under pulse-like ground excitation. *Earthquake Engineering & Structural Dynamics*, 43(10):1463–1481, jan 2014.

[112] S. Veeraraghavan, J. F. Hall, and S. Krishnan. Modeling the rocking and sliding of free-standing objects using rigid body dynamics. *Journal of Engineering Mechanics*, 146(6):04020041, jun 2020.

[113] E. Voyagaki, I. N. Psycharis, and G. Mylonakis. Complex response of a rocking block to a full-cycle pulse. *Journal of Engineering Mechanics*, 140(6):04014024, jun 2014.

[114] E. W. Weisstein. Convex hull (https://demonstrations.wolfram.com/convexhull/). *From MathWorld–A Wolfram Web Resource.*, 2019.

[115] L. Yanheng and B. Shi. Response of 3d free axisymmetric rigid objects under seismic excitations. *Graduate University of Chinese Academy of Sciences, Beijing 100049, China*, 07 2008.

[116] C.-S. Yim and A. K. Chopra. Earthquake response of structures with partial uplift on winkler foundation. *Earthquake Engineering & Structural Dynamics*, 12(2):263–281, 1984.

[117] C.-S. Yim, A. K. Chopra, and J. Penzien. Rocking response of rigid blocks to earthquakes. *Earthquake Engineering & Structural Dynamics*, 8(6):565–587, 1980.

[118] S. C. S. Yim and H. Lin. Nonlinear impact and chaotic response of slender rocking objects. *Journal of Engineering Mechanics*, 117(9):2079–2100, sep 1991.

[119] J. Zhang and N. Makris. Rocking response of free-standing blocks under cycloidal pulses. *Journal of Engineering Mechanics*, 127(5):473–483, may 2001.

[120] D. Zulli, A. Contento, and A. D. Egidio. 3d model of rigid block with a rectangular base subject to pulse-type excitation. *International Journal of Non-Linear Mechanics*, 47(6):679–687, jul 2012.